2001

Rotational-resolved photoelectron spectroscopy and energy-selected photoelectron-photoion coincidence spectroscopy using synchrotron radiation

Song Yang
Iowa State University

INFORMATION TO USERS

This manuscript has been reproduced from the microfilm master. UMI films the text directly from the original or copy submitted. Thus, some thesis and dissertation copies are in typewriter face, while others may be from any type of computer printer.

The quality of this reproduction is dependent upon the quality of the copy submitted. Broken or indistinct print, colored or poor quality illustrations and photographs, print bleedthrough, substandard margins, and improper alignment can adversely affect reproduction.

In the unlikely event that the author did not send UMI a complete manuscript and there are missing pages, these will be noted. Also, if unauthorized copyright material had to be removed, a note will indicate the deletion.

Oversize materials (e.g., maps, drawings, charts) are reproduced by sectioning the original, beginning at the upper left-hand corner and continuing from left to right in equal sections with small overlaps.

Photographs included in the original manuscript have been reproduced xerographically in this copy. Higher quality 6" x 9" black and white photographic prints are available for any photographs or illustrations appearing in this copy for an additional charge. Contact UMI directly to order.

ProQuest Information and Learning
300 North Zeeb Road, Ann Arbor, MI 48106-1346 USA
800-521-0600

Rotational-resolved photoelectron spectroscopy and energy-selected photoelectron-photoion coincidence spectroscopy using synchrotron radiation

by

Yang Song

A dissertation submitted to the graduate faculty

in partial fulfillment of the requirements for the degree of

DOCTOR OF PHILOSOPHY

Major: Physical Chemistry

Program of Study Committee:
Cheuk-Yiu Ng, Major Professor
Mark S. Gordon
Gerald J. Small
Edward S. Yeung
Kai-Ming Ho

Iowa State University

Ames, Iowa

2001

UMI Number: 3034223

ProQuest Information and Learning Company
300 North Zeeb Road
P.O. Box 1346
Ann Arbor, MI 48106-1346

Graduate College

Iowa State University

This is to certify that the Doctoral dissertation of

Yang Song

has met the dessertation requirements of Iowa State University

Signatures have been redacted for privacy

For my Mom

TABLE OF CONTENTS

CHAPTER 1. INTRODUCTION

Dissertation Organization

All of the experiments presented in this thesis were performed at the Chemical Dynamics Beamline (CDB) associated with the Advanced Light Source (ALS), Earnest Orlando Lawrence Berkeley National Laboratory (LBNL) and University of California, Berkeley (UCB). Two major research projects are reported in this thesis, as Part I and Part II. Part I mainly discusses the development and application of so-called high resolution pulsed field ionization photoelectron (PFI-PE) spectroscopy, covered by chapter 2 (methodology and development) and chapter 3-6 (application on O_2 and NO). The second part reports the newly developed energy-selected pulsed field ionization photoelectron photoion coincidence (PFI-PEPICO) spectroscopy realized using multi-bunch synchrotron radiation (Chapter 7) and its application on several molecular systems (Chapter 8-10). The whole thesis consists of nine papers that are formatted for publication in professional journals. Five papers have been published previously, and the other four have been submitted for publication. Each paper appears as a separate chapter in the thesis. The figures, tables, and references contained in each chapter refer only to that particular chapter with the references given at the end of each chapter.

Overview

The vacuum ultraviolet (VUV) light source generated by synchrotron radiation operated by the Advanced Light Source (ALS) at Lawrence Berkeley National Laboratory (LBNL) is an excellent national facility with worldwide reputation as a highly efficient photon source. With its desirable energy range (6-30 eV), high photon flux (10^{12}), high resolution ($E/\Delta E$=120,000) and excellent stability and easy of tenability, quite a few chemical reactions critical to fundamental understanding of combustion, atmospheric, environmental and interstellar chemistry have been investigated as routine operation. The photon source consists of a 10-cm period undulator, a rare gas filter for the suppression of high-order undulator harmonics, and a 6.65-m off plane Eagle monochromator and three endstations to perform different experiments. (Figure 1-1.)

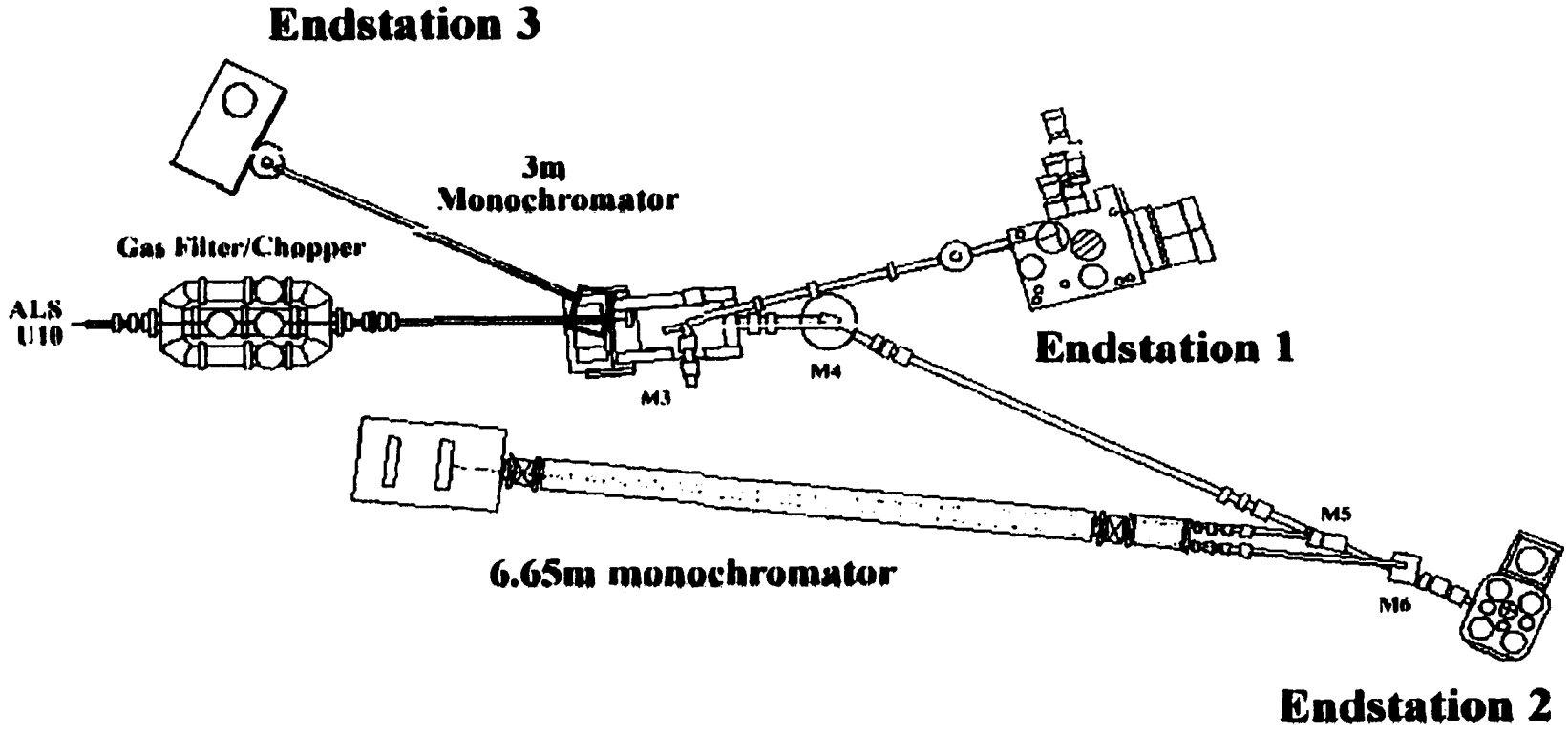

Figure 1-1 Schematic layout of Chemical Dynamics Beamline at Advance Light Source. This beamline consists of a 10 cm period undulator (upstream, not shown here), a gas filter equipped with a beam chopper, two monochromators, 6 mirrors and 3 endstations.

Endstation 2 is capable of high-resolution photoionization studies of major schemes, which will be discussed next. The schematic diagram of endstation 2 of CDB at ALS is shown in Figure 1-2. Basically, it consists of several differentially pumped chambers as labeled in the figure by several turbo molecular pumps (STP 400 ~ 2000) to maintain a vacuum of 10^{-8}~10^{-6} torr. The typical operation endstation 2 involves the linear time-of-flight photoion-photoelectron spectrometer (series of horizontal lenses) in the center of main chamber. Higher resolution mass spectroscopy requires the ion detection by the reflectron in tandem with the linear spectrometer. The recent collaborative ion-molecule reaction project with US Air Force employs the double octopole with a ion-molecule reaction cell followed by a quadrupole mass spectrometer.

One of the routine operational functionality of endstation 2 is the high resolution pulsed field ionization photoelectron measurements using monochromatized multibunch synchrotron radiation. By employing a simple electron time-of-flight (TOF) spectrometer, we show that PFI-PEs produced by the PFI in the dark gap of a synchrotron ring period can be cleanly separated from prompt background photoelectrons. A near complete suppression of prompt electrons was achieved in PFI-PE measurements by gating the PFI-PE TOF peak, as indicated by monitoring background electron counts at the Ar(11s') autoionizing Rydberg peak, which is adjacent to the $Ar^+(^2P_{3/2})$ PFI-PE band. . We have demonstrated instrumental resolutions of 1.0 cm^{-1} (FWHM) and 1.9 cm^{-1} (FWHM) in the PFI-PE bands for $Xe^+(^2P_{3/2})$ and $Ar^+(^2P_{3/2})$ at 12.123 eV and 15.760 eV, respectively. (Chapter 2) Using this scheme (and partially previous scheme using hemispherical energy analyzer, see M. Evans, ISU Ph.D. thesis, 1999), we have obtained rotationally resolved PFI-PE bands of $O_2^+(X^2\Pi_{3/2,1/2g}, V^+=0\text{-}38)$, $O_2^+(A^2\Pi_u, v^+=0\text{-}12)$ and $O_2^+(a^4\Pi_u, v^+=0\text{-}18)$ in the energy range of 12.05-18.2 eV (Chapter 3, 4 and 5) and $NO^+(a^3\Sigma^+, V^+ = 0\text{-}16)$ [co-authored article, not included in this thesis, see *J. of Chem. Phys.*, **111**,1937(1999)], $NO^+(A'^1\Sigma^-, v^+ = 0\text{-}17)$ [Chapter 6], and $NO^+(b\ ^3\Pi, w\ ^3\Delta, b^3\Sigma^-, W^1\Delta$ and $A^1\Pi$, analyzed and in preparation for publication, not included in this thesis) in the energy range of 15.6-20.4 eV. The analysis of many of these highly excited rovibronic states provides accurate spectroscopic constants for the first time.

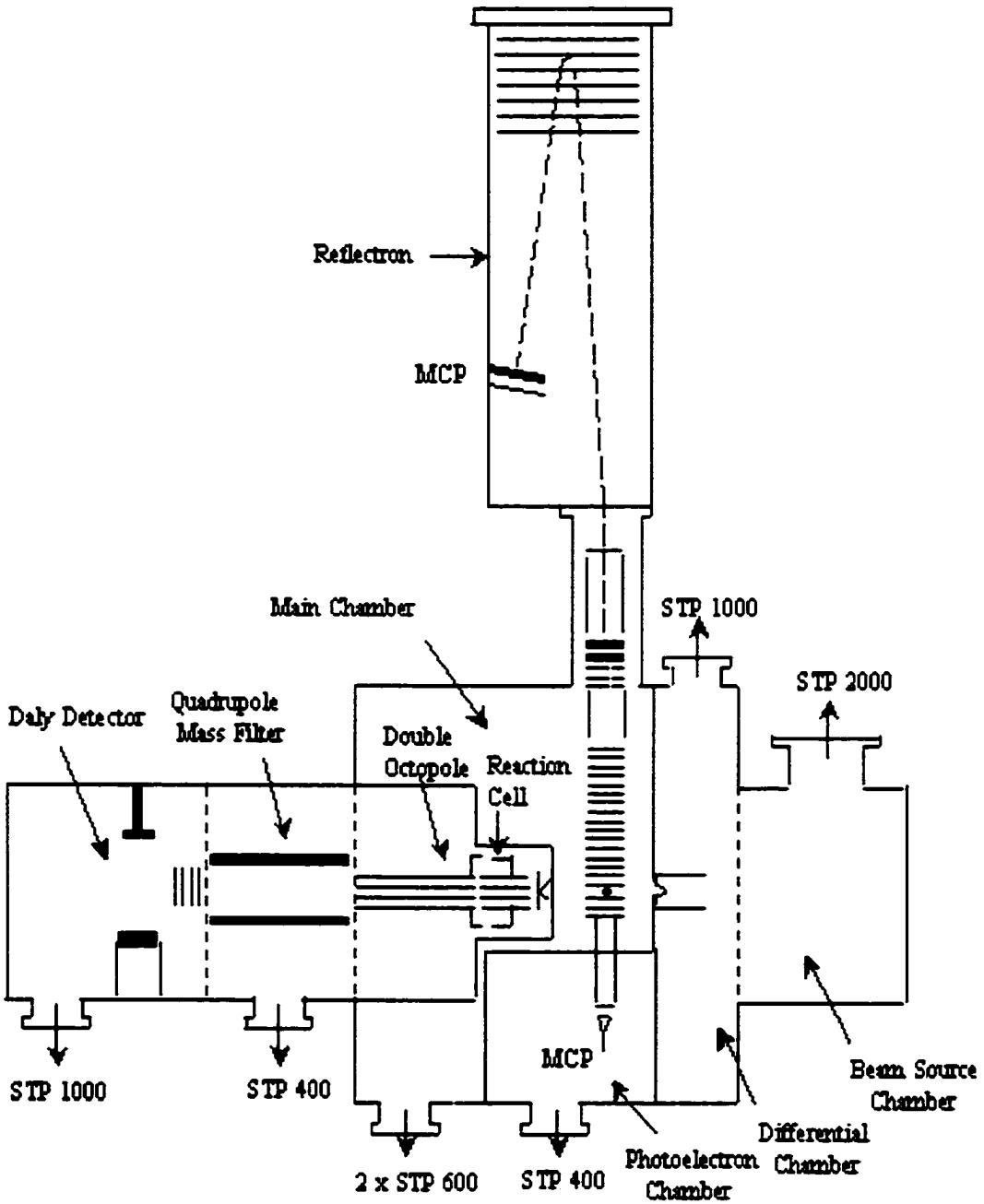

Fig 1-2 Schematic Diagram of Endstation 2.

Another novel scheme is the energy-selected high-resolution pulsed field ionization photoelectron photoion coincidence (PFI-PEPICO) measurement of the dissociation of small molecules using two and multi-bunch synchrotron radiation. We show that this technique provides an ion internal state (or energy) selection limited only by the PFI-PE measurement. Employing a shaped pulse for PFI and ion extraction, a resolution of 0.6 meV (FWHM) is observed in the PFI-PEPICO bands for $Ar^+(^2P_{3/2,1/2})$. As demonstrated in the PFI-PEPICO study of the process, $O_2 + h\nu \rightarrow O_2^-(b^4\Sigma_g^-, v^-=4, N^-) + e^- \rightarrow O^-(^4S) + O(^3P) + e^-$, the dissociation of $O_2^-(b^4\Sigma_g^-, v^-=4)$ in specific rotational N^- levels can be examined. (Chapter 7) The PFI-PEPICO study of the dissociation of CH_3^- from CH_4 also reveals the lifetime effects and dc field effects on the observed intensities for CH_3^- and CH_4^+. The observation of a step-like feature in the PFI-PE measurement confirms the lifetime switch mechanism. (Chapter 11) The high-resolution for PFI-PEPICO measurements, along with the ability to distinguish the CH_3^- fragments due to the supersonically cooled CH_4 beam from those formed by the thermal CH_4 sample, has allowed the determination of a highly accurate dissociation threshold for CH_3^- from CH_4. Similar studies are performed for C_2H_2, C_2H_5Br, iso-C_3H_7X (X=Br, I), CH_3X (X=Br, I), NH_3 and CD_4 so that highly accurate themochemical quantities are derived. [For, NH_3, CH_3X (X=Br, I) and CD_4, see chapter 8, 9 and 10, respectively. For other molecules, co-authored articles are not included in this thesis.]

Of these chapters, Chapter 3-6, 8-10 are first authored articles, while Chapter 2, 7 and 11 are co-authored articles, in which the author played an essential role in the experiments but involved in partial writing of the papers. Chapter 2 and 7 served as the methodology of PFI-PE and PFI-PEPICO, based on which the applications are developed and related molecular systems are investigated, discussed by Chapter 3-6 and 8-10, respectively. For this reason, these two articles are included in this dissertation. Chapter 11, published in *Physical Review Letters*, reported an important observation associated with PFI-PEPICO studies of many molecules. Dr. G.K. Jarvis and the author are the major contributors of the project, which was in collaboration with K.M Weitzel et al as visiting scientists. Therefore, it is appropriate to include this article as an important chapter as well.

PART I
ROTATIONAL-RESOLVED PULISED FIELD IONIZATION PHOTOELECTRON STUDY OF O_2^+ AND NO^+

CHAPTER 2. HIGH RESOLUTION PULSED FIELD IONIZATION PHOTOELECTRON SPECTROSCOPY USING MULTI-BUNCH SYNCHROTRON RADIATION: TIME-OF-FLIGHT SELECTION SCHEME

A paper published in *Review of Scientific Instruments*, **70**, 2615 (1999)

G.K Jarvis, Y. Song and C.Y. Ng

Abstract

We have developed an efficient electron time-of-flight (TOF) selection scheme for high resolution pulsed field ionization (PFI) photoelectron (PFI-PE) measurements using monochromatized multi-bunch undulator synchrotron radiation at the Advanced Light Source. By employing a simple electron time-of-flight (TOF) spectrometer, we show that PFI-PEs produced by the PFI in the dark gap of a synchrotron ring period can be cleanly separated from prompt background photoelectrons. A near complete suppression of prompt electrons was achieved in PFI-PE measurements by gating the PFI-PE TOF peak, as indicated by monitoring background electron counts at the Ar(11s') autoionizing Rydberg peak, which is adjacent to the $Ar^+(^2P_{3/2})$ PFI-PE band. The rotational-resolved PFI-PE band for H_2^+ ($X^2\Sigma_g^+$, $v^+=0$) measured using this electron TOF selection scheme is nearly free from residues of nearby autoionizating features, which were observed in the previous measurement by employing an electron spectrometer equipped with a hemispherical energy analyzer. This comparison indicates that the TOF PFI-PE scheme is significantly more effective in suppressing the hot-electron background. In addition to attaining a high PFI-PE transmission, a major advantage of the electron TOF scheme is that it allows the use of a smaller pulsed electric field and thus results in a higher instrumental PFI-PE resolution. We have demonstrated instrumental resolutions of 1.0 cm^{-1} (FWHM) and 1.9 cm^{-1} (FWHM) in the PFI-PE bands for $Xe^+(^2P_{3/2})$ and $Ar^+(^2P_{3/2})$ at 12.123 eV and 15.760 eV, respectively. These resolutions are more than a factor 2 better than those achieved in previous synchrotron based PFI-PE studies.

I. INTRODUCTION

Pulsed field ionization (PFI) photoelectron (PFI-PE) detection schemes are superior as spectroscopic techniques in terms of achievable resolutions compared to conventional threshold photoelectron (TPE) measurements.[1-3] In the discussion below, we refer to PFI-PEs and TPEs as electrons formed at energies slightly below and above, respectively, the true ionization energy (IE). The most common TPE detection schemes incorporate a steradiancy-type analyzer,[4-7] which is essentially a tube-like structure that defines a finite solid angle for the acceptance of electrons. Since TPEs are formed with near zero kinetic energies, their collection can be achieved using a small dc electric field, whereas hot or prompt electrons ejected isotropically with finite kinetic energies are strongly discriminated by the specific acceptance solid angle of the steradiancy analyzer. Since hot electrons moving directly towards the detector are not discriminated against, the transmission function of such analyzers results in a high-energy tail, that consequently limits the attainable resolution in TPE measurements. When an ionization threshold is close to strong autoionizing Rydberg states, undesirable residues of these nearby autoionization states are often observed in addition to true TPE peaks. The hot-electron tail of the transmission function can be reduced by combining the electron time-of-flight (TOF) technique[8,9] or by adding a differential energy analyzer, such as a hemispherical energy analyzer, in tandem to the steradiancy analyzer.[10] The employment of a differential energy analyzer has the disadvantage of lowering the electron transmission. Incorporating the electron TOF scheme in synchrotron based TPE measurements, Morioka and co-workers have demonstrated a resolution of 1 meV (FWHM).[11] However, this TOF-TPE method generally requires a single-bunch or a two-bunch synchrotron operation,[8,9,11] in which adjacent synchrotron light pulses are separated by ≈300 ns. Since the reduction in vacuum ultraviolet (VUV) intensities in a single- or a two-bunch mode is more than a factor of ten compared to that in a multi-bunch operation, the application of the TOF-TPE scheme has been limited in synchrotron based TPE measurements.

The laser based PFI-PE techniques[1-3] have been shown to overcome the hot-tail problem associated with the TPE transmission function. In the UV/VUV laser PFI-PE schemes, the PFI electric field, which ionizes high-n Rydberg species formed by

photoexcitation, is delayed by a few μs relative to the light pulse, thus allowing the prompt background electrons to escape from the detection zone and be eliminated from the final spectra. There is general agreement that the extended lifetimes for high-n Rydberg states observed in PFI-PE experiments are due to l- and m_l-mixings induced by stray electric fields and/or by coexisting background ions formed during laser-molecule interactions.[13,14] The PFI-PE resolution depends on both the laser optical band-pass and the strength (F) of the electric field pulse. Since the width[15] of PFI-PEs is proportional to $F^{1/2}$, the key to achieve a high PFI-PE resolution with a fixed optical band-pass is to apply a small F for the PFI. It has been shown previously that PFI-PE resolutions close to the laser optical band-pass are attainable.[1]

Recently, a novel synchrotron based PFI-PE experimental scheme has been developed by our group at the chemical dynamics beamline of the Advanced Light Source (ALS).[10,16-18] These experiments make use of the dark gap of 16-112 ns in the ALS synchrotron ring period to apply the ionizing electric field pulse. Using an electron spectrometer consisting of a steradiancy analyzer and a hemispherical energy analyzer arranged in tandem, we have shown that PFI-PEs can be detected with little contamination from prompt electron background for a delay of only ≈8 ns with respect to the beginning of the dark gap.[10,16,17] Limited by the nature of the previous synchrotron based PFI-PE scheme and also by a typically poorer optical resolution than that of UV/VUV lasers, the best PFI-PE resolution achieved was 3.2 cm^{-1} (FWHM) as illustrated in the observed PFI-PE band of $Kr^+(^2P_{3/2})$.[17] In previous PFI-PE experiments from the ALS, the minimization of prompt electron contaminations from nearby autoionizing states relies partly on the chromatic aberration of the electrostatic lens system.[10] In order to achieve a high PFI-PE transmission through the electron spectrometer, it is necessary to apply a sufficiently high pulsed electric field, which essentially sets the limit for the attainable PFI-PE resolution.[10] Even with extreme care in optimizing the PFI-PE electron spectrometer, a small high-energy transmission tail is still discernible in most previous synchrotron based PFI-PE measurements.[10,16-18] The discrimination of hot- electron background can be monitored by the electron counts at an energy corresponding to the Ar(1 1s′) Rydberg state, which lies ≈4.3 meV higher in energy than the $Ar^+(^2P_{3/2})$ PFI-PE band.[10,16,17] The background

electron intensity at Ar(11s') is usually found to be ≈1% of that at the $Ar^+(^2P_{3/2})$ PFI-PE peak. Although small, this incomplete suppression may still hamper identification of weak PE bands, especially in the presence of strong autoionizing structure.[18]

In this article, we describe a highly efficient synchrotron based PFI-PE detection method, which takes advantage of the TOF difference of prompt electrons and PFI-PEs. By employing a simple electron TOF spectrometer, we show that almost complete separation of PFI-PEs and prompt background electrons can be achieved. The gating of the PFI-PEs thus leads to a near complete suppression of prompt electrons. In the previous PFI-PE study of H_2^+ ($X\ ^2\Sigma_g^+$ v^+ = 0, 2, 9 and 11),[18] the PFI-PE spectra are found to be contaminated by residue peaks arising from many strong autoionizing Rydberg resonances. Consequently, the observed relative PFI-PE peak intensities may not reflect the actual PFI-PE cross sections. We show here that the PFI-PE band for H_2^+ ($X\ ^2\Sigma_g^+$ v^+ = 0) obtained using this new TOF PFI-PE scheme is essentially free from residues of strong autoionizing structures observed in the previous measurement.[18] Hence, the H_2^+ PFI-PE band recorded in this experiment should provide more reliable PFI-PE cross sections.

Furthermore, since the electron transmission of the TOF PFI-PE selection scheme is not strongly affected by the pulsed electric field for the PFI, a lower Stark electric field pulse can be used. This leads to higher achievable PFI-PE resolutions. To illustrate this advantage, we show below the PFI-PE bands for $Xe^+(^2P_{3/2})$ and $Ar^+(^2P_{3/2})$ recorded using the TOF PFI-PE method, achieving resolutions unmatched in previous synchrotron based PFI-PE experiments.[10,16-18]

II. EXPERIMENTAL CONSIDERATIONS

The experiments were carried out at the Chemical Dynamics Beamline[19-21] of the ALS associated with the Lawrence Berkeley National Laboratory. The Beamline consists of a 10 cm period undulator, a gas harmonic filter,[21] a 6.65m off-plane Eagle mounted monochromator and a photoelectron-photoion spectrometer, all of which have been described in detail previously.[10,16-21] In this experiment, Ar was used as the filter gas and thus high undulator harmonics at energies above the IE of Ar (15.760 eV) were essentially eliminated. The filtered undulator VUV light beam, which consists of predominantly the

first undulator harmonic, was directed into the monochromator, where the VUV photon beam was dispersed by either a 2400 lines/mm grating (dispersion = 0.64 Å/mm) or a 4800 lines /mm (dispersion = 0.32 Å/mm). The resulting monochromatic VUV beam was then focused into the photoionization/photoexcitation (PI/PEX) region of the photoelectron-photoion apparatus. In this experiment, monochromator entrance/exit slits used were either 10/10 or 30/30 μm. The photon energy calibration was achieved using the known IEs or photoionization transitions of Ar, Xe, and H_2.[17-19] All gas samples were introduced as an effusive beam through a metal orifice with a diameter of 0.5 mm at room temperature and a distance of 0.5 cm from the PI/PEX region.

The electron TOF spectrometer used in this study has been modified from the one used in our previous experiments.[10,16-19] The main difference was that the hemispherical analyzer has been removed and only a steradiancy analyzer was used as an electron TOF spectrometer. A schematic diagram showing the present lens arrangement for the electron and ion TOF detection can be seen in Fig. 2-1. The distance between lenses I1 and E1 was 1.0 cm. The mid-point between lenses I1 and E1 defined the PI/PEX region. The apertures in lenses E1 and E4 used here were 10 mm and 2 mm in diameter, respectively. Micro-spherical plates (MSP) were used as the electron and ion detectors.

The PFI schemes employed here and previously[13-19] make use of the dark gap – a short time lapse in every ring period, where no synchrotron light is emitted from the source. Typical operating conditions for the ALS have been changed slightly from our previous publications[16-18,20-26] to accommodate the various different timing experiments that take place at ours and other beamlines. Currently, the entire orbit contains 272 bunches each of 50 ps duration and separated by 2 ns. There is a 112-ns dark gap at the end of each ring period for removing ions formed in the orbit. Occasionally, a high current spike (typically 10 mA) is injected into the dark gap at bunch 312 relative to the first bunch after the dark gap. Even with this spike present, a true dark gap of 80 ns after the last of the multi-bunches is present, which is sufficient for performing our experiment, although electron discrimination is slightly poorer. All experiments presented here were carried out

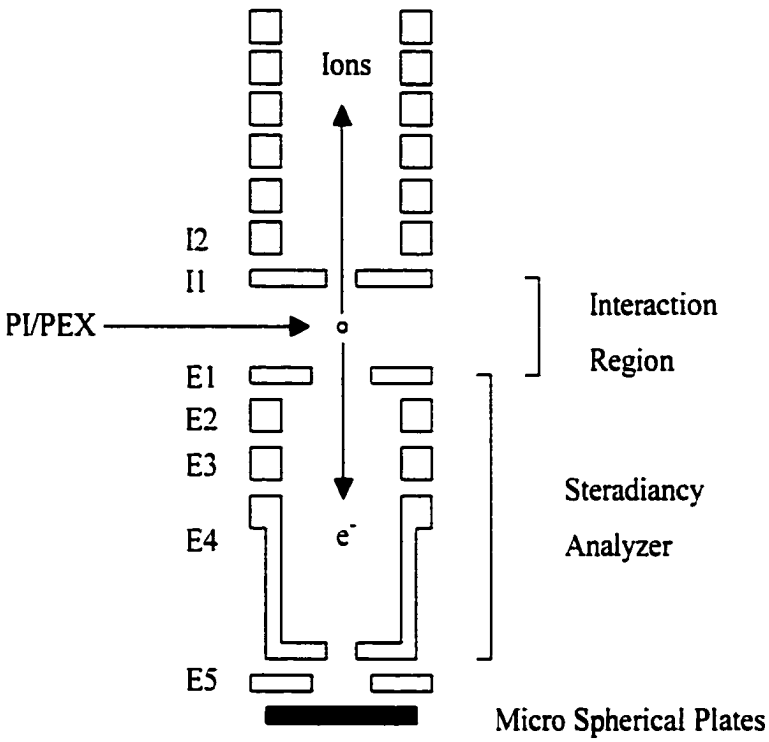

Figure 2-1. Schematic diagram showing the electrostatic lens arrangement, the ion and electron TOF spectrometer. The electron and ion detectors are micro-spherical plates (MSP). The ion drift tube and ion MSP detector are not shown in the figure.

during the normal multi-bunch operation of the ALS with no high-current spike, i.e., with a dark gap of 112 ns. However, we note that the TOF PFI-PE selection scheme described below can be implemented with a dark gap down to 80 ns.

Here, we use Ar as the gas sample to illustrate the TOF-PFI-PE selection method. In this scheme, a dc voltage of -0.14 V was applied to lens I1 for the purpose of hot electron extraction. Prior to the application of the electric field pulse, lens E1 was set at the ground potential. This has the effect of pushing hot electrons arising from autoionization and direct ionization towards the electron detector as soon as they were formed. Typical voltages applied to lenses I2, E2, E3, E4 and E5 were –20, 0.5, 3.0, 2.0, and 500 V, respectively. The front grid of the MSP was set at 500 V. The electron flight distance is 6.8 cm, which was determined by the distance between the PI/PEX region and E5. This flight distance, along with the voltage settings for the lenses, determines the TOF of prompt electrons. The TOF for PFI-PEs also depends on the height and width of the electric field pulse applied for the Stark field ionization.

Figure 2-2(a) shows the emitting pattern of the ALS light pulses in the multi-bunch operation. The two shaded areas represent stacks of uniformly spaced synchrotron micro-light bunches (width of individual bunches = 50 ps, separation between adjacent bunches = 2 ns). For clarity, the 112-ns dark gap is shown centered in the 656 ns ring period in Fig. 2-2(a). Following a delay of some 20-60 ns with respect to the beginning of the dark gap, an electric field pulse in the range of 0.3-1.5 V/cm was applied to lens E1 [see Fig. 2-2(b)]. The frequency of the electric field pulse for the PFI was 1.53 MHz, consistent with the ring period.

When the photon energy was set to coincide with the $Ar^+(^2P_{3/2})$ PFI-PE peak at 15.7596 eV, the observed TOF spectrum (solid circles) for PFI-PEs was found to exhibit a single peak with a full width of ≈40 ns as shown in Fig. 2-2(c). We note that the time zero of the TOF spectra shown in Fig. 2-2(c) corresponds to the triggering bunch-marking pulse provided by the ALS, the position of which is arbitrary. Partly due to the small VUV spot size (0.2x0.3 mm^2) at the PI/PEX region,[19] the observed TOF peak for PFI-PEs was expected to be narrow. We note that the observed full width of 40 ns is equal to the width of the electric field pulse for the PFI. This observation indicates that the PFI-PEs formed

Figure 2-2. The timing structures for (a) the pattern of VUV light bunches emitted in the ALS multi-bunch mode; (b) the electric field pulses applied to lens E1 (see Fig. 1); and (c) the electron TOF spectra of PFI-PEs (●) as observed at the $Ar^{+}(^{2}P_{3/2})$ PFI-PE peak and hot or prompt electrons (○) as observed at the Ar(1 1s') autoionizing state.

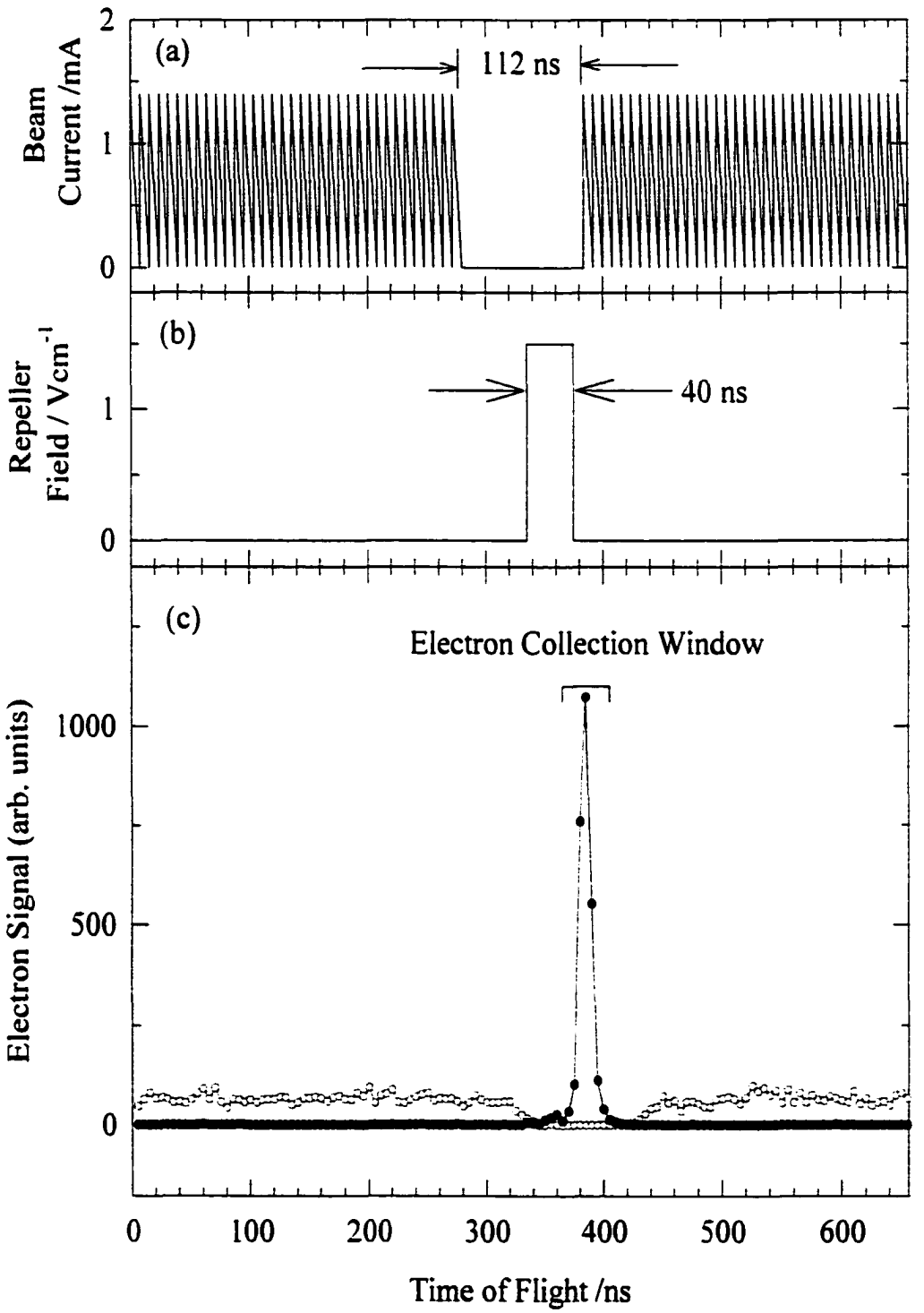
(a)
112 ns
Beam Current /mA
2
1
0
(b)
40 ns
Repeller Field / Vcm^{-1}
1
0
(c)
Electron Collection Window
Electron Signal (arb. units)
1000
500
0
0
100
200
300
400
500
600
Time of Flight /ns

within 40 ns during the application of the Stark pulses were highly mono-energetic with little dispersion as they traveled from the PI/PEX region to the electron MSP detector. No prompt electrons can be observed at 15.7596 eV because this energy is below the IE of Ar. It can be seen from the comparison with the positions of the Stark pulse [Fig.2-2(b)] and the TOF peak for PFI-PEs that the TOF for PFI-PEs from the PI/PEX region to the electron MSP detector is ≈50 ns. As the photon energy was slightly increased above the IE for the formation of $Ar^+(^2P_{3/2})$, the single TOF peak for PFI-PEs disappears and an electron TOF spectrum for prompt electrons resembling the synchrotron orbit pattern was observed as these electrons are extracted continuously by the small dc field. The electron TOF spectrum (open circles) observed using a 1.5 V/cm Stark pulse with the photon energy set at 15.7655 eV corresponding to the position of the Ar(11s') autoionizing Rydberg state is also shown in Fig. 2-2(c). In this spectrum, a small electron signal due to prompt electrons was observed uniformly in time except in a window of ≈110 ns corresponding to the width of the dark gap, where essentially no electrons were formed.

The location of the TOF peak for PFI-PEs in the TOF spectrum depends on the height of the Stark pulse and the delay with respect to the beginning of the dark gap. These parameters were adjusted such that the TOF peak for the PFI-PEs fell in the middle of the 110-ns TOF window where no hot electrons were observed and thus achieved a clear separation of prompt electrons from PFI-PEs. As a result, PFI-PEs can be easily detected free from background prompt electrons by setting a gate with a width corresponding to the width of the TOF peak for PFI-PEs as shown in Fig. 2-2(c).

The gating of the PFI-PE counts was done using a LeCroy Model 622 coincidence unit. The timing or bunch-marker pulse from the ALS was a NIM pulse that was ≈24 ns wide. This pulse was typically shaped down to 4 ns using a Stanford Research Systems (SRS) pulse generator. The PFI-PE signal arrived at the electron MSP was passed first through an amplifier and then a discriminator. The resulting PFI-PE signal pulse was further shaped using another SRS pulse generator to the range of 1-10 ns. In the present experiment, the width of the shaped PFI-PE signal pulse was typically set at 10 ns. The coincidence unit received the shaped bunch-marker pulse and the shaped PFI-PE signal pulse as inputs. We then changed the delay of the shaped PFI-PE signal pulse until it

overlapped with the shaped bunch-marker pulse. The coincidence unit only gave out an output pulse when the two pulses overlap. The minimum overlap between the two pulses is 1 ns. For a typical pulse width of 4 ns for the shaped bunch-marker pulse and that of 10 ns for the shaped electron signal pulse, the TOF resolution or effective gate width was 16 ns. Higher TOF resolutions down to 1 ns can be obtained, though this proved unnecessary due to the adequate separation of electron TOFs. We have used a gate width varied in the range of 20-40 ns and found that the increase of the PFI-PE counts was small. The prompt electron suppression efficiency decreases rapidly when the gate width was increased to >40 ns, in accordance with the TOF spectra observed in Fig. 2-2(c). We note that the width of the PFI-PE TOF peak depends on the height and width of the Stark pulse.

We found that even with lenses I1 and E1 held at 0 V dc, field penetration from adjacent lenses I2 and E2 still allowed for extraction of the prompt electrons toward the electron detector with sufficient time separation for discrimination. The TOF spectrum for prompt electrons observed with the photon energy set at the Ar(11s') autoionizing Rydberg state using a nominal dc repeller field of 0 V/cm for the PI/PEX region was similar to that (open circles) shown in Fig. 2-2(c).

III. RESULTS

In order to illustrate the superior performance of the TOF PFI-PE scheme as compared to the previous synchrotron based PFI-PE method[16-18,22-26] in terms of the achievable resolution and prompt electron background suppression, we show below the PFI-PE spectra for $Ar^+(^2P_{3/2})$, $Xe^+(^2P_{3/2})$, and $H_2^+(v^+=0, N^+)$ obtained using the TOF PFI-PE method.

A. PFI-PE bands for Ar^+ ($^2P_{3/2}$) and Xe^+ ($^2P_{3/2}$)

Figure 2-3(a) depicts the photoelectron spectrum for Ar in the region of 15.768-15.773 eV observed by collecting all electrons arriving at the electron MSP detector. In this case, the electron TOF spectrometer performed as a steradiancy analyzer for TPE detection. The 2400 lines/mm grating was used with monochromator entrance/exit slits set at 30/30 μm. As expected, the spectrum shown in Fig. 2-3(a) is essentially a TPE spectrum exhibiting the characteristic hot electron tail. The intensity of the autoionizing Ar(11s'') Rydberg peak [marked in Fig. 2-3(a)] is stronger than that of the $Ar^+(^2P_{3/2})$ TPE peak. The

Figure 2-3 (a) TPE spectrum for Ar in the range 15.756–15.770 eV observed by collecting all electrons arrived at the electron MSP detector. The electron TOF spectrometer was used as a steradiancy analyzer. (b) PFI-PE spectrum for Ar in the range 15.756–15.770 eV obtained using the TOF PFI-PE selection scheme. The 2400 lines/mm was used. The monochromator entrance/exit slits are set at 30/30 μm for both (a) and (b) corresponding to a nominal wavelength resolution of 0.0192 Å (FWHM).

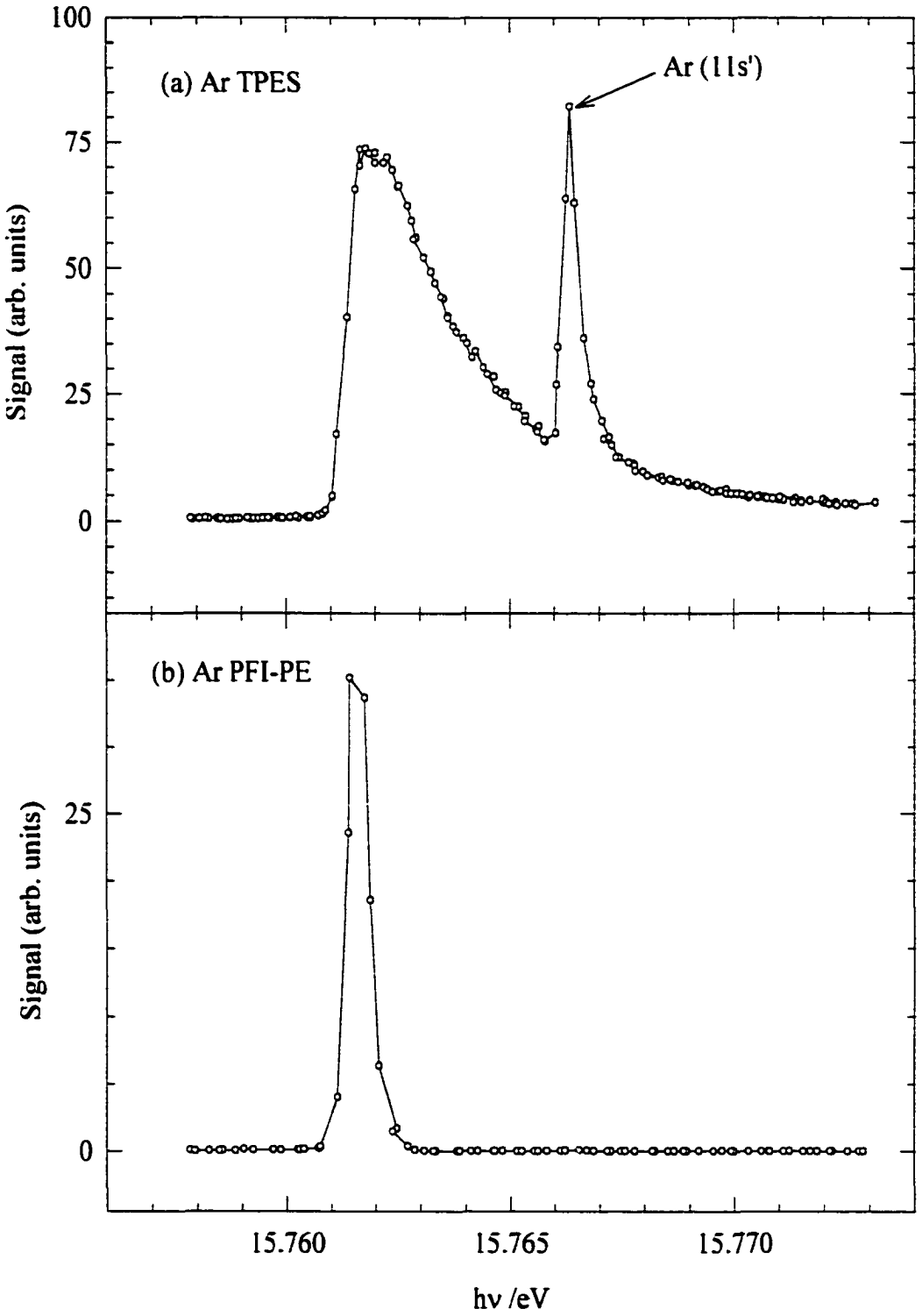
(a) Ar TPES
Ar (11s')
Signal (arb. units)
100
75
50
25
0
(b) Ar PFI-PE
Signal (arb. units)
25
0
15.760
15.765
15.770
hν /eV

PFI-PE band for $Ar^+(^2P_{3/2})$ depicted in Fig. 2-3(b) was recorded using a nominal dc field of 0 V/cm across lenses I1 and E1 and a 1.5 V/cm pulsed electric field of 40 ns duration for the PFI. As shown in Fig. 2-3(b), a near complete suppression of the Ar(11s') was achieved. The actual intensity at Ar(11s') was <0.2 % of the $Ar^+(^2P_{3/2})$ intensity when the above TOF gating scheme was incorporated. This is approximately 10 times better than previous results obtained using a hemispherical analyzer for PFI-PE detection.[10]

As pointed out above, the previous PFI-PE detection scheme using a hemispherical energy analyzer requires a sufficiently high Stark pulse for attaining a high electron transmission. The relatively high Stark pulse required also limits the attainable PFI-PE resolution. The transmission of PFI-PEs in this TOF selection scheme does not have a strong dependence on the applied pulsed electric field. Figures 2-4(a) and 2-4(b) show the PFI-PE bands of $Xe^+(^2P_{3/2})$ and $Ar^+(^2P_{3/2})$ in the regions of 12.128-12.131eV and 15.758-15.762 eV, respectively, measured using the TOF PFI-PE detection method. The pulsed field used in these measurements was ≈0.3 V/cm. The Gaussian fit to these PFI-PE spectra reveals a resolution of 1.0 cm^{-1} (FWHM) for the $Xe^+(^2P_{3/2})$ bands and 1.9 cm^{-1} (FWHM) for the $Ar^+(^2P_{3/2})$ band. These resolutions are more than a factor of two better than the best resolutions recorded for these PFI-PE bands in previous ALS experiments and are close to the best resolution (0.8 cm^{-1}, FWHM) reported using VUV laser PFI-PE techniques at ≈18 eV.[27] The resolutions of these spectra are limited by both the VUV optical resolution and the pulsed field used. We expect that the optical resolution can be improved by operating the monochromator in second or third order. Hence, the attainable resolution for this TOF PFI-PE method can be further improved.

B. PFI-PE band for H_2^+ ($X\ ^2\Sigma_g^+$, $v^+ = 0$)

The PFI-PE spectrum for H_2^+ ($X\ ^2\Sigma_g^+$, $v^+ = 0$) in the energy range of 15.34-15.47 eV obtained using the TOF PFI-PE scheme with a 0 V/cm dc field at the PI/PEX region and 1.5 V/cm Stark pulsed field is depicted in Fig. 2-5(a). Using the 2400 lines/mm grating and monochromator entrance/exit slits sizes of 10/10 μm, the nominal wavelength resolution used was 0.0064 Å (FWHM). Figure 2-5(b) shows the H_2^+ ($X\ ^2\Sigma_g^+$, $v^+ = 0$) spectrum in the same energy range recorded previously using a tandem steradiancy-

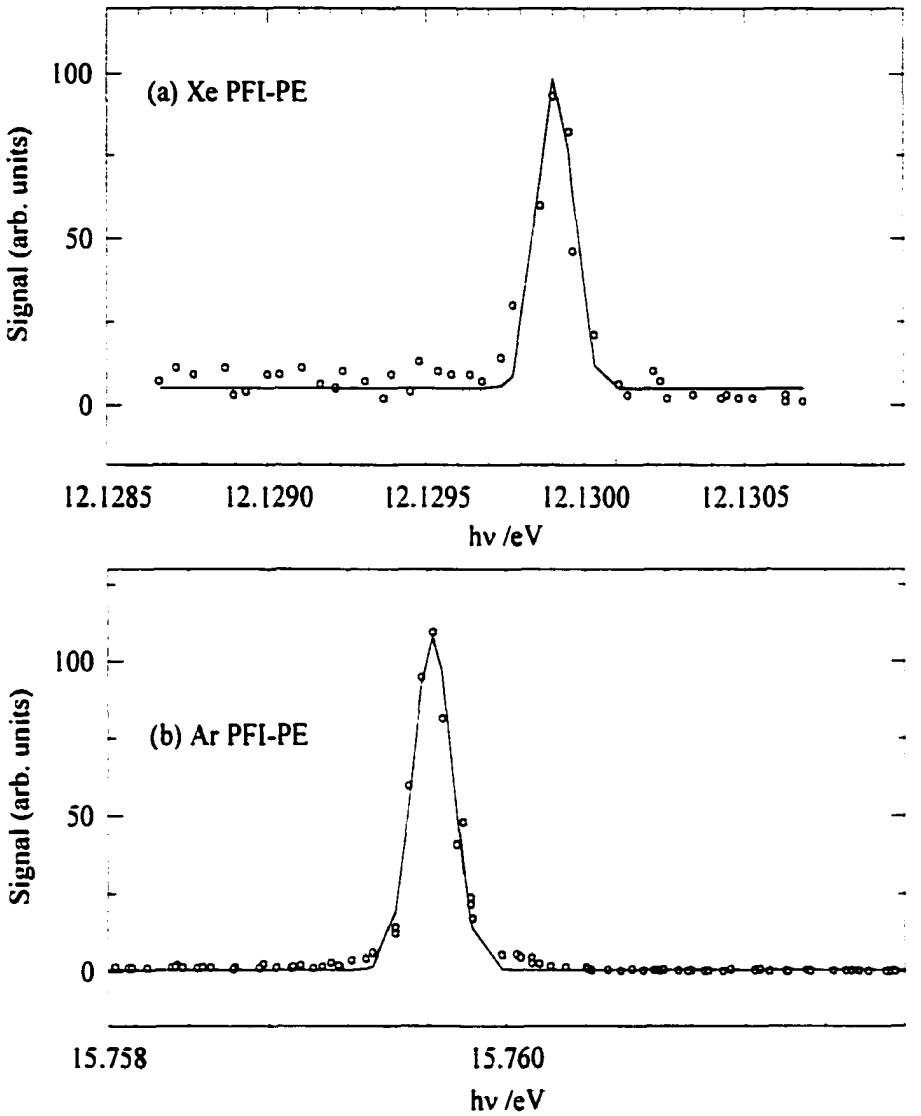

Figure 2-4 (a) PFI-PE band for $Xe^{+}(^{2}P_{3/2})$ (open circles) obtained using a pulsed field of 0.3 V/cm. A Gaussian fit obtained using a least squares fit is also shown (line), revealing a FWHM maximum of 1.0 ± 0.2 cm^{-1}. (b) Experimental PFI-PE band for $Ar^{+}(^{2}P_{3/2})$ (open circles) obtained using a pulsed field of 0.3 V/cm. A Gaussian fit obtained using a least squares fit is also shown (line), revealing a FWHM of 1.9 ± 0.3 cm^{-1}. The 4800 lines/mm grating was used. The monochromator entrance/exit slits are set at 30/30 μm for both (a) and (b) corresponding to a nominal wavelength resolution of 0.0096 Å (FWHM).

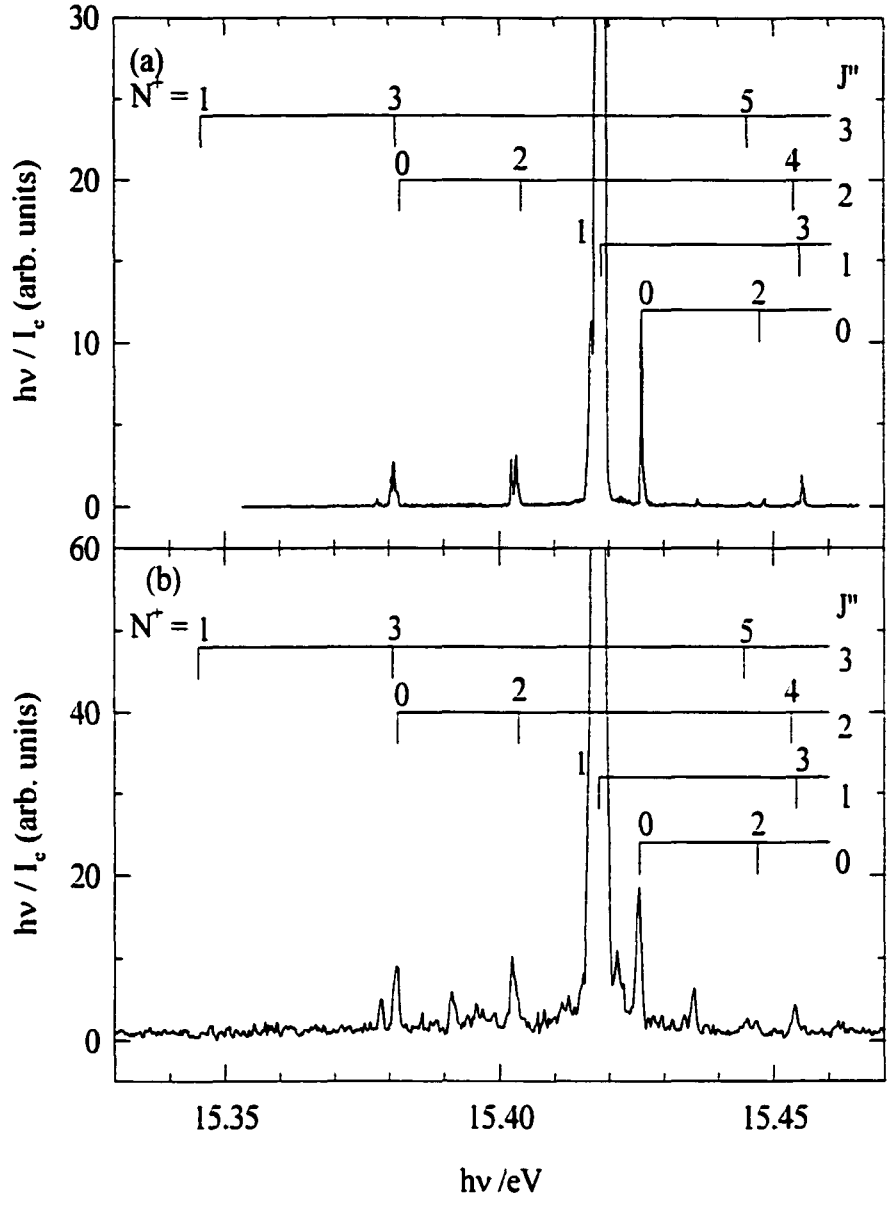

Figure 2-5 PFI-PE spectrum for H_2^+ ($X^2\Sigma_g^+$, $v^+ = 0$) recorded (a) using electron TOF analysis with a 0 V/cm dc field , and a 1.5 V/cm pulsed field across the interaction region. The 4800 lines grating was used. The monochromator entrance/exit slits are set at 10/10 μm corresponding to a nominal resolution of 0.0064 Å (FWHM), (b) using a hemispherical and steradiancy analyzer in tandem and a 0.67 V cm^{-1} pulsed field at a nominal wavelength resolution of 0.048 Å (FWHM).

hemispherical spectrometer at a nominal optical resolution of 0.048 Å [see Fig. 2-5(b)].[18] We note that the actual resolution is always lower than the nominal resolution. On the basis of previous measurements, we estimate that the actual resolution for the spectra of Fig. 2-5(a) was 0.013 Å (FWHM), a factor two lower than the nominal resolution. The actual resolution for the spectrum of Fig. 2-5(b) was expected to be similar to the nominal resolution of 0.05 Å (FWHM). The pulsed electric field used for recording the spectrum of Fig. 2-5(b) was 0.67 V/cm.

The positioning of rotational transitions (N^+, J″) from rotational J″ levels for H_2 to rotational N^+ levels for H_2^+ are marked in Figs. 2-5(a) and 2-5(b). By far the strongest peaks in these spectra are the (1,1) transitions. The strength of this transition is shown to result from the coupling with a near-resonance low-*n* Rydberg state converging to a high ionization threshold.[28] The resolution of the spectrum shown in Fig. 2-5(a) is better than that of Fig. 2-5(b). This is due in part to a better wavelength resolution used in the measurement of the spectrum of Fig. 2-5(a). In the previous experiment,[18] we had examined the achievable resolution by using a higher wavelength resolution and found that the observed PFI-PE resolution could not be significantly improved because of contamination by strong nearby autoionizing resonances as shown in Fig. 2-5(b). In view of this pervious exercise, we may conclude that the higher resolution observed in Fig. 2-5(a) is due partly to a better suppression of prompt electrons. Nearly all the background peaks originating from strong autoionizing states seen in Fig. 2-5(b) are suppressed in the spectrum of Fig. 2-5(a). Two exceptions are the peaks observed at 15.378 and 15.436 eV, which cannot be accounted for by direct ionization processes. These correspond to relatively intense autoionizing states observed in the photoionization cross section[29] and their observation here reflects the fact that suppression of hot electrons is still not complete.

The strongest (1, 1) peaks of Figs 2-5(a) and 2-5(b) are normalized to the same intensities. The relative intensities for other rotation transitions observed in Fig. 2-5(a) are weaker than those resolved in Fig. 2-5(b). Nevertheless, the relative intensities for (N^+, J″) transitions observed in Figs. 2-5(a) and 2-5(b) are in reasonable agreement. Since the spectrum of Fig. 2-5(a) is essentially free from contamination of autoionizing resonances,

it provides a more reliable measure for the relative photoionization cross sections of the marked rotational transitions. Based on the FWHM of the (0, 0) transition, we estimate that the PFI-PE resolution for the spectrum of Fig. 2-5(a) is 2.5 cm^{-1} (FWHM), significantly higher than ≈7 cm^{-1} (FWHM) attained in the spectrum of Fig. 2-5(b). The (0, 2) and (4, 2) transitions, which completely overlap with the stronger (3, 3) and (3, 1) transitions, respectively, in Fig. 2-5(b), are resolved into shoulder peaks in Fig. 2-5(a). In the present experiment, a doublet is observed at the position of the (2, 2) transition. Furthermore, a shoulder peak is evident at the low energy side of the (1, 1) transition. The detailed simulation of the H_2^+ PFI-PE spectra using the multichannel quantum defect theory is in progress and will be published elsewhere.[28]

IV. DISCUSSION

The spectra presented in Figs. 4(a), 4(b), 5(a) and 5(b) have demonstrated that the TOF PFI-PE detection method described here is superior compared to the previous synchrotron based PFI-PE measurement schemes[10] in both resolution and background electron suppression. The basic difference between this and the previous arrangement is that the hemispherical energy analyzer is eliminated in the present setup. Consequently, the electron transmission through the analyzer should be higher. Since the TOF axis is perpendicular to the VUV light beam, the TOF resolution is determined only by the height of the VUV beam along the TOF axis. It should be possible to significantly increase the PFI-PE signal by enlarging the entrance and exit apertures of the TOF spectrometer without affecting the TOF resolution. When a 0 V/cm dc electric field is maintained at the PI/PEX region, it is possible to adjusted the height and width of the Stark electric field pulse such that the PFI-PEs formed in the PI/PEX region remain essentially mono-energetic as they travel toward the MSP detector. When this condition is fulfilled, the TOF peak measured by the electron MSP detector is expected to be narrow and be independent of the entrance and exit apertures of the electron TOF spectrometer.

One of the advantages of synchrotron based PFI-PE experiments is that the measured effective lifetimes for high-*n* Rydberg states are less susceptible to perturbation of ions due to the low ion density produced in a synchrotron experiment.[18,25,26] However,

the maximum lifetimes that can be measured by the previous synchrotron based PFI-PE scheme is shown to be limited by the velocity of the neutral Rydberg species and the size of the acceptance aperture for PFI-PE detection.[18,25,26] For example, for an electron acceptance zone defined by a circular aperture of 3 mm in diameter, a thermal Rydberg species of mass 30 amu is expected to move out of the acceptance zone in 2.0 μs. Thus, if the effective lifetime for these high-*n* Rydberg species is >2.0 μs. it cannot be measured using the previous PFI-PE scheme. Since the TOF PFI-PE detection scheme can be made using large entrance and exit apertures, this limitation for effective lifetime measurements does not apply to this TOF PFI-PE method.

In photoelectron-photoion coincidence (PEPICO) measurements, the extraction of the correlated photoion is often triggered by the arrival of the photoelectron to the electron detector. If the TOF of the photoelectron is long, the correlated ion may move away from the ion detection zone and thus significantly lower the sensitivity of PEPICO measurements. In the present TOF PFI-PE detection scheme, the use of a short TOF spectrometer has shortened the electron TOF from the PI/PEX region to the electron detector to ≈50 ns, making it an attractive scheme for coincidence measurements.[30]

ACKNOWLEDGEMENTS

This work was supported by the Director, Office of Energy Research, Office of Basic Energy Sciences, Chemical Science Division of the U.S. Department of Energy Under Contract No. W-7405-Eng-82 for the Ames Laboratory and Contract No. DE-AC03-76SF00098 for the Lawrence Berkeley National Laboratory.

References

1 *High Resolution Laser Photoionization and Photoelectron Studies*, edited by I. Powis, T. Baer and C. Y. Ng. Wiley Series in Ion Chemistry and Phsics. (Wiley, Chichester 1995).

2 G. Reiser, W. Habenicht, K. Muller-Dethlefs and E. W Schlag, *Chem. Phys. Lett.* **152**, 119 (1988)

3 K. Muller-Dethlefs, M. Sander, and E. W Schlag, *Z Naturforsch. Teil A*, **39**, 1089 (1984)

4 D. Valerjo, R. R. Herm and M. G. Inghram, *J. Chem. Phys.* **46**, 4495 (1967).

5 W. B. Peatman, T.B. Borne and E. W. Schlag, *Chem. Phys. Lett.* **3**, 492 (1969).

6 T. Baer, W. B. Peatman and E. W. Schlag, *Chem. Phys. Lett.* **4**, 243 (1969).

7 R. Spohr, P. M. Guyon, W. A. Chupka and J. Berkowitz, *Rev Sci. Instrum.* **42**, 1872 (1971).

8. E. Waterstradt, R. Jung, H.-J Deitrich and K. Muller-Dethlefs, *Rev. Sci Instrum.* **64**, 3104 (1993)

9. R. I. Hall, A. McConkey, K. Ellis, G. Dawber, L. Avaldi, M. A. MacDonald, and G. C. King, *Meas. Sci. Technol.* **3**, 316 (1992).

10. C.-W. Hsu, M. Evans, P. A. Heinmann, and C. Y. Ng, *Rev. Sci. Instrum.*, **68**, 1694 (1997).

11. Y. Morioka, Y. Lu, T. Matsui, T. Tanaka, H. Yoshii, T. Hayaishi, and R. I. Hall, *J. Chem. Phys.* **104**, 9357 (1996).

12. K. –M. Weitzel and F. Guthe, *Chem. Phys. Lett.* **251**, 295 (1996).

13. W. A. Chupka, *J. Chem. Phys.* **98**, 4520 (1993).

14. J. Jortner and M. Bixon, *J. Chem. Phys.* **99**, 3133 (1995).

15. T. F. Gallagher, *Rydberg Atoms* (Cambridge University Press, Cambridge, 1994).

16. C.-W. Hsu, P. A. Heinmann, M. Evans, S. Stimson, T. Fenn, and C. Y. Ng, *J.Chem. Phys.* **106**, 8931 (1997).

17. C.-W. Hsu, M. Evans, S. Stimson, C. Y. Ng, and P. Heimann, *Chem. Phys.* **231**, 121 (1998).

18. S. Stimson, Y.-J Chen, M. Evans, C.-L Liao, C.Y. Ng, C.-W Hsu and P. Heimann, *Chem. Phys. Lett.* **289**, 507 (1998).

19. P. Heinmann, M. Koike, C.-W. Hsu, M. Evans, K. T. Lu, C. Y. Ng, A. Suits, and Y. T. Lee, *Rev. Sci. Instrum.*, **68**, 1945 (1997).

20. C.-W. Hsu, M. Evans, P. Heinmann, K. T. Lu, and C. Y. Ng, *J. Chem Phys.* **105**, 3950 (1996).

21. A.G. Suits, P. Heinmann, X. Yang, M. Evans, C.-W. Hsu, D. A. Blank, K. -T, Lu, A. Kung, and Y. T. Lee, *Rev. Sci. Instrum.* **66**, 4841 (1995).

22. R. C. Shiell, M. Evans, S. Stimson, C.-W. Hsu, C. Y. Ng, and J. W. Hepburn, *Phys. Rev. Lett.* **80**, 472 (1998).

23. S. Stimson, M. Evans, C. Y. Ng, C. Destandau, G. Chambaud, P. Rosmus, C.-W. Hsu, and P. Heimann, *J. Chem. Phys.* **108**, 6205 (1998).

24. C.-W. Hsu, M. Evan, S. Stimson, and C. Y. Ng, *J. Chem. Phys.* **108**, 4701 (1998).

25. C.-W. Hsu, M. Evans, S. Stimson, and C. Y. Ng, *J. Chem. Phys.* **109**, 1285 (1998).

26. M. Evans, S. Stimson, C. Y. Ng, C.-W. Hsu, and G. K. Jarvis, *J. Chem. Phys.* **110**, xxxx (1999).

27. H. Palm and F. Merkt, *Chem. Phys. Lett.* **284**, 419 (1998).

28. G. K. Jarvis, C.-L. Liao, S. Stimson, M. Evans, Y. Song, S.-Q. Hou, C. Y. Ng, and T. Softley, to be published.

29. P. Dehmer and W. A. Chupka, *J. Chem. Phys.* **65**, 2243 (1976).

30. G. K. Jarvis, Y. Song, and C. Y. Ng, *Rev. Sci. Instrum.*, in preparation.

CHAPTER 3. ROTATIONALLY RESOLVED PULSED FIELD IONIZATION PHOTOELECTRON BANDS OF $O_2^+(X^2\Pi_{3/2,1/2g}, v^+=0\text{-}38)$ IN THE ENERGY RANGE OF 12.05-18.15 eV

A paper published in *Journal of Chemical Physics*, **111**, 1905 (1999)

Y. Song, M. Evans, C.Y. Ng, C.-W. Hsu and G. K. Jarvis

Abstract

We have obtained rotationally resolved pulsed field ionization photoelectron (PFI-PE) spectra for O_2 in the energy range of 12.05-18.15 eV, covering ionization transitions $O_2^+(X^2\Pi_{1/2,3/2g}, v^+=0\text{-}38, J^+) \leftarrow O_2(X^3\Sigma_g^-, v^+=0, N'')$. While the PFI-PE bands for $O_2^+(X^2\Pi_{1/2,3/2g}, v^+ = 3\text{-}5, 9, 11, 12, 22,$ and 25-38) reported here are the first rotational-resolved photoelectron measurements, the PFI-PE bands for $O_2^+(X^2\Pi_{1/2,3/2g}, v^+=25\text{-}38)$ represent the first rotationally resolved spectroscopic data for these states. The simulation of spectra obtained at rotational temperatures of about 20 and 220 K allows the unambiguous identification of $O_2^+(X^2\Pi_{1/2,3/2g}, v^+\geq 21)$ PFI-PE bands, the majority of which overlap with prominent PFI-PE bands for $O_2^+(A^2\Pi_u, v^+=0\text{-}12)$ and $O_2^+(a^4\Pi_u, v^+=0\text{-}18)$. Combining with spectroscopic data obtained in the previous emission study and the present PFI-PE experiment, we have obtained accurate Duham-type expansion coefficients for ionization energies, vibrational constants, rotational constants, and spin-orbit splitting constants covering the $O_2^+(X^2\Pi_{1/2,3/2g}, v^+=0\text{-}38)$ states. Significant local intensity enhancements due to near-resonant autoionization were observed in PFI-PE bands for $O_2^+(X^2\Pi_{1/2,3/2g}, v^+ =0\text{-}14)$. The energy region of these states is known to manifest a high density of very strong autoionizing low-*n* Rydberg states. The observation of a long PFI-PE vibrational progression with a relatively smooth band intensity profile is also in accord with the direct excitation model for the production of highly vibrationally excited $O_2^+(X^2\Pi_{1/2,3/2g})$ states in the Franck-Condon gap region. Since this experiment was carried out under relatively high rotational temperatures for O_2, the PFI-PE data reveal higher rotational transitions and numerous local intensity enhancements, which were not observed

in previous vacuum ultraviolet laser studies using a cold O_2 molecular beam. The rotational branches found here indicate that photoelectrons are formed predominantly in continuum states with orbital angular momenta l = 1,3 and 5.

I. INTRODUCTION

The development of pulsed field ionization photoelectron (PFI-PE) techniques has resulted in great improvement in energy resolution for photoelectron spectroscopic studies.[1-3] The application of PFI-PE methods has not only allowed more accurate spectroscopic measurements for cations, but also more detailed investigations of molecular photoionization dynamics of small molecules by providing information about the photoelectron continuum states.[3] The majority of previous single-photon PFI-PE studies have been performed using vacuum ultraviolet (VUV) laser sources.[4-8] The recent demonstration[9-13] of PFI-PE measurements by employing high-resolution monochromatized multi-bunch synchrotron radiation has greatly increased the energy range (6-30 eV) of experimentation as compared to that (<19 eV) accessible in VUV laser studies. The most attractive feature of a synchrotron light source is its ease of tunability, making rotationally resolved PFI-PE measurements for many molecules a routine operation.[14-20]

Accurate spectroscopic constants for the $O_2^+(X\ ^2\Pi_{1/2,3/2g},\ v^+\leq 11)$ states has been determined in a comprehensive analysis of the $O_2^+(A^2\Pi_u) \rightarrow O_2^+(X\ ^2\Pi_g)$ emission system.[21] Threshold photoelectron (TPE) and PFI-PE detection schemes have been shown to be valuable for probing highly vibrationally excited states for cations lying in the Franck-Condon gap region, which is not accessible by normal optical spectroscopy methods.[8,22-26] The recent rotationally resolved molecular beam PFI-PE study of Kong and Hepburn using tunable VUV lasers have greatly extended the spectroscopic data for higher vibrational levels of $O_2^+(X\ ^2\Pi_{1/2,3/2g})$ up to v^+=24.[8] Despite this heroic experiment, which covers the widest energy range of all previous VUV laser studies, energy gaps, where the $O_2^+(X\ ^2\Pi_{1/2,3/2g},\ v^+$=3-5 and 9, 11, and 12) states appear, have not yet been examined. The previous VUV laser studies[6,8] used a cold supersonic O_2 beam. Consequently, individual

vibrational PFI-PE bands are restricted only to transitions originated from a few low rotational levels of $O_2(X^3\Sigma_g^-)$. In a recent high-resolution TPE study, highly excited vibrational bands up to v^+=43 have been observed.[25]

In this paper, we present the analysis of PFI-PE data for $O_2^+(X\ ^2\Pi_{1/2,3/2g}, v^+$=0-38) obtained using high-resolution monochromatized multi-bunch synchrotron radiation at Chemical Dynamics beamline[27] of the Advanced Light Source (ALS). Similar synchrotron based PFI-PE studies on $O_2^+(b^4\Sigma_g^-, 2^2\Pi_u, B^2\Sigma_g^-, {}^2\Sigma_u^-$; and $c^4\Sigma_u^-)$,[11,12,18-20] $NO^+(X^1\Sigma^+, v^+$ = 0-32),[21] $H_2^+(X^2\Sigma_g^+, v^+$=0-18),[16] $OCS^+(X^2\Pi)$,[17] and satellite states[14,15] below 25 eV in Xe have been reported recently. Since most spectra presented here are taken at O_2 rotational temperatures of 220 K, many more rotational transitions are observed as compared to the case using a cold O_2 sample. Consequently, many local intensity enhancements due to Rydberg state perturbations, which were not accessible to previous molecular beam VUV laser PFI-PE experiments, are observed in the present PFI-PE study. Even though extensive overlaps exist between vibrational bands for $O_2^+(X^2\Pi_{1/2,3/2g})$ and $O_2^+(a^4\Pi_u, v^+)$ [and/or $O_2^+(A^2\Pi_u)$] at energies above 16.4 eV, we are still able to make unambiguous identifications of individual vibrational bands for these states by spectral simulations of PFI-PE bands obtained at 20 and 220 K. The analysis of PFI-PE bands for $O_2^+(X\ ^2\Pi_{1/2,3/2g}$, v^+=25-38) has provided new spectroscopic constants for these vibrational levels.

II. EXPERIMENT

The design and performance of the high-resolution photoionization facility of the Chemical Dynamics Beamline at the ALS has been described previously.[10,12,13,27] Briefly, the major components include a 10 cm period undulator, a gas harmonic filter, a 6.65m off-plane Eagle monochromator, and a photoion-photoelectron apparatus.

In the present experiment, helium is used in the harmonic gas filter, where higher undulator harmonics with photon energies greater than 24.59 eV are suppressed. The fundamental light from the undulator is then directed into the 6.65 m monochromator and dispersed by a 4800 lines/mm grating (dispersion = 0.32 Å/mm) before entering the experimental apparatus. The PFI-PE bands for $O_2^+(X^2\Pi_{1/2,3/2g}, v^+$=0-10 and 13-38) were

measured using the 4800 lines/mm grating and monochromator entrance/exit slits of 50-200 μm, achieving wavelength resolutions of 0.016-0.052 Å (FWHM). The photon energy step size was varied in the range of 0.1-0.25 meV.

The ALS storage ring is capable of filling 328 electron buckets in a period of 656 ns. Each electron bucket emits a light pulse of 50 ps with a time separation of 2 ns between successive bunches.[27] In each storage ring periods, a dark gap (16 ns) consisting of 8 consecutive unfilled buckets exists for the ejection of cations from the orbit. Thus, the present experiment is performed in the multibunch mode with 320 bunches in the synchrotron orbit, corresponding to a repetition rate of 488 MHz.

The procedures for PFI-PE measurements using the photoion-photoelectron apparatus have been described previously in detail.[10,12] The electron spectrometer, which consists of a steradiancy analyzer and a hemispherical energy analyzer arranged in tandem, was used to filter prompt electrons. For measurements of the $O_2^+(X^2\Pi_{1/2,3/2g}, v^+=0\text{-}10$ and 13-38) PFI-PE bands, a pulsed electric field (height = 0.67 V/cm, width = 40 ns) was applied every three synchrotron periods, i.e., 1.97 μs. Thus, the repetition rate of the electric field pulses was 0.51 MHz.[10]

A continuous molecular beam of pure O_2 was produced by supersonic expansion through a stainless steel nozzle (diameter = 0.127 mm) at a stagnation pressure of 760 Torr and a nozzle temperature of 298 K.[12] The molecular beam was skimmed by a circular skimmer (diameter = 1 mm) before intersecting the monochromatized VUV light beam 7 cm downstream in the photoionization region. As shown below, the simulation of PFI-PE spectra suggests that the rotational temperature for O_2 achieved is about 220 K in this experiment.

The $O_2^+(X^2\Pi_{1/2,3/2g}, v^+=11$ and 12) PFI-PE bands were recorded in another experiment performed more than two years later than the PFI-PE measurement of the $O_2^+(X^2\Pi_{1/2,3/2g}, v^+=0\text{-}10$ and 13-38) bands. A new synchrotron based PFI-PE detection scheme, which relies on the time-of-flight (TOF) selection of PFI-PEs, is used in the recent study.[13] By employing a synchrotron dark gap of ≥80 ns, we show that the TOF peak for PFI-PEs can be adjusted to arrive in the dark gap with little contamination by prompt

electrons. This new scheme not only is more effective in suppression of prompt electrons, but also has a higher electron transmission. Using a 2400 lines/mm grating and monochromator entrance/exit slits of 50-100 μm, the wavelength resolution achieved in this PFI-PE experiment was 0.032-0.064 Å (FWHM). For the measurement of the $O_2^+(X^2\Pi_{1/2,3/2g}, v^+=11$ and 12) bands, the O_2 sample was introduced in the form of an effusive beam, and thus the O_2 rotational temperature was expected to ≈298 K.[12,20]

The PFI-PE band for $O_2^+(X^2\Pi_{1/2,3/2g}, v^+=28)$ is nearly in completed overlap with the strong $O_2^+(a^4\Pi_u, v^+=8)$ and $O_2^+(A^2\Pi_u, v^+=0)$ bands. In order to identify the $O_2^+(X^2\Pi_{1/2,3/2g}, v^+=28)$ bands, we have recently re-examined the PFI-PE spectrum of O_2 in the region of 17.010-17.060 eV using the new PFI-PE TOF method and a supersonically cooled O_2 beam, which achieves a rotational temperature of ≈20 K.

The absolute photon energy scale was calibrated using the $Xe^+(^2P_{3/2})$, $Kr^+(^2P_{3/2})$, $Ar^+(^2P_{3/2})$ and $Ne^+(^2P_{3/2})$. PFI-PE bands recorded under the same experimental conditions before and after each scan.[12,27] This calibration procedure assumes that the Stark shift for ionization thresholds of O_2 and the rare gases are identical. On the basis of previous experiments, the accuracy of the energy calibration is believed to be within ±0.5 meV.[16]

III. RESULTS AND DISCUSSIONS

The main electronic configuration for the $O_2(X^3\Sigma_g^-)$ ground state is $KK(2\sigma_g)^2(2\sigma_u)^2(3\sigma_g)^2(1\pi_u)^4(1\pi_g)^2$. The $O_2^+(X^2\Pi_g)$ ground state is formed by the removal of an electron from the anti-bonding $1\pi_g$ orbital. Taking into account the spin-orbit interaction, $O_2^+(X^2\Pi_{1/2,g})$ becomes the ground ionic state, which lies about 200 cm^{-1} below the spin-orbit excited $O_2^+(^2\Pi_{3/2g})$ state. Since the $O_2^+(X^2\Pi_{1/2,3/2g})$ states are more stable than the neutral ground $O_2(X^3\Sigma_g^-)$ state, the Franck-Condon factors (FCFs) for photoionization transitions $O_2^+(X^2\Pi_g, v^+) \leftarrow O_2(X^3\Sigma_g^-, v''=0)$ are known to have the maximum at $v^+=1$ as revealed in the HeI and HeII photoelectron spectra of O_2.[28,29] The FCFs for $v^+>5$ is negligibly small.

A. Relative vibrational band intensities for $O_2^+(X^2\Pi_{1/2,3/2g}, v^+=0\text{-}38)$

The photoionization efficiency (PIE) spectrum of O_2, together with its TPE spectrum, has been reported numerous times in the past.[8,22-25,30] The PIE spectrum reveals very pronounced autoionizing structures in the energy range of ≈12.0-14.0 eV. Autoionizing resonances with lesser intensities are also discernible from 14 to 18 eV in the PIE spectrum. The TPE intensity profile for vibrational bands of $O_2^+(X^2\Pi_g, v^+=0\text{-}22)$, instead of showing the Franck-Condon profile, is found to follow closely with the intensity profile of autoionizing resonances observed in the PIE spectrum.[22,23] This observation indicates that the formation of higher vibrational states $v^+ > 5$ in the Franck-Condon gap region is partly due to perturbations of nearby autoionzing low-n Rydberg interloper states.[31] A previous NeI photoelectron experiment[32] also show a long vibrational progression for the $O_2^+(X^2\Pi_g)$ state. However, we note that the mechanism for ion state productions in TPE measurements is different from that in the NeI experiment.[32]

Figure 3-1 shows the PFI-PE bands for $O_2^+(X^2\Pi_g, v^+)$ in the energy range of 11.8-18.2 eV. The positions of the $v^+ = 0\text{-}38$ levels are marked in the figure. Note that the PFI-PE intensity [I(e⁻)] of the spectrum is normalized to the VUV intensity [I(hν)]. For the two most intense peaks, $v^+ = 3$ and 4, the normalized intensities [I(e⁻)/I(hν)] go up to 27 and 93, respectively. The weakest band is $v^+ = 11$, with a normalized intensity of only ≈0.05% that for $v^+ = 4$. The doublet structures of individual PFI-PE vibrational bands correspond to the spin-orbit states $O_2^+(X^2\Pi_{1/2g})$ and $O_2^+(^2\Pi_{3/2g})$.

We show in Fig. 3-2(a) and 2(b) the PFI-PE spectrum of O_2 in the region of 16.05-18.14 eV, where the $O_2^+(a^4\Pi_u$, and $A^2\Pi_u)$ states also appear. The positions for the $O_2^+(X^2\Pi_{1/2,3/2g}, v^+=20\text{-}38$; $a^4\Pi_u, v^+=0\text{-}18$; and $A^2\Pi_u, v^+=0\text{-}12)$ bands are marked in Figs 3-2(a) and 3-2(b). As shown in these figures, significant overlaps occur between the $O_2^+(X^2\Pi_{1/2,3/2g}, v^+=21\text{-}38)$ bands and the $O_2^+(a^4\Pi_u, v^+=0\text{-}18$; $A^2\Pi_u, v^+=0\text{-}12)$ bands in this energy region. The overwhelming domination of the $O_2^+(a^4\Pi_u, v^+=0\text{-}18$; $A^2\Pi_u, v^+=0\text{-}12)$ states makes the identification and analysis of the $O_2^+(X^2\Pi_{1/2,3/2g}, v^+=21\text{-}38)$ bands difficult. However, we have been able to identify these bands by spectral simulation of experimental rotational features. The intensities for $O_2^+(X^2\Pi_{1/2,3/2g}, v^+=27\text{-}29)$ shown in

Figure 3-1. The PFI-PE bands for $O_2^+(X^2\Pi_g, v^+=0\text{-}38)$ in the energy range of 11.8~18.2 eV. The positions for these bands are marked. Nate that the maximum intensities the $v^+=3$ and 4 bands are 27 and 93, respectively. The band intensities for $v^+=27\text{-}29$ are based of simulation. The intensities for the $v^+=22$, 26, and 30 bands are enhanced due to overlap with vibrational bands of $O_2^+(a^4\Pi_u)$ and $O_2^+(A^2\Pi_u)$.

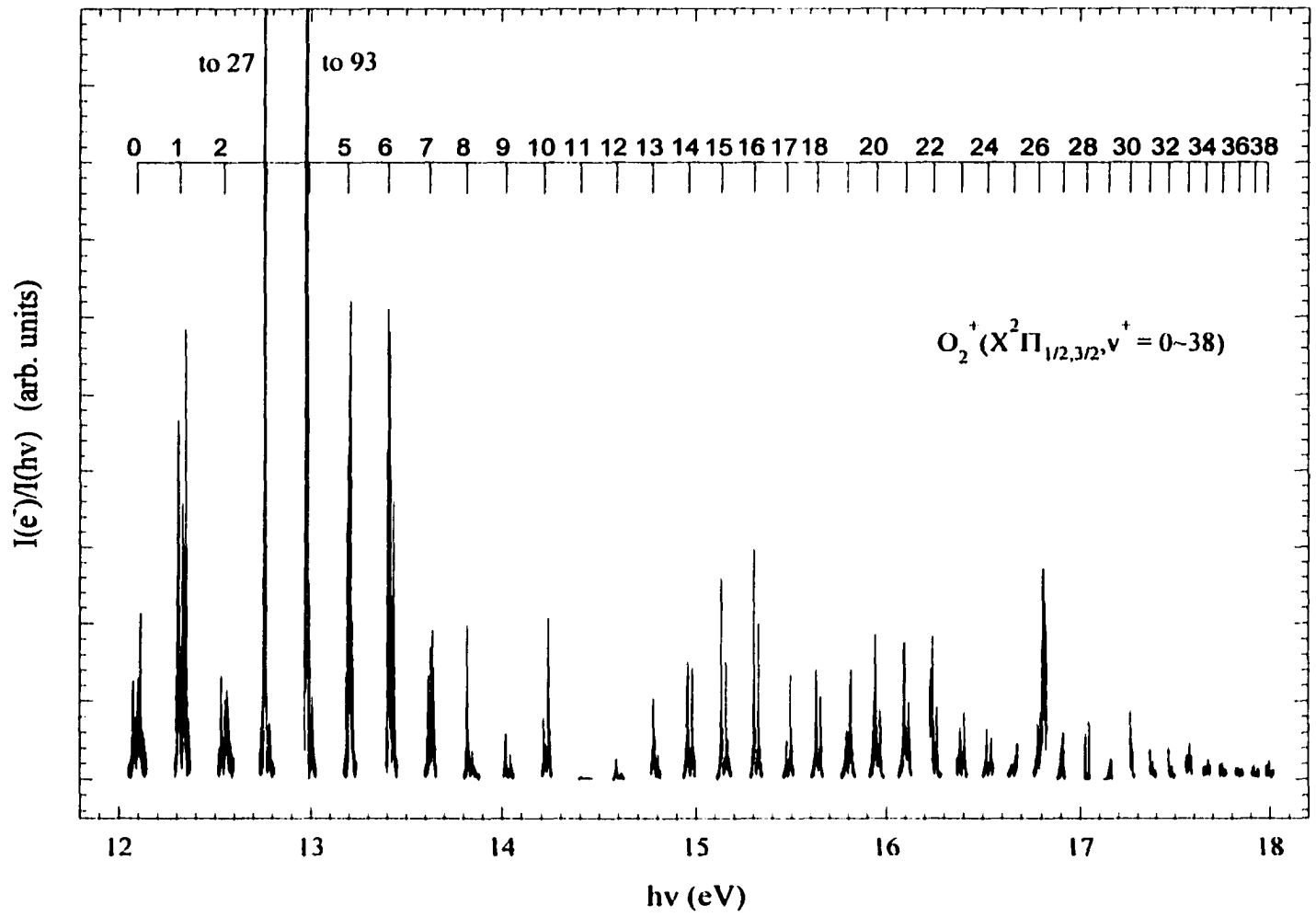
to 27
to 93
0 1 2 5 6 7 8 9 10 11 12 13 14 15 16 17 18 20 22 24 26 28 30 32 34 36 38
$O_2^+(X^2\Pi_{1/2,3/2}, v^+ = 0\sim38)$
I(e⁻)/I(hv) (arb. units)
12 13 14 15 16 17 18
hv (eV)

Figure 3-2. PFI-PE spectra for $O_2^+(X^2\Pi_{1/2,3/2g}, a^4\Pi_u$, and $A^2\Pi_u)$ in the regions of (a) 15.90-16.96 eV and (b) 16.96-18.16 eV. The positions for the $O_2^+(X^2\Pi_{1/2,3/2g}$, $v^+=20$-38), $O_2^+(a^4\Pi_u$, $v^+=0$-18), and $O_2^+(A^2\Pi_u$, $v^+=0$-12) are marked. The spectra were obtained using an O_2 molecular beam with an estimated rotational temperature of 220 K.

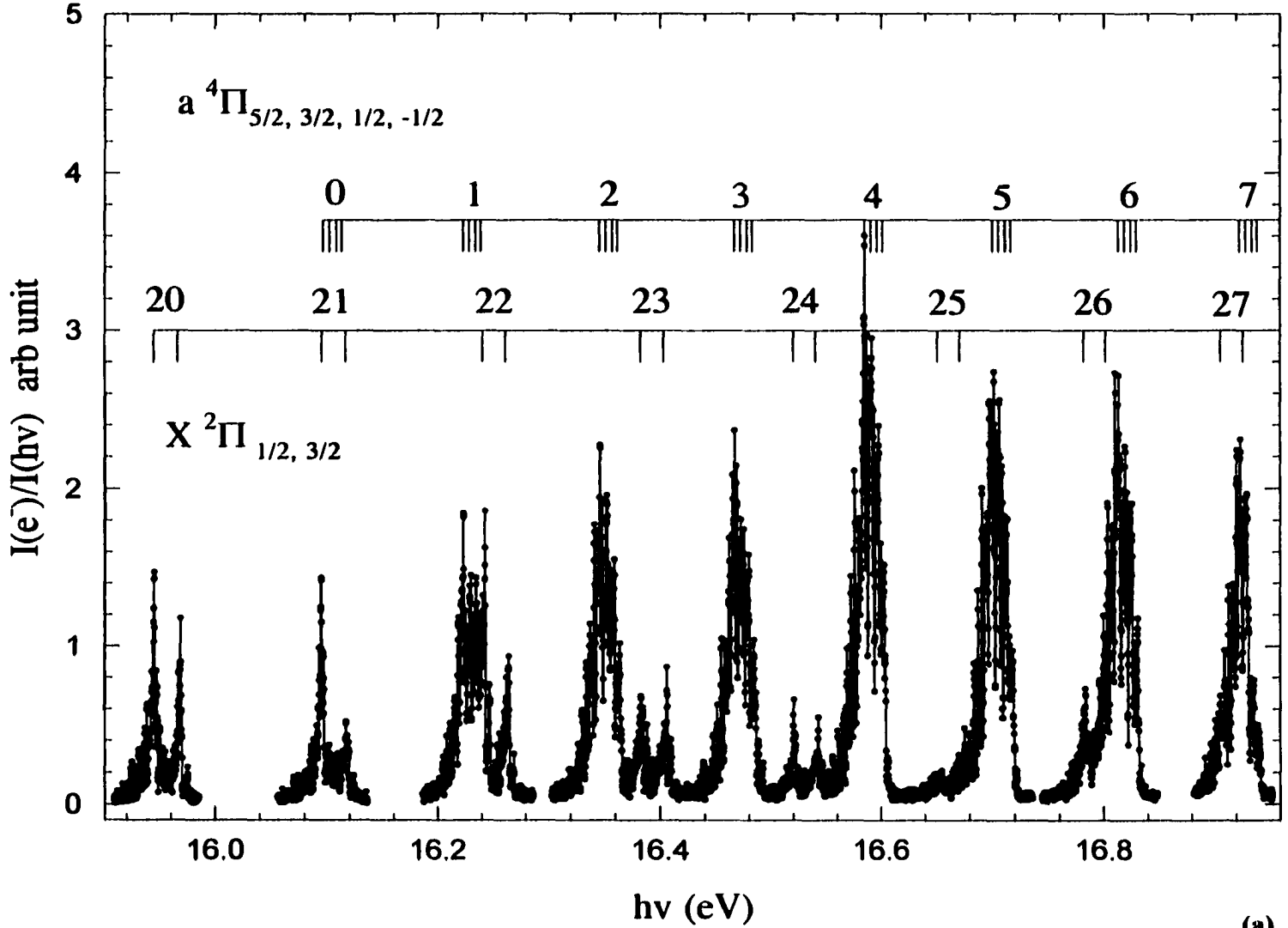
a $^4\Pi_{5/2, 3/2, 1/2, -1/2}$
0 1 2 3 4 5 6 7
20 21 22 23 24 25 26 27
X $^2\Pi_{1/2, 3/2}$
I(e⁻)/I(hv) arb unit
0 1 2 3 4 5
16.0 16.2 16.4 16.6 16.8
hv (eV)

(a)

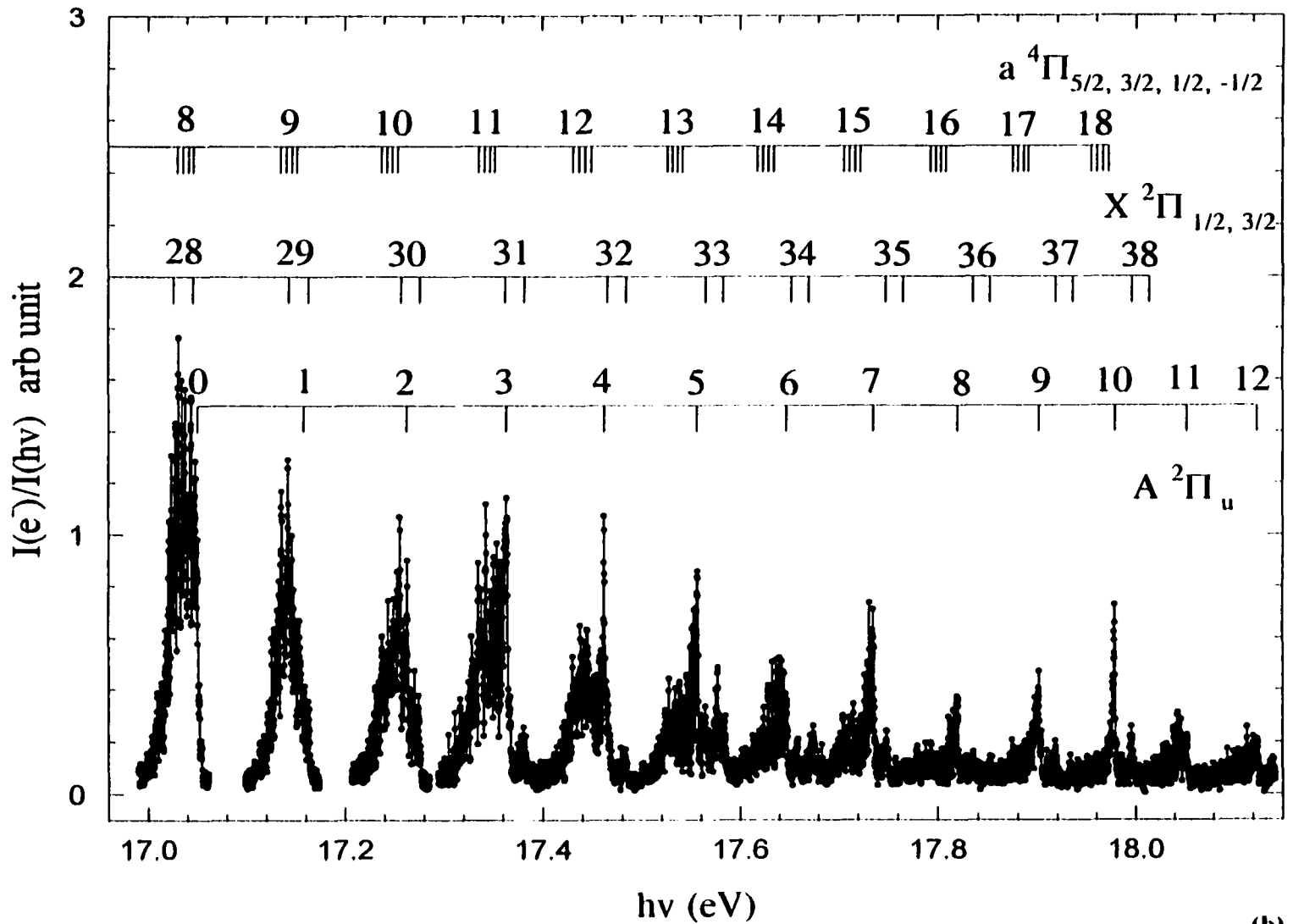

(b)

Figure 3-2 (continued)

Fig. 3-1 are based on spectral simulation (see section III.B).[33] We note that for the $O_2^+(X^2\Pi_{1/2,3/2g}, v^+=22, 26, \text{and } 30)$ bands, the intensity of either the $^2\Pi_{1/2g}$ or $^2\Pi_{3/2g}$ component was enhanced due to overlaps with vibrational bands of the $O_2^+(a^4\Pi_u)$ and/or $O_2^+(A^2\Pi_u)$ states. After taking into account contributions from the latter states by simulation, we find the intensities for the $O_2^+(X^2\Pi_{1/2,3/2g}, v^+=22, 26, \text{and } 30)$ bands are similar to those for adjacent $O_2^+(X^2\Pi_g\ v^+=23\text{-}25 \text{ and } 31\text{-}33)$ bands.

Due to the nearby autoionizing mechanism,[31] the relative intensities for PFI-PE vibrational bands and those for the spin-orbit states of individual vibrational bands are expected to depend on the rotational temperature of O_2. The relative intensities for $O_2^+(X^2\Pi_{1/2,3/2g}, v^+=6\text{-}8, 10, 13\text{-}24)$ as represented by the maximum peak height of the strongest $J^+ \leftarrow N''=1/2$ rotational branch have been reported by Kong and Hepburn.[8] Since the rotational temperature (≈10 K) achieved in the latter experiement is significantly lower than that (220-298 K) for the experiment of Fig. 3-1, some difference in relative vibrational band intensities observed in the two experiments are to be expected. Although the band intensities for $v^+=8$ and 15 observed in the present study are higher than those found by Kong and Hepburn,[8] we find general agreement between the relative intensities of PFI-PE bands for $v^+=6\text{-}24$ observed here and those obtained in the molecular beam VUV laser study.

Since TPEs and PFI-PEs represent photoelectrons formed slightly above and below the true ionization threshold, the degrees of perturbation by nearby autoionizing Rydberg states in the formation of TPEs and PFI-PEs can be different. Hence, the relative intensities for the TPE and PFI-PE vibrational bands are also expected to be different. However, we find that the relative band intensities observed in the high-resolution TPE spectra for $O_2^+(X^2\Pi_{1/2,3/2g}, v^+=0\text{-}21)$[22] at energies below the $IE[O_2^+(a^4\Pi_u)]$ are in general agreement with those found in the PFI-PE spectrum of Fig. 3-1. The relative spin-orbit state intensities for individual vibrational bands observed in the TPE spectrum[22] for a 298 K O_2 sample are also in fair agreement with those found in this PFI-PE experiment.

B. Spectral simulation and assignment of rotational branches

The Buckingham-Orr–Sichel (BOS) model[34] is used to predict the rotational line strengthens σ ($J^+ \leftarrow N''$) for the single-photon ionization transitions $O_2^+(X^2\Pi_{1/2,3/2g}, v^+, J^+) \leftarrow O_2(X^3\Sigma_g^-, v'', N'')$ relevant to the present experiment. Here, N'' is the rotational quantum number for the ground neutral $O_2(X^3\Sigma_g^-)$ state and J^+ is the total angular momentum for the ground cation $O_2^+(X^2\Pi_{1/2,3/2g})$ state. The J^+ value for the $O_2^+(X^2\Pi_{1/2,g})$ [$O_2^+(X^2\Pi_{3/2g})$] state is equal to $N^+ + ½$ [$N^+ + 3/2$], where N^+ is the rotational quantum number for O_2^+. In accordance with this model, the relative rotational intensities can be expressed by the equation,

$$\sigma(N^- \leftarrow N'') \propto \sum_\lambda Q(\lambda; N^-, N'')C_\lambda, \tag{1}$$

where Q is a factor determined by angular momentum coupling constants (Clebsch Gordon coefficients), and C_λ is a factor associated with the electronic transition moments, which is the linear combination of electron transition amplitudes of the possible orbital angular momenta l of the ejected photoelectron. The value λ can be considered as the orbital angular momentum quantum number associated with the electron partial wave prior to photoexcitation and is related to l by the relation,

$$l - 1 \le \lambda \le l + 1. \tag{2}$$

The photoionization process $O_2^+(^2\Pi_g) \leftarrow O_2(X^3\Sigma_g^-)$ can be described by a Hund's case (b) $\rightarrow$ (a) transition.[35] Thus, the Q factor is expressed as,

$$Q(\lambda; N^-, N'') = (2N^-+1)(2S^++1)^{-1} \sum_{\chi=\lambda-1/2}^{\lambda+1/2} \begin{pmatrix} \lambda & S^+ & \chi \\ \Delta\Lambda & \Sigma^+ & \Lambda^- - \Omega^+ \end{pmatrix}^2 \begin{pmatrix} N^+ & \chi & N'' \\ -\Omega^+ & \Omega^+ - \Lambda'' & \Lambda'' \end{pmatrix}^2. \tag{3}$$

Here, $\Delta\Lambda = \Lambda^+ - \Lambda''$ and $\Omega^+ = |\Lambda^+ \pm \Sigma^+|$, where Λ^+ and Σ^+ are the electronic orbital angular momentum and electron spin angular momentum projected on the axis of O_2^+ and Λ'' is the

electronic angular momentum projected on the axis of O_2, and S^+ is the total spin angular momentum of the final O_2^+ ionic state.

Due to the nuclear spin statistics, the even N" rotational levels in $O_2(X^3\Sigma_g^-)$ do not exist.[35] The spin-rotation splittings for $O_2(X^3\Sigma_g^-)$ are in the range of 0.1-0.2 meV for each rotational state. Although the present PFI-PE energy resolution of 0.5-0.6 meV (4-5 cm^{-1}, FWHM) cannot resolve these splittings, rotational transitions originated from the three fine structure sublevels F_1, F_2, and F_3 of $O_2(X^3\Sigma_g^-, v"=0)$ have been taken into account in the simulation. For simulation of the PFI-PE bands for $O_2^+(^2\Pi_{1/2,3/2g}, v^+)$ obtained using a supersonic O_2 beam, the rotational temperature is a fitting parameter. We find that the rotational temperature of 220±20 K gives the best fit to the experimental spectra shown in Figs. 3-1, 3-2(a), and 3-2(b). Since the PFI-PE bands for $O_2^+(^2\Pi_{1/2,3/2g}, v^+= 11$ and 12) were measured using an effusive O_2 sample, the O_2 rotational temperature for these bands are fixed as 298 K in the simulation.

For a Σ to Π transition ($\Delta\Lambda = 1$), the first 3-j symbol determines that C_0 is zero for the photoionization process. We have been able to simulate all experimental PFI-PE vibrational bands using the set of BOS coefficients (C_1, C_2, C_3, C_4). Thus, the major rotational branches contributing to these vibrational bands are $\Delta N = N^+ - N" =$ -4, -3, -2, -1, 0, 1, 2, 3 and 4 designated as M, N, O, P, Q, R, S, T and U branches, respectively. A Gaussian linewidth of 5 cm^{-1} (FWHM) is used as the instrumental resolution profile in the simulation. The best fitted BOS coefficients for the $O_2^+(^2\Pi_{1/2,3/2g}, v^+= 0$-38) are listed in Table 1. For the one-photon $O_2^+(X^2\Pi_g) \leftarrow O_2(X^3\Sigma_g^-)$ ionization transition, the overall symmetry of the final state must be ungerade, which requires that l be odd. The highest rotational branch observed is $|\Delta N| = 4$, indicating that the highest l value of 3. Thus, the photoelectron continuum states are restricted mostly to l = 1 and 3. This observation is in accord with the conclusion based on the VUV laser PFI-PE study[5] of $O_2^+(^2\Pi_{1/2,3/2g}, v^+=0)$ using a 298 K O_2 sample.

As indicated above, the PFI-PE bands for $O_2^+(^2\Pi_{1/2,3/2g}, v^+= 0$-2, 6-8, 10, and 13-24) were obtained previously using VUV lasers and supersonically cooled O_2 samples (rotational temperatures = 5-10 K).[6,8] For the $O_2^+(^2\Pi_{1/2,3/2g}, v^+=0)$ PFI-PE band, it was also

Table 3-I. The best fitted BOS coefficients (C_i, i = 1-4)[a] obtained in the simulation of the PFI-PE bands for $O_2^+(X^2\Pi_{1/2,3/2g}, v^+)$.

v^+	C_1	C_2	C_3	C_4
0	0.30/0.00	0.70/0.00	0.00/0.50	0.00/0.50
1	0.50/0.25	0.50/0.25	0.00/0.25	0.00/0.25
2	0.20/0.00	0.80/0.00	0.00/0.20	0.00/0.80
3	0.50/0.40	0.50/0.40	0.00/0.10	0.00/0.10
4	1.00/0.40	0.00/0.40	0.00/0.10	0.00/0.10
5	0.40.0.56	0.50/0.42	0.10/0.01	0.00/0.01
6	0.55/0.45	0.20/0.45	0.20/0.05	0.10/0.05
7	0.30/0.30	0.35/0.40	0.35/0.30	0.00/0.00
8	0.50/0.00	0.50/0.00	0.00/0.50	0.00/0.50
9	0.50/0.10	0.50/0.10	0.00/0.40	0.00/0.40
10	0.10/0.70	0.40/0.10	0.40/0.10	0.10/0.10
11	0.20/0.40	0.20/0.40	0.30/0.10	0.30/0.10
12	0.90/0.00	0.10/0.00	0.00/0.50	0.00/0.50
13	0.70/0.20	0.20/0.30	0.08/0.30	0.02/0.20
14	0.50/0.40	0.50/0.40	0.00/0.10	0.00/0.10
15	0.25/0.25	0.75/0.25	0.00/0.25	0.00/0.25
16	0.50/0.20	0.50/0.20	0.00/0.30	0.00/0.30
17	0.50/0.10	0.50/0.30	0.00/0.40	0.00/0.20
18	0.50/0.10	0.50/0.30	0.00/0.30	0.00/0.30
19	0.25/0.10	0.25/0.10	0.25/0.20	0.25/0.60
20	0.40/0.20	0.60/0.20	0.00/0.30	0.00/0.30
21	0.40/0.10	0.60/0.10	0.00/0.40	0.00/0.40
22	0.70/0.05	0.10/0.05	0.10/0.90	0.10/0.00
23	0.00/0.00	0.50/0.00	0.40/0.90	0.10/0.10
24	1.00/0.02	0.00/0.02	0.00/0.90	0.00/0.06
25	0.50/0.00	0.50/0.50	0.00/0.50	0.00/0.00
26	1.00/0.10	0.00/0.10	0.00/0.40	0.00/0.40
27[b]	0.05/0.10	0.20/0.25	0.70/0.40	0.05/0.25
28	0.40/0.10	0.40/0.40	0.10/0.40	0.10/0.10
29[b]	0.20/1.00	0.20/0.00	0.10/0.00	0.50/0.00
30	0.00/1.00	0.00/0.00	0.00/0.00	1.00/0.00
31	1.00/0.80	0.00/0.20	0.00/0.00	0.00/0.00
32	0.80/0.56	0.20/0.42	0.00/0.01	0.00/0.01
33	0.40/0.45	0.20/0.45	0.20/0.05	0.20/0.05
34	0.75/0.45	0.25/0.45	0.00/0.05	0.00/0.05
35	0.60/0.50	0.30/0.50	0.05/0.00	0.05/0.00
36	0.50/0.40	0.50/0.40	0.00/0.10	0.00/0.10
37	0.80/0.40	0.20/0.40	0.00/0.10	0.00/0.10
38	0.80/0.50	0.00/0.05	0.00/0.00	0.20/0.00

Table 3-I (Continued)

a) The first and second values for each C_i entry are for the $^2\Pi_{1/2g}$ and $^2\Pi_{3/2g}$ bands, respectively.

b) Due to the serious overlaps between $O_2^+(X^2\Pi_g, v^+=27 \text{ and } 29)$ and $(a^4\Pi_u, v^+=7 \text{ and } 9)$, respectively, the BOS coefficients for the $O_2^+(X^2\Pi_{3/2g}, v^+=27)$ and $O_2^+(X^2\Pi_{1/2g}, v^+=29)$ are estimates.

recorded in VUV laser experiment using an effusive beam.[5] We find the latter $O_2^+(^2\Pi_{1/2,3/2g}, v^+=0)$ band is in excellent agreement with that observed in the present study. The prominent peaks observed in the $O_2^+(^2\Pi_{1/2,3/2g}, v^+=0\text{-}38)$ bands are mostly due to the rotational branch heads (or the turn around rotational transitions of rotational branches). The rotational branches for the $O_2^+(^2\Pi_{1/2,3/2g}, v^+=0\text{-}11)$ PFI-PE bands are found to shade to the blue with the branch heads appeared on the low-energy side. For the $O_2^+(^2\Pi_{1/2,3/2g}, v^+=14\text{-}38)$ PFI-PE bands, the rotational branches are observed to shade to the red with the branch heads appeared on the high-energy side.

Taking into account the published[5,6,8] PFI-PE data at $O_2^+(^2\Pi_{1/2,3/2g}, v^+\leq 24)$, we have selected to show in Figs. 3-3(a)-(f) the detailed structures resolved in the PFI-PE bands for $O_2^+(^2\Pi_{1/2,3/2g}, v^+=1, 3\text{-}5, 9, \text{and } 11)$, respectively. The upper spectra (open circles) in these figures are the experimental data, while the simulated vibrational spectra are plotted as the lower spectra (solid circles). The position for rotational transitions $O_2^+(X^4\Pi_{1/2g}, v^+, N^+) \leftarrow O_2(X^3\Sigma_g^-, v'', N'')$ and $O_2^+(^2\Pi_{3/2g}, v^+, N^+) \leftarrow O_2(X^3\Sigma_g^-, v'', N'')$ are indicated by respective downward pointing and upward pointing stick marks in Figs. 3-3(a)-(f). The numbers given below or above the stick marks in the figures are the N'' values. The BOS fits shown in Figs. 3-3(a)- 3-3(f), typical of the quality of simulation for $O_2^+(^2\Pi_{1/2,3/2g}, v^+\leq 14)$, are reasonably good, but not excellent, due to perturbations by nearby autoionizing Rydberg states, giving rise to strong local intensity enhancements.

The detailed simulation of the overlapping bands of Figs. 3-2(a) and 3-2(b) involving the $O_2^+(X^2\Pi_g, a^4\Pi_u, \text{and } A^2\Pi_u)$ states in the region of 16.4-18.2 eV will be presented in a forthcoming article.[33] As examples, we choose to show here only the identification of $O_2^+(^2\Pi_{1/2g}, v^+=22)$ and $O_2^+(X^2\Pi_{1/2,3/2g}, v^+=28)$ based on the BOS simulation. The PFI-PE band for $O_2^+(^2\Pi_{1/2g}, v^+=22)$ has not been reported in the previous VUV laser PFI-PE study[8] because of the serious overlap with the $O_2^+(a^4\Pi_u, v^+=1)$ band. On the basis of the BOS simulation, we have unambiguously identified the $O_2^+(^2\Pi_{1/2,3/2g}, v^+=22)$ and $O_2^+(a^4\Pi_u, v^+=1)$ bands. Figure 3-4(a) shows the deconvoluted (or simulated) spectra for the $O_2^+(^2\Pi_{1/2,3/2g}, v^+=22)$ band. The deconvoluted spectrum for the $O_2^+(a^4\Pi_u, v^+=1)$ band is shown at the bottom of Fig. 3-4(b). As shown in Fig. 3-4(b), the sum of

Figure 3-3. PIE-PE spectra for O_2^+($X^2\Pi_{1/2,3/2g}$ v'). (a) v'=1, (b) v'=3, (c) v'=4, (d) v'=5, (e) v'=9, (f) v'=11, (g) v'=34, and (h) v'=37. The rotational transitions for the $O_2^+(X^2\Pi_{1/2g})$ and $O_2^+(X^2\Pi_{3/2g})$ are marked using downward pointing and upward pointing sticks, respectively. All experimental spectra (open circles) were taken using an O_2 molecular beam with an estimated rotational temperature of 220 K except that for v'=11, which was recorded with an effusive beam with a rotational temperature of 298 K. The simulated spectra (solid line) are shown as the bottom spectra.

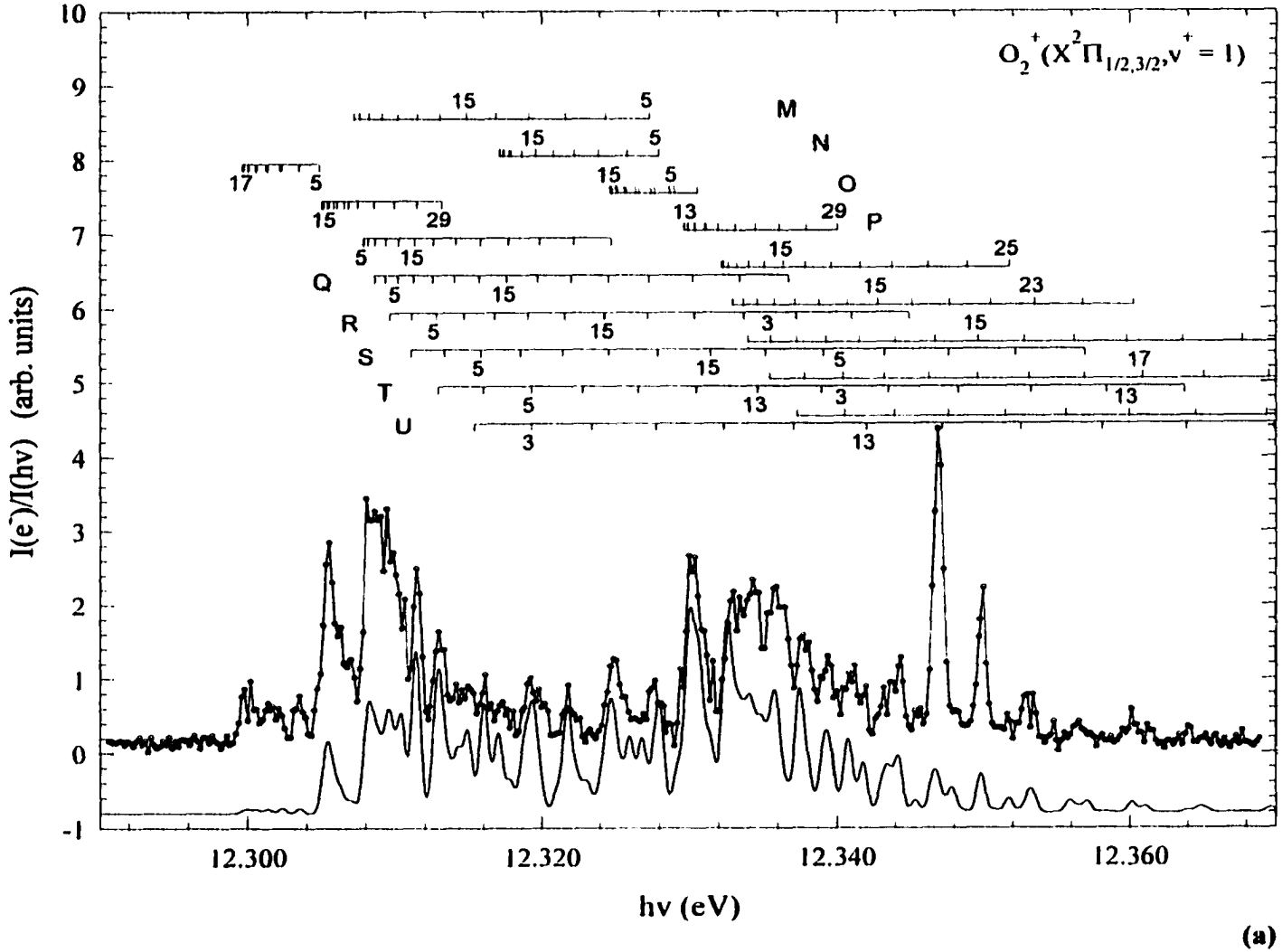
$O_2^+(X^2\Pi_{1/2,3/2}, v^+ = 1)$
M
N
O
P
Q
R
S
T
U
I(e⁻)/I(hv) (arb. units)
hv (eV)
12.300
12.320
12.340
12.360

(a)

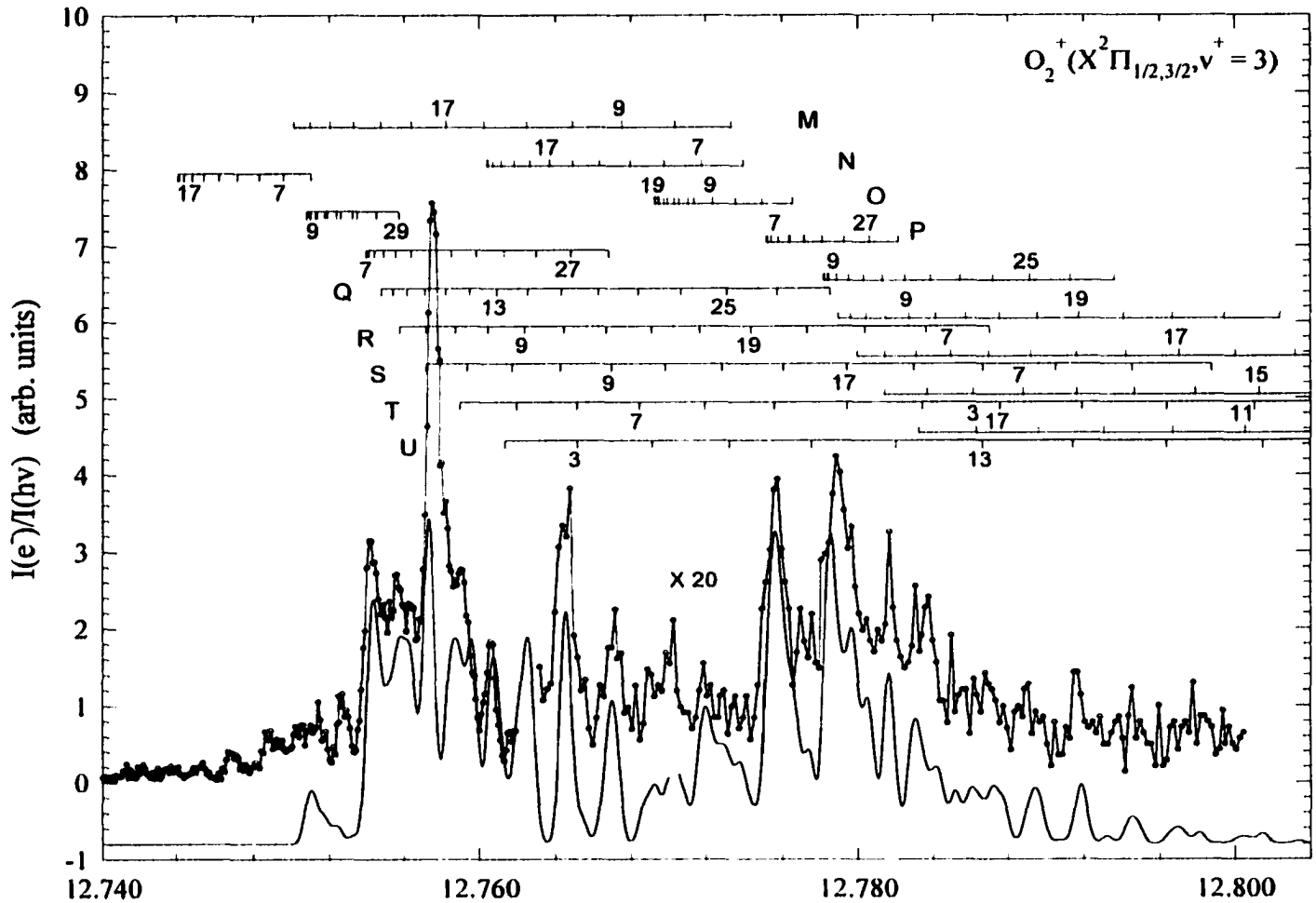

Figure 3-3 (continued) **(b)**

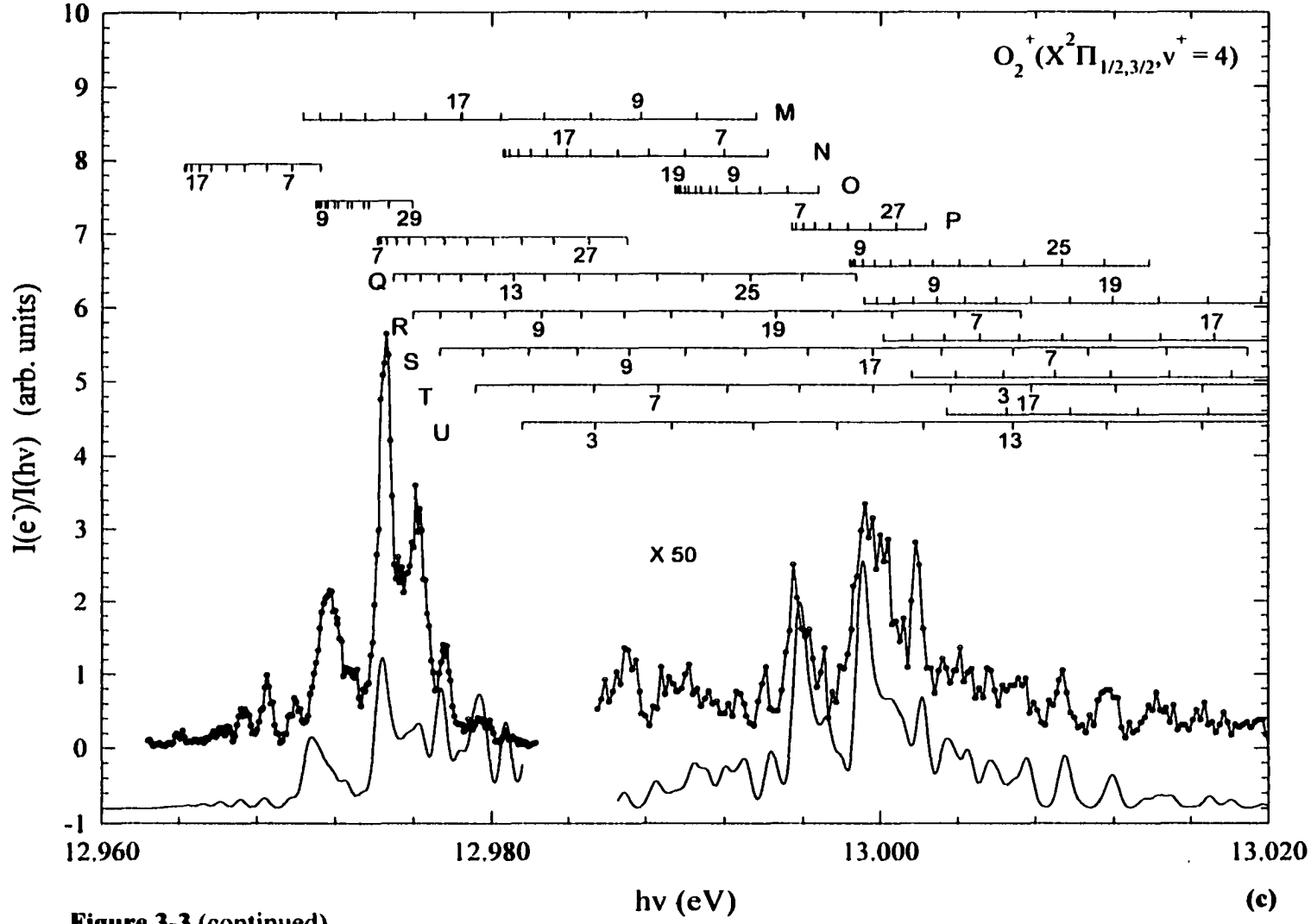

Figure 3-3 (continued)

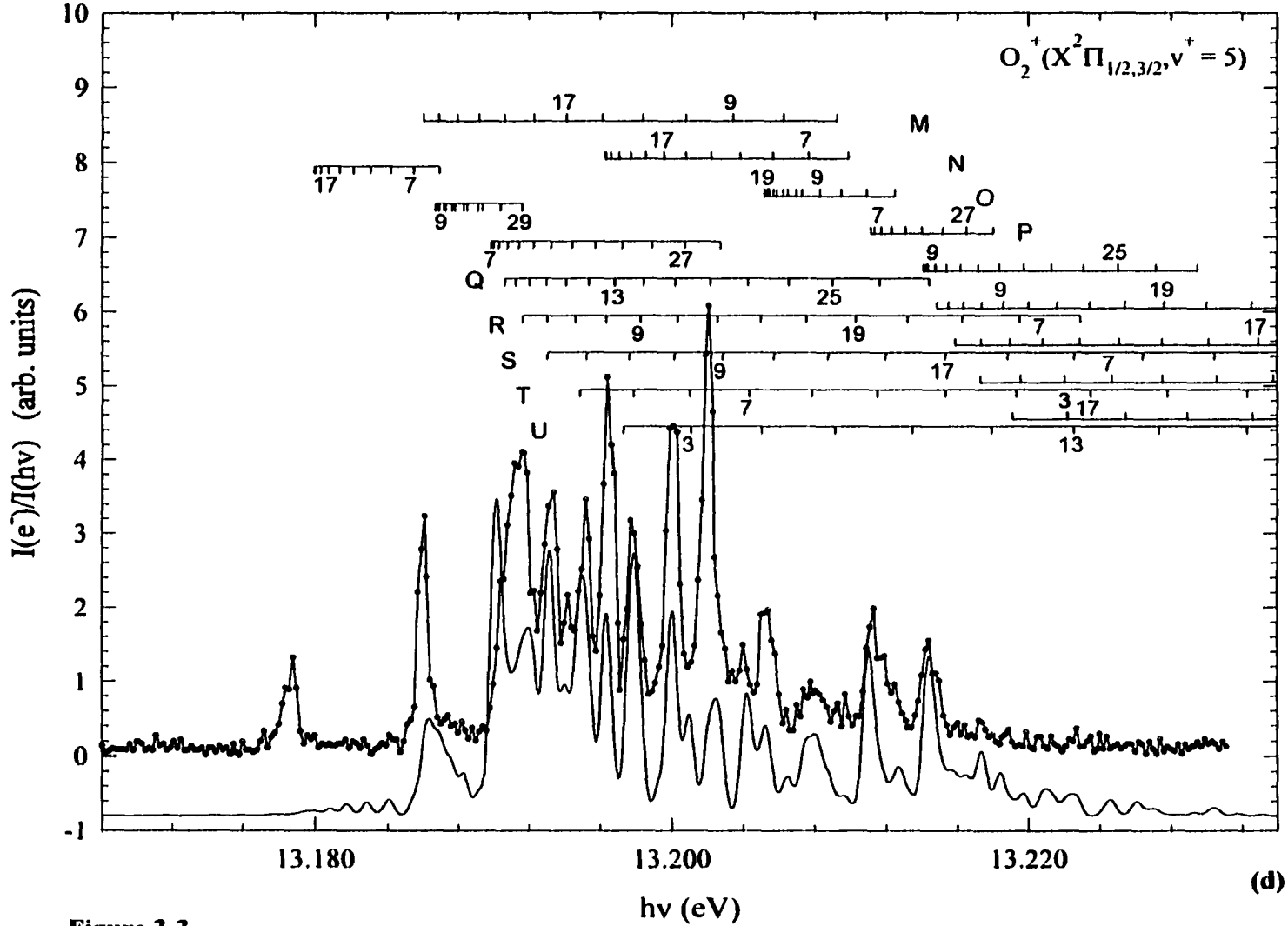
$O_2^+(X^2\Pi_{1/2,3/2}, v^+ = 5)$
I(e⁻)/I(hv) (arb. units)
hv (eV)
13.180
13.200
13.220
(d)
M
N
O
P
Q
R
S
T
U

Figure 3-3

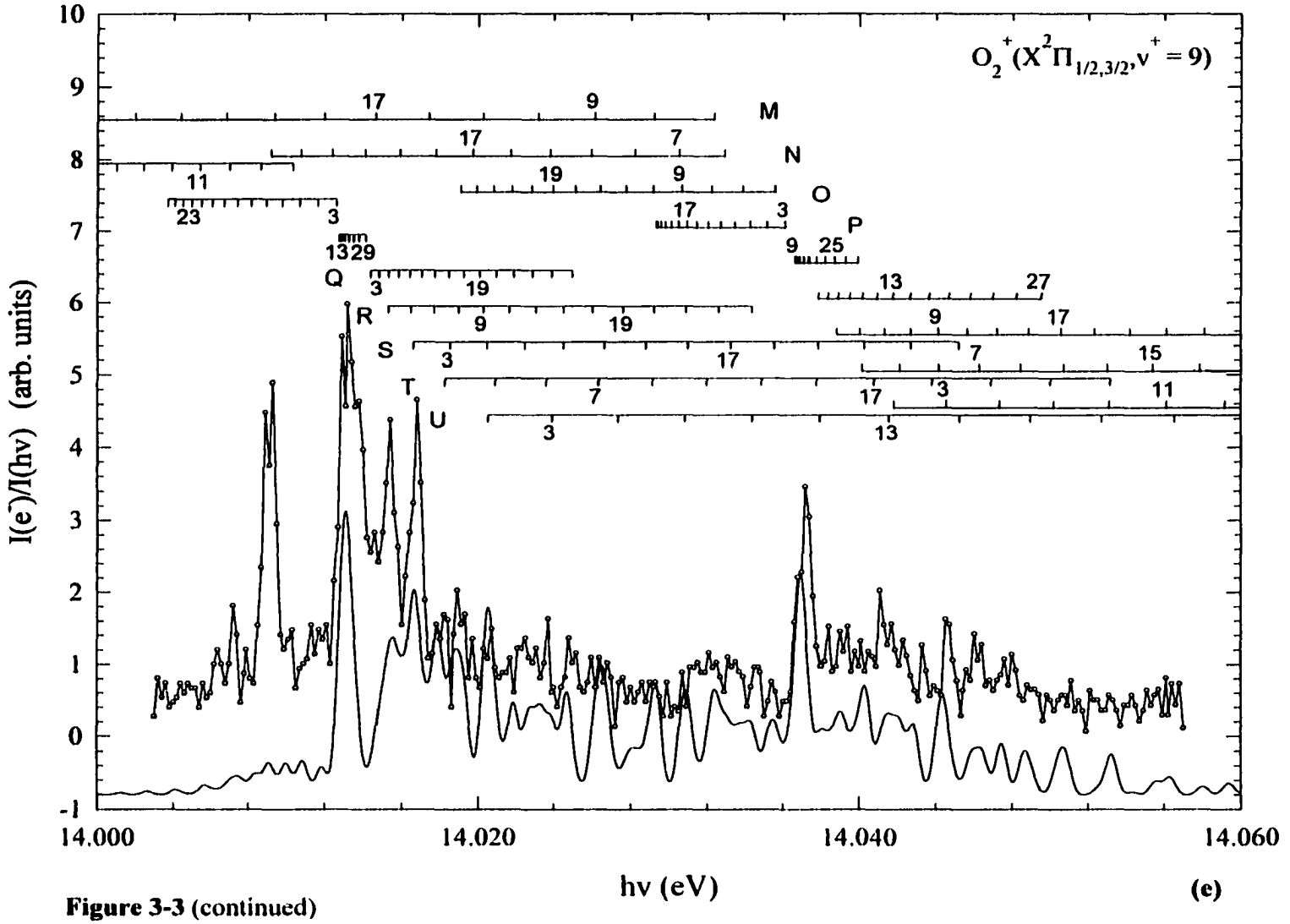

Figure 3-3 (continued)

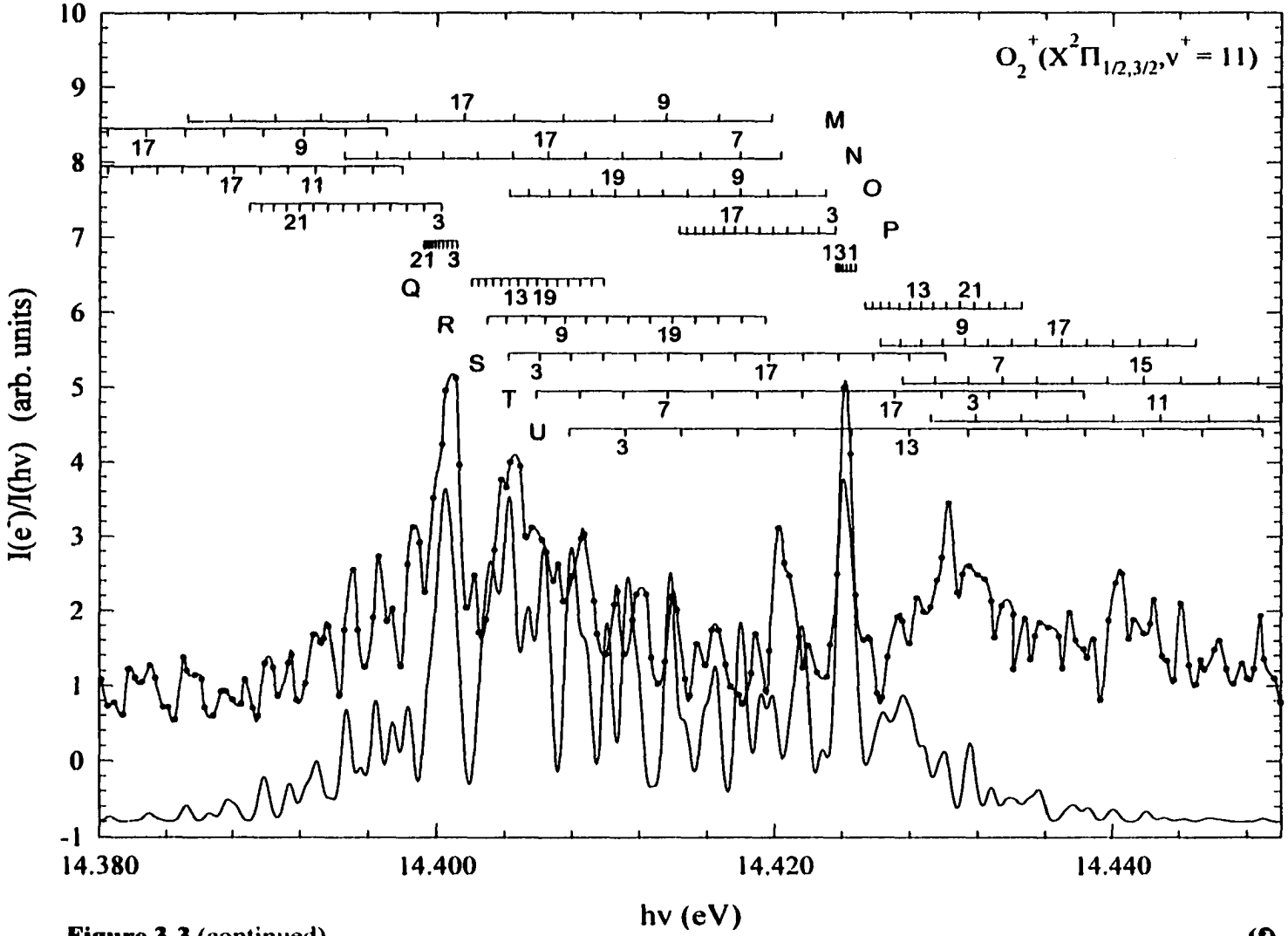

Figure 3-3 (continued)

(f)

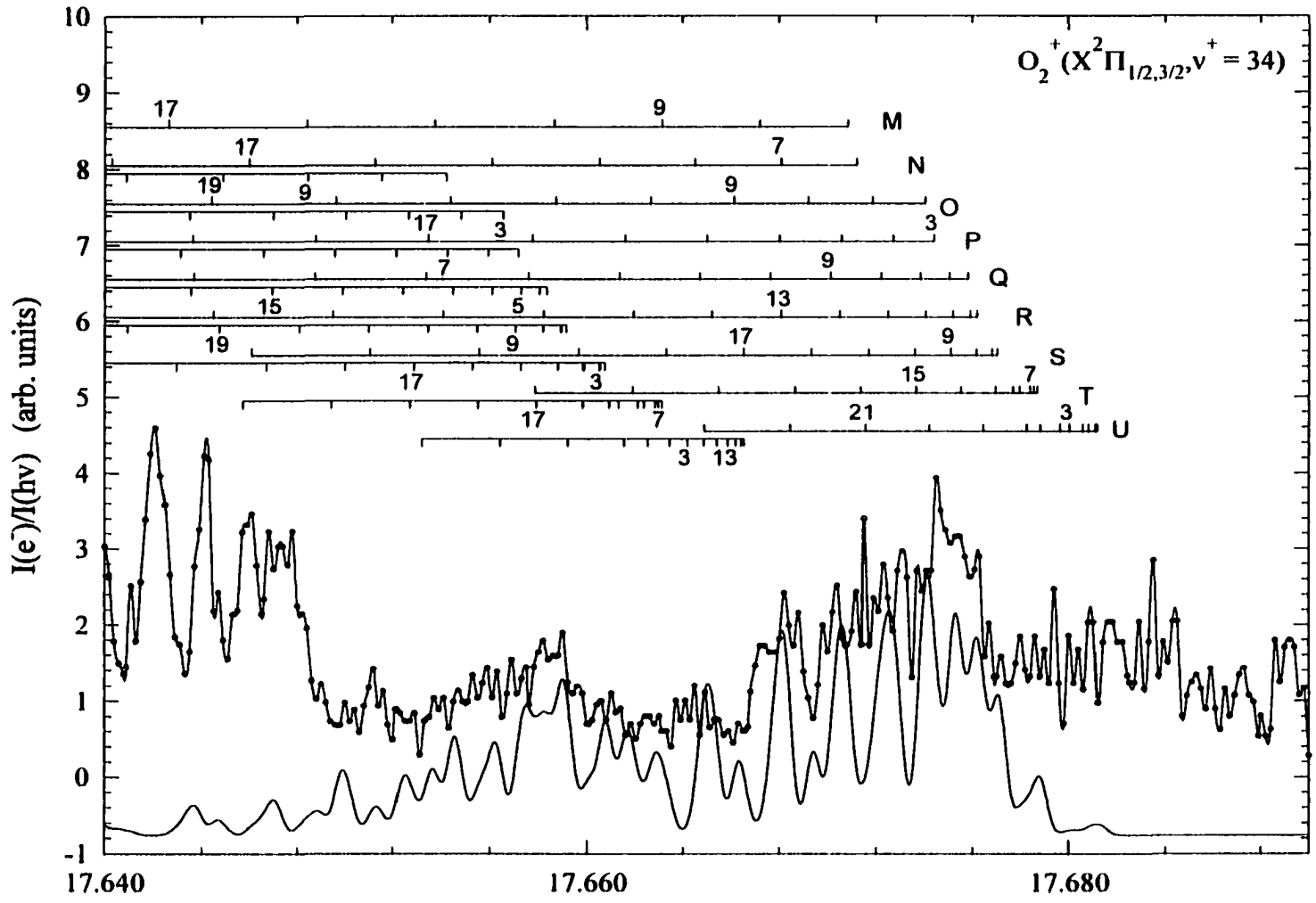

Figure 3-3 (continued) **(g)**

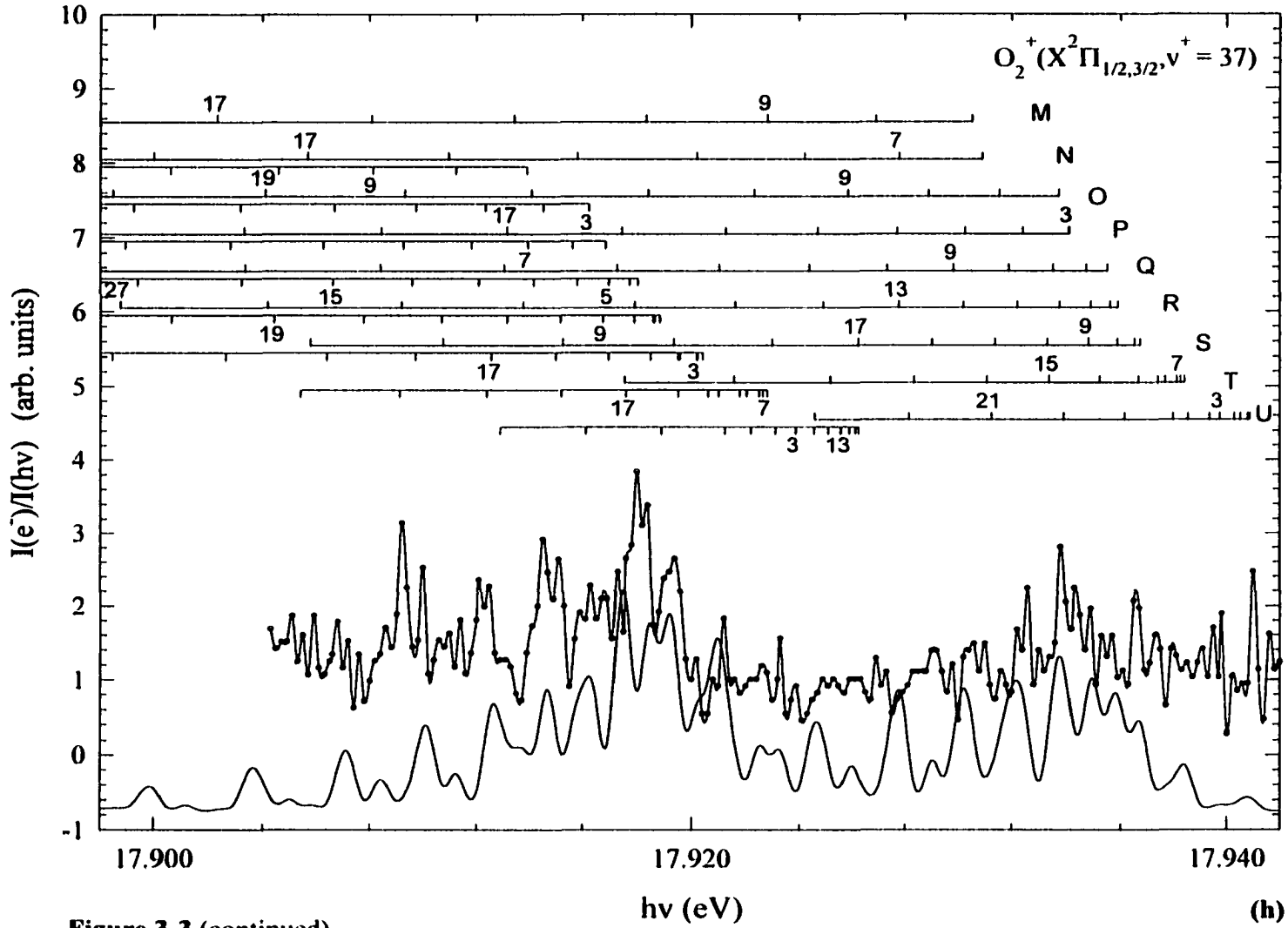

Figure 3-3 (continued)

Figure 3-4. (a) Deconvoluted (or simulated) PFI-PE band for $O_2^+(X^2\Pi_{1/2,3/2g}, v^+=22)$. The rotational transitions for the $O_2^+(X^2\Pi_{1/2g})$ and $O_2^+(X^2\Pi_{3/2g})$ are marked using downward pointing and upward pointing sticks, respectively. (a) The upper spectrum is the experimental PFI-PE spectrum for O_2 in the region of 16.10-16.28 eV obtained using an O_2 sample with a rotational temperature of 220 K; the deconvoluted (or simulated) PFI-PE band for $O_2^+(a^4\Pi_u, v^+=1)$ is shown as the bottom spectra; and the middle spectrum represents the sum of the deconvoluted (simulated) bands for $O_2^+(X^2\Pi_{1/2,3/2g}, v^+=22)$ and $O_2^+(a^4\Pi_u, v^+=1)$.

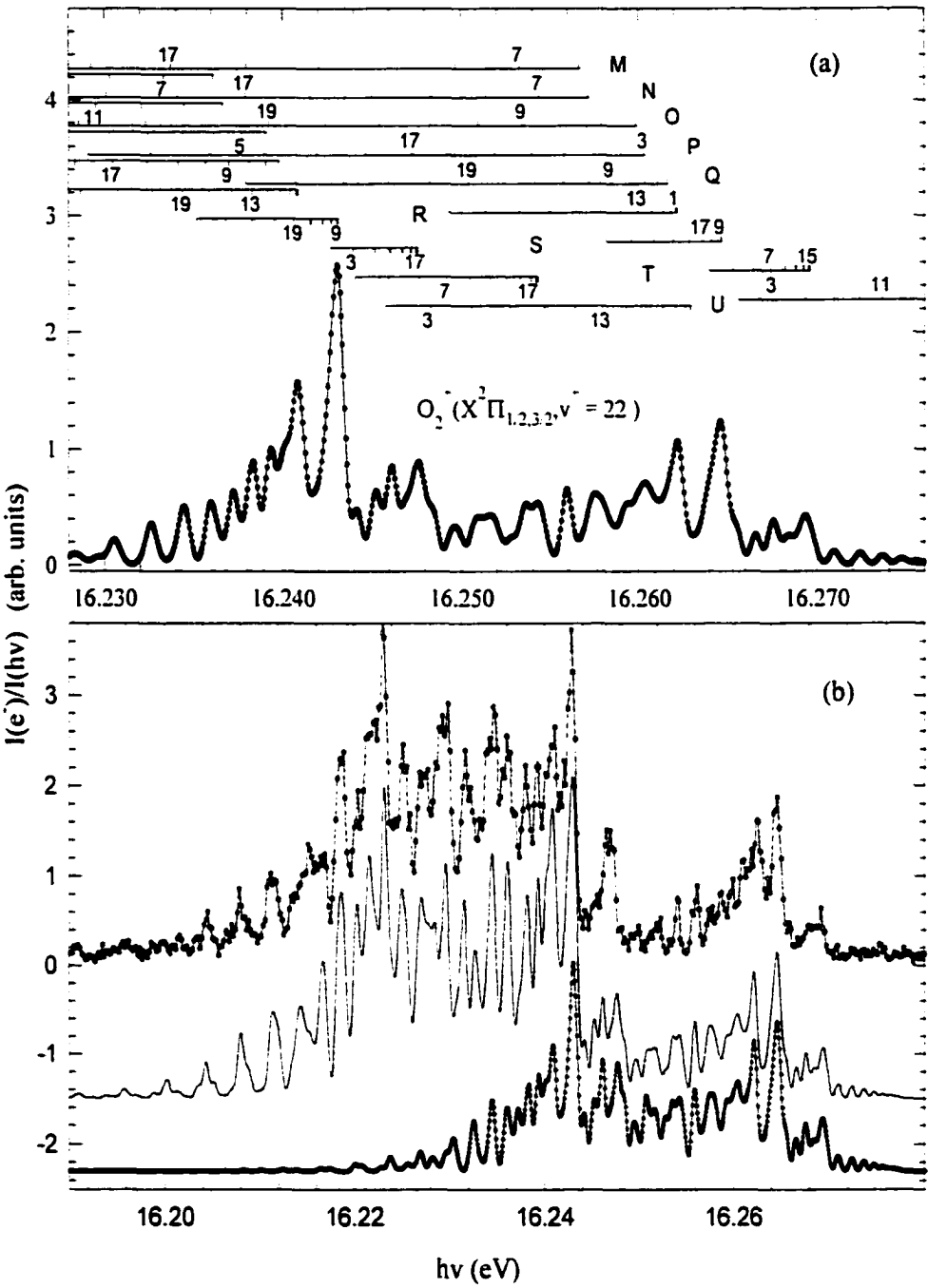
(a)
M
N
O
P
Q
R
S
T
U
$O_2^-(X^2\Pi_{1,2,3,2},v^- = 22)$
(b)
I(e⁻)/I(hv) (arb. units)
hv (eV)

Figure 3-5 (a) Deconvoluted (or simulated) PFI-PE band for $O_2^+(X^2\Pi_{1/2,3/2g}, v^+=28)$. The rotational transitions for the $O_2^+(X^2\Pi_{1/2g})$ and $O_2^+(X^2\Pi_{3/2g})$ are marked using downward pointing and upward pointing sticks, respectively. (a) The upper spectrum is the experimental PFI-PE spectrum for O_2 in the region of 17.01-17.06 eV obtained using an O_2 sample with a rotational temperature of 20 K; the deconvoluted (or simulated) PFI-PE band for $O_2^+(a^4\Pi_u, v^+=8)$ is shown as the bottom spectra; and the middle spectrum represents the sum of the deconvoluted (simulated) bands for $O_2^+(X^2\Pi_{1/2,3/2g}, v^+=28)$ and $O_2^+(a^4\Pi_u, v^+=8)$. The simulation shows that the contribution of the $O_2^+(A^2\Pi_u, v^+=0)$ to the observed spectrum is minor.

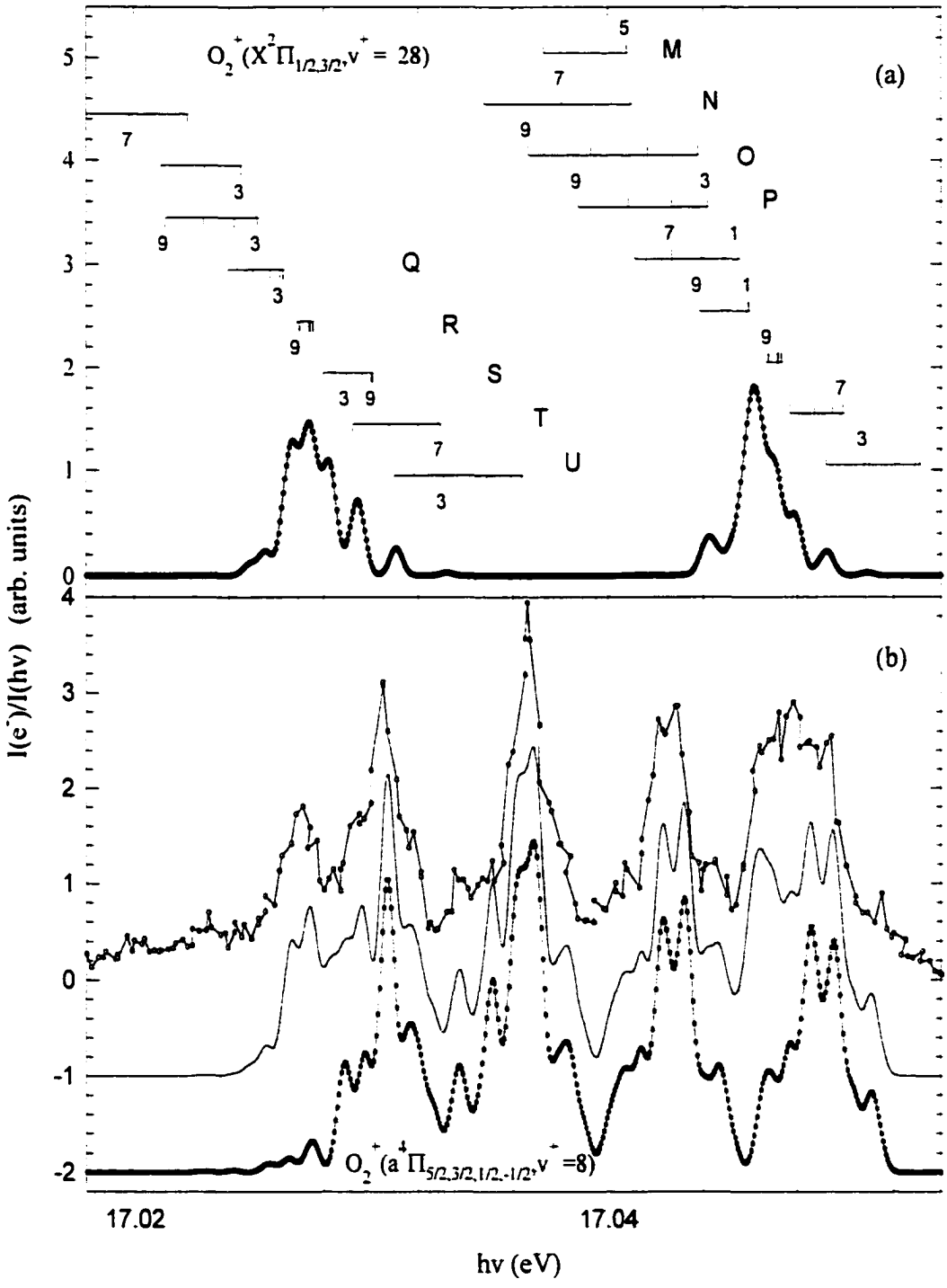
$O_2^+(X^2\Pi_{1/2,3/2}, v^+ = 28)$
(a)
M
N
O
P
Q
R
S
T
U
(b)
$O_2^+(a^4\Pi_{5/2,3/2,1/2,-1/2}, v^+ = 8)$
I(e⁻)/I(hv) (arb. units)
hv (eV)
17.02
17.04

these two simulated bands (middle spectrum) is in excellent agreement with the experimental spectrum (open circles, upper spectrum).

The most serious overlaps involving vibrational bands of the $O_2^+(X^2\Pi_g$, $a^4\Pi_u$, and $A^2\Pi_u)$ states occur in the region of 16.88-17.18 eV, where the $O_2^+(a^4\Pi_u$, $v^+=7$-$9)$ PFI-PE bands are the overwhelmingly dominant features [see Figs. 3-2(a) and 3-2(b)]. The deconvolution of the $O_2^+(^2\Pi_{1/2,3/2g}$, $v^+=26$, 27, and 29) bands from the $O_2^+(a^4\Pi_u$, $v^+=7$, 9) and $O_2^+(A^2\Pi_u$, $v^+=1)$ PFI-PE bands has also been achieved by simulation of the 298 K bands shown in Figs 3-2(a) and 2(b).[33] However, the deconvolution of the $O_2^+(^2\Pi_{1/2,3/2g}$, $v^+=28)$ band from the $O_2^+(a^4\Pi_u$, $v^+=8)$ and $O_2^+(A^2\Pi_u$, $v^+=0)$ bands requires the PFI-PE measurement using a supersonically cooled O_2 sample, achieving a rotational temperature $\approx$ 20 K. Figure 3-5 shows this cold PFI-PE spectrum for O_2 in the region of 17.01-17.06 eV. By assuming a rotational temperature of 20 K, we have obtained excellent BOS fit to the experimental spectrum. As shown in Fig. 3-5, the major contributions to the spectrum is from the $O_2^+(X^2\Pi_{1/2,3/2g}$, $v^+=28)$ state (a double structure) and the $O_2^+(a^4\Pi_u$, $v^+=8)$ state (a quartet structure). The PFI-PE band for $O_2^+(A^2\Pi_u$, $v^+=0)$ only constitutes a very minor part of the experimental spectrum.

The $O_2^+(X^2\Pi_{1/2,3/2g}$, $v^+=33$-$38)$ bands only suffer from minor interference from vibrational bands of the $O_2^+(a^4\Pi_u$, and $A^2\Pi_u)$ states [see Fig. 3-2(b)]. Hence, their identifications are relatively straight forwards. As examples, we show in Figs. 3-3(g) and 3(h) the PFI-PE bands for $O_2^+(^2\Pi_{1/2,3/2g}$, $v^+=34$ and 37), respectively, in an expanded energy scale and their simulation. As shown in these figures, the agreement between the experimental (upper curve, opened circles) and simulated (lower curve, solid circles) spectra is satisfactory. We note that rotational features for $O_2^+(^2\Pi_{1/2,3/2g}$, $v^+>38)$ are too weak to be positively identified in the spectrum of Fig. 3-2(b).

C. Mechanism for the formation of highly vibrationally excited $O_2^+(X^2\Pi_{1/2,3/2g})$ states

As shown in the PFI-PE band of Fig. 3-3(a), strong enhancements are observed for rotational transitions S(13) and S(15) associated with the formation of $O_2^+(^2\Pi_{3/2g}$, $v^+=1)$. The enhancements for the $\Delta N = 0$ (Q), ±1(R and P), -2(O), and -3(N) rotational branches

associated with the formation of $O_2^+(^2\Pi_{1/2g}, v^+=1)$ are also clearly discernible. For the spectra of $v^+ =3$ and 4 shown in Figs 3-3(c) and 3-3(d), the intensity for the $O_2^+(^2\Pi_{1/2g})$ band is overwhelmingly higher than that for the $O_2^+(^2\Pi_{3/2g})$ band, by a factor of 20 and 50, respectively. In addition, the rotational line intensities for S(1) of $O_2^+(^2\Pi_{1/2g}, v^+=3)$ and Q(5) of $O_2^+(^2\Pi_{1/2g}, v^+=4)$ are strongly enhanced. Many strong rotational intensity enhancements are also evident in the spectra of the $O_2^+(X^2\Pi_{1/2,3/2g}, v^+=5$ and 9) states shown in Figs. 3-3(d) and 3-3(e). The simulation of the spectrum for $O_2^+(X^2\Pi_{1/2,3/2g}, v^+=11)$ shows that this bands is relatively free from local enhancements, except the moderate enhancement for transitions at energy >14.428 eV associated with the $O_2^+(^2\Pi_{3/2g})$ state. The simulated and experimental spectra for $O_2^+(X^2\Pi_{1/2,3/2g}, v^+=12)$ (not shown here) are in very good accord.

Local rotational intensity distortions due to nearby Rydberg state perturbations are still discernible for higher $O_2^+(^2\Pi_{1/2,3/2g}, v^+=15$-24) vibrational bands. However, the magnitude and frequency of such enhancements resolved in these higher vibrational bands are relatively minor compared to those for the lower $O_2^+(X^2\Pi_{1/2,3/2g}, v^+<15)$ vobrational bands. We find that the corresponding BOS simulated spectra and experimental PFI-PE bands for $O_2^+(X^2\Pi_{1/2,3/2g}, v^+=15$-38) are generally in good agreement, indicating that perturbations due to nearby Rydberg States are not important.

The intensity perturbations observed in PFI-PE spectra could associate with near-resonant autoionization,[31] shape resonance[6] and/or interactions with dissociative[8,37] neutral states. In order for the near-resonant autoionization mechanism to significantly influence the intensities, the threshold of these rovibronic states have to be close to one or more low-n autoionizing interloper Rydberg states. This nearby autoionization mechanism is most likely responsible for local enhancements of rotational transitions observed in PFI-PE bands. The ground $O_2^+(X^2\Pi_g)$ state is formed by the ejection of a $1\pi_g$ electron, the shape resonance of which has been documented to happen near the ionization threshold.[6,38] Rotational branch intensities (and photoelectron angular distributions) observed in a high-resolution photoelectron experiment contain information on the partial wave character of shape resonance. The internuclear distance dependence of the electronic transition

moment associated with this shape resonance can lead to a dependence of the rotational branch intensity on the ion vibrational state. In a recent combined PFI-PE experimental and theoretical studies, Braunstein *et al* have examined the effect of the shape resonance on the rotational line-strengths for the v^+=0-2 states.[6] Evidence is found of a systematic change in the electron wave functions in the v^+=0-2 bands, which was attributed to the effect of shape resonance of the $1\pi_g$ electron. However, the effect of shape resonance is indiscernible in the more recent PFI-PE experiment of Kong and Hepburn,[8] covering vibrational bands for $O_2^+(X^2\Pi_g, v^+=6\text{-}24)$ in the Franck-Condon gap region. By comparison with the PIE and PFI-PE spectra in the ranges of 13.33-16.58 eV, they found that the majority of the vibrational PFI-PE bands appear in the continuum region of the PIE spectrum, not coincide with any autoionizing states. In order to rationalize this observation, Hong and Hepburn[8] have proposed a direct excitation model, invoking the direct excitation to a continuum neutral state with a step repulsive potential. Such a repulsive state can interact with long-lived high-*n* Rydberg states uniformly throughout a wide energy range. Therefore, it is possible to observe a long progression of PFI-PE bands in the Franck-condon gap region. The relatively smooth profile for PFI-PE vibrational band intensities observed (Fig. 3-1) in the Franck-Condon gap region, together with the generally good agreement observed between BOS simulated and experimental PFI-PE bands for $v^+>14$, seems to lend support to the direct excitation model.

Similar to the previous observation, we found that C_1 and C_2 are the dominant BOS coefficients for most vibrational bands (see Table 1), indicating that the *p*- and *d*-partial waves of the ground electron wave function give the major contribution to the ionizing transitions. For most of the vibrational bands, the values for C_3 and C_4 are small. Within a vibrational band, the BOS coefficients for the $O_2^+(X^2\Pi_{1/2g})$ and $O_2^+(X^2\Pi_{3/2g})$ components are mostly different. Furthermore, a great deal of fluctuations is observed for the BOS coefficients (C_1, C_2, C_3, C_4) as v^+ is increased. Generally, a greater fluctuation of BOS coefficients was observed on the $^2\Pi_{1/2}$ component. The BOS model would predict identical BOS coefficients for all the vibrational levels and spin-orbit components. The observed deviations of BOS coefficients from predictions of the original BOS model are

indicative of strong local perturbations due to the near-resonant autoionizing Rydberg states. The fluctuation of BOS coefficients is inconsistent with the previous report on rotationally resolved PFI-PE vibrational bands for v^+=0-2,[6] where a systematic change in the electron wave functions was observed.

D. Spectroscopic constants for $O_2^+(X^2\Pi_{1/2,3/2g})$

The energy expressions used for $O_2(X^3\Sigma_g^-, v'', N'')$ and $O_2^+(X^2\Pi_g, v^+, N^+)$ are

$$E(v'', N'') = E_e'' + \omega_e''(v'' + 1/2) - \omega_e''\chi_e''(v'' + 1/2)^2 + B_v'' N''(N'' + 1), \quad (4)$$

and

$$E^+(v^+, N^+) = E_e^+ + \omega_e^+(v^+ + 1/2) - \omega_e^+\chi_e^+(v^+ + 1/2)^2 + B_v^+ N^+(N^+ + 1) - B_v^+\Omega^2 \pm 1/2A_v^+ \quad (5)$$

respectively, where $B_v'' = B_e'' - \alpha''(v'' + 1/2)$ and $B_v^+ = B_e^+ - \alpha^+(v^+ + 1/2)$. In Eq. (5), $-1/2A_v^+$ is for Ω=1/2 component and $+1/2\ A_v^+$ is for the Ω = 3/2 component of the $O_2^+(X^2\Pi_g)$ state. The values B_e'' = 1.44563 cm^{-1}, B_e^+ =1.6913 cm^{-1}, α'' = 0.01593, α^+ = 0.01976, ω_e^+ = 1904.7 cm^{-1}, and $\omega_e^+\chi_e^+$ =16.259 cm^{-1} are taken from Refs. 35 and 36. We calculate the ionizing transition energies as:

$$\Delta E(v^+, N^+) = E(v^+, N^+) - E(v''=0, N''=1) = T_v + B_v^+ N^+(N^+ + 1) - B_v^+\Omega^2 \pm 1/2A_v^+ \quad (6)$$

where $T_v = T(v^+, v''=0, N''=1) = [E_e^+ - E_e'' + \omega_e^+(v^+ + 1/2) - \omega_e^+\chi_e^+(v^+ + 1/2)^2 - \omega_e''(1/2) + 1/4\ \omega_e''\chi_e'' - 2B_v'']$, noting that the IEs for different v^+ states correspond to energies for the ionization transitions $O_2^+[X^2\Pi_g, F_1(v^+, N^+ = 0)] \leftarrow O_2[X^3\Sigma_g^-, F_2(v''=0, N''=1)]$.

The T_v, A_v^+, and B_v^+ values for v^+=0-38 obtained by the BOS simulation are listed in Table II. We have also included in the table values obtained in the previous high-resolution emission[21] and VUV laser PFI-PE studies.[5,6,8] Using the IE value[8] of 97347.0 cm^{-1} and high-resolution spectroscopic data[21] obtained in the emission study, we have calculated the T_v values for $O_2^+(X^2\Pi_{1/2g}, v^+ \leq 11)$ (see Table II). We find that all T_v values obtained here and those reported in previous measurements[8,21] are in excellent agreement (within 5 cm^{-1}, the accuracy of energy calibration) except the values for v^+=0 and 2. The T_v values of 97441 and

Table II. Spectroscopic constants for O_2^+ ($X^2\Pi_g$, v^+=0-38)

	T_v (cm)$^{-1}$		B_v (cm)$^{-1}$		A_v (cm)$^{-1}$	
v^+	This work	Ref.[a]	This work	Ref.[a]	This work	Ref.[a]
0	97441	97447.9	1.68	1.68	200.2	200.3
1	99325	99321.0	1.66	1.66	199.5	199.7
2	101154	101161.4	1.64	1.64	199.0	199.0
3	102969	102968.4	1.62	1.62	198.5	198.4
4	104745	104743.7	1.60	1.60	197.6	197.7
5	106485	106485.5	1.59	1.58	198.0	196.9
6	108196	108195.0	1.56	1.56	196.6	196.1
7	109871	109871.8	1.54	1.54	195.0	195.3
8	111515	111516.4	1.52	1.52	193.1	194.4
9	113126	113126.5	1.50	1.50	192.5	193.5
10	114706	114706.0	1.48	1.48	192.2	192.6
11	116252	116252.9	1.47	1.46	191.0	191.6
12	117768	——	1.44	——	190.0	——
13	119251	119250.7	1.42	1.42	189.4	189.4
14	120699	120697.9	1.40	1.40	188.0	188.5
15	122114	122112.4	1.38	1.38	187.0	188.8
16	123497	123494.4	1.36	1.36	185.0	187.1
17	124844	124841.7	1.34	1.34	183.5	183.5
18	126156	126159.2	1.32	1.32	183.0	183.8
19	127438	127437.7	1.30	1.31	179.3	182.8
20	128686	128688.1	1.28	1.29	182.0	188.0
21	129902	129896.9	1.25	1.27	177.0	177.2
22	131075	——	1.25	1.25	174.0	——
23	132218	132221.7	1.22	1.23	173.0	171.3
24	133326	133330.0	1.19	1.21	169.0	169.3

Table 3-II. (Continued)

	T_v (cm)$^{-1}$		B_v (cm)$^{-1}$		A_v (cm)$^{-1}$	
v^+	This work	Ref.[a]	This work	Ref.[a]	This work	Ref.[a]
25	134400	——	1.17	——	168.0	——
26	135436	——	1.17	——	165.0	——
27	136440	——	1.15	——	163.0	——
28	137405	——	1.13	——	161.0	——
29	138350	——	1.11	——	159.0	——
30	139256	——	1.10	——	155.0	——
31	140118	——	1.07	——	155.0	——
32	140946	——	1.04	——	150.0	——
33	141756	——	1.02	——	147.0	——
34	142496	——	1.00	——	146.0	——
35	143220	——	1.01	——	144.0	——
36	143921	——	0.98	——	141.0	——
37	144591	——	1.00	——	142.0	——
38	145220	——	0.95	——	141.0	——

a) Derived from Ref. 21 for v^+=0~11; Others are from Ref. 8

101154 cm^{-1} for v^+=0 and 2 measured in the present experiment are higher than values obtained in the emission and VUV laser PFI-PE studies by 7 cm^{-1}. Two values of 97347.0±1.3 and 97348±2 cm^{-1} for the IE[$O_2^+(X^2\Pi_{1/2g})$] determined in previous VUV laser PFI-PE measurements are in agreement. These IE values are likely to be more reliable than the IE[$O_2^+(X^2\Pi_{1/2g})$] value of 97345cm^{-1} determined here because of the more accurate energy calculation in the laser studies. We note that the T_v values for v^+=12, 22, and 25-38 are determined for the first time.

Referring to Table II, we can also see good agreement on B_v^+ and A_v^+ values derived from this work and previous[8,21] measurements. The accuracy for the B_v^+ and A_v^+ (v^+=0-11) constants determined from the rotational analysis of the $O_2^+(X^2\Pi_g) \leftarrow O_2^+(A^2\Pi_u)$ emission bands are by far the most accurate compared to those of the PFI-PE measurements. However, the PFI-PE measurements of Kong anf Hepburn and the present study have greatly extended the range of B_v^+ and A_v^+ values beyond v^+>11, which are inaccessible to optical studies. The maximum deviation between the B_v^+ values obtained here and those previous measurements for $v^+ \leq 24$ is 0.02 cm^{-1}, suggesting that B_v^+ values derived for v^+=25-38 in the BOS simulation are reliable. Figure 3-6 shows the plots for B_v^+ and A_v^+ as a function of v^+. The error bars for the B_v^+ and A_v^+ are indicated in the figure. Although the A_v^+ value of 182.0 cm^{-1} for v^+=20 determined here is lower than that of 188.0 cm^{-1} reported by Kong and Hepburn, it is interesting that both experiments show the A_v^+ (v^+=20) value to be greater than A_v^+ values for the adjacent v^+=19 and 21 states. This observation suggests that the variation of A_v^+ versus v^+ (Fig. 3-6) may not be a smooth function.

We have determined the expanding coefficients X_i, i = 0-4, for Y_v (= T_v, A_v^+, and B_v^+) in a Duham-type expansion of the form shown in Eq. (7) covering v^+=0-38 (see Table III).

$$Y_v = \sum_i X_i (v + \frac{1}{2})^i . \qquad (7)$$

The accuracy of spectroscopic constants determined in the emission study of Coxon and Haley[21] are significantly higher than those obtained in the PFI-PE studies. Thus, we use the spectroscopic values for v^+=0-11 from the emission study, together with T_v, A_v^+, and B_v^+

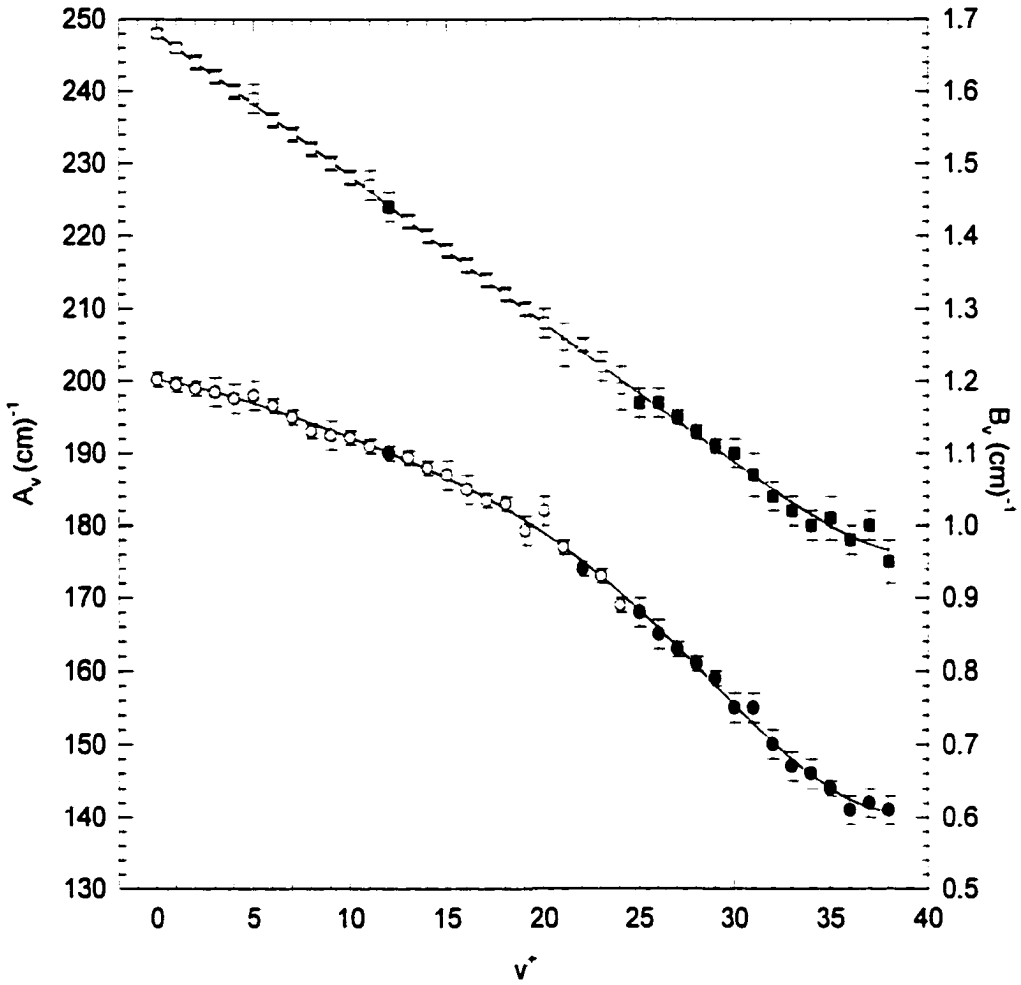

Figure 3-6. Plots of the spin-orbit splitting constants A_v^+ (solid circles) and rotational constants B_v^+ (open squares) versus v^+ for $O_2^+(X^2\Pi_g, v^+=0\text{-}38)$. Error bars for these values are indicated in the figure.

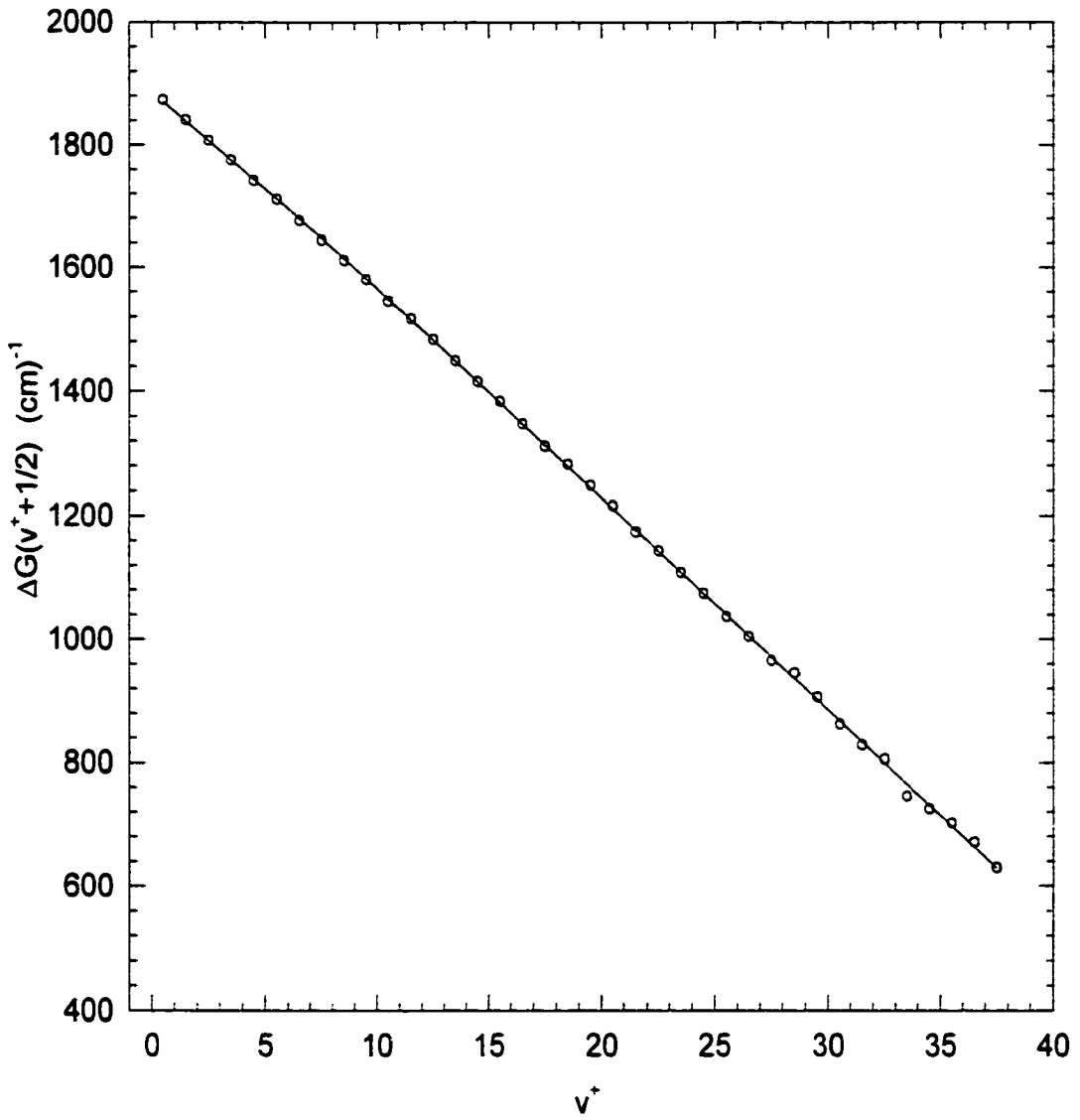

Figure 3-7. (a) Plot of the vibrational spacing $\Delta G(v^+)$ versus $(v^+ + 1/2)$. The $\Delta G(v^+)$ are calculated using the T_v data of Table 3-II. We note that the T_v data for $O_2^+(X^2\Pi_g, v^+=0\text{-}11)$ are from Ref. 21 and those for $O_2^+(X^2\Pi_g, v^+=12\text{-}38)$ are based on this work.

values for v^+=12-38 determined in the present study, as the experimental results. The expansion coefficients X_i, i = 0-4, which give the best fit to the experimental T_v, A_v^+, and B_v^+ values for v^+=0-38 are listed in Table III to compare with those reported in Refs. 8 and 21 for v^+=0-24 and v^+=0-11, respectively.

A plot of the vibrational spacing $\Delta G(v^+)$ versus $(v^+ + 1/2)$ is depicted in Fig. 3-7. The solid line represents the least square polynomial fit of experimental data. The dissociation limit of $O_2^+(X^2\Pi_g)$ [$O(^3P) + O^+(^4S_0)$] is known to be 18.733±0.003 eV.[39] Thus, v^+=38 at 18.0050±0.0005 eV covers up to ≈90% of well depth. The highest excited v^+ level of $O_2^+(X^2\Pi_g)$ observed previously with vibrational resolution is v^+= 45.[29] Based on the polynomial used in the curve fitting of $\Delta G(v^+)$, we have solved for the root of $\Delta G(v^+_{max}) = 0$ and obtained v^+_{max} = 56.3, where v^+_{max} is the maximum v^+ level sustained by the potential well. We note that this result is in excellent agreement with v^+_{max} = 56 and v^+_{max}= 56.5 derived by Akahori et al.[25] and Samson and Gardner[29] respectively.

IV. CONCLUSIONS

Using the broadly tunable high-resolution undulator synchrotron source at the Chemical Dynamics Beamline of the Advanced Light Source, we have obtained rotationally resolved photoelectron bands for $O_2^+(X^2\Pi_{1/2,3/2g}, v^+$=0-38) in the energy range of 12.01-18.15 eV. The IE values and spectroscopic constants for v^+=0-11 and 13-24 derived from the BOS simulation are in excellent agreement with previous emission[21] and VUV laser[5,6,8] PFI-PE studies. Spectral simulations have provided new IE values and spectroscopic constants for $O_2^+(X^2\Pi_{1/2,3/2g}, v^+$=12, 22, and 25-38). The rotational branches observed here indicate that the photoelectrons are formed predominantly in continuum states with orbital angular momentua l =1 ,3 and 5.

Numerous local intensity enhancements are observed for $O_2^+(X^2\Pi_{1/2,3/2g}, v^+$=0-14), indicative of stong perturbations of rotational transitions by the nearby resonance autoionizing mechanisms.[31] The spectra observed for $O_2^+(X^2\Pi_{1/2,3/2g}, v^+$=14-38) are generally in good accord with the BOS simulation. This observation, together with the smooth intensity profile observed for these higher vibrtational bands, can be taken as support of the "direct" excitation

mechanism proposed by Kong and Hepburn,[8] which invoke an intermediate neutral repulsive state. The results of this experiment and those for $NO^+(X\ ^1\Sigma^+, v^+=0\text{-}31)$ indicate that both the nearby resonance autoionizaing mechanisms and the direct excitation are likely to be operative, giving rise to finite intensities for higher vibrationally excited states in the Franck-Condon gap region. As expected, the intensity enhancement due to the nearby resonance autoionizing mechanism is usually significantly greater than that by the direct excitation mechanism.

ACKNOWLEDGEMENTS

This work was supported by the Director, Office of Energy Research, Office of Basic Energy Sciences, Chemical Science Division of the U.S. Department of Energy Under Contract No. W-7405-Eng-82 for the Ames Laboratory and Contract No. DE-AC03-76SF00098 for the Lawrence Berkeley National Laboratory. Y.S. is the recipient of the Wall Fellowhsip for 1999-2000. M.E. acknowledges the GAANN Fellowship for 1996-1997 and the Dow Fellowship for 1997-1998.

References

1. K. Müller-Dethlef, M. Sander, and E. W. Schlag, *Chem. Phys. Lett.* **112**, 291 (1984).
2. K. Müller-Dethlef and E. W. Schlag, *Ann. Rev. Phys. Chem.* **42**, 109 (1991).
3. I. Powis, T. Baer, and C. Y. Ng, editors, "High Resolution Laser Photoionization and Photoelectron Studies", *Wiley Series in Ion Chem. and Phys.* (Wiley, Chichester, 1995) and references therein.
4. R. T. Wiedman and M. G. White, in "High Resolution Laser Photoionization and Photoelectron Studies", edited by I. Powis, T. Baer, and C. Y. Ng, *Wiley Series in Ion Chem. and Phys.* (Wiley, Chichester, 1995), Chap. 3, p. 79.
5. R. G. Tonkyn, J. W. Winniczek, and M. G. White, *Chem. Phys. Lett.* **164**, 137 (1989).

6. M. Braunstein, V. McKoy, S. N. Dixit, R. G. Tonkyn, and M. G. White, *J. Chem. Phys.* **93**, 5345 (1990).
7. W. Kong, D. Rodgers and J. W. Hepburn, *Chem. Phys. Lett.* **203**, 497 (1993).
8. W. Kong and J. W. Hepburn, *Can. J. Phys.* **72**, 1284 (1994).
9. K.-M. Weitzel and F. Güthe, *Chem. Phys. Lett.* **251**, 295 (1996).
10. C.-W. Hsu, M. Evans. P. A. Heimann, and C. Y. Ng, *Rev. Sci. Instrum.*, **68**, 1694 (1997).
11. C.-W. Hsu, P. A. Heimann, M. Evans, S. Stimson, T. Fenn, and C. Y. Ng, *J. Chem. Phys.* **106**, 8931 (1997).
12. C.-W. Hsu, M. Evans, S. Stimson, C. Y. Ng, and P. Heimann, *Chem. Phys.* **231**, 121 (1998).
13. G. K. Jarvis, Y. Song, and C. Y. Ng, *Rev. Sci. Instrum.*, accepted.
14. R. C. Shiell, M. Evans, S. Stimson, C.-W. Hsu, C. Y. Ng, and J. W. Hepburn, *Phys. Rev. Lett.* **80**, 472 (1998).
15. R. C. Shiell, M. Evans, S. Stimson, C.-W. Hsu, C. Y. Ng, and J. W. Hepburn, *Phys. Rev. A*, in press.
16. S. Stimson, Y.-J. Chen, M. Evans, C.-L. Liao, C. Y. Ng, C.-W. Hsu, and P. Heimann, *Chem. Phys. Lett.* **289**, 507 (1998).
17. S. Stimson, M. Evans, C. Y. Ng, C. Destandau, G. Chambaud, P. Rosmus, C.-W. Hsu, and P. Heimann, *J. Chem. Phys.* **108**, 6205 (1998).
18. C.-W. Hsu, M. Evan, S. Stimson, and C. Y. Ng, *J. Chem. Phys.* **108**, 4701 (1998).
19. C.-W. Hsu, M. Evans, S. Stimson, and C. Y. Ng, *J. Chem. Phys.* **109**, 1285 (1998).
20. M. Evans, S. Stimson, C. Y. Ng, C.-W. Hsu, and G. K. Jarvis, *J. Chem. Phys.* **110**, 315 (1999).
21. J. A. Coxon and M. P. Haley, *J. Mol. Spectrosc.* **108**, 119 (1984).
22. K. Ellis, R. I. Hall, L. Avaldi, G. Dawber, A. McConkey, L. Andric, and G. C. King, *J. Phys. B* **27**, 3415 (1994).
23. P. M. Guyon, T. Baer, and I. Nenner, *J. Chem. Phys.* **78**, 3665 (1983).
24. F. Merkt, P. M. Guyon, and J. Hepburn, *Chem. Phys.* **173**, 479 (1993).

25. T. Akahori, Y. Morioka, T. Tanaka, H. Yoshii, T. Hayaishi and K.Ito. *J. Chem. Phys.* **107**, 4875(1997).

26. G. K. Jarvis, M. Evans, and C. Y. Ng, *J. Chem. Phys.*, submitted.

27. P. Heimann, M. Koike, C.-W. Hsu, M. Evans, K. T. Lu, C. Y. Ng, A. Suits, and Y. T. Lee, *Rev. Sci. nstrum.* **68**, 1945 (1997).

28. O. Edqvust, E. Lindholm, L. E. Selin, L. Åsbrink, *Physica Scripta* **1**, 25 (1970).

29. J. A. Samson and J. L. Gardner, *J. Chem. Phys.* **67**, 755 (1977).

30. P. M. Dehmer and W. A. Chupka, J. Chem. Phys. **62**, 4525 (1975); also see unpublished results, in J. Berkowitz, "Photoabsorption, Photoionization, and Photoelectron Spectroscopy" (Academic, New York, 1979), p.233.

31. T. Baer and P.-M. Guyon, in "High Resolution Laser Photoionization and Photoelectron Studies", edited by I. Powis, T. Baer, and C. Y. Ng, *Wiley Series in Ion Chem. and Phys.* (Wiley, Chichester, 1995), Chap. 1, p. 1.

32. G. B. Branton, D. C. Frost, T. Makita, C. A. McDowell, and I. A. Stenhouse, *Philos. Trans. R. Soc. London*, A: **268**, 77 (1970).

33. Y. Song, M. Evans, C. Y. Ng, G. K. Jarvis, and C.-W. Hsu, to be published.

34. A. D. Buckingham, B. J. Orr, J. M. Sichel, *Phil. Trans. Roy. Soc. Lond.* A **268**, 147 (1970).

35. G. Herzberg, :Molecular Spectra and Molecular Structure, Vol. I, Spectra of Diatomic Molecules (Van Nostrand, Princeton, NJ, 1950).

36. K.P. Huber and G. Herzberg, *Molecular Spectra and Molecular Structure*, Constants of Diatomic Molecules, Vol. IV (Van Nostrand, New York, 1974).

37. A. Giusti-Suzor and Ch. Jungen, *J. Chem. Phys.* **80**, 986 (1984).

38. M. Braunstein and V. McKoy, *J. Chem. Phys.* **90**, 2575 (1989); and references therein.

CHAPTER 4. ROTATIONALLY RESOLVED PULSED FIELD IONIZATION PHOTOELECTRON BANDS FOR $O_2^+(A^2\Pi_u, v^+=0\text{-}12)$ IN THE ENERGY RANGE OF 17.0-18.2 eV

A paper published in *Journal of Chemical Physics*, **112**, 1271 (2000)

Y. Song, M. Evans, C.Y. Ng, C.-W. Hsu and G. K. Jarvis

Abstract:

We have obtained rotationally resolved pulsed field ionization photoelectron (PFI-PE) spectra for O_2 in the energy range of 17.05-18.13 eV, covering the ionization transitions $O_2^+(A^2\Pi_u, v^+=0\text{-}12, N^+) \leftarrow O_2\ (X^3\Sigma_g^-, v''=0, N'')$. Although these $O_2^+(A^2\Pi_u, v^+)$ PFI-PE bands have significant overlaps with vibrational bands for $O_2^+(a^4\Pi_u)$ and $O_2^+(X^2\Pi_g)$, we have identified all the $O_2^+(A^2\Pi_u, v^+=0\text{-}12)$ bands by simulation of spectra obtained using supersonically cooled O_2 samples with rotational temperatures ≈20 and 220 K. While these $v^+=0\text{-}12$ PFI-PE bands represent the first rotationally resolved photoelectron data for $O_2^+(A^2\Pi_u)$, the PFI-PE bands for $O_2^+(A^2\Pi_u, v^+=9$ and 10) are the first rotationally resolved spectroscopic data for these levels. The simulation also allows the determination of accurate ionization energies, vibrational constants, and rotational constants for $O_2^+(A^2\Pi_u, v^+=0\text{-}12)$. The analysis of the PFI-PE spectra supports the conclusion of the previous emission study that the $O_2^+(A^2\Pi_u, v^+=9$ and 10) states are strongly perturbed by a nearby electronic state.

I. INTRODUCTION

In a recent series of synchrotron-based pulsed field ionization (PFI) photoelectron (PFI-PE) experiments, we have obtained and analyzed rotational-resolved PFI-PE vibrational bands for the $O_2^+(X^2\Pi_g, b^4\Sigma_g^-, 2^2\Pi_u, B^2\Sigma_g^-, {}^2\Sigma_u^-$ and $c^4\Sigma_u^-)$,[1-6] $NO^+(X^1\Sigma^+$ and $a^3\Sigma^+)$,[7,8] and $CO^+(X^2\Sigma^+, A^2\Pi, D^2\Pi$, and $3^2\Sigma^+)$[9-11] states. A major advantage of synchrotron studies is the capability to cover a wide photon energy range, allowing a long vibrational

progression of an electronic state to be examined. This capability has been clearly demonstrated in the recent comprehensive PFI-PE studies of $O_2^+(X^2\Pi_g$, $b^4\Sigma_g^-$, and $B^2\Sigma_g^-$),[2,5,6] $NO^+(X^1\Sigma^+$ and $a^3\Sigma^+$),[7,8] and $CO^+(X^2\Sigma^+$ and $A^2\Pi$).[9,10] Synchrotron-based PFI-PE studies are complementary to vacuum ultraviolet (VUV) laser PFI-PE measurements,[12] which often cover a narrower energy range, but can be performed at a higher resolution.[13] In addition to providing accurate ionization energies (IEs) and new spectroscopic constants, the rotational-resolved synchrotron-based PFI-PE studies have revealed fundamental insight into the threshold photoionization dynamics[12] of O_2, NO, and CO, which cannot be obtained in traditional ion spectroscopic measurements based on absorption and ion emission.[14]

The spectroscopy for $O_2^+(A^2\Pi_u, v^+)$ is relatively well known.[14-17] On the basis of a comprehensive analysis of the of $O_2^+(A^2\Pi_u) \rightarrow O_2^+(X^2\Pi_g)$ emission system, Coxon and Haley[14] have obtained highly accurate spectroscopic constants for $O_2^+(A^2\Pi_u$, v+=0-8 and 11-15). However, the vibrational and rotational constants for the $O_2^+(A^2\Pi_u$, v+=9 and 10) levels have only been interpolated in the latter study. It is well known from previous photoelectron studies that the vibrational bands for $O_2^+(A^2\Pi_u)$ are in serious overlap with those of the $O_2^+(X^2\Pi_g$ and $a^4\Pi_u)$ states.[6,15,17] This, together with the high multiplicities of the electronic states involved, has made the clear identification of these vibronic bands difficult in previous photoelectron spectroscopic studies.[17-19] In a recent synchrotron-based threshold photoelectron (TPE) study employing the penetration field technique, along with the rotational cooling of the O_2 sample using the supersonic beam technique, Morioka and co-workers have successfully identified most of the vibrational bands for the $O_2^+(X^2\Pi_g$, $a^4\Pi_u$, and $A^2\Pi_u$,) states in the energy region of interest to the present study.[15] Although the vibrational bands for $O_2^+(A^2\Pi_u, v^+)$ at energies close to its dissociation limit have been assigned in Ref. 15, the photoelectron bands are only recorded and analyzed to the vibrationally resolved level.

This report is one among a series of articles[1-6] on the detailed photoelectron study of O_2. Here, we present the analysis of the rotational-resolved PFI-PE data for $O_2^+(A^2\Pi_u$, v+=0-12) obtained using an O_2 sample at ≈220 K. Due to the weakness of the $O_2^+(A^2\Pi_u$,

v^+=0) band, its clear identification is only possible by using a cold (≈20 K) O_2 sample achieved in a supersonic expansion. The PFI-PE bands for $O_2^+(A^2\Pi_u, v^+=1\text{-}3,5)$ have also been examined using the 20 K O_2 sample for confirmation of the spectral simulation. The simulation of these PFI-PE data allows the determination of accurate IEs, vibrational constants, and rotational constants for $O_2^+(A^2\Pi_u, v^+=0\text{-}12)$.

II. EXPERIMENT

The design and performance of the high-resolution VUV photoionization facility of the Chemical Dynamics Beamline at the Advanced Light Source (ALS) has been described previously.[2,20-23] Briefly, the major components include a 10-cm period undulator, a gas harmonic filter, a 6.65m off-plane Eagle monochromator, and a photoion-photoelectron apparatus.[2,20-22]

In the present experiment, helium is used in the harmonic gas filter, where higher undulator harmonics with photon energies greater than 24.59 eV are suppressed. The fundamental light from the undulator is then directed into the 6.65 m monochromator and dispersed by a 4800 lines/mm grating (dispersion = 0.32 Å/mm) before entering the experimental apparatus. The PFI-PE bands were measured using the 4800 lines/mm grating and monochromator entrance/exit slits of 50-200 μm, achieving wavelength resolutions of 0.016-0.064 Å (full-width-at-half-maximum, FWHM). The photon energy step size was varied in the range of 0.1-0.25 meV.

The ALS storage ring is capable of filling 328 electron buckets in a period of 656 ns. Each electron bucket emits a light pulse of 50 ps with a time separation of 2 ns between successive bunches.[23] In each storage ring periods, a dark gap (16 ns) consisting of 8 consecutive unfilled buckets exists for the ejection of cations from the orbit. A multibunch operation with a dark gap of 16 ns corresponds to 320 bunches in the synchrotron orbit or a repetition rate of 488 MHz.

The procedures for PFI-PE measurements using the photoion-photoelectron apparatus have been described previously in detail.[2,20-22] The electron spectrometer, which consists of a steradiancy analyzer and a hemispherical energy analyzer arranged in tandem,

was used to filter prompt electrons. For measurements of PFI-PE bands, a pulsed electric field (height = 0.67 V/cm, width = 40 ns) was applied every three synchrotron periods, i.e., 1.97 μs. Thus, the repetition rate of the electric field pulses was 0.51 MHz.

A continuous molecular beam of pure O_2 was produced by supersonic expansion through a stainless steel nozzle (diameter = 0.127 mm) at a stagnation pressure of 760 Torr and a nozzle temperature of 298 K. The molecular beam was skimmed by a circular skimmer (diameter = 1 mm) before intersecting the monochromatized VUV light beam 7 cm downstream in the photoionization region. As shown below, the simulation of PFI-PE spectra suggests that the rotational temperature for O_2 achieved is ≈220 K in this experiment.

Recently, the $O_2^+(A^2\Pi_u, v^+=0\text{-}3 \text{ and } 5)$ PFI-PE bands were re-examined in another experiment performed about three years later using a colder O_2 molecular beam sample with a rotational temperature of ≈20 K. A new synchrotron based PFI-PE detection scheme, which relies on the time-of-flight (TOF) selection of PFI-PEs, is used in this recent study.[24] By employing a synchrotron dark gap of ≥80 ns, we show that the TOF peak for PFI-PEs can be adjusted to arrive in the dark gap with little contamination by prompt electrons. This new scheme not only is more effective in suppression of prompt electrons, but also has a higher electron transmission. Using a 2400 lines/mm grating and monochromator entrance/exit slits of 50-100 μm, the wavelength resolution achieved in this PFI-PE experiment was 0.032-0.064 Å (FWHM).

The absolute photon energy scale was calibrated using the $Ar^+(^2P_{3/2})$, and $Ne^+(^2P_{3/2})$ PFI-PE bands recorded under the same experimental conditions before and after each scan.[2,21-23] This calibration procedure assumes that the Stark shift for ionization thresholds of O_2 and the rare gases are identical. On the basis of previous experiments,[1-9,25] the accuracy of the energy calibration is believed to be within ±0.5 meV.

III. RESULTS AND DISCUSSION

The main electronic configuration for the $O_2(X^3\Sigma_g^-)$ ground state is $KK(2\sigma_g)^2(2\sigma_u)^2(3\sigma_g)^2(1\pi_u)^4(1\pi_g)^2$. The ejection of an electron from a $1\pi_u$ bonding orbital

results in the $O_2^+(a^4\Pi_u)$ and $O_2^+(A^2\Pi_u)$ excited states. Both these excited states, together with the ground $O_2^+(X^2\Pi_g)$ state, converge to the first dissociation limit $O(^3P) + O^+(^4S_0)$, but with significantly shallower potential wells than that of the $O_2^+(X^2\Pi_g)$ state.[26]

In the energy region (17.00-18.15 eV) of interest to the present experiment, we have identified rotational-resolved vibrational bands for $O_2^+(X^2\Pi_g, v^+=28\text{-}38)$, $O_2^+(a^4\Pi_u, v^+=8\text{-}18)$, and $O_2^+(A^2\Pi_u, v^+=0\text{-}12)$ [see Fig. 2(b) of Ref. 6]. The analysis of the vibrational PFI-PE bands for $O_2^+(X^2\Pi_g)$ has been reported recently.[6] Generally, each of the $v^+=0\text{-}12$ PFI-PE bands for the $O_2^+(A^2\Pi_u)$ state overlaps with the respective $v^+=8\text{-}20$ PFI-PE vibrational bands of the $O_2^+(a^4\Pi_u)$ state. While the overlaps between the respective $O_2^+(a^4\Pi_u, v^+=8\text{-}10)$ and $O_2^+(A^2\Pi_u, v^+=0\text{-}2)$ bands are very serious, the structures for the $O_2^+(a^4\Pi_u, v^+>17)$ state give only minor interference to the PFI-PE bands for $O_2^+(A^2\Pi_u, v^+=9\text{-}12)$. The $O_2^+(X^2\Pi_g, v^+=28\text{-}32)$ PFI-PE bands also have significant overlap with the respective $O_2^+(A^2\Pi_u, v^+=0\text{-}4)$ bands.[6]

Taking into account the spectra reported in other publications on the analysis of the $O_2^+(X^2\Pi_g, v^+)$[6] and $O_2^+(a^4\Pi_u, v^+)$[27] states, we have selected to show in Figs. 4-1(a)-4-1(f) the respective mixed experimental PFI-PE bands (open circles, top spectra of lower panels) for $O_2^+(A^2\Pi_u, v+=3\text{-}8)$ obtained using an O_2 sample with a rotational temperature of ≈220 K. Figures 4-2(a)-4-2(d) depict the experimental PFI-PE bands (open circles, top spectra) for $O_2^+(A^2\Pi_u, v+=0\text{-}3)$ measured using a cold O_2 molecular beam sample (rotational temperature ≈20 K). The experiment spectrum of Fig. 4-2(a) was obtained by subtracting the deconvoluted band for $O_2^+(a^4\Pi_u, v+=8)$ [bottom spectrum (solid line) shown in Fig. 5(b) of Ref. 6] from the mixed experimental spectrum [top spectrum (open circles) shown in Fig. 5(b) of Ref. 6]. We note that this subtracted spectrum consists of contributions from both the $O_2^+(X^2\Pi_g, v+=28)$ and $O_2^+(A^2\Pi_u, v+=0)$ bands. The 20 K spectra of Figs. 4-2(a)- 4-2(d) reveal essentially a single peak for the $O_2^+(A^2\Pi_u, v+=0\text{-}3)$ PFI-PE bands. The mixed experimental PFI-PE bands (open circles, upper spectra) for $O_2^+(A^2\Pi_u, v^+=9, 10, 11$ and 12) are plotted in Fig. 4-3. These vibrational PFI-PE bands are aligned by their IEs determined in the simulation as described below.

Figure 4-1. Deconvolution of the PFI-PE bands for $O_2^+(A^2\Pi_{1/2,3/2u})$ (a) $v^+=3$, (b) $v^+=4$, (c) $v^+=5$, (d) $v^+=6$, (e) $v^+=7$, and (f) $v^+=8$ from the corresponding mixed bands by BOS simulation. (upper panels): The deconvoluted PFI-PE bands for $O_2^+(A^2\Pi_{1/2,3/2u}, v^+=3\text{-}8)$. The rotational transitions to the $O_2^+(A^2\Pi_{1/2u}, v^+, N^+)$ and $O_2^+(A^2\Pi_{3/2u}, v^+, N^+)$ from O_2 $(X^3\Sigma_g^-, v''=0, N'')$ are marked using downward pointing and upward pointing stick marks, respectively. The ΔJ rotational branches are also marked. (Lower panels): The top spectra (open circles) are the mixed experimental PFI-PE spectra obtained using an O_2 sample with a rotational temperature of ≈220 K. The deconvoluted PFI-PE bands (solid lines) for $O_2^+(a^4\Pi_u, v^+=11\text{-}16)$ and $O_2^+(X^2\Pi_{1/2,3/2g}, v^+=31$ and $32)$ are shown as the bottom spectra. The middle spectra (solid lines) represent the sums of the deconvoluted bands.

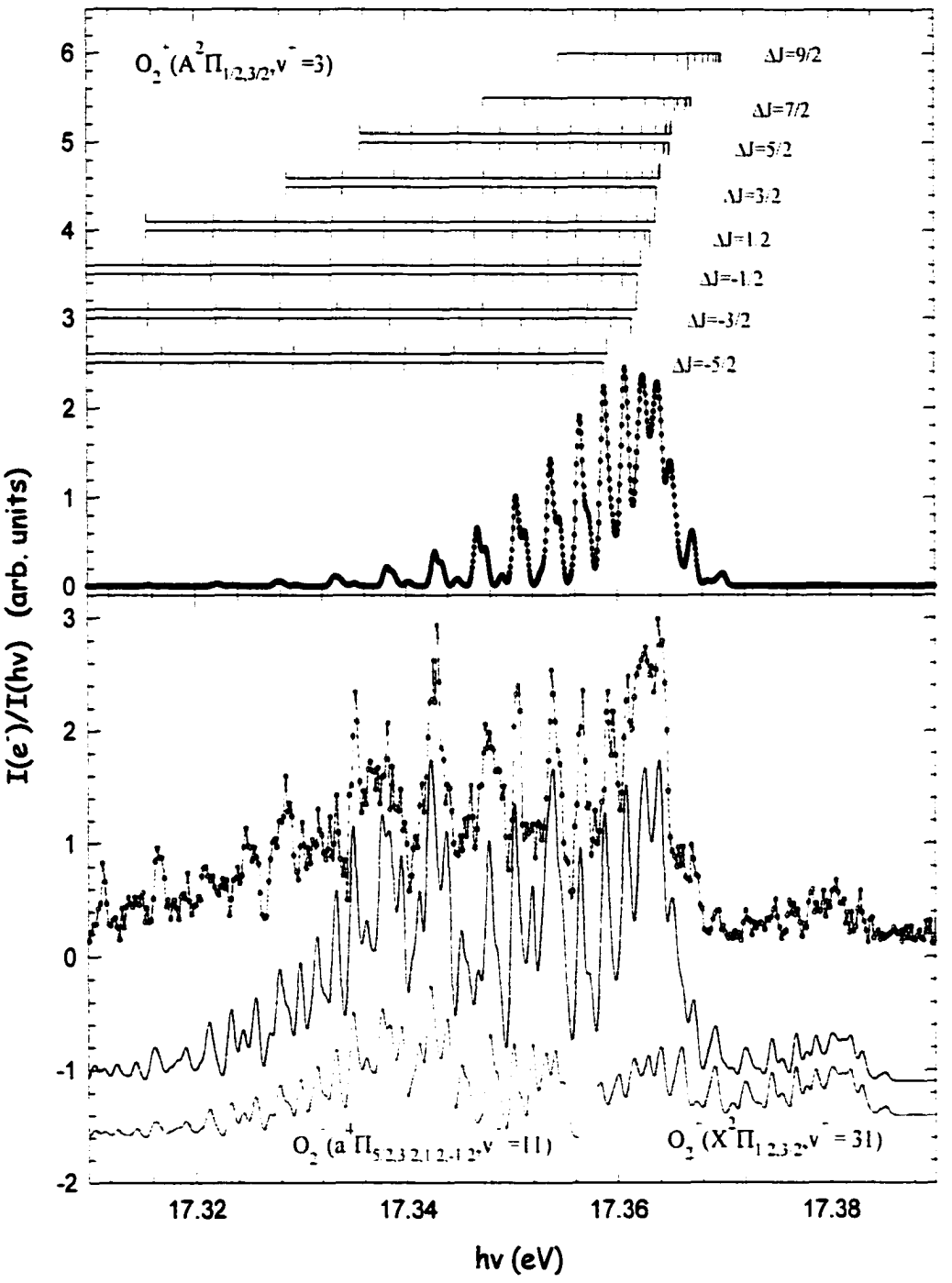
$O_2^+(A^2\Pi_{1/2,3/2},v^+=3)$
ΔJ=9/2
ΔJ=7/2
ΔJ=5/2
ΔJ=3/2
ΔJ=1/2
ΔJ=-1/2
ΔJ=-3/2
ΔJ=-5/2
$O_2^-(a^4\Pi_{5/2,3/2,1/2,-1/2},v^-=11)$
$O_2^-(X^2\Pi_{1/2,3/2},v^-=31)$
I(e⁻)/I(hv) (arb. units)
hv (eV)
17.32
17.34
17.36
17.38

(a)

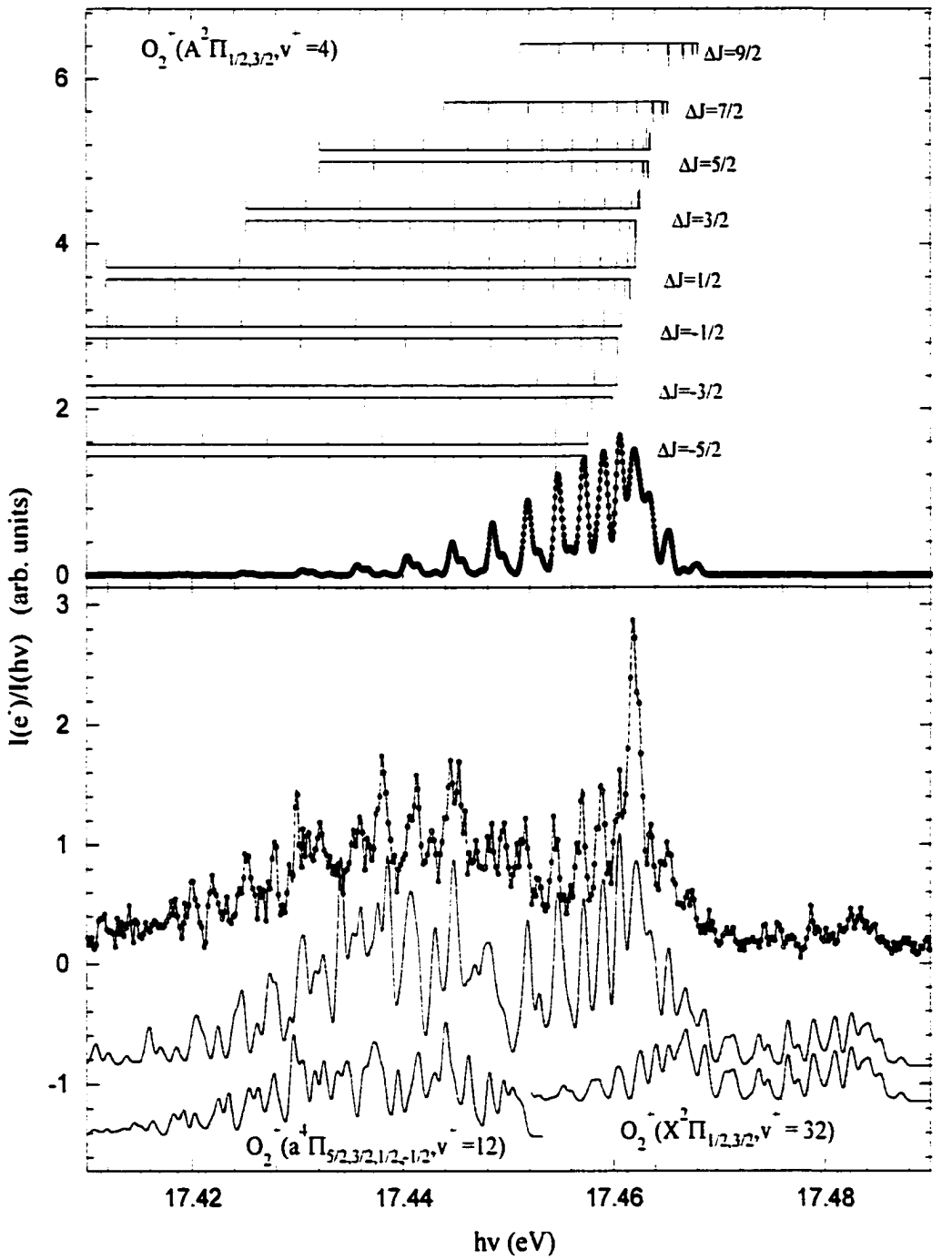

(b)

Figure 4-1 (Continued)

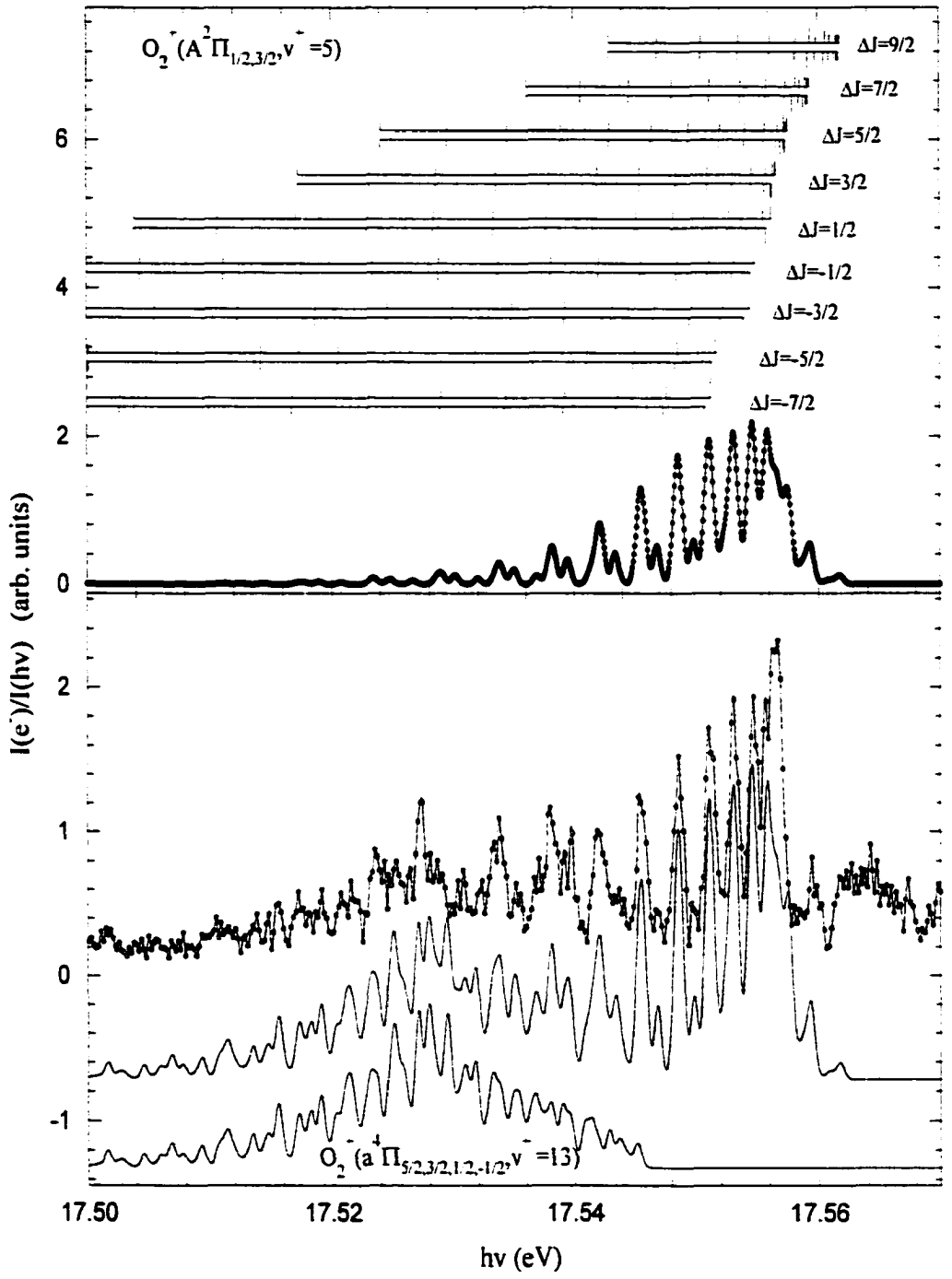

(c)

Figure 4-1 (Continued)

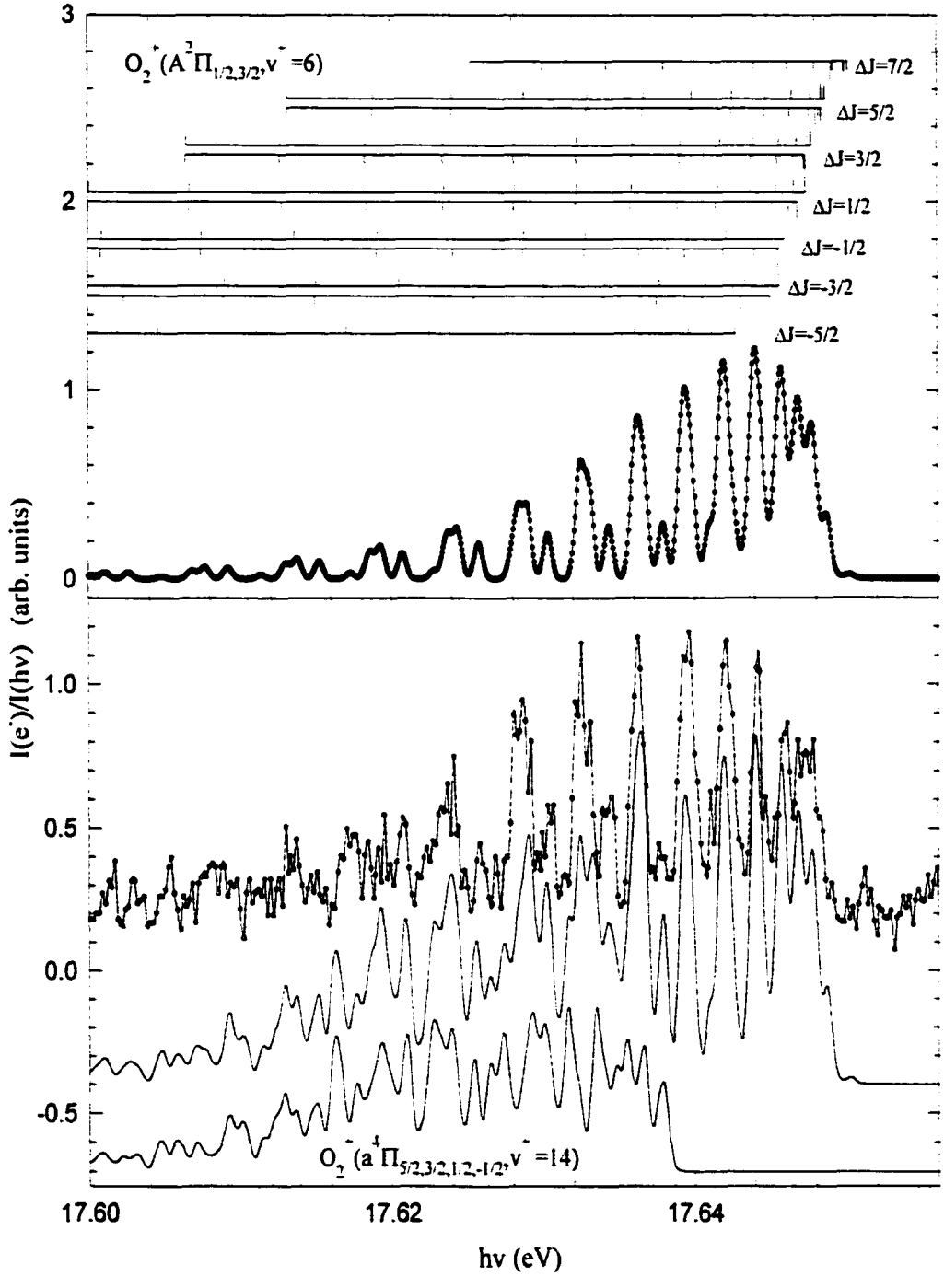

(d)

Figure 4-1 (Continued)

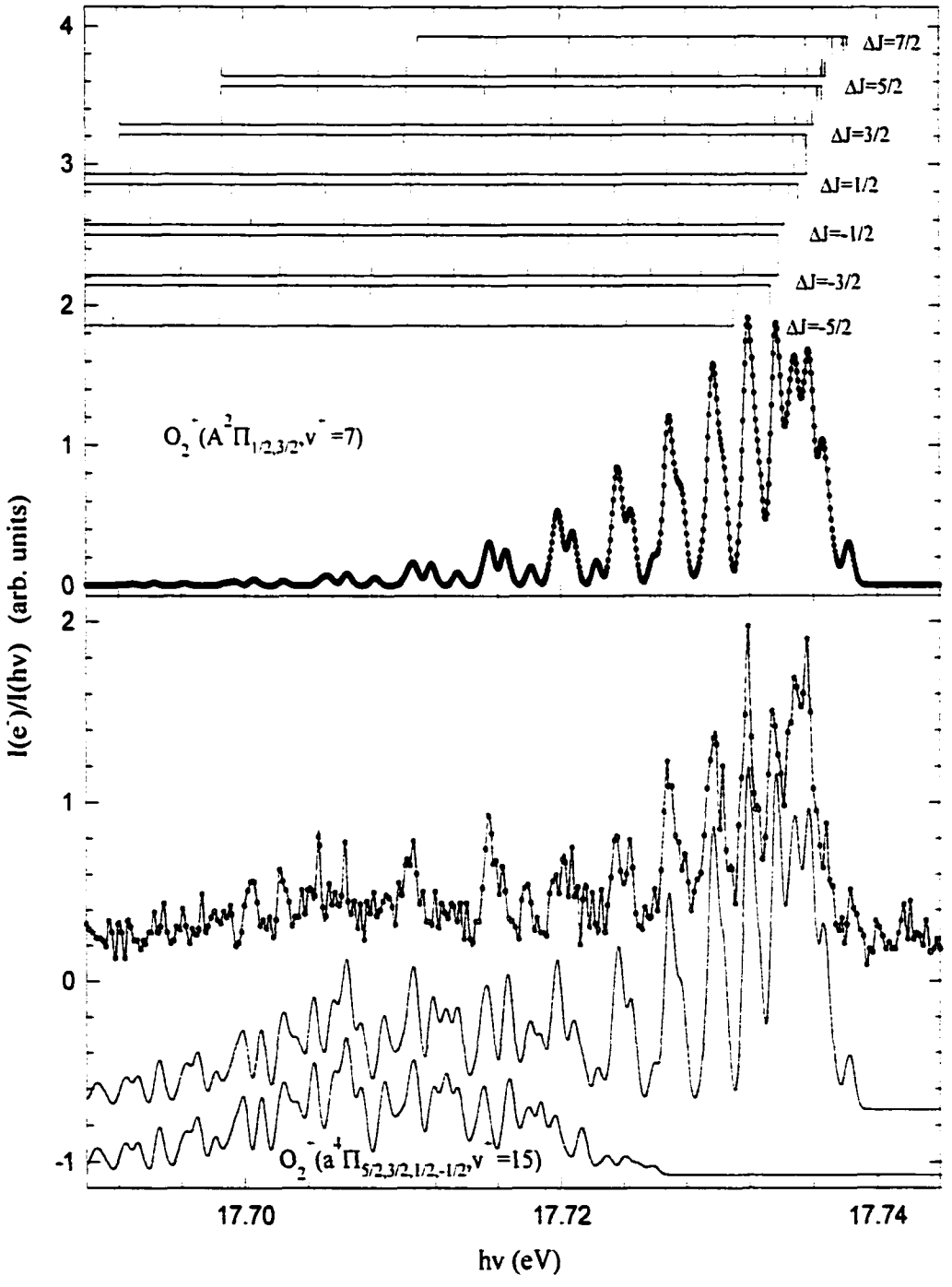

Figure 4-1 (Continued)

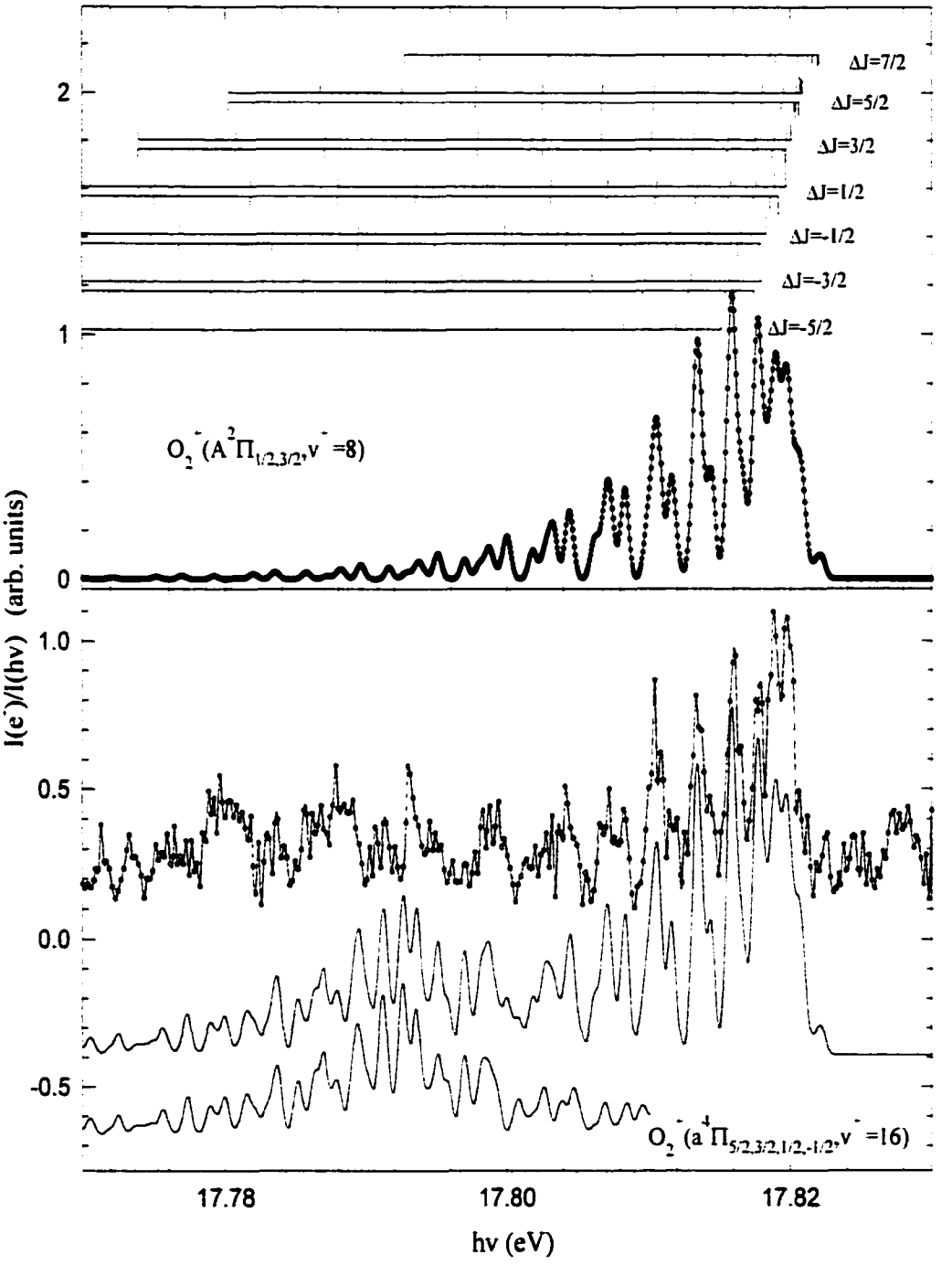

(f)

Figure 4-1 (Continued)

Figure 4-2. Simulations (bottom spectra, solid lines) of experimental PFI-PE bands (top spectra, open circles) for $O_2^+(A^2\Pi_u)$ (a) $v^+=0$, (b) $v^+=1$, (c) $v^+=2$, and (d) $v^+=3$ obtained using an O_2 sample with a rotational temperature of ≈20 K. The experimental PFI-PE band of (a) is obtained by subtracting the deconvoluted band for $O_2^+(a^4\Pi_u, v^+=8)$ from the mixed experimental spectrum (see Ref. 6). The deconvoluted spectrum (dashed curve) for $O_2^+(a^2\Pi_{3/2g}, v^+=28)$ is also shown in (a). The rotational transitions to the $O_2^+(A^2\Pi_{1/2u}, v^+, N^+)$ and $O_2^+(A^2\Pi_{3/2u}, v^+, N^+)$ from O_2 ($X^3\Sigma_g^-$, $v''=0$, N'') are marked using downward pointing and upward pointing stick marks, respectively. The ΔJ rotational branches are also marked.

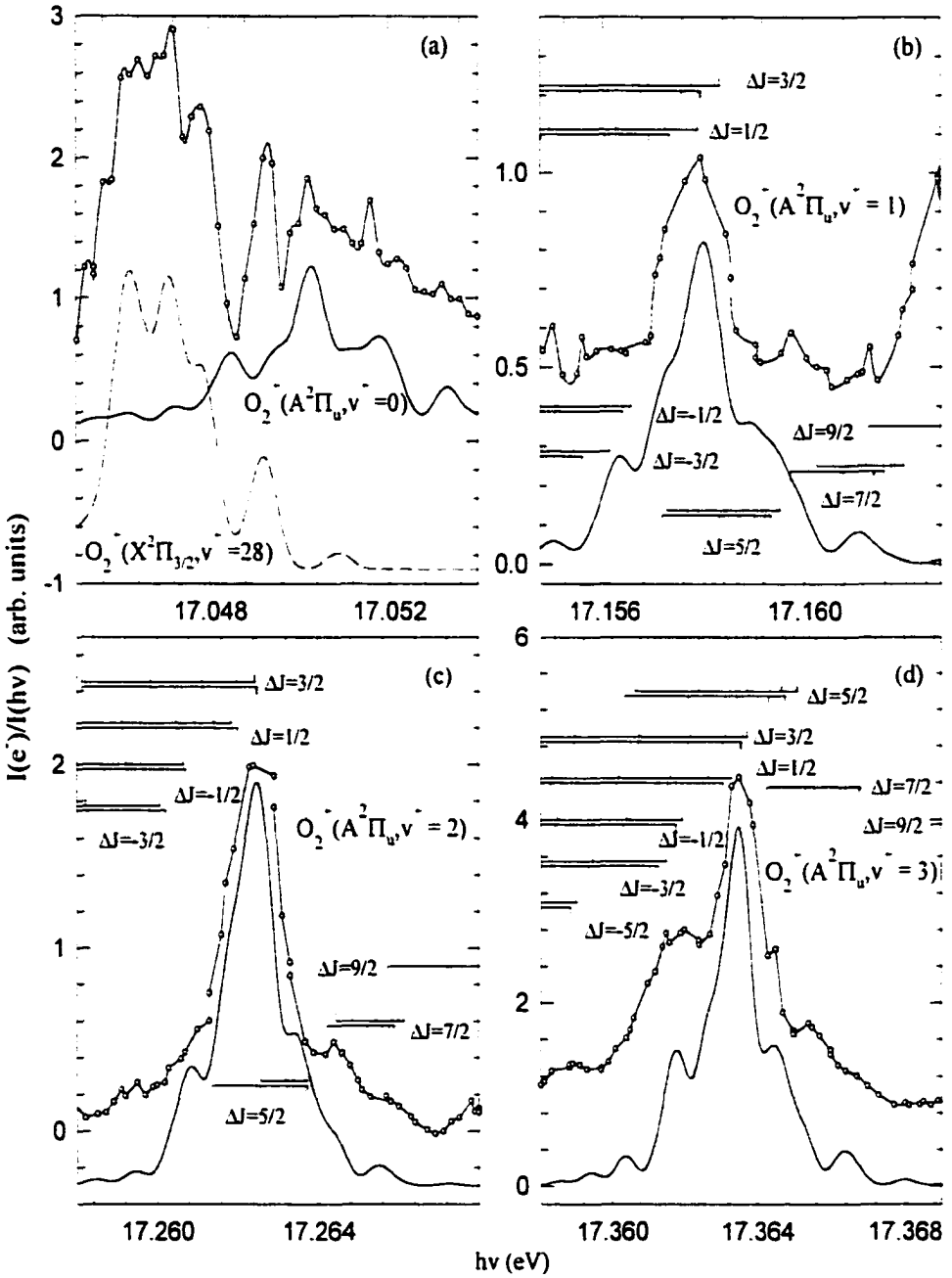
(a)
$O_2^-(A^2\Pi_u, v^-=0)$
$-O_2^-(X^2\Pi_{3/2}, v^-=28)$
(b)
$O_2^-(A^2\Pi_u, v^-=1)$
ΔJ=3/2
ΔJ=1/2
ΔJ=-1/2
ΔJ=-3/2
ΔJ=9/2
ΔJ=7/2
ΔJ=5/2
(c)
$O_2^-(A^2\Pi_u, v^-=2)$
ΔJ=3/2
ΔJ=1/2
ΔJ=-1/2
ΔJ=-3/2
ΔJ=9/2
ΔJ=7/2
ΔJ=5/2
(d)
$O_2^-(A^2\Pi_u, v^-=3)$
ΔJ=5/2
ΔJ=3/2
ΔJ=1/2
ΔJ=7/2
ΔJ=9/2
ΔJ=-1/2
ΔJ=-3/2
ΔJ=-5/2
I(e⁻)/I(hv) (arb. units)
hv (eV)

Figure 4-3. Simulated and experimental PFI-PE spectra for $O_2^+(A^2\Pi_{3/2u}, v^+=9\text{-}12)$. The horizontal scale is $h\nu$ - $IE(v^+)$, where $h\nu$ is the photon energy. For each v^+ state, the upper spectrum (open circles) is the experimental spectrum, while the simulated spectrum (solide line) is shown underneath the experimental curve.

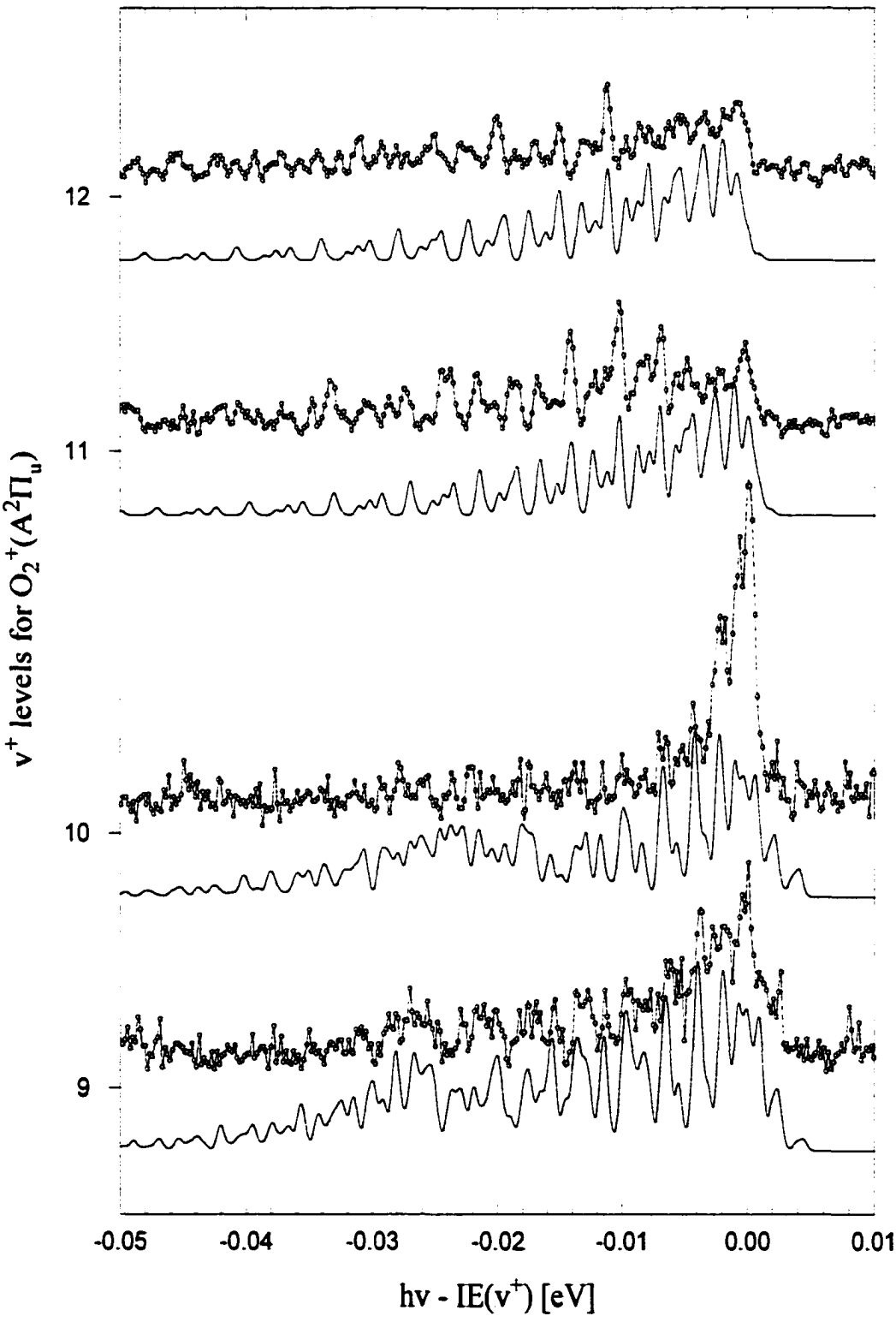
12
11
10
9
v+ levels for O2+(A2Πu)
-0.05
-0.04
-0.03
-0.02
-0.01
0.00
0.01
hv - IE(v+) [eV]

The PFI-PE intensities [I(e^-)] are normalized by the VUV photon intensities [I(hv)] measured using a tungsten photoelectric detector. The detection efficiency for the tungsten detector as a function of VUV photon energy has been corrected based on the known photoelectric yield of tungsten.[28] The I(e^-)/I(hv) scales for experimental spectra plotted within Figs. 4-1(a)- 4-1(f) or 4-2(a)- 4-2(d) or 8 show the actual relative PFI-PE intensities observed in the experiment. The intensity for the $O_2^+(A^2\Pi_u, v^+=1)$ band is higher than that for $O_2^+(A^2\Pi_u, v^+=0)$, but lower than that for $O_2^+(A^2\Pi_u, v^+=2)$. The structures for the $O_2^+(A^2\Pi_u, v^+\geq3)$ bands are the dominant components of the mixed PFI-PE bands observed at higher energies. The intensity for vibrational bands of $O_2^+(A^2\Pi_u, v^+)$ reaches a global maximum at $v^+=3$ and then decreases gradually from $v^+=3$ toward higher high vibrational levels up to $v^+=6$ as expected based on the Franck-Condon consideration. However, the PFI-PE band intensity for $O_2^+(A^2\Pi_u)$ exhibits two other local maxima at $v^+=7$ and 10. We note that the maximum intensity for the $v^+=9$ is also higher than that for $v^+=8$. These band intensity deviations from the Franck-Condon behavior are indicative of perturbative ionization mechanisms involving other electronic states.

A. Spectral simulation and assignment of rotational branches

The relative intensities for rotational structures resolved in individual vibrational PFI-PE bands for $O_2^+(A^2\Pi_u, v^+=0\text{-}12)$ were simulated using the Buckingham-Orr–Sichel (BOS) model,[29] which was derived to predict rotational line strength observed in single-photon ionization of diatomic molecules. This procedure has been described in detail previously.[2,6,8] The BOS model is a one-electron model and does not take into account any channel interactions. The BOS coefficients C_λ's are predicted to be identical for all the vibrational levels and spin-orbit components. These predictions were not confirmed in the present and previous experiments, indicative of the existence of channel interactions due to perturbation by other states. Thus, the BOS simulation employed here should be viewed as empirical in nature.

The ionization transition $O_2^+(A^2\Pi_{1/2,3/2u}) \leftarrow O_2(X^3\Sigma_g^-)$ can be classified as a Hund's case (b) to (a) transition and is similar to the $O_2^+(X^2\Pi_{1/2,3/2g}) \leftarrow O_2(X^3\Sigma_g^-)$ system. Since the detailed discussion on simulation of the latter system has been reported previously,[6] we

have omitted the redundant description here. As in previous studies, this simulation uses the known spectroscopic constants for $O_2(X^3\Sigma_g^-, v''=0)$.[30] Furthermore, the simulation has taken into account transitions involving the three fine-structure sublevel F_1, F_2, and F_3 of $O_2(X^3\Sigma_g^-, v''=0)$ despite the fact that the present experiment cannot resolve the fine-structure transitions.[2] We assume that the rotational populations for O_2 are governed by the Boltzmann distribution characterized by a rotational temperature. Thus, the rotational temperature for O_2, along with the BOS coefficients and rotational constants for $O_2^+(A^2\Pi_{1/2,3/2u}, v^+)$, is a fitting parameter. On the basis of spectral simulations, we estimate that the PFI-PE spectra of Figs. 4-1(a)- 4-1(f) and 3 are measured using an O_2 sample with a rotational temperature of 220±20 K. For the spectra of Figs. 4-2(a)- 4-2(d), we estimate that the rotational temperature of the O_2 sample is ≈20 K. A Gaussian line width of 5 cm^{-1} (FWHM) is used as the instrumental resolution profile in the simulation.

For a Σ to Π transition ($\Delta\Lambda$ =1), the first 3-j symbol requires that the BOS coefficient C_0 is zero for the photoionization process. The best fitted BOS coefficients for the $O_2^+(A^2\Pi_{1/2,3/2u}, v^+$= 0-12) PFI-PE bands are listed in Table 4-1. We have been able to simulate the v^+=0-2, 6-8, 11, and 12 PFI-PE bands using only C_1 for both Ω components. All other experimental PFI-PE vibrational bands were satisfactorily simulated using the BOS coefficients (C_1, C_2) for both Ω components, except that for v^+=10, Ω=1/2, where C_3 is also required. The observation of dominant (C_1, C_2) coefficients indicates that the *p*- and *d*-partial waves of the ground electron wave function are the major contributors in the ionizing transitions. Although the uncertainties for the C_λ values are relatively high (±0.2), the deviations of the BOS coefficients from the general trend are still discernible for the v^+ =9 and 10 bands. For the v^+=9 band, C_2 (=0.8) is significantly greater than that for C_1 (=0.2), whereas C_3 is nonzero for the v^+=10 band. This observation is indicative of perturbation by other states in the neighborhood of v^+=9 and 10. As shown in Fig. 4-3, the experimental spectrum for the v^+=10 band has a substantially higher intensity and a narrower width compared to those for the adjacent bands.

The deconvoluted PFI-PE bands (solid line) for $O_2^+(A^2\Pi_{1/2}, v^+$=3-8) obtained by simulation are shown in the upper panels of Figs 4-1(a)- 4-1(f), respectively. We also

Table 4-I. The best fitted BOS coefficients (C_i, i = 1,2)[a] obtained in the simulation of the PFI-PE bands for $O_2^+(A^2\Pi_{1/2,3/2u}, v^+)$.

v^+	C_1	C_2
0	1.00/1.00	0.00/0.00
1	1.00/1.00	0.00/0.00
2	1.00/1.00	0.00/0.00
3	0.50/1.00	0.50/0.00
4	0.50/1.00	0.50/0.00
5	0.50/0.50	0.50/0.50
6	1.00/1.00	0.00/0.00
7	1.00/1.00	0.00/0.00
8	1.00/1.00	0.00/0.00
9	0.20/0.20	0.80/0.80
10[b]	0.50/1.00	0.20/0.00
11	1.00/1.00	0.00/0.00
12	1.00/1.00	0.00/0.00

a) All C_i values have an uncertainty of ± 0.2. The 1st and 2nd values for each C_i (i=1,2) entry are for the $^2\Pi_{1/2g}$ and $^2\Pi_{3/2g}$ components, respectively.

b) For $O_2^+(A^2\Pi_{1/2u}, v^+=10)$, C_3=0.30

show the deconvoluted PFI-PE bands (solid lines, bottom spectra) for $O_2^+(a^4\Pi_u, v^+=11\text{-}16)$ and $O_2^-(X^2\Pi_{3/2,1/2g}, v^+=31$ and 32) in the lower panels of Figs. 4-1(a) and4-1(f). The middle spectra (solid lines) shown in the lower panels of Figs. 4-1(a) and 4-1(f) are composite simulated spectra, representing the sums of the corresponding deconvoluted spectra. Good agreement is found between the composite simulated spectra and the experimental PFI-PE bands for for $O_2^+(A^2\Pi_{1/2}, v^+=3\text{-}8)$. The simulated spectra (solid lines below the experimental spectra) for the $O_2^-(A^2\Pi_{1/2u}, v^-=9$, 11, and 12) bands are also in reasonable agreement with the experimental bands except for $O_2^-(A^2\Pi_{1/2u}, v^-=10)$. The poor BOS fit to the $v^-=10$ PFI-PE band can be taken as evidence of strong perturbation by other states. We note that the simulated spectra of $O_2^+(A^2\Pi_{1/2u}, v^-=9$ and 10) have taken into account the contribution from $O_2^-(a^4\Pi_u, v^-=17$ and 18) bands, respectively. The simulated spectra for $O_2^-(A^2\Pi_{3/2,1/2u}, v^-=11$ and 12) have not included the respective contributions from that for $O_2^-(a^4\Pi_u, v^-=19$ and 20). Some weak features at the low energy tails of the $O_2^-(A^2\Pi_{1/2u}, v^-=11$ and 12) bands might have the origin from the $O_2^+(a^4\Pi_u, v^-=19$ and 20) bands. The BOS fits for the cold PFI-PE bands for $O_2^-(A^2\Pi_{1/2}$, $v^-=0\text{-}3$) are plotted as the lower spectra (solid lines) in Figs. 4-2(a)- 4-2(d), respectively. The deconvoluted spectrum for $O_2^-(X^2\Pi_{1/2}, v^-=28)$ are shown as the dashed curve in Fig. 4-2(a). We note that good fits to both the 20 and 220 K spectra for $O_2^-(A^2\Pi_{1/2}, v^-=1\text{-}3)$ are observed using the same set of BOS coefficients listed in Table 4-I.

The simulation shows that prominent peaks observed in the $O_2^-(A^2\Pi_{1/2,3/2}, v^-=0\text{-}12)$ bands are mostly due to the rotational branch heads (or the turn around rotational transitions of rotational branches). In Figs. 4-1(a)- 4-1(f) and 2(a)-2(d), the assignments of rotational transitions, $O_2^-(A^2\Pi_{1/2u}, v^+, N^-) \leftarrow O_2(X^3\Sigma_g^-, v''=0, N'')$ and $O_2^+(^2\Pi_{3/2}, v^-, N^-) \leftarrow O_2(X^3\Sigma_g^-, v''=0, N'')$, are indicated by respective downward pointing and upward pointing stick marks. The rotational branches, ΔJ = -7/2, -5/2, -3/2, -1/2, 1/2, 3/2, 5/2, 7/2, and 9/2 (corresponding to the M, N, O, P, Q, R, S, T and U branches, respectively) are also marked in these figures. For individual ΔJ branches, the positions of the first and second transitions are indicated by progressively shorter stick marks, thus revealing the origin and

direction of the rotational branches. We note that for the v^+ = 0-2, 6-8, 11, and 12 bands, whose C_2 is zero, the U branch is not observed.

We consistently observed a mismatch between the position of the band maximum observed in the experimental spectrum and that in the simulated spectra. As shown in Figs. 4-1(b), 4-1(c), 4-1(e), and 4-3, the band maximum observed in the experimental spectra for $O_2^+(A^2\Pi_u, v^+=4, 5, \text{and } 7\text{-}12)$ are found to be at slightly higher energies than those of the corresponding simulated spectra. The intense, sharp peak at 17.462 eV resolved in the $v^+=4$ band is consistent with a local enhancement by the near-resonant autoionization mechanism. The structure observed for the $v^+=10$ band is likely to result from a different mechanism. The rotational features at the low energy side of the main structure at 17.979 eV of the $v^+=10$ band appears to be significantly suppressed. This observation is manifested by the special set of BOS coefficients needed for the simulation of the $v^+=10$ band.

In the previous emission study,[14] Coxon and Haley also observed strong perturbation of the $O_2^+(A^2\Pi_u, v^+=9\text{-}10)$ states, which have prohibited the determination of spectroscpic constants for these vibrational levels. They suggested the presence of a perturbative state near $v^+=9$. They also pointed out that a possible candidate for such a perturbative state is the $^2\Sigma_u^+$ state, which was predicted in *ab intio* configuration interaction calculations of Beebe et al.[31] and Marian et al.[32] This state has a shallow well and correlate to the first dissociation limit, $O(^3P) + O^+(^4S)$, as that for the $O_2^+(A^2\Pi_u$ and $X^2\Pi_g)$ states. In this experiment, the special sets of BOS coefficients needed for the simulation of the $O_2^+(A^2\Pi_u, v^+=9$ and $10)$ bands can be taken as support that these states are strongly perturbed. In view of the observation in the present experiment that the $v^+=10$ band is more strongly perturbed than the $v^+=9$ band, we would suggest that such a perturbative state, if exists, most likely lies closer to the $O_2^+(A^2\Pi_u, v^+=10)$ level at 17.98 eV.

B. Spectroscopic constants for $O_2^+(A^2\Pi_u, v^+=0\text{-}12)$

There has been a controversy about the spin-orbit coupling constants (A_v^+) for $O_2^+(A^2\Pi_u)$ in terms of both sign and values. Stevens reported that the A_v^+ value for $O_2^+(A^2\Pi_u)$ at low v^+ levels was regular with a value of +8.2 cm^{-1}.[33] However, the later

experiment of Bozoky et al.[34] showed that A_v^+ is negative for v^+=0. 5 and 6 and positive for v^+=8. A detailed discussion on this issue was given by Albritton et al.[35] who concluded that the A_v^+ value for $O_2^+(A^2\Pi_u)$ is most likely inverted at low v^+ but changed from inverted to regular between v^+=5 and 6. Based on the least square analysis of the emission data, Coxon and Haley[14] obtained A_v^+ values for v^+=0-8 and 11-15 of $O_2^+(A^2\Pi_u)$, which are in accord with Albritton's conclusion. We have listed these A_v^+ values for $O_2^+(A^2\Pi_u$, v^+=0-8 and 11-12) in Table 4-II. However, since these A_v^+ values are small ($|A_v^+| \leq 6$ cm^{-1}) and comparable to our intrumental resolution of 4-5 cm^{-1} (FWHM), it is difficult to make accurate determination of A_v^+ for $O_2^+(A^2\Pi_u)$ in the present study. For this reason, we have used the A_v^+ data of Coxon and Haley in the BOS simulation. It appears that negative A_v^+ values give a better fit for low v^+. We conclude that the PFI-PE data presented here are consistent with $|A_v^+| \leq 6$ cm^{-1} for $O_2^+(A^2\Pi_{3/2,1/2u}, v^+$=0-12).

The energy expressions used for $O_2(^3\Sigma_g^-, v'', N'')$ and $O_2^+(A^2\Pi_u, v^+, N^+)$ are

$$E(v'', N'') = E_e'' + \omega_e''(v'' + 1/2) - \omega_e''\chi_e''(v'' + 1/2)^2 + B_v'' N''(N'' + 1), \quad (1)$$

and

$$E^+(v^+, N^+) = E_e^+ + \omega_e^+(v^+ + 1/2) - \omega_e^+\chi_e^+(v^+ + 1/2)^2 + B_v^+ N^+(N^+ + 1) - B_v^+\Omega^2 \pm 1/2A_v^+ . \quad (2)$$

respectively, where $B_v^+ = B_e^+ - \alpha^+(v^+ + 1/2)$ and $B_v'' = B_e'' - \alpha''(v'' + 1/2)$. In Eq. (2), $-1/2A_v^+$ ($+1/2A_v^+$) is for Ω=1/2 component and $+1/2\ A_v^+$ ($-1/2A_v^+$) is for the Ω = 3/2 component of the $O_2^+(A^2\Pi_u)$ state for the regular (inverted) case. The values B_e'' =1.44563 cm^{-1} and α'' =0.01593 cm^{-1} are taken from Ref. 30. We calculate the ionizing transition energies as:

$$\Delta E(v^+, N^+) = E(v^+, N^+) - E(v''=0, N''=1) = T_v^+ + B_v^+ N^+(N^+ + 1) - B_v^+\Omega^2 \pm 1/2A_v^+ \quad (3)$$

where $T_v^+ = T(v^+, v''=0, N''=1) = [E_e^+ - E_e'' + \omega_e^+(v^+ + 1/2) - \omega_e^+\chi_e^+(v^+ + 1/2)^2 - \omega_e''(1/2) + 1/4\ \omega_e''\chi_e'' - 2B_v'']$, noting that the IEs for different v^+ states correspond to energies for the ionization transitions $O_2^+[A^2\Pi_u, F_1(v^+, N^+ = 0)] \leftarrow O_2[X^3\Sigma_g^-, F_2(v''=0, N''=1)]$.

Table 4-II. Spectroscopic constants for O_2^+ ($A^2\Pi_u$ v^+=0-12)

	T_v (cm^{-1})	Δv (cm^{-1})		B_{v^+} (cm^{-1})		A_{v^+} (cm^{-1})
v^+	This work	This work	Ref. 14	This work	Ref. 14	Ref. 14
0	137518	869	871.5	1.050	1.0521	-3.50
1	138387	845	844.2	1.030	1.0233	-3.16
2	139230	817	817.0	1.020	1.0123	-2.78
3	140047	794	789.7	0.994	0.9920	-2.28
4	140841	759	762.5	0.975	0.9716	-1.69
5	141600	735	735.2	0.955	0.9509	-0.99.
6	142335	712	708.1	0.939	0.9301	-0.22
7	143047	678	681.0	0.910	0.9088	0.6
8	143725	658	654.6[a]	0.887	0.8872	2.6
9	144383	625	627.6[a]	0.878	-----	------
10	145008	599	601.1[a]	0.870	-----	------
11	145607	571	573.8	0.820	0.8220	5.5
12	146187	—	547.5	0.810	0.8011	6.1

a) Since v^+=9 and 10 were not resolved. these values are interpolated.

The T_v^- and B_v^- values for $O_2^-(A^2\Pi_u, v^-=0\text{-}12)$ obtained by the BOS simulation are listed in Table 4-II. We have also calculated the vibrational spacings (Δv) as given in the table. We have also included in Table 4-II the B_v^- and Δv values obtained in the previous high-resolution emission study for comparison with the present results. We estimate that the uncertainties of T_v^- and B_v^- values determined here are ±4 cm-1 and ±0.005 cm^{-1}, respectively. From Table 4-II, we can see excellent agreement of Δv between this work and those determined in Refs. 14 and 15. The B_v^- values derived from the present work also show excellent agreement with those from Ref. 14, with the largest discrepancy of 0.009 cm^{-1}. We note that for $v^-=9$ and 10, the IE and B_v^- values are determined for the first time.

Vibrational and rotational constants obtained were fitted to Eqs. (4) and (5), respectively, to obtain the vibrational (ω_e^-, $\omega_e^- x_e^-$, $\omega_e^- y_e^-$, and $\omega_e^- z_e^-$) and rotational (B_e^-, α_e^-, and γ_e^-) Dunham coefficients.

$$IE(v^-) = T_e^- + \omega_e^-(v^- + \tfrac{1}{2}) - \omega_e^- x_e^-(v^- + \tfrac{1}{2})^2 + \omega_e^- y_e^-(v^- + \tfrac{1}{2})^3 + \omega_e^- z_e^-(v^- + \tfrac{1}{2})^4 \quad (4)$$

$$B_v^- = B_e^- - \alpha_e^-(v^- + \tfrac{1}{2}) + \gamma_e^-(v^- + \tfrac{1}{2})^2 \quad (5)$$

These Dunham type coefficients obtained by the least squares fit are listed in Table 4-III for comparison with those reported in Refs. 14 and 15. In general, the vibrational and rotational Dunham coefficients determined here is in excellent agreement with the literature values. Since the T_e^-, ω_e^-, $\omega_e^- x_e^-$, $\omega_e^- y_e^-$ determined in Ref 15 are based only on vibrationally resolved data, our present results should be more accurate. However, we note that the rotational constants determined from the rotational analysis of the $O_2^-(X^2\Pi_g) \leftarrow O_2^-(A^2\Pi_u)$ emission bands are far more accurate compared to those of the current PFI-PE measurement.

We also performed the least square polynomial fit of the vibrational spacing $\Delta G(v^-)$ as a function of $v^- + 1/2$. Based on the polynomial used in the fit of $\Delta G(v^-)$, we have solved

Table 4-III. Comparison of vibrational and rotational constants determined here and in Reference for O_2^- ($A^2\Pi_u$, v^-=0-12).[a]

Dunham constants	This Work (cm^{-1})	Ref. 14 (cm^{-1})	Ref 15 (cm^{-1})
T_e	137073.2(3.2)	137068.5(4.2)[b]	137069(8)
		40572.5(0.2)[c]	
ω_e	895.06(3.46)	898.10(0.33)	894.4(2.8)
$\omega_e x_e$	12.687(1.080)	13.22(0.15)	12.96(0.26)
$\omega_e y_e$	-0.081(0.013)	-0.098(0.029)	-0.021(0.007)
$\omega_e z_e$	2.32×10^{-3}(4.76×10^{-3})	9.4×10^{-3}(2.5×10^{-3})	----------
B_e	1.0598(6.458)	1.061900(31)	
α_e	0.0180 (0.00023)	0.0196258(135)	
γ_e	-1.604×10^{-4}(1.716×10^{-4})	$-8.51(39)\times10^{-5}$	

a) The error bars are given in the parentheses.

b) This T_e value of for the O_2^- ($A^2\Pi_u$) state is the sum of the T_e value [96496±4 cm^{-1}. Ref. 6] for O_2^- ($X^2\Pi_g$) [meaured with respect to the O_2 ground potential] and the T_e value [40572.5± 0.2 cm^{-1}. Ref. 14] for O_2^- ($A^2\Pi_u$) [measured with respect to the O_2^- ground potential].

c) The T_e value obtained from Ref. 14 for O_2^- ($A^2\Pi_u$) measured with respect to the O_2^- ground potential.

for the root of $\Delta G(v^+_{max}) = 0$ and obtained $v^-_{max} = 31.5$, where v^-_{max} is the maximum v^- level sustained by the potential well. We note that this result is in agreement with $v^-_{max} = 31$ derived by Akahori et al.[6] However, since the vibrational levels we accessed is only up to v+=12, the results of this experiment cannot verify the existence of a small potential hump for the potential curve of $O_2^-(A^2\Pi_u)$ above the dissociation limit $O(^3P) + O^-(^4S)$ as proposed by Akahori et al.

IV. CONCLUSIONS

We have obtained rotationally resolved PFI-PE bands for $O_2^-(A^2\Pi_u, v^-=0\text{-}12)$ in the energy range of 17.0-18.2 eV. The IE values and spectroscopic constants for $O_2^-(A^2\Pi_u, v^-=0\text{-}8, 11, \text{and } 12)$ obtained from the BOS simulation of the PFI-PE data are in excellent agreement with the previous emission and TPE studies. Spectral simulations have provided new spectroscopic constants for the $O_2^-(A^2\Pi_{1/2,3/2u}, v^-=9 \text{ and } 10)$ states.

A significant suppression of the rotational features is observed for the $v^-=10$ band. This and the observed intensity profile for the $O_2^-(A^2\Pi_u, v^-=6\text{-}10)$ bands are consistent with the previous suggestion that the $v^-=6\text{-}10$ levels are perturbed by the $^2\Sigma^-_u$ state predicted by *ab initio* calculations. The PFI-PE data obtained in the present experiment indicate that $|A_v^-| \leq 6\ cm^{-1}$ for $O_2^-(A^2\Pi_{3/2,1/2u}, v^-=0\text{-}12)$.

Acknowledgements:

This work was supported by the Director, Office of Energy Research, Office of Basic Energy Sciences, Chemical Sciences Division of the U.S. Department of Energy under Contract No. DE-AC03-76SF00098 for the Lawrence Berkeley National Laboratory and Contract No. W-7405-Eng-82 for the Ames Laboratory. Y.S. acknowledges the Wall Fellowship for 1999-2000. M.E. acknowledges the GAANN Fellowship for 1996-1997 and the Dow Fellowship for 1997-1998.

References

1. C.-W. Hsu, P. Heimann, M. Evans, S. Stimson, T. Fenn, and C. Y. Ng, *J. Chem. Phys.* **106**, 8931 (1997).
2. C.-W. Hsu, P. Heimann, M. Evans, S. Stimson, and C. Y. Ng, *Chem. Phys.* **231**, 121-143 (1998).
3. C.-W. Hsu, M. Evan, S. Stimson, and C. Y. Ng, *J. Chem. Phys.* **108**, 4701 (1998).
4. C.-W. Hsu, M. Evans, S. Stimson, and C. Y. Ng, *J. Chem. Phys.* **109**, 1285 (1998).
5. M. Evans, S. Stimson, C. Y. Ng, C.-W. Hsu, and G. K. Jarvis, *J. Chem. Phys.* **110**, 315 (1999).
6. Y. Song, M. Evans, C. Y. Ng, C.-W. Hsu, and G. K. Jarvis, *J. Chem. Phys.*, in press.
7. G. K. Jarvis, Y. Song, and C. Y. Ng, *J. Chem. Phys.*, in press.
8. G. K. Jarvis, M. Evans, C. Y. Ng, and K. Mitsuke, *J. Chem. Phys.*, in press.
9. M. Evans and C. Y. Ng, *J. Chem. Phys.*, submitted.
10. D. Fedorov, M. Evans, M. Gordon, and C. Y. Ng, *J. Chem. Phys.*, accepted.
11. R. C. Shiell, M. Evans, S. Stimson, C. Y. Ng, and J. W. Hepburn, *Chem. Phys. Lett.*, submitted.
12. I. Powis, T. Baer, and C. Y. Ng, editors, "High Resolution Laser Photoionization and Photoelectron Studies", *Wiley Series in Ion Chem. and Phys.* (Wiley, Chichester, 1995) and references therein.
13. H. Palm and F. Merkt, *Phys. Rev. Lett.* **81**, 1385 (1998).
14. J. A. Coxon and M. P. Haley, *J. Mol. Spectrosc.* **108**, 119 (1984).
15. T. Akahori, Y. Morioka, T. Tanaka, H. Yoshii, T. Hayaishi and K.Ito. *J. Chem. Phys.* **107**, 4875 (1997).
16. K.P. Huber and G. Herzberg, *Molecular Spectra and Molecular Structure*, Constants of Diatomic Molecules, Vol. IV (Van Nostrand, New York, 1974).
17. K. Ellis, R. I. Hall, L. Avaldi, G. Dawber, A. McConkey, L. Andric, and G. C. King, *J. Phys. B* **27**, 3415 (1994).
18. O. Edqvust, E. Lindholm, L. E. Selin, L. Åsbrink, *Physica Scripta* **1**, 25 (1970).
19. J. A. Samson and J. L. Gardner, *J. Chem. Phys.* **67**, 755 (1977).

20. C. Y. Ng. in "Photoionization and Photodetachment". edited by C. Y. Ng (World Scientific. Singapore. 1999). *Adv. Ser Phys. Chem.*. Vol. 10A. in press.

21. C.-W. Hsu, M. Evans, P. Heimann, K. T. Lu. and C. Y. Ng. *J. Chem. Phys.* **105**. 3950 (1996).

22. C.-W. Hsu, M. Evans. C. Y. Ng, P. Heimann. *Rev. Sci. Instrum.* **68**, 1694 (1997).

23. P. Heimann, M. Koike, C.-W. Hsu. M. Evans. K. T. Lu, C. Y. Ng. A. Suits. and Y. T. Lee. *Rev. Sci. Instrum.* **68**. 1945 (1997).

24. G. K. Jarvis. Y. Song, and C. Y. Ng. *Rev. Sci. Instrum.* **70**, 2615 (1999).

25. S. Stimson. Y.-J. Chen. M. Evans. C.-L. Liao. C. Y. Ng, C.-W. Hsu. and P. Heimann. *Chem. Phys. Lett.* **289**, 507 (1998).

26. P. H. Krupenie. *J. Phys. Chem. Ref. Data* **1**. 423 (1972).

27. Y. Song. M. Evans. C. Y. Ng. C.-W. Hsu. and G. K. Jarvis. *J. Chem. Phys.*. in preparation.

28. R. B. Cairns and J. A. R. Samson. *J. Opt. Soc. Am.* **56**. 1568 (1966).

29. A. D. Buckingham. B. J. Orr. J. M. Sichel. *Phil. Trans. Roy. Soc. Lond. A* **268**. 147 (1970).

30. K. P. Huber and G. Herzberg. "Molecular Spectra and Molecular Structure. Vol. IV. Constants of Diatomic Molecules" (Van Nostrand. New York. 1979).

31. N. H. F. Beebe. E. W. Thulstrup. and A. Anderson. *J. Chem. Phys.* **64**. 2080 (1976).

32. C. M. Marian. R. Marian. S. D. Peyerimhoff. B. A. Hess. R. J. Buenker. and G. Seger. *Mol. Phys.* **46**. 779 (1982).

33. D. S. Stevens. *Phys. Rev.* **38**. 1292 (1931).

34. L. Bozoky. *Z. Physik* **104**. 275 (1937).

35. D. L. Albritton. W. J. Harrop. A. L. Schmeltekopf. and R. N. Zare. *J. Mol. Spectrosc.* **41**, 89 (1973).

CHAPTER 5. ROTATIONALLY RESOLVED PULSED FIELD IONIZATION PHOTOELECTRON BANDS FOR $O_2^+(a^4\Pi_u, v^+=0\text{-}18)$ IN THE ENERGY RANGE OF 16.0-18.0 eV

A paper published in *Journal of Chemical Physics*, **112**, 1306 (2000)

Y. Song, M. Evans, C.Y. Ng, C.-W. Hsu and G. K. Jarvis

Abstract:

We have obtained rotationally resolved pulsed field ionization-photoelectron (PFI-PE) spectra of O_2 in the energy range of 16.0-18.0 eV, covering ionization transitions $O_2^+(a^4\Pi_u, v^+=0\text{-}18, J^+) \leftarrow O_2(X^3\Sigma_g^-, v''=0, N'')$. Although these PFI-PE bands for $O_2^+(a^4\Pi_u, v^+)$ have significant overlaps with those for $O_2^+(X^2\Pi_g)$ and $O_2^+(A^2\Pi_u)$, we have identified all the $O_2^+(a^4\Pi_u, v^+=0\text{-}18)$ bands by simulation of spectra obtained using supersonically cooled O_2 samples with rotational temperatures ≈20 and 220 K. While the $v^+=4\text{-}18$ PFI-PE bands represent the first rotationally resolved photoelectron data for $O_2^+(a^4\Pi_u)$, the PFI-PE bands for $O_2^+(a^4\Pi_u, v^+=10\text{-}18)$ are the first rotationally resolved spectroscopic data for these levels. The simulation also allows the determination of accurate ionization energies, vibrational constants, and rotational constants for $O_2^+(a^2\Pi_u, v^+=0\text{-}18)$. The observed intensities of spin-orbit components for the majority of vibrational bands for $O_2^+(a^2\Pi_u, v^+)$ are in accordance with the forced spin-orbit/rotational autoionization mechanism.

I. INTRODUCTION

Pulsed field ionization (PFI) photoelectron (PFI-PE) technique has been established to be a valuable method for spectroscopic and energetic studies of cations.[1-3] This technique was originally developed as a laser based method. Previous experiments have shown that rotationally resolved photoelectron measurements can be readily achieved for diatomic molecules and specific polyatomic species using this technique.[3] In the past few years, we have successfully implemented this method using the high-resolution vacuum ultraviolet (VUV) facility at the Chemical Dynamics Beamline of the Advance Light

Source (ALS), attaining PFI-PE resolutions in the range of 1-6 cm^{-1} (full width half maximum, FWHM).[4-8] These resolutions are close to that (0.3-4 cm^{-1}) achieved in VUV laser PFI-PE studies.[3,9] The advantage of using synchrotron radiation is its ease of tunability, covering the full VUV range of 6-30 eV.[5] By employing the synchrotron-based PFI-PE detection schemes, we have obtained rotationally resolved PFI-PE spectra for O_2,[6,10-15] NO,[16,17] and CO[18,19] covering the full energy range from their ionization energies (IEs) to ≈25 eV.

In a series of recent publications, we have reported detailed analyses of rotationally resolved PFI-PE vibrational bands for $O_2^+(X^2\Pi_g, A^2\Pi_u\ b^4\Sigma_g^-, 2^2\Pi_u, B^2\Sigma_g^-, {}^2\Sigma_u^-$ and $c^4\Sigma_u^-$)[6,11-15] observed in the region of 12-25 eV. In addition to providing valuable information on the dynamics concerning the formation and decay of these states, these PFI-PE studies have also yielded new spectroscopy constants, especially for highly vibrationally excited levels, which cannot be observed in traditional spectroscopic studies. In this article, we report the analysis of the rotationally resolved PFI-PE bands for $O_2^+(a^4\Pi_u, v^+=0\text{-}18)$. Accurate spectroscopic data for $O_2^+(a^4\Pi_u, v^+=0\text{-}9)$ are available from high-resolution emission and laser photofragment studies.[20,21] Kong and Hepburn[22] have obtained rotationally resolved PFI-PE bands for $O_2^+(a^4\Pi_u, v^+=0\text{-}3)$ using VUV lasers, providing accurate IEs for the formation of these v^+-levels. However, due to the use of a cold (10 K) supersonic O_2 beam in this VUV laser study, individual vibrational PFI-PE bands only reveal a few low rotational transitions. We note that vibrational resolved threshold photoelectron (TPE) bands for $O_2^+(a^4\Pi_u, v^+=0\text{-}20$ and 23) have also been identified in a recent synchrotron study using the high-resolution penetration field technique.[23]

II. EXPERIMENT

The design and performance of the high-resolution photoionization facility of the Chemical Dynamics Beamline at the ALS has been described previously.[4-8] Briefly, the major components include a 10-cm period undulator, a gas harmonic filter, a 6.65-m off-plane Eagle monochromator, and a photoion-photoelectron apparatus.[2,20-22]

In the present experiment, helium is used in the harmonic gas filter, where higher undulator harmonics with photon energies greater than 24.59 eV are suppressed. The fundamental light from the undulator is then directed into the 6.65 m monochromator and dispersed by a 4800 lines/mm grating (dispersion = 0.32 Å/mm) before entering the experimental apparatus. The PFI-PE bands were measured using the 4800 lines/mm grating and monochromator entrance/exit slits of 50-200 μm, achieving wavelength resolutions of 0.016-0.064 Å (FWHM). The photon energy step size was varied in the range of 0.1-0.25 meV.

The ALS storage ring is capable of filling 328 electron buckets in a period of 656 ns. Each electron bucket emits a light pulse of 50 ps with a time separation of 2 ns between successive bunches.[5] In each storage ring periods, a dark gap (16 ns) consisting of 8 consecutive unfilled buckets exists for the ejection of cations from the orbit. Thus, the present experiment is performed in the multibunch mode with 320 bunches in the synchrotron orbit, corresponding to a repetition rate of 488 MHz.

The procedures for PFI-PE measurements using the photoion-photoelectron apparatus have been described previously in detail.[4-8] The electron spectrometer, which consists of a steradiancy analyzer and a hemispherical energy analyzer arranged in tandem, was used to filter prompt electrons. For measurements of PFI-PE bands, a pulsed electric field (height = 0.67 V/cm, width = 40 ns) was applied every three synchrotron periods, i.e., 1.97 μs. Thus, the repetition rate of the PFI pulses was 0.51 MHz.

A continuous molecular beam of pure O_2 was produced by supersonic expansion through a stainless steel nozzle (diameter = 0.127 mm) at a stagnation pressure of 760 Torr and a nozzle temperature of 298 K. The molecular beam was skimmed by a circular skimmer (diameter = 1 mm) before intersecting the monochromatized VUV light beam 7 cm downstream in the photoionization region. As shown below, the simulation of PFI-PE spectra suggests that the rotational temperature for O_2 achieved is ≈220 K in this experiment.

The $O_2^+(a^2\Pi_u, v^+=0, 2,$ and 6-11) PFI-PE bands were re-examined in another experiment performed about three years later using a colder O_2 molecular beam sample

with a rotational temperature of ≈20 K. A new synchrotron-based PFI-PE detection scheme, which relies on the time-of-flight (TOF) selection of PFI-PEs, is used in the recent study.[7] By employing a synchrotron dark gap of ≥80 ns, we show that the TOF peak for PFI-PEs can be adjusted to arrive in the dark gap with little contamination by prompt electrons. This new scheme not only is more effective in suppression of prompt electrons, but also has a higher electron transmission. Using a 2400 lines/mm grating and monochromator entrance/exit slits of 50-100 μm, the wavelength resolution achieved in this PFI-PE experiment was 0.032-0.064 Å (FWHM). Spectra were flux normalized using the photon signal obtained at a tungsten detector positioned behind the PI/PEX region intercepting the monochromatized VUV beam. The VUV detection efficiency of the tungsten detector as a function of photon energy was corrected for using the known photoelectric yield curve.[24]

The absolute photon energy (hν) scale was calibrated using the $Ar^+(^2P_{3/2})$, and $Ne^+(^2P_{3/2})$ PFI-PE bands recorded under the same experimental conditions before and after each scan.[4-7] This calibration procedure assumes that the Stark shift for ionization energies (IEs) of O_2 and the rare gases are identical. On the basis of previous experiments, the accuracy of the energy calibration is believed to be within ±0.5 meV.[4-8, 10-18, 25]

III. RESULTS AND DISCUSSION

The main electronic configuration for the $O_2(X^3\Sigma_g^-)$ ground state is $KK(2\sigma_g)^2(2\sigma_u)^2(3\sigma_g)^2(1\pi_u)^4(1\pi_g)^2$. The $O_2^+(a^4\Pi_u)$ and $O_2^+(A^2\Pi_u)$ states are resulted from the removal of an electron from the $1\pi_u$ bonding orbital. In the case of the $O_2^+(a^4\Pi_u)$ state, the coupling between Λ^+ and Σ^+ gives rise to the quartet spin-orbit components $F_1(^4\Pi_{5/2})$, $F_2(^4\Pi_{3/2})$, $F_3(^4\Pi_{1/2})$, and $F_4(^4\Pi_{1/2})$, which are characterized by the quantum number $\Omega^+ = |\Lambda^+ \pm \Sigma^+| = |5/2|$, $|3/2|$, $|1/2|$, and $|-1/2|$, respectively. Here Λ^+ and Σ^+ are the electronic orbital angular momentum and electron spin angular momentum projected on the axis of O_2^+. Due to the high multiplicity, the vibrational PFI-PE bands for $O_2^+(a^4\Pi_u)$ are expected to exhibit complicated rotational structures.

In the energy region (16.0-18.0 eV) of interest to this experiment, we have resolved vibrational bands for $O_2^+(X^2\Pi_g, v^+=21\text{-}38)$, $O_2^+(a^4\Pi_u, v^+=0\text{-}18)$, and $O_2^+(A^2\Pi_u, v^+=0\text{-}12)$.[14,15] The analyses for the PFI-PE bands for $O_2^+(X^2\Pi_g, v^+=0\text{-}38)$[14] and $O_2^+(A^2\Pi_u, v^+=0\text{-}12)$[15] have been reported recently. The analysis of the $O_2^+(a^4\Pi_u, v^+=0\text{-}18)$ bands is complicated by the near exact degeneracy between $O_2^+(a^4\Pi_u, v^+=0,1,7\text{-}9)$ and $O_2^+(X^2\Pi_g, v^+=21, 22, 27\text{-}29)$, respectively. The serious overlaps between the $O_2^+(a^4\Pi_u, v^+=8\text{-}10)$ and $O_2^+(A^2\Pi_u, v^+=0\text{-}2)$ PFI-PE bands have also been noted,[14] especially in the 220 K spectra. As shown below, the measurement of the PFI-PE bands associated with $O_2^+(a^4\Pi_u, v^+=7\text{-}10)$ using the 20 K O_2 beam sample is essential in the identification of these v^+ bands.

Taking into account the previously reported PFI-PE spectra for $O_2^+(a^4\Pi_u, v^+)$,[14,15] we have selected to show in Figs. 5-1, 5-2, 5-3, 5-4(a), 5-5(a), and 5-6(a) the experimental PFI-PE bands (open circles) associated with $O_2^+(a^4\Pi_u, v^+=2\text{-}4, 5, 6, 7, 9, \text{and } 10)$, respectively. These spectra were recorded using a 220 K O_2 beam sample. The 220 K spectrum associated with $O_2^+(a^4\Pi_u, v^+=8)$ is also included in Fig. 5-1. The respective experimental PFI-PE bands (open circles) associated with $O_2^+(a^4\Pi_u, v^+=7, 9, \text{and } 10)$ measured using a 20 K O_2 beam sample are depicted in Figs. 5-4(b), 5-5(b), and 5-6(b).

A. Spectral simulation and assignment of rotational branches

The intensities for rotational transitions resolved in individual PFI-PE bands for $O_2^+(a^4\Pi_u, v^+=0\text{-}18)$ were simulated using the Buckingham-Orr–Sichel (BOS) model,[26] which was derived to predict rotational line strengths observed in single-photon ionization of diatomic molecules. The single-photon ionization transitions involved here are $O_2^+(a^4\Pi_{5/2,3/2,1/2,-1/2u}, v^+, J^+) \leftarrow O_2(X^3\Sigma_g^-, v'', N'')$, where N'' is the rotational quantum number for the neutral $O_2(X^3\Sigma_g^-)$ ground state and J^+ is the total angular momentum for the cationic $O_2^+(a^4\Pi_{5/2,3/2,1/2,-1/2u})$ excited state. The J^+ value is equal to $N^+ + \Omega^+$, where N^+ is the rotational quantum number for $O_2^+(a^4\Pi_u)$. In accordance with the BOS model, the relative rotational intensities can be expressed by the equation,

$$\sigma(N^+ \leftarrow N'') \propto \sum_\lambda Q(\lambda; N^+, N'')C_\lambda, \qquad (1)$$

Figure 5-1. Simulated and experimental PFI-PE spectra for $O_2^-(a^4\Pi_u, v^-=2\text{-}4$ and 8) obtained using a 220 K O_2 sample. The horizontal scale is hν - IE(v^-), where hν is the photon energy. For each v^- state, the upper spectrum (open circles) is the experimental spectrum, while the simulated spectrum (solid curve) is shown underneath the experimental curve. The simulated spectrum for $v^-=8$ has included contributions from the PFI-PE bands for $O_2^-(a^4\Pi_u, v^-=8)$ and $O_2^-(A^2\Pi_u, v^-=0)$ (Ref. 14).

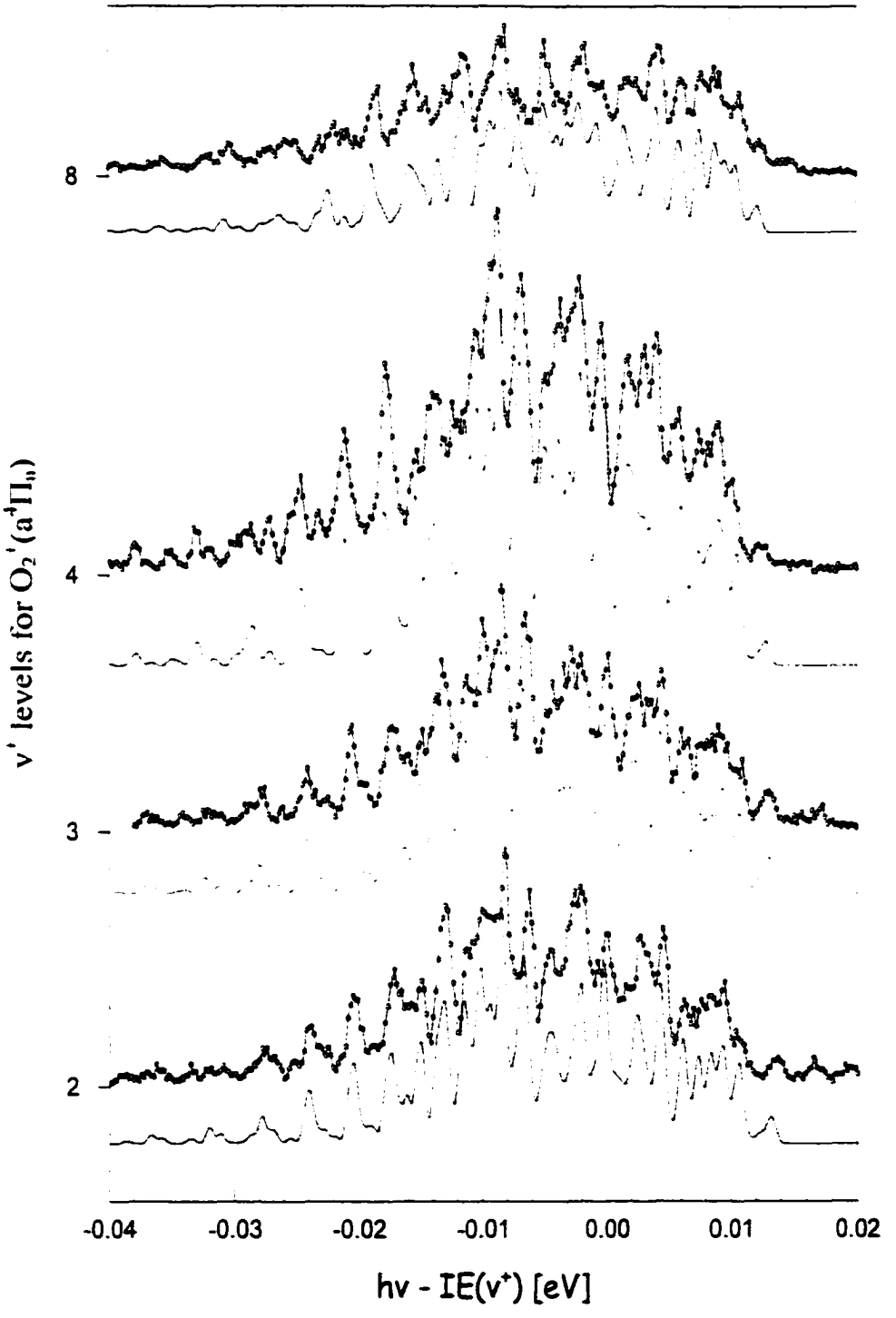
8
4
3
2
v' levels for $O_2^+(a^4\Pi_u)$
-0.04
-0.03
-0.02
-0.01
0.00
0.01
0.02
hv - IE(v+) [eV]

Figure 5-2 Simulated (solid line) and experimental PFI-PE bands (open circles) for $O_2^+(a^4\Pi_u, v^+=5)$ obtained using an O_2 sample with a rotational temperature of ≈220 K. The rotational transitions to the $O_2^+(a^4\Pi_{5/2,3/2,1/2,-1/2u}, v^+, J^+)$ from O_2 ($X^3\Sigma_g^-$, $v''=0$, N'') are marked using downward pointing stick marks. The ΔJ rotational branches are also marked.

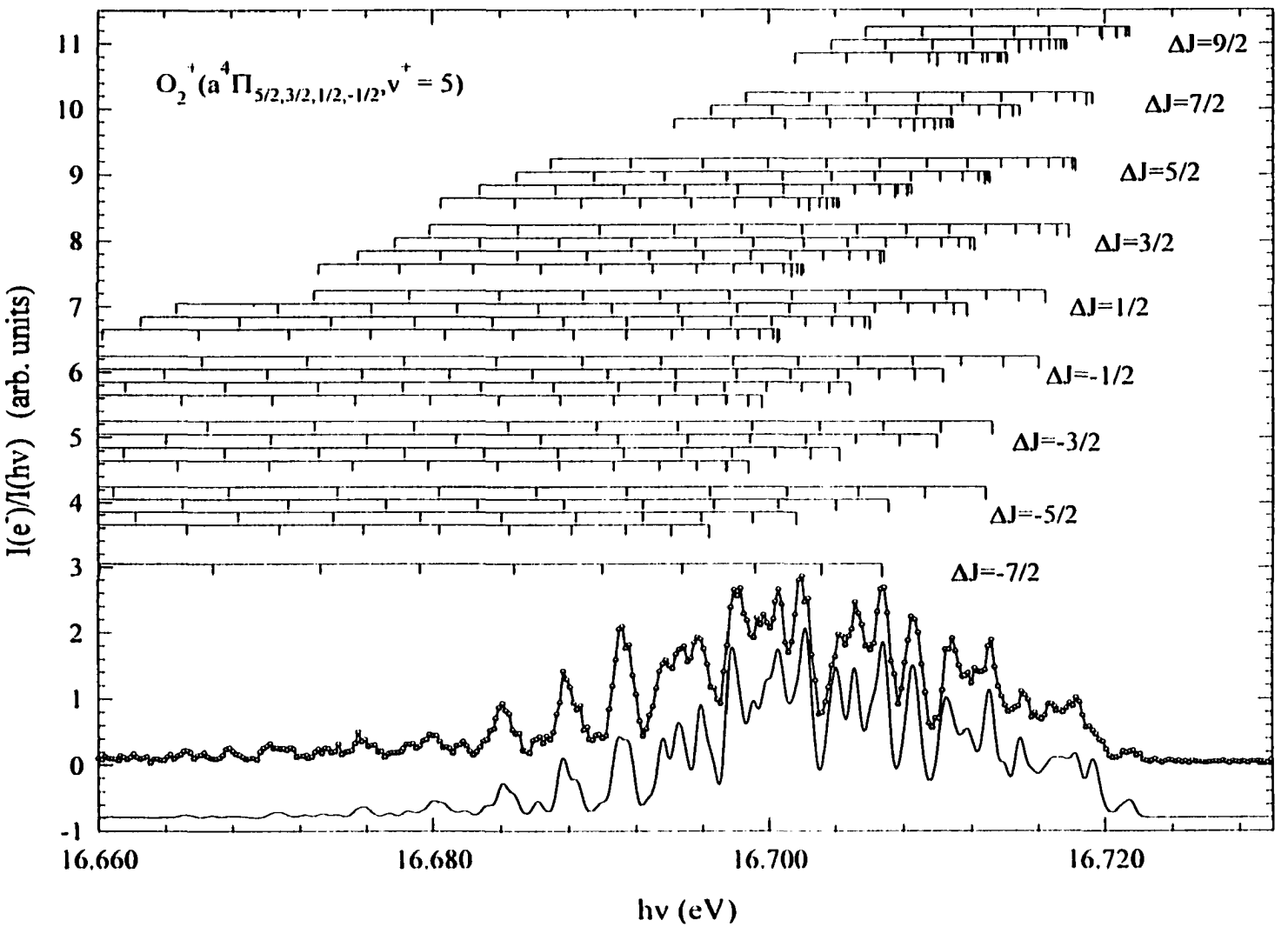
$O_2^+(a^4\Pi_{5/2,3/2,1/2,-1/2}, v^+ = 5)$
ΔJ=9/2
ΔJ=7/2
ΔJ=5/2
ΔJ=3/2
ΔJ=1/2
ΔJ=-1/2
ΔJ=-3/2
ΔJ=-5/2
ΔJ=-7/2
I(e⁻)/I(hv) (arb. units)
hv (eV)
16.660
16.680
16.700
16.720

Figure 5-3 Simulation of experimental PFI-PE spectrum (open circles) associated with O_2^+ ($a^4\Pi_u$, $v^+=6$) and O_2^+ ($X^2\Pi_g$, $v^+=26$) obtained using an O_2 sample with a rotational temperature of ≈220 K. The deconvoluted bands (dashed curves) for $O_2^+(X^2\Pi_{3/2,1/2g}, v^+=26)$ and O_2^+ ($a^4\Pi_{5/2,3/2,1/2,\ 1/2u}$, $v^+=6$) are shown at the bottom of the figure. The sum of these deconvoluted bands yields the simulated spectrum (top solid curve) for the experimental spectrum.

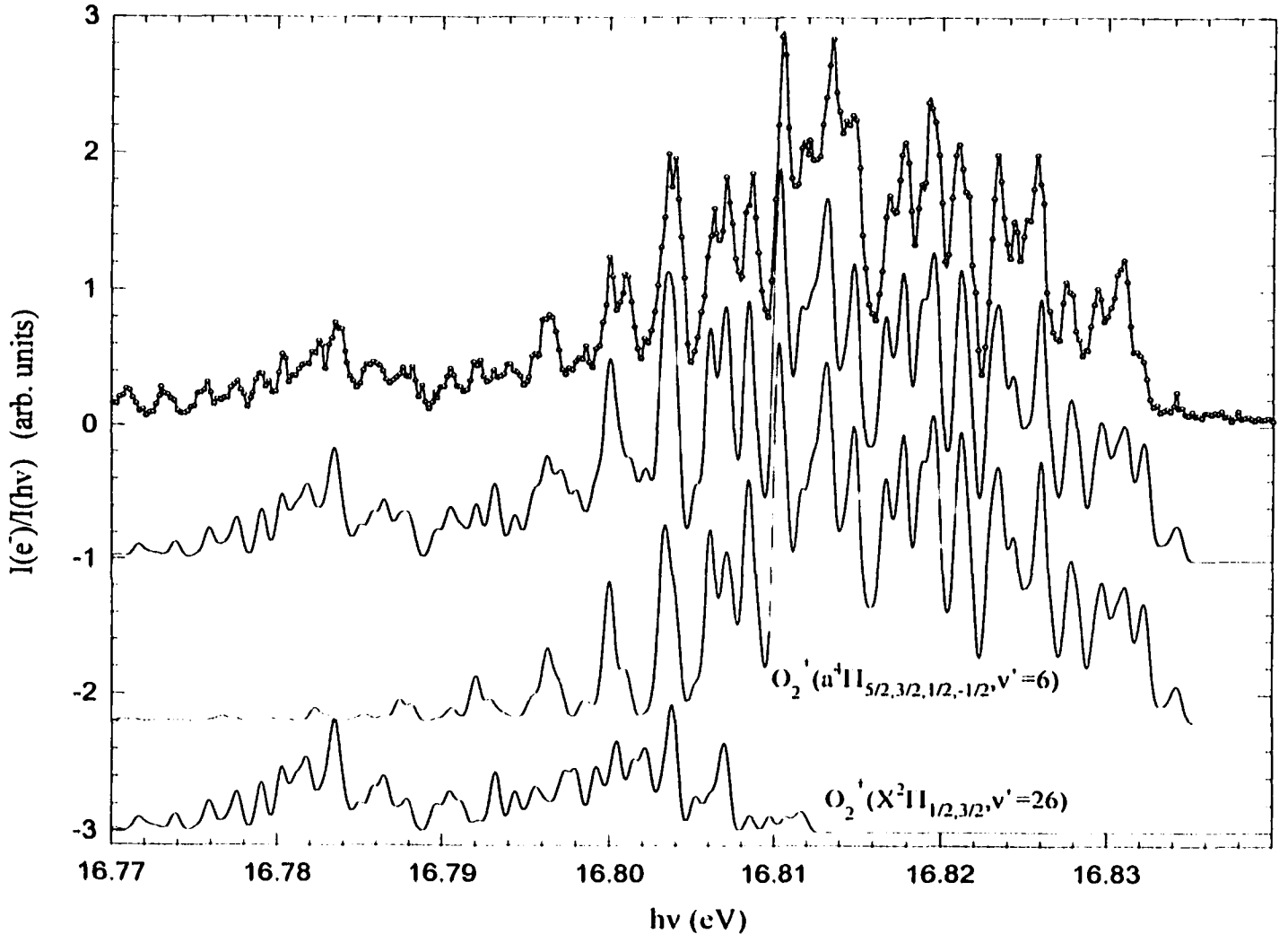
3
2
1
0
-1
-2
-3
I(e⁻)/I(hν) (arb. units)
16.77
16.78
16.79
16.80
16.81
16.82
16.83
hν (eV)
O2+(a4Π5/2,3/2,1/2,-1/2,v'=6)
O2+(X2Π1/2,3/2,v'=26)

Figure 5-4. Simulation of the experimental PFI-PE spectra (open circles) associated with $O_2^+(X^2\Pi_{3/2,1/2g}, v^+=27)$ and $O_2^+(a^4\Pi_{5/2,3/2,1/2,-1/2u}, v^+=7)$ obtained using O_2 samples with rotational temperatures of (a) 220 K and (b) 20 K. The deconvoluted bands (solid curves) for $O_2^+(X^2\Pi_{3/2,1/2g}, v^+=27)$ and $O_2^+(a^4\Pi_{5/2,3/2,1/2,-1/2u}, v^+=7)$ are shown at the bottom of (b). The overall simulated spectra (solid curves) below the experimental PFI-PE spectra of (a) and (b) are obtained by summing deconvoluted bands for 20 and 220 K, respectively.

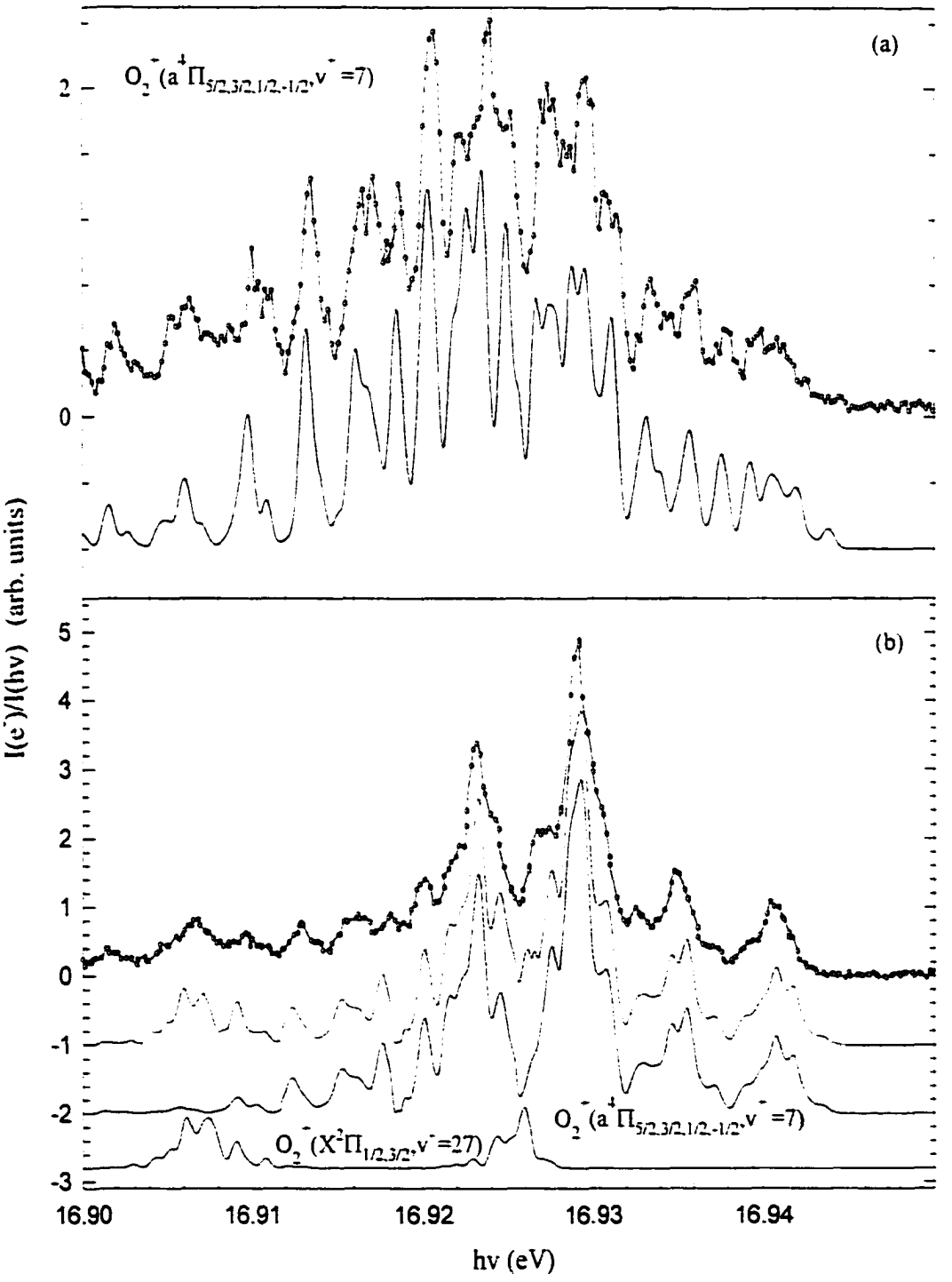
(a)
$O_2^-(a^4\Pi_{5/2,3/2,1/2,-1/2}, v^-=7)$
2
0
(b)
5
4
3
2
1
0
-1
-2
-3
$O_2^-(a^4\Pi_{5/2,3/2,1/2,-1/2}, v^-=7)$
$O_2^-(X^2\Pi_{1/2,3/2}, v^-=27)$
16.90
16.91
16.92
16.93
16.94
hv (eV)
I(e⁻)/I(hv) (arb. units)

Figure 5-5. Simulation of the experimental PFI-PE spectra (open circles) associated with $O_2^+(X^2\Pi_{3/2,1/2g}, v^+=29)$, O_2^+ $(a^4\Pi_{5/2,3/2,1/2,-1/2u}, v^+=9)$, and $O_2^+(A^2\Pi_{3/2,1/2u}, v^+=1)$, obtained using O_2 samples with rotational temperatures of (a) 220 K and (b) 20 K. The deconvoluted bands (solid curves) for $O_2^+(X^2\Pi_{3/2,1/2g}, v^+=29)$, O_2^+ $(a^4\Pi_{5/2,3/2,1/2,-1/2u}, v^+=9)$, and $O_2^+(A^2\Pi_{3/2,1/2u}, v^+=1)$ are shown at the bottom of (b). The overall simulated spectra (solid curves) below the experimental PFI-PE spectra of (a) and (b) are obtained by summing deconvoluted bands for 20 and 220 K, respectively.

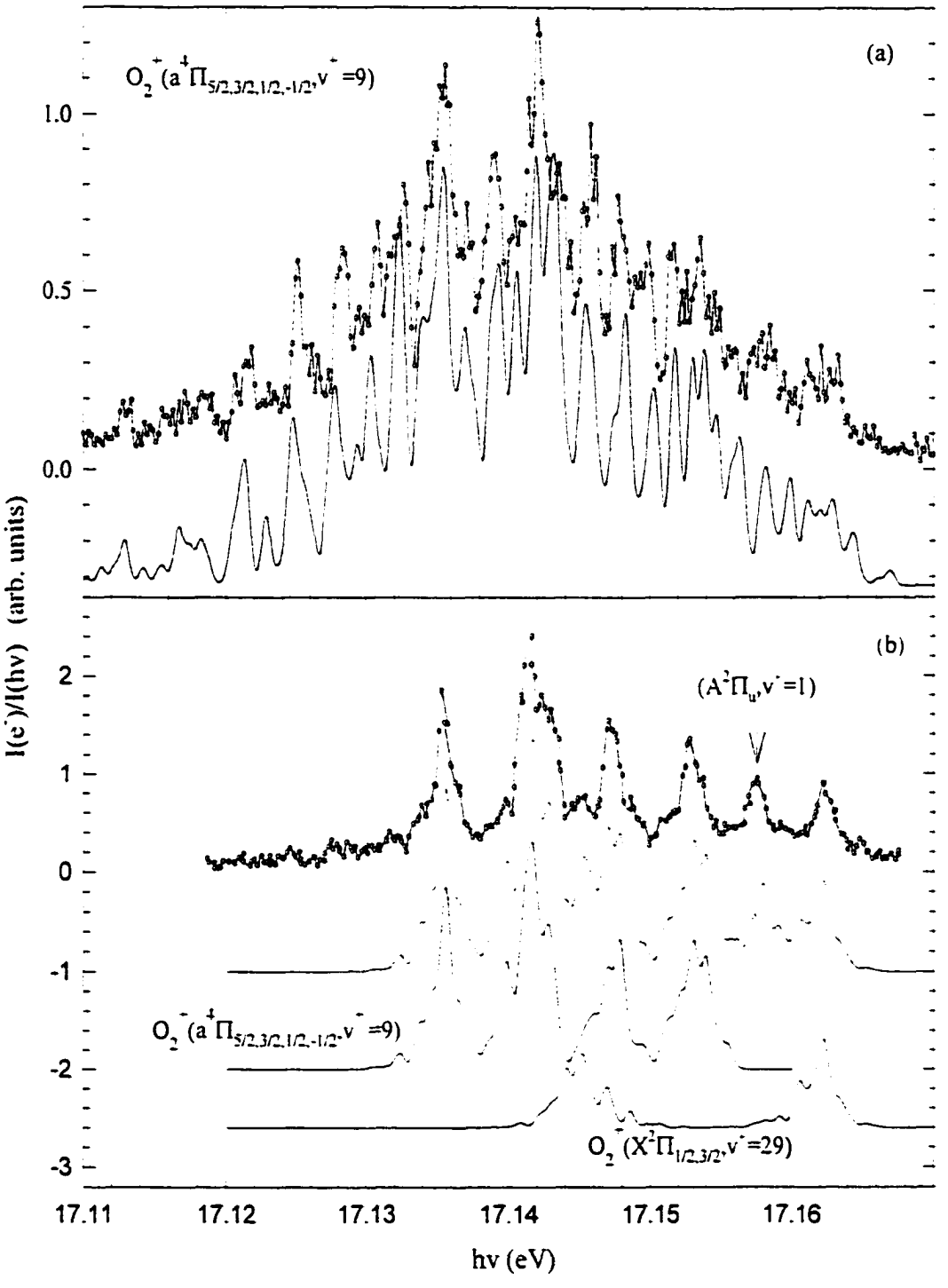
(a)
$O_2^+(a^4\Pi_{5/2,3/2,1/2,-1/2}, v^+=9)$
1.0
0.5
0.0
(b)
$(A^2\Pi_u, v^+=1)$
2
1
0
-1
-2
-3
$O_2^+(a^4\Pi_{5/2,3/2,1/2,-1/2}, v^+=9)$
$O_2^+(X^2\Pi_{1/2,3/2}, v^+=29)$
I(e⁻)/I(hv) (arb. units)
17.11
17.12
17.13
17.14
17.15
17.16
hv (eV)

Figure 5-6. Simulation of the experimental PFI-PE spectra (open circles) associated with $O_2^+(X^2\Pi_{3/2,1/2g}, v^+=30)$, O_2^+ $(a^4\Pi_{5/2,3/2,1/2,-1/2u}, v^+=10)$, and $O_2^+(A^2\Pi_{3/2,1/2u}, v^+=2)$ obtained using O_2 samples with rotational temperatures of (a) 220 K and (b) 20 K. The deconvoluted bands (solid curves) for $O_2^+(X^2\Pi_{3/2,1/2g}, v^+=30)$ and $O_2^+(A^2\Pi_{3/2,1/2u}, v^+=2)$ are shown at the bottom of (b). The overall simulated spectra (solid curves) below the experimental PFI-PE spectra of (a) and (b) are obtained by summing deconvoluted bands for 20 and 220 K, respectively.

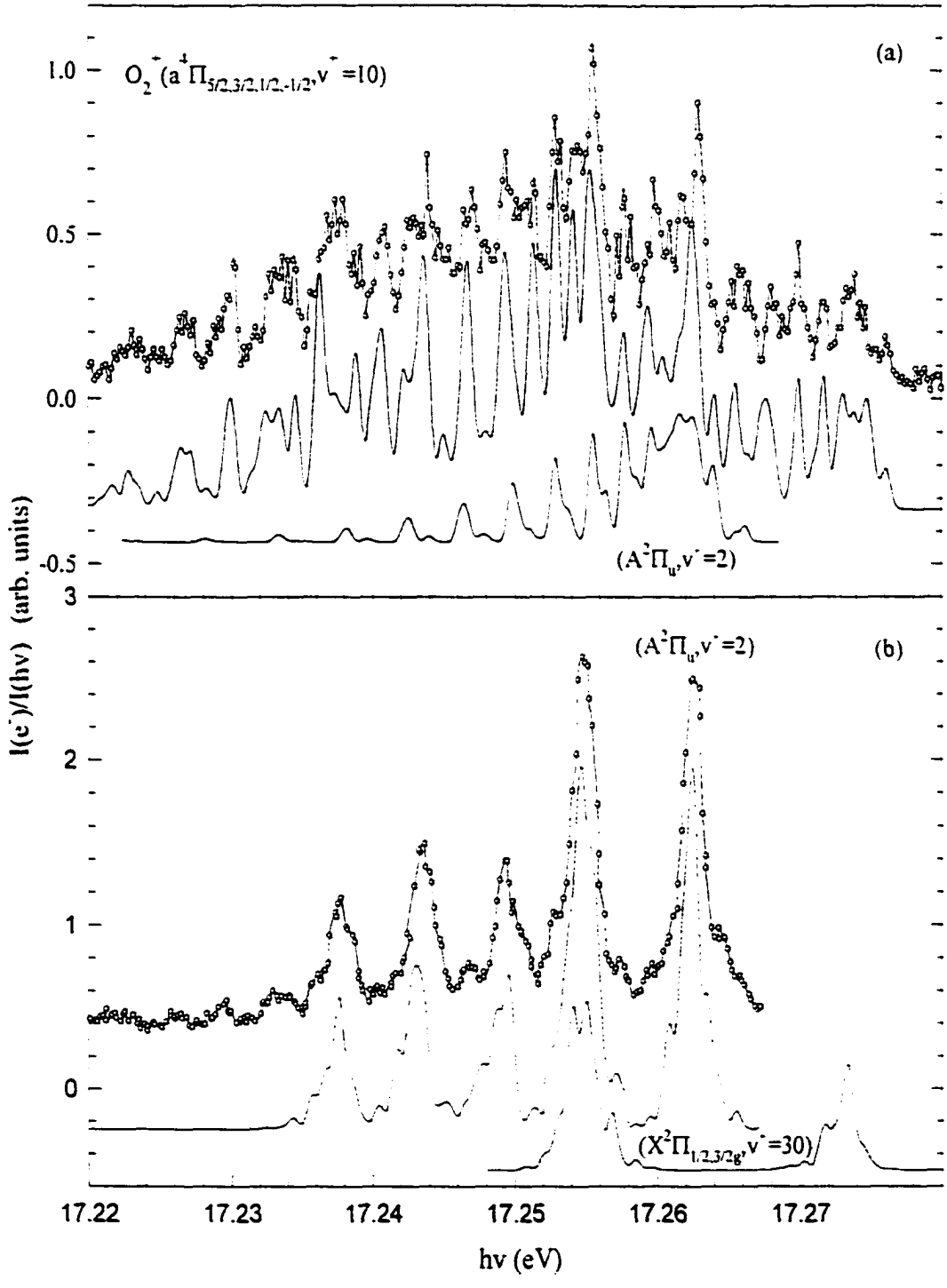
(a)
$O_2^+(a^4\Pi_{5/2,3/2,1/2,-1/2}, v^+=10)$
$(A^2\Pi_u, v^+=2)$
(b)
$(A^2\Pi_u, v^+=2)$
$(X^2\Pi_{1/2,3/2g}, v^+=30)$
I(e⁻)/I(hv) (arb. units)
hv (eV)
1.0
0.5
0.0
-0.5
3
2
1
0
17.22
17.23
17.24
17.25
17.26
17.27

where Q is a factor determined by angular momentum coupling cases (Clebsch Gordon coefficients) and C_λ is a factor associated with the electronic transition moments, which is the linear combination of electron transition amplitudes of the possible orbital angular momenta l of the ejected photoelectron. The value λ can be considered as the orbital angular momentum quantum number associated with the electron partial wave prior to photoexcitation and is related to l by the relation.

$$l-1 \le \lambda \le l+1. \tag{2}$$

The BOS model has considered only the Hund's cases (a) and (b). As pointed out previously, the $O_2^-(a^4\Pi_u)$ state belongs to an intermediate coupling case.[22] Since the BOS model does not included perturbative mechanisms involving channel couplings.[26,27] which are known to occur in the photoionization of O_2,[14,15] the BOS simulation presented here should be considered as empirical in nature. For this reason, instead of performing a rigorous BOS simulation of treating the $O_2^-(a^4\Pi_u)$ state as an intermediate coupling case, we assume that the photoionization process $O_2^-(a^4\Pi_u) \leftarrow O_2(X^3\Sigma_g^-)$ follows a Hund's case (b) $\rightarrow$ (a) transition. This is similar to our previous treatment of photoionization transitions $O_2^-(X^2\Pi_g) \leftarrow O_2(X^3\Sigma_g^-)$ and $O_2^-(A^2\Pi_u) \leftarrow O_2(X^3\Sigma_g^-)$. The simulation program used previously for simulation of the latter transitions was modified to accommodate the four spin-orbit components. Here, we consider the transitions from $O_2(X^3\Sigma_g^-)$ to individual spin-orbit components as independent. Thus, the best fit to the experimental spectrum is obtained by summing the simulated PFI-PE bands for the spin-orbit components after proper scaling of their intensities. For a Hund's case (b) $\rightarrow$ (a) transition, the Q factor is expressed as,

$$Q(\lambda; N^-, N'') = (2N^-+1)(2S^++1)^{-1} \sum_{\chi=\lambda-1/2}^{\lambda+1/2} \begin{pmatrix} \lambda & S^+ & \chi \\ \Delta\Lambda & \Sigma^+ & \Lambda^- - \Omega^- \end{pmatrix}^2 \begin{pmatrix} N^- & \chi & N'' \\ -\Omega^- & \Omega^- - \Lambda'' & \Lambda'' \end{pmatrix}^2. \tag{3}$$

Here, $\Delta\Lambda = \Lambda^+ - \Lambda''$, where Λ'' is the electronic angular momentum projected on the axis of O_2, and S^- is the total spin angular momentum of the final O_2^- ionic state.

Due to the nuclear spin statistics, the even N" rotational levels in $O_2(X^3\Sigma_g^-)$ do not exist.[28] The spin-rotation splittings for $O_2(X^3\Sigma_g^-)$ are in the range of 0.1-0.2 meV for each rotational state. Although the present PFI-PE energy resolution of 0.5-0.6 meV (4-5 cm^{-1}, FWHM) cannot resolve these splittings, rotational transitions originating from the three fine structure sublevels of $O_2(X^3\Sigma_g^-, v''=0)$ have been taken into account in the simulation. For simulation of the vibrational PFI-PE bands for $O_2^-(a^4\Pi_u)$ obtained using a supersonic O_2 beam, the rotational temperature is a fitting parameter. We find that the rotational temperature of 220±20 K gives the best fit to the experimental spectra shown in Figs. 5-1, 5-2, 5-3, 5-4(a), 5-5(a), and 5-6(a). A rotational temperature of 20±5 K is found to provide the best fit to the PFI-PE bands for $O_2^-(a^4\Pi_{5/2,3/2,1/2,-1/2u}, v^-= 7, 9,$ and 10) shown in Figs. 5-4(b), 5-5(b), and 5-6(b).

For a Σ to Π transition ($\Delta\Lambda = 1$), the first 3-j symbol requires that C_0 is zero for the photoionization process. Furthermore, C_1 is also predicted to be zero by the 3-j symbol for $O_2^-(a^4\Pi_{5/2}, v^-)$ PFI-PE bands, indicating that the accompanying l value for $O_2^-(a^4\Pi_{5/2}, v^-)$ cannot be zero. The vibrational PFI-PE bands for the $O_2^-(a^4\Pi_{5/2})$ spin-orbit component can be simulated using the BOS coefficients (C_2, C_3, C_4). For the other three spin-orbit components, we have been able to simulate all experimental PFI-PE vibrational bands using the set of BOS coefficients (C_1, C_2, C_3, C_4). A Gaussian linewidth of 5 cm^{-1} (FWHM) is used as the instrumental resolution profile in the simulation. The best fitted BOS coefficients for the $O_2^+(a^4\Pi_{5/2,3/2,1/2,-1/2u}, v^+= 0\text{-}18)$ bands are listed in Table 5-I.

We have obtained the PFI-PE spectra associated with $O_2^-(a^4\Pi_u, v^-=0)$ using both the thermal (220 K) and cold (20 K) O_2 samples. Due to the domination of the band for $O_2^+(X^2\Pi g, v^+=21)$, the clear identification of the $O_2^+(a^4\Pi_u, v^+=0)$ PFI-PE band is only possible using the 20 K spectrum. Since the latter spectrum is nearly identical to that reported recently by Kong and Hepburn,[22] it is not shown here. The PFI-PE band for $O_2^+(a^4\Pi_{1/2u}, v^+=1)$ was also found to overlap strongly with that for $O_2^-(X^2\Pi_{1/2g}, v^-=21)$. The 220 K spectra of these bands have been simulated and reported previously.[14]

Table 5-I. The best fitted BOS coefficients C_λ (λ=1-4)[a] for the spin orbit components $F_1(a^4\Pi_{5/2})$, $F_2(a^4\Pi_{3/2})$, $F_3(a^4\Pi_{1/2})$, and $F_4(a^4\Pi_{-1/2})$ of $O_2^-(a\,^4\Pi_u, v^-=0\text{-}18)$.

v^-	F_1[b]	F_2[c]	F_3[c]	F_4[c]
0	0.80/0.10/0.10	0.25/0.25/0.25/0.25	0.50/0.50/0.00/0.00	0.50/0.50/0.00/0.00
1	0.90/0.10/0.00	0.37/0.10/0.23/0.31	0.45/0.15/0.20/0.20	0.90/0.00/0.00/0.10
2	0.65/0.35/0.00	0.00/0.00/0.85/0.15	0.60/0.20/0.00/0.20	0.70/0.00/0.30/0.00
3	0.70/0.20/0.10	0.10/0.10/0.55/0.25	0.40/0.00/0.00/0.60	0.60/0.00/0.35/0.05
4	0.85/0.15/0.00	0.19/0.19/0.39/0.23	0.40/0.10/0.00/0.50	0.80/0.00/0.20/0.00
5	0.64/0.36/0.00	0.21/0.21/0.35/0.23	0.50/0.25/0.00/0.25	0.50/0.00/0.00/0.50
6	1.00/0.00/0.00	0.20/0.25/0.25/0.30	0.50/0.25/0.00/0.25	0.50/0.00/0.00/0.50
7	1.00/0.00/0.00	0.20/0.20/0.45/0.15	0.50/0.25/0.00/0.25	0.50/0.00/0.00/0.50
8	1.00/0.00/0.00	0.20/0.20/0.45/0.15	0.65/0.18/0.00/0.17	0.45/0.00/0.00/0.55
9	1.00/0.00/0.00	0.00/0.00/0.70/0.30	0.65/0.18/0.00/0.17	0.40/0.00/0.05/0.55
10	1.00/0.00/0.00	0.40/0.40/0.10/0.10	1.00/0.00/0.00/0.00	0.80/0.00/0.20/0.00
11	0.00/1.00/0.00	0.00/0.00/1.00/0.00	1.00/0.00/0.00/0.00	1.00/0.00/0.00/0.00
12	0.80/0.20/0.00	0.50/0.50/0.00/0.00	0.50/0.50/0.00/0.00	1.00/0.00/0.00/0.00
13	0.00/0.50/0.50	0.00/0.00/0.50/0.50	0.56/0.42/0.01/0.01	1.00/0.00/0.00/0.00
14	0.50/0.50/0.00	0.50/0.50/0.00/0.00	0.40/0.10/0.25/0.25	0.25/0.25/0.25/0.25
15	1.00/0.00/0.00	0.25/0.25/0.25/0.25	0.50/0.50/0.00/0.00	0.00/0.00/0.50/0.50
16	1.00/0.00/0.00	1.00/0.00/0.00/0.00	1.00/0.00/0.00/0.00	0.50/0.50/0.00/0.00
17	1.00/0.00/0.00	1.00/0.00/0.00/0.00	0.50/0.50/0.00/0.00	0.50/0.50/0.00/0.00
18	1.00/0.00/0.00	0.56/0.42/0.01/0.01	0.56/0.42/0.01/0.01	0.56/0.42/0.01/0.01

a) All C_λ values have an uncertainty of $\pm$ 0.2.

b) The three values for the F_1 entry correspond to C_2, C_3 and C_4 since $C_1 = 0$.

c) The four values for the F_2, F_3, and F_4 entries correspond to C_1, C_2, C_3 and C_4.

Figures 5-1 and 5-2 show the respective rotationally resolved PFI-PE bands (open circles) for the $O_2^+(a^4\Pi_{1/2u}, v^+=2\text{-}4$ and 5) states obtained using the 220 K sample. The energy scale use here is (hv-IE), such that these experimental PFI-PE bands are aligned by their IEs determined in the simulation. We note that these spectra have little contributions from other states. Although these experimental bands have complicated structures, we have obtained excellent fits [solid curves below experimental bands of Figs. 5-1 and 5-2] based on the BOS model. As an example of rotational assignments, we show the positions of rotational transitions $O_2^+(a^4\Pi_{5/2,3/2,1/2,-1/2u}, v^+=5, J^+) \leftarrow O_2(X^3\Sigma_g^-, v'', N'')$ in Fig. 5-2 by downward pointing stick marks. The rotational branches ΔJ = -7/2, -5/2, -3/2, -1/2, 1/2, 3/2, 5/2, 7/2, and 9/2 (corresponding to the M, N, O, P, Q, R, S, T and U branches, respectively) are also marked in this figure. For individual ΔJ branches, the positions of the first and second transitions are indicated by progressively shorter stick marks, thus revealing the origin and direction of the rotational branches. Generally, for each ΔJ values, there are contributions from four spin-orbit components, except for high $|\Delta J|$ values. We note that for ΔJ=-7/2, only the Ω=3/2 component is observed, whereas for ΔJ = 7/2 and 9/2, the Ω=5/2 component is absent. This observation is consistently found for all of the vibrational bands. The simulation shows that prominent peaks observed in all 220 K $O_2^+(a^4\Pi_{1/2,3/2}, v^+)$ bands are due mostly to rotational branch heads (i.e., turn around rotational transitions of rotational branches).

The 220 K PFI-PE spectrum (open circles of Fig. 5-3) in the region of 16.77-16.84 eV has contribution from the PFI-PE bands for $O_2^+(a^4\Pi_u, v^+=6)$ and $O_2^+(X^2\Pi_g, v^+=26)$. Although the $O_2^+(X^2\Pi_{1/2g}, v^+=26)$ component, which peaks at ≈16.784 eV, is separated from the PFI-PE band for $O_2^+(a^4\Pi_u, v^+=6)$, the $O_2^+(X^2\Pi_{3/2g}, v^+=26)$ component has significant overlap with the low energy tail of the $O_2^+(a^4\Pi_u, v^+=6)$ band. The simulated spectra (solid curves) for the $O_2^+(X^2\Pi_{1/2,3/2g}, v^+=26)$ and $O_2^+(a^4\Pi_u, v^+=6)$ bands are shown at the bottom of Fig. 5-3. The sum of these simulated bands gives the overall simulated spectrum (top solid curve) for the experimental PFI-PE spectrum (open circles).

As mentioned above, the observed PFI-PE bands of $O_2^+(a^4\Pi_u, v^+=7\text{-}10)$ using the 220 K O_2 sample have serious overlaps with the respective $O_2^+(X^2\Pi_g, v^+=27\text{-}30)$ bands.

The strong overlaps between the $O_2^-(a^4\Pi_u, v^+=8\text{-}10)$ and $O_2^-(A^2\Pi_u, v^+=0\text{-}2)$ bands, respectively, also complicate the analysis. Due to the high rotational populations for O_2, the experimental PFI-PE spectra associated with the $O_2^-(a^4\Pi_u, v^-=7, 9, \text{and } 10)$ bands obtained using the 220 K samples [shown in Figs. 5-4(a), 5-5(a) and 5-6(a), respectively] reveal complex structures and do not allow clear identifications of individual bands. We have shown previously that the 20 K PFI-PE spectrum associated with $O_2^-(a^4\Pi_u, v^-=8)$ makes possible the unambiguous simulation, yielding individual contributions of the PFI-PE bands for $O_2^-(a^4\Pi_u, v^-=8)$, $O_2^-(A^2\Pi_u, v^-=0)$, and $O_2^-(X^2\Pi_g, v^-=28)$.[14,15] Since this 20 K spectrum has been reported previously,[14] we only show here the 220 K mixed spectrum (open circles, top spectrum of Fig. 5-1) for $O_2^-(a^4\Pi_u, v^-=8)$, $O_2^-(A^2\Pi_u, v^-=0)$, and $O_2^-(X^2\Pi_g, v^-=28)$. The overall simulated spectrum (solid curve below the top spectrum of Fig. 5-1), which is obtained by summing the deconvoluted PFI-PE bands for $O_2^-(a^4\Pi_u, v^-=8)$, $O_2^-(A^2\Pi_u, v^-=0)$, and $O_2^-(X^2\Pi_g, v^-=28)$, is in excellent agreement with this 220 K mixed experimental spectrum.

The 20 K PFI-PE spectra (solid circles) associated with the $O_2^-(a^4\Pi_u, v^-=7, 9, \text{and } 10)$ bands are shown in Figs5- 4(b), 5-5(b) and 5-6(b) for comparison with the corresponding 220 K spectra (solid circles) of Figs. 5-4(a), 5-5(a), and 5-6(a). As expected, the 20 K spectra are greatly simplified because of the significantly lower rotational populations of the O_2 sample. Similar to the observation of the 20 K spectrum associated with the $O_2^+(a^4\Pi_u, v^-=8)$ band, all the $O_2^-(a^4\Pi_u, v^-=7, 9, \text{and } 10)$ bands exhibit quartet structures. Combined with the 20 K and 220 K measurements, we have been able to simulate the spectra shown in Figs. 5-4~5-6. The deconvoluted spectra for $O_2^-(X^2\Pi_g, v^+=27, 29, \text{and } 30)$ (bottom solid curves) and $O_2^-(a^4\Pi_u, v^-=7, 9, \text{and } 10)$ (second to the bottom solid curves) are shown in Figs. 5-4(b), 5-5(b), and 5-6(b), respectively. The overall simulated spectra [top solid curves of Figs. 5-4(b), 5-5(b), and 5-6(b)] are obtained by summing the corresponding deconvoluted bands for $O_2^+(X^2\Pi_g, v^+=27, 29, \text{and } 30)$ and $O_2^-(a^4\Pi_u, v^+=7, 9, \text{and } 10)$. These overall simulated spectra are in excellent agreement with the respective experimental spectra (open circles) of Figs. 5-4(b)- 5-6(b). Good accord is also found between the overall simulated spectra (solid curves) and the

corresponding 220 K spectra (solid circles) of Figs. 5-4(a), 5-5(a), and 5-6(a). We note that the overall simulated spectra shown in Figs. 5-5(b) and 5-6(b) have included the respective contributions from $O_2^-(A^2\Pi_u, v^-=1$ and $2)$.[15] The positions (17.1578 and 17.2623 eV) of the latter states are marked in Figs 5-5(b) and 5-6(b).

The PFI-PE bands for $O_2^-(a^4\Pi_{5/2,3/2,1/2,-1/2u}$ $v^-=11$-18) and their simulations have been reported in Ref. 15. We have also collected a 20 K spectrum for $O_2^-(a^4\Pi_{5/2,3/2,1/2,-1/2u}$, $v^-=11$) (not shown here), which reveals similar structures as observed in the 20 K spectrum associated with $O_2^-(a^4\Pi_{5/2,3/2,1/2,1/2u}$ $v^-=10$) [open circles of Fig. 5-6(b)]. Due to the weakness of the PFI-PE bands for $O_2^-(a^4\Pi_{5/2,3/2,1/2,-1/2u}$, $v^-=19$ and 20), they were not observed within the sensitivity of this experiment.

As we pointed out above, the BOS simulation does not included channel couplings and thus should be considered as empirical in nature. However, the excellent fits observed between the BOS fits and the PFI-PE bands of $O_2^-(a^4\Pi_{5/2,3/2,1/2,-1/2u}$, $v^-=0$-18) seem to suggest that perturbative processes, such as the nearby resonance autoionization mechanism, are not important for the formation of these states.

B. Intensity investigation and photoionization mechanism

The complete 220 K spectrum in the region of 16-18 eV, which shows the general PFI-PE band intensity distribution for $O_2^-(X^2\Pi_{3/2,1/2g}$, $v^-=21$-38; $a^4\Pi_{5/2,3/2,1/2,-1/2u}$ $v^-=0$-18; and $A^4\Pi_{3/2,1/2u}$, $v^-=0$-12) has been reported previously.[14] We note that the relative intensity distribution of this PFI-PE spectrum is similar to that of the vibrationally resolved TPE spectrum obtained recently by Akahori et al.[23] Both the PFI-PE and TPE spectra reveals a global maximum at $O_2^-(a^4\Pi_{5/2,3/2,1/2,1/2u}$, $v^-=4$). The latter TPE study did not provide an intensity analysis for the $O_2^-(a^4\Pi_{5/2,3/2,1/2,1/2u}$, v^-) states.

The relative PFI-PE band intensities for $O_2^-(a^4\Pi_{5/2,3/2,1/2,-1/2u}$, $v^-=0$-18) obtained in the present experiment are listed in Table 5-II for comparison with those reported in previous PFI-PE, TPE, and HeI studies. The Franck-Condon Factors (FCFs) obtained by theoretical calculations[29] are also included in Table 5-II. The relative vibrational band intensities and FCFs given in Table 5-II are arbitrarily normalized to 1.00 at $v^-=3$. The relative intensities for PFI-PE bands of $O_2^-(a^4\Pi_{5/2,3/2,1/2,-1/2u}$, $v^-=0$, 1, and 6-18), which

Table II. Relative Intensities of PFI-PE bands for $O_2^+(a\,^4\Pi_{5/2,3/2,1/2,1/2}\,v^+=0\text{-}18)$.

v^+	Relative Intensities[a]			Relative Intensities[e]			
	PFI-PE[b]	HeI/TPE[c]	FCF[d]	F_1	F_2	F_3	F_4
0	0.12	0.07	0.12	27	23	24	26
	(0.10)	(0.10)	(0.09)				
1	0.78	0.33	0.39	34	26	26	14
	(0.60)	(0.43)	(0.34)				
2	0.96	0.70	0.73	33	29	23	15
	(0.81)	(0.71)	(0.69)				
3	1.00	1.00	1.00	35	26	24	15
	(1.00)	(1.00)	(1.00)				
4	1.51	1.19	1.23	33	29	23	15
		(1.19)	[1.19][d]				
5	1.15	1.22	1.27	35	31	22	12
6	1.15	1.11	1.23	33	29	24	14
7	0.96	0.96	1.15	42	36	14	8
				(31)	(45)	(14)	(10)
8	0.75	0.74	1.00	29	26	24	21
				(25)	(31)	(23)	(21)
9	0.54	0.56	0.73	29	31	25	15
				(26)	(33)	(22)	(19)
10	0.45	0.41	0.54	23	24	24	29
				(23)	(25)	(24)	(28)
11	0.48	---	0.42	26	32	22	20
				(22)	(34)	(24)	(21)
12	0.27	---	0.27	24	29	28	19

Table 5-II (continued)

v^+	Relative Intensities[a]			Relative Intensities[e]			
	PFI-PE[b]	HeI/TPE[c]	FCF[d]	F_1	F_2	F_3	F_4
13	0.20	---	0.23	22	33	25	20
14	0.15	---	0.19	23	25	27	25
15	0.14	---	0.12	28	26	23	23
16	0.09	---	0.08	33	37	19	11
17	0.09	---	0.08	23	24	27	26
18	0.07	---	0.04	24	26	28	22

a) The band intensity for $v^+=3$ is arbitrarily normalized to 1.00. Estimated uncertainty is about ±0.02.

b) This work. Estimated uncertainties are ±0.02. The PFI-PE band intensities for $v^+=0$-3 obtained in the VUV laser study (Ref. 22) are given in parenthesis.

c) Band intensities reported in the HeI photoelectron study of Ref 29. The TPE band intensities for $v^+=0$-4 reported in Ref. 30 are given in paratheses.

d) Calculated FCFs from Ref. 29. For $v^+=1$-3, FCFs from Ref. 22 are listed in the parenthesis.

e) From Ref. 29

f) Relative spin-orbit component intensities normalized to 100 derived from thermal (220 K) spectra. For $v^+=7$-11, those intensities derived from cooled spectra (25 K) are listed in the parentheses. Estimated uncertainty is about ±2 for all the entries, except for F_4 component of $v^+=1$ and 10, whose uncertainty is about ±4 due to serious overlapping with other bands.

g) For PFI-PE, He/TPE and FCFs, intensities are normalized with respect to $v^+=3$

overlap with PFI-PE bands of other states, are determined by simulation. Due to the low resolutions used, the relative intensities reported previously for v^+=0-11 in the HeI experiment[29] and v^+=0-4 in the TPE measurement[30] should be considered as rough estimates. Although the relative intensities for v^+=0-3 determined in the VUV laser study[22] are based on spectra measured using a 10 K O_2 beam sample as compared to a 220 K sample of this study, we find good accord between the VUV laser results and the present measurements. General agreement is also observed among the relative vibrational band intensities obtained in PFI-PE, TPE and HeI studies. Taking into account the experimental uncertainties, the PFI-PE intensity distribution obtained in the present experiment[22,29,30] is consistent with the predicted Franck-Condon pattern.[29] However, both the HeI spectra[29] and calculated[29] FCFs indicate that the v^+=5 band has the highest intensity, while the maximum occurs at v^+=4 in the PFI-PE and TPE[23] spectra. Furthermore, the PFI-PE intensities[22] for v^+=0-2 are found to be significantly higher compared to the results of the TPE[30] and HeI[29] studies and calculated[29] FCFs.

The last four columns in Table 5-II list the relative PFI-PE intensities for individual spin-orbit components observed in this study. The sum of the relative PFI-PE intensities for the four spin-orbit components of a given v^+ level is arbitrarily normalized to 100. For v^+=1-9, we find that the intensities for the spin-orbit components are in the order $F_1(a^4\Pi_{5/2}) \geq F_2(a^4\Pi_{3/2}) > F_3(a^4\Pi_{1/2}) > F_4(a^4\Pi_{1/2})$. The intensity of the highest energy spin-orbit component $F_4(a^4\Pi_{1/2})$ for v^+=11, 12, 15, and 16 are also found to be lowest. This observation is in accord with that found in the PFI-PE bands for $O_2^+(a^4\Pi_{5/2,3/2,1/2,-1/2u}, v^+$=1 and 2) recorded in the previous VUV laser study.[22] The observed intensities distributions for the spin-orbit components were attributed to the forced spin-orbit/rotational autoionization mechanism.[31-34] This forced autoionization mechanism is field induced and strongly depends on the field strength. Our observation of the lower intensities for the high-energy spin-orbit components for v^+=1-9 is consistent with the decay of the high-energy spin-orbit components by the field induced spin-orbit/rotational autoionization. The enhancements observed for the low-energy spin-orbit components for hydrogen halides[32-34] resulting from this mechanism have been well documented.

For v^+=0 and 7-11, relative intensities (values in parentheses) for the spin-orbit components based on the 20 K PFI-PE spectra are included in Table 5-II. For v^+=7-11, we find that the relative intensity for $F_1(a^4\Pi_{5/2})$ derived from the 20 K spectrum is lower and that for $F_4(a^4\Pi_{1/2})$ is higher as compared to the corresponding values derived from the 220 K spectrum. That is, the forced autoionization mechanism is less apparent in the 20 K spectrum. The greater effect observed for the forced spin-orbit/rotational autoionization mechanism at 220 K can be attributed to the fact that more rotational channels are available at 220 K for contribution to the intensity enhancements compared to that at 20 K. Similar observations were found previously in other systems.[35]

C. Spectroscopic constants for $O_2^+(a^4\Pi_u, v^+=0\text{-}18)$

The general energy expressions used for $O_2(X^3\Sigma_g^-, v'', N'')$ and $O_2^+(a^4\Pi_u, v^+, N^+)$ are

$$E(v'', N'') = E_e'' + \omega_e''(v'' + 1/2) - \omega_e''\chi_e''(v'' + 1/2)^2 + B_v''N''(N'' + 1), \quad (4)$$

and

$$E^+(v^+, N^+) = E_e^+ + \omega_e^+(v^+ + 1/2) - \omega_e^+\chi_e^+(v^+ + 1/2)^2 + B_v^+N^+(N^+ + 1) \quad (5)$$

respectively, where $B_v'' = B_e'' - \alpha''(v'' + 1/2)$ and $B_v^+ = B_e^+ - \alpha^+(v^+ + 1/2)$. The values B_e'' = 1.44563 cm^{-1}, α'' = 0.01593 are taken from Refs. 28 and 36. Including the rotation-electronic coupling [required be Hund's case (a)] and the spin-orbit interaction, the energy expression for $O_2^+(a^4\Pi_u, v^+, N^+)$ becomes,[28]

$$E^+(v^+, N^+, \Sigma^+) = E^+(v^+, N^+) - Bv^+\Omega^{+2} + A_v^+\Lambda^+\Sigma^+, \quad (6)$$

where A_v^+ is spin-orbit splitting constant, Λ^+=1 for $a^4\Pi_u$, Σ^+ = 3/2, 1/2, -1/2, and -3/2, and Ω^+ = 5/2, 3/2, ½, and ½. We calculate the ionizing transition energies as:

$$\Delta E(v^+, N^+, \Sigma^+) = E(v^+, N^+, \Sigma^+) - E(v''=0, N''=1) = T_v + B_v^+N^+(N^+ + 1) - B_v^+\Omega^{+2} + A_v^+\Sigma^+, \quad (7)$$

where $T_{v^+} = T(v^+, v''=0, N''=1) = [E_e^+ - E_e'' + \omega_e^+(v^+ + 1/2) - \omega_e^+\chi_e^+(v^+ + 1/2)^2 - \omega_e''(1/2) + 1/4\ \omega_e''\chi_e'' - 2B_v'']$. Although the $N''=0$ level for $O_2(X^3\Sigma_g^-)$ is not allowed due to nuclear spin statistics, we have defined here that the IE values for individual spin-orbit components of a given v^+ state correspond to the energy difference between $O_2^+(a^4\Pi_u, v^+, F_i, i=1\text{-}4, N^+=0)$ and $O_2(X^3\Sigma_g^-, v''=0, N''=0)$.

The T_{v^+}, A_v^+, and B_v^+ values for $v^+ = 0$–18 obtained by the BOS simulation in the present experiment are listed in Table 5-III. Using the T_{v^+} value[14] of 129892 cm^{-1} for $v^+ = 0$ obtained in the VUV laser PFI-PE study,[22] together with spectroscopic data determined in the previous emission study,[20,21] we have calculated the T_{v^+} values $O_2^+(a^4\Pi_u, v^+=0\text{-}9)$. The deviation between these latter values (listed Table 5-III) and the corresponding values obtained here are within ±4 cm^{-1}. The A_v^+ values for $v^+=0\text{-}9$ obtained in the previous emission study[20,21] are also included in Table 5-III. Due to the higher resolution achieved, these emission values for A_v^+ are expected to be more accurate than results of this PFI-PE study. Nevertheless, the two sets of A_v^+ vales for $v^+=0\text{-}9$ are found to be in excellent accord with the maximum discrepancy to be less than 2 cm^{-1}, which is equal to the estimate error for A_v^+ for $v^+=0\text{-}14$ determined in the present study. Due to the weakness of the PFI-PE bands for $v^+=15\text{-}18$, we estimate the error for A_v^+ of these states obtained here to be 3 cm^{-1}. The values for A_v^+, $v^+=0\text{-}20$, have also been reported in the TPE study of Akahori et al.[23] Their values are compared to those obtained here and in the emission study in Fig. 5-7. Although the A_v^+ values are believed to be the least reliable, it is interesting that the oscillations of A_v^+ observed in the range of $v^+ = 9\text{-}18$ in the present study seems to coincide with those reported by Akahori et al. The B_v^+ values for $v^+=0\text{-}9$ obtained in the present study are also in excellent agreement with those of Refs. 20 and 21. The uncertainties for the B_v^+ values determined here are estimated to be ±0.010 cm^{-1}. Due to the higher resolution achieved, the T_{v^+}, A_v^+, and B_v^+ values for $v^+=0\text{-}9$ obtained in the emission study[20,21] are expected to be more accurate than results of this PFI-PE study.

Values for the IEs of individual spin-orbit components for $v^+=0\text{-}18$ are listed in Table 5-III. The IE values for $v^+=0\text{-}6$ obtained in the previous TPE study of Morioka et al.[37] are given in parentheses for comparison with those of the present study in Table 5-III. The

Table 5-III. Spectroscopic constants for O_2^+ ($a\ ^4\Pi_{5/2,3/2,1/2,-1/2}$ $v^+ = 0$-18)

v^+	T_v (cm^{-1})		IE (eV)[d,e]				A_v^+ (cm^{-1})		B_v^+ (cm^{-1})	
	This work[a]	Refs. 20-22[b,c]	F_1	F_2	F_3	F_4	This work[f]	Refs. 20 and 21	This work[g]	Refs. 20 and 21[c]
0	129892.9	129894.33	16.0960	16.1016	16.1074	16.1123	-48.0	-47.79	1.090	1.097
	(16.1047)	[16.1048]	(16.096)			(16.117)				[1.098]
1	130913.2	130909.17	16.2225	16.2281	16.2339	16.2387	-48.0	-47.80	1.081	1.082
	(16.2312)	[16.2307]	(16.222)	(16.229)	(16.234)	(16.240)				[1.082]
2	131906.0	131903.37	16.3456	16.3512	16.3570	16.3618	-48.0	-47.77	1.065	1.066
	(16.3543)	[16.3539]	(16.344)	(16.350)	(16.356)	(16.361)				[1.066]
3	132879.5	132876.92	16.4663	16.4719	16.4777	16.4825	-48.0	-47.74	1.050	1.051
	(16.4750)	[16.4746]	(16.463)	(16.469)	(16.475)	(16.479)				[1.050]
4	133833.2	133829.55	16.5845	16.5901	16.5960	16.6008	-48.0	-47.71	1.034	1.035
	(16.5932)	[16.5927]	(16.580)	(16.585)	(16.592)	(16.596)				[1.034]
5	134764.0	134761.21	16.7001	16.7056	16.7113	16.7160	-47.0	-47.64	1.018	1.019
	(16.7086)	[16.7083]	(16.697)	(16.703)	(16.709)	(16.714)				[1.018]
6	135673.7	135671.63	16.8127	16.8183	16.8242	16.8290	-48.0	-47.55	1.002	1.003
	(16.8214)	[16.8212]	(16.804)	(16.810)	(16.817)	(16.823)				[1.003]

Table 5-III (Continued)

	T_v (cm^{-1})		IE (eV)[d,e]				A_v^+ (cm^{-1})		B_v^+ (cm^{-1})	
v^+	This work[a]	Refs. 20-22[b,c]	F_1	F_2	F_3	F_4	This work[f]	Refs. 20 and 21	This work[g]	Refs. 20 and 21[c]
7	136562.0	136560.48	16.9230	16.9286	16.9343	16.9390	-48.0	-47.44	0.987	0.987
	(16.9315)	[16.9314]								[0.987]
8	137430.0	137427.29	17.0304	17.0361	17.0419	17.0467	-48.0	-47.06	0.971	0.975
	(17.0392)	[17.0389]								[0.972]
9	138275.0	138274.44	17.1351	17.1408	17.1468	17.1517	-49.0	-47.13	0.955	0.956
	(17.1439)	[17.1437]								[0.956]
10	139096.0	----------	17.2375	17.2429	17.2482	17.2537	-46.0	-------	0.939	--------
	(17.2457)	[17.2456]								[0.941]
11	139897.0	----------	17.3365	17.3421	17.3478	17.3524	-47.0	-------	0.914	--------
	(17.3450)	[17.3448]								[0.925]
12	140670.6	----------	17.4316	17.4377	17.4439	17.4500	-51.0	-------	0.895	--------
	(17.4409)	[17.4413]								[0.909]
13	141427.2	----------	17.5270	17.5320	17.5372	17.5421	-43.0	-------	0.915	--------
	(17.5347)	[17.5352]								[0.894]
14	142170.4	----------	17.6183	17.6239	17.6296	17.6349	-47.0	-------	0.900	--------
	(17.6269)	[17.6265]								[0.878]

Table 5-III (Continued)

	T_v (cm^{-1})		IE (eV)[d,e]				A_v^+ (cm^{-1})		B_v^+ (cm^{-1})	
v^+	This work[a]	Refs. 20-22[b,c]	F_1	F_2	F_3	F_4	This work[f]	Refs. 20 and 21	This work[g]	Refs. 20 and 21[c]
15	142882.1	----------	17.7066	17.7121	17.7179	17.7232	-47.0	-------	0.850	--------
	(17.7151)	[17.7152]								[0.862]
16	143578.1	----------	17.7936	17.7987	17.8039	17.8087	-43.0	-------	0.844	--------
	(17.8014)	[17.8012]								[0.846]
17	144242.7	----------	17.8755	17.8809	17.8865	17.8910	-46.0	-------	0.829	--------
	(17.8838)	[17.8842]								[0.829]
18	144889.1	----------	17.9550	17.9609	17.9670	17.9727	-45.0	-------	0.813	--------
	(17.9640)	[17.9639]								[0.813]

a) The T_v values in eV are listed in the parentheses.

b) Values for v^+=0-9 are derived from Refs. 20-22.

c) Values in square brackets are best-fitted values to experimental T_v values according to the Dunham polynomial [Eq. (8)]. For experimental T_v values for v^+=0-9 are based on Refs. 20-22 and those for v^+=10-18 experiment values are based on this work. See the text.

d) The IE values for these spin-orbit components given here correspond to the ΔN=0 (or Q branch) trnasitions O_2^+ ($a^4\Pi_u$, v^+, F_i, i =1-4) ← $O_2(X^3\Sigma_g^-, v''=0, N''=1)$.

e) Values for v^+=0-6 reported in Ref. 37 are given in parenthesis.

f) Estimated uncertainties are ±2 cm^{-1} for v^+=0-14 and ±3 cm^{-1} for v^+=15-18.

g) Estimated uncertainties are ±0.01 cm^{-1}.

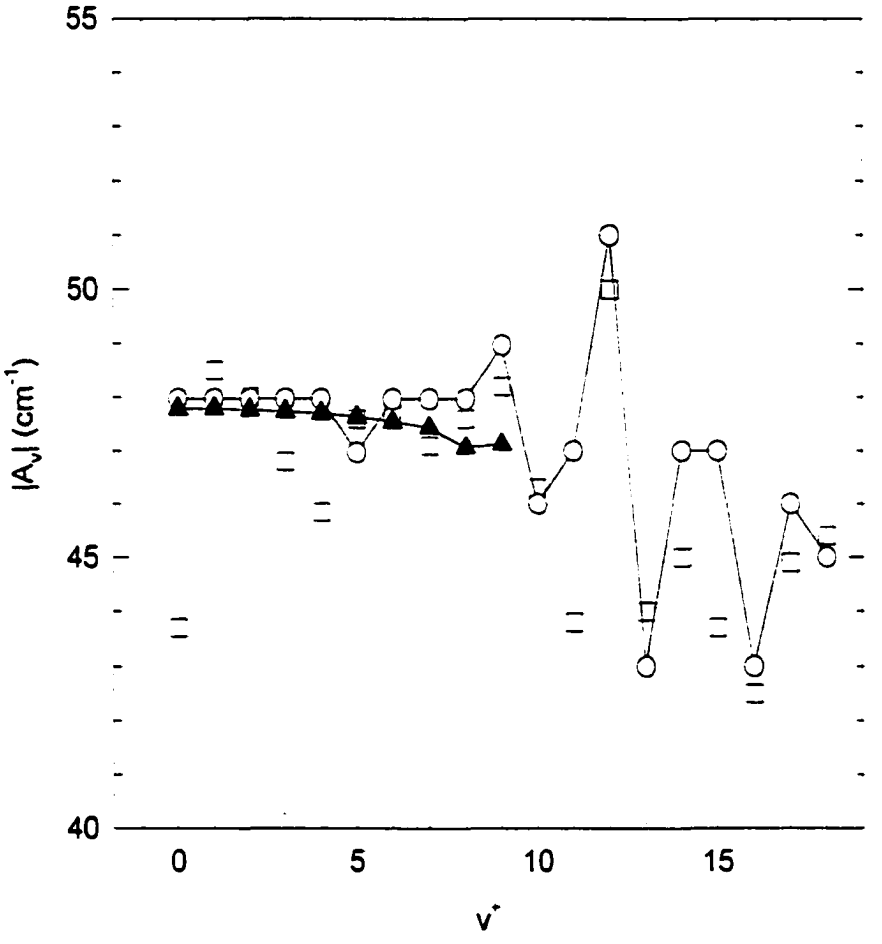

Figure 5-7. Comparison of the $|A_{v+}|$ values for v^+=0-18 obtained in the present study (open circles). in Refs. 18 and 19 (solid triangles), and in Ref. 23 (open squares).

Table 5-IV. Dunham-type vibrational and rotational constants for O_2^- ($a^4\Pi_u$ v^-=0-18).

Dunham constants	This Work (cm^{-1})[a]	Refs. 20 and 21 (cm^{-1})[a]
T_e	129378.32(3.16)	0
ω_e	1035.93(2.31)	1035.51904(345)
$\omega_e x_e$	-10.20(0.49)	-10.3821(232)
$\omega_e \gamma_e$	0.0395(0.039)	0.0329(0.0070)
$\omega_e z$	-7.52×10^{-4}(1.02×10^{-3})	$-6.37(95)\times10^{-3}$
B_e	1.1067(0.0097)	1.1047580(484)
α_e	1.67×10^{-2} (0.45×10^{-2})	1.54762 (233) $\times10^{-2}$
γ_e	1.3255×10^{-4} (5.445×10^{-4})	$1.164(619)\times10^{-6}$

a) Error bars are given in parentheses.

maximum discrepancy between corresponding IE(v^+=0-5) values obtained in the TPE study and in the present study is less than 5 meV. However, the IE values for v^+=6 obtained in the TPE measurement are found to deviate from those determined here by ≈8 meV.

The T_v^+ and B_v^+ values for v^+=0-9 obtained based on the emission and VUV laser studies and those for v^+=10-18 determined in the present study represent the best sets of experimental T_{v^+} and B_v^+ values for v^+=0-18. These experimental T_{v^+} and B_v^+ values are fitted to Eqs. (8) and (9), respectively, to obtain the vibrational (ω_e^+, $\omega_e^+x_e^+$, $\omega_e^+y_e^+$, and $\omega_e^+z_e^+$) and rotational (B_e^+, α_e^+, and γ_e^+) constants.

$$T(v^+) = T_e^+ + \omega_e^+ (v^+ + ½) - \omega_e^+x_e^+ (v^+ + ½)^2 + \omega_e^+y_e^+ (v^+ + ½)^3 + \omega_e^+ z_e^+ (v^+ + ½)^4 \quad (8)$$

$$Bv^+ = B_e^+ - \alpha_e^+ (v^+ + ½) + \gamma_e^+ (v^+ + ½)^2 \quad (9)$$

The Dunham type vibrational and rotational coefficients thus obtained by the least squares fits are listed in Table 5-IV for comparison with those reported in Refs. 20 and 21. In general, the vibrational and rotational Dunham coefficients determined here are in excellent agreement with the literature values.

IV. CONCLUSIONS.

We have obtained rotationally resolved PFI-PE bands for $O_2^+(a^4\Pi_u, v^+=0\text{-}18)$ in the energy range of 16.0-18.0 eV. The IE values and spectroscopic constants for $O_2^+(a^4\Pi_u, v^+=0\text{-}9)$ obtained from the BOS simulation of the PFI-PE data are in excellent agreement with the previous emission and VUV laser based PFI-PE studies. Spectral simulations have provided new spectroscopic constants for the $O_2^+(a^4\Pi_u, v^+=10\text{-}18)$ states. The observed PFI-PE band intensities for the spin-orbit components of $O_2^+(a^4\Pi_u, v^+=1\text{-}9)$ reveal the general trend $F_1(a^4\Pi_{5/2}) \geq F_2(a^4\Pi_{3/2}) > F_3(a^4\Pi_{1/2}) > F_4(a^4\Pi_{1/2})$. This observation is consistent with the forced spin-orbit/rotational autoionization mechanism.

Acknowledgements:

This work was supported by the Director, Office of Energy Research, Office of Basic Energy Sciences, Chemical Sciences Division of the U.S. Department of Energy under Contract No. DE-AC03-76SF00098 for the Lawrence Berkeley National Laboratory and Contract No. W-7405-Eng-82 for the Ames Laboratory. C.Y.N. acknowledges partial support by AFOSR. Y.S. acknowledges the Wall Fellowship for 1999-2000. M.E. acknowledges the Dow Fellowship for 1997-1998.

References

1. K. Müller-Dethlef, M. Sander, and E. W. Schlag, *Chem. Phys. Lett.* **112**, 291 (1984).
2. K. Müller-Dethlef and E. W. Schlag, *Ann. Rev. Phys. Chem.* **42**, 109 (1991).
3. I. Powis, T. Baer, and C. Y. Ng, editors, "High Resolution Laser Photoionization and Photoelectron Studies", *Wiley Series in Ion Chem. and Phys.* (Wiley, Chichester, 1995) and references therein.
4. C.-W. Hsu, M. Evans, P. A. Heimann, and C. Y. Ng, *Rev. Sci. Instrum.*, **68**, 1694 (1997).
5. P. Heimann, M. Koike, C.-W. Hsu, D. Blank, X. M. Yang, A. Suits, Y. T. Lee, M. Evans, C. Y. Ng, C. Flaim, and H. A. Padmore, *Rev. Sci. Instrum.* **68**, 1945 (1997).
6. C.-W. Hsu, M. Evans, S. Stimson, C. Y. Ng, and P. Heimann, *Chem. Phys.* **231**, 121 (1998).
7. G. K. Jarvis, Y. Song, and C. Y. Ng, *Rev. Sci. Instrum.* **70**, 2615 (1999).
8. C. Y. Ng, in "Photoionization and Photodetachment", edited by C. Y. Ng, (World Scientific, Singapore, 1999), *Adv. Ser. Phys. Chem.* **10A**, in press.
9. H. Palm and F. Merkt, *Phys. Rev. Lett.* **81**, 1385 (1998).
10. C.-W. Hsu, M. Evans, S. Stimson, C. Y. Ng, and P. Heimann, *J. Chem. Phys.* **106**, 8931 (1997).
11. C.-W. Hsu, M. Evan, S. Stimson, and C. Y. Ng, *J. Chem. Phys.* **108**, 4701 (1998).
12. C.-W. Hsu, M. Evans, S. Stimson, and C. Y. Ng, *J. Chem. Phys.* **109**, 1285 (1998).

13. M. Evans, S. Stimson, C. Y. Ng, C.-W. Hsu, and G. K. Jarvis, *J. Chem. Phys.* **110**, 315 (1999).

14. Y. Song, M. Evans, C. Y. Ng, C.-W. Hsu, and G. K. Jarvis, *J. Chem. Phys.* **111**, 1905 (1999).

15. Y. Song, M. Evans, C. Y. Ng, C.-W. Hsu, and G. K. Jarvis, *J. Chem. Phys.*, submitted.

16. G. K. Jarvis, M. Evans, C. Y. Ng, and K. Mitsuke, *J. Chem. Phys.* **111**, 3058 (1999).

17. G. K. Jarvis, Y. Song, and C. Y. Ng, *J. Chem. Phys.* **111**, 1937 (1999).

18. D. Fedorov, M. Evans, M. Gordon, and C. Y. Ng, *J. Chem. Phys.* **111**, xxxx (1999).

19. M. Evans and C. Y. Ng, *J. Chem. Phys.* **111**, xxxx (1999).

20. P. C. Cosby, J.-B. Ozenne, J. T. Moseley, and D. L. Albritton, J. Mol. Spectrosc. **79**, 203 (1980).

21. J. C. Hansen, J. T. Moseley, and P. C. Cosby, J. Mol. Spectrosc. **173**, 48 (1983).

22. W. Kong and J. W. Hepburn, Int. J. Mass Spectrom. Ion Proc. **159**, 27 (1996).

23. T. Akahori, Y. Morioka, T. Tanaka, H. Yoshii, T. hayaishi, and K. Ito, J. Chem. Phys. **107**, 4875 (1997).

24. R. B. Cairns and J. A. R. Samson, *J. Opt. Soc. Am.* **56**, 1568 (1966).

25. S. Stimson, Y.-J. Chen, M. Evans, C.-L. Liao, C. Y. Ng, C.-W. Hsu, and P. Heimann, *Chem. Phys. Lett.* **289**, 507 (1998).

26. A. D. Buckingham, B. J. Orr, J. M. Sichel, *Phil. Trans. Roy. Soc. Lond. A*, **268**, 147 (1970).

27. T. Baer, P.-M. Guyon, in "High Resolution Laser Photoionization and Photoelectron Studies", *Wiley Series in Ion Chem. and Phys.* (Wiley, Chichester, 1995), p. 1.

28. G. Herzberg, *Molecular Spectra and Molecular Structure, Vol. IV. Constants of Diatomic Molecules* (Van Nostrand, new York, 1979).

29. O. Edquivst, E. Lindholm, L E. Selin, and L. Asbrink, *Phys. Scri.* **1**, 25 (1970).

30. F. Merkt, P. M. Guyon, and J. W. Hepburn, *Chem. Phys.* **173**, 479 (1993).

31. F. Merkt, H. H. Fielding, and T. P. Softley, *Chem. Phys. lett.* **202**, 153 (1993).

32. A, Mank, D. Rodgers, and J. W. hepburn, *Chem. Phys. Lett.* **219**, 169 (1994).

33. Y. F. Zhu, E. R. Grant, K. Wang, C. McKoy, and H. Lefebvre-Brion, *J. Chem.Phys.* **100**, 8633 (1994).

34. H. Lefebvre-Brion, *Chem. Phys. Lett.* **253**, 43 (1996).

35. F. Merkt and T. P. Softley, *Int. Rev. Phys. Chem.* **12**, 205 (1993).

36. K. P. Huber and G. Herzberg, "Molecular Spectra and Molecular Structure, Vol. IV, Constants of Diatomic Mo O_2^- ($a^4\Pi_u$, v^-=6) lecules" (Van Nostrand, New York, 1979).

37. Y. Morioka, Y. Yu, T. Matsui, K. Ito, and T. Hayaishi, *J. Phys.* B **26**, L535 (1993).

CHAPTER 6. ROTATIONAL-RESOLVED PULSED FIELD IONIZATION-PHOTOELECTRON STUDY OF $NO^+(A'^1\Sigma^-, v^+ = 0\text{-}17)$ IN THE ENERGY RANGE OF 17.70-20.10 eV

A paper to be published in *Journal of Chemical Physics*, **115**, (2001)

Y. Song, G. K. Jarvis, C.Y. Ng, and R.A. Dressler

Abstract:

We have obtained partially rotationally resolved pulsed field ionization-photoelectron (PFI-PE) spectra of NO in the energy range of 17.70-20.10 eV, covering ionization transitions of $NO^+(A'^1\Sigma^-, v^+ = 0\text{-}17, J^+) \leftarrow NO(X^2\Pi_{3/2,1/2}, v''=0, J'')$. The PFI-PE bands for $NO^+(A'^1\Sigma^-, v^+ = 0\text{-}17)$ obtained here represent the first spectroscopic data that allow the direct determination of rotational constants for these states. As in previous studies, the PFI-PE bands are simulated using the Buckingham-Orr-Sichel model as an empirical scheme to derive reliable spectroscopic constants. The simulation, together with comparison with previous HeI photoelectron data, has also provided information on intensity enhancements of PFI-PE bands. Accurate spectroscopic constants for $NO^+(A'^1\Sigma^-, v^+ = 0\text{-}17)$ obtained in the present study include ionization energies, vibrational constants (ω_e=1272.03 ± 1.45 cm^{-1}, $\omega_e\chi_e$=11.924 ± 0.188 cm^{-1}, and $\omega_e y_e$ = -0.059 ±0.007 cm^{-1}), and rotational constants [B_e=1.3562 ± 0.0024 cm^{-1}, α_e=0.01780 ± 0.00061 cm^{-1}, and γ_e = -(1.574 ± 0.328) x10^{-4} cm^{-1}]. The simulation indicates that continuum photoelectron states can be formed with orbital angular momenta l up to 5, which corresponds to the maximum total angular momentum transfer of $|\Delta J|$ = 13/2. Since the dominant rotational branches observed are ΔJ = ±1/2, ±3/2, ±5/2, ±7/2, and +9/2, we conclude that continuum photoelectron states are predominantly produced in l =0-3 in the threshold photoionization of $NO(X^2\Pi_{3/2,1/2})$ to form $NO^+(A'^1\Sigma^-, v^+ = 0\text{-}17)$.

I. INTRODUCTION

The nitric oxide cation NO^+, being isoelectronic with N_2 and CO, is among the most stable chemical species. Partly due to its exceptional stability, NO^+ is a terminal ion in several plasma environments, and is known to be among the most active species in atmospheric reaction cycles at lower altitudes.[1-3] Thus, the detailed spectroscopic investigation of NO^+ is of interest to plasma and atmospheric science. Edquivst *et al.*[4] performed an extensive HeI photoelectron spectroscopic investigation of NO, which resulted in the identification of many electronic states, such as $NO^+(X^1\Sigma^+, a^3\Sigma^+, b^3\Pi, w^3\Delta, b^3\Sigma^-, A'^1\Sigma^- W^1\Delta$, and $A^1\Pi$). Due to the relatively low photoelectron energy resolution used, this study only provided information at the vibrational level for NO^+. The recent high-resolution studies of NO using laser pulsed field ionization (PFI)-photoelectron (PFI-PE) schemes[5-8] have resulted in rotationally resolved photoelectron spectra for a few vibrational bands of $NO^+(X\ ^1\Sigma^+$ and $a\ ^3\Sigma^+)$, yielding highly accurate ionization energy (IEs) values for these states. Using the newly developed synchrotron-based PFI-PE techniques, we have measured recently the rotationally resolved PFI-PE bands for $NO^+(X\ ^1\Sigma^+, v^+=0\text{-}32)$ and $NO^+(a\ ^3\Sigma^+, v^+=0\text{-}16)$ in the full energy range of 9.2-18.2 eV.[9,10]

The photoelectron bands for $NO^+(A'^1\Sigma^+, v^+=0\text{-}7)$ with IEs above 17.8 eV have been observed in the HeI study.[4] The potential curves for NO^+ at energies >17.6 eV are known to be congested with a high density of vibronic levels.[11] This, together with the small Franck-Condon factors (FCFs),[4] has prevented the observation of photoelectron bands for higher v^+ states of $NO^+(A'^1\Sigma^+)$. To our knowledge, no rotationally resolved spectroscopic data for $NO^+(A'^1\Sigma^+)$ have been reported previously. Here, we present the analysis of partially rotationally resolved PFI-PE bands for $NO^+(A'^1\Sigma^+, v^+=0\text{-}17)$ appearing in the energy range of 17.70-20.10 eV. By simulating the PFI-PE bands using the Buckingham-Orr-Sichel (BOS) model[12] as an empirical scheme, we have obtained accurate IEs and vibrational and rotational constants for these vibronic states. As in previous studies,[9,10,13-17] we were able to provide unambiguous identification of overlapping PFI-PE bands for $NO^+(A'^1\Sigma^+, v^+=0\text{-}17)$ by a comprehensive rotational analysis of all vibronic bands

involved. The BOS analysis has also revealed local perturbations of rotational branch and vibrational band intensities for $NO^+(A'^1\Sigma^-, v^+)$.

Because of near-resonance autoionization processes, a threshold photoelectron experiment at the vibrationally resolved level usually cannot provide accurate FCFs for the direct photoionization process, which contain information about the equilibrium bond distances for the cationic states. However, in a rotationally resolved PFI-PE study, the equilibrium bond distances for cationic states can be derived from the rotational constants, which in turn provide information for construction of the electronic potential energy curve for the cation. Accurate spectroscopic constants covering a wide range of vibronic states obtained in our recent PFI-PE studies on diatomic molecules,[9,10,13-17] such as O_2 and CO, have stimulated state-of-the-art *ab initio* calculations.[14,18] An important goal of the present study is to derive a wide range of vibrational and rotational constants for $NO^+(A'^1\Sigma^-)$, together with those for other electronic NO^+ states, for comparison with potential energy surfaces obtained in ongoing high-level *ab initio* calculations.[19] Highly accurate IE values determined in this and previous PFI-PE studies[9,10,,13-17] would also be useful for the identification of neutral Rydberg states of NO, O_2, and CO by providing reliable convergence limits of the Rydberg series, which are difficult to obtain by other techniques.

II. EXPERIMENT

The experiments were carried out using the high-resolution photoelectron-photoion apparatus[20-22] of the Chemical Dynamics Beamline at the Advanced Light Source (ALS). In the present experiment, Ne was used as the filter gas to suppress higher undulator harmonics with photon energies greater than 21.56 eV. Undulator light of the first harmonic emerging from the gas filter was directed into the 6.65 m Eagle monochromator and dispersed by a 2400 lines/mm grating (dispersion = 0.64 Å/mm) before entering the photoelectron-photoion apparatus. Monochromator entrance/exit slits of 50/50 μm were used for the measurement of PFI-PE vibrational bands presented here. The photon energy scale was calibrated using the $Xe^+(^2P_{3/2})$, $Kr^+(^2P_{3/2})$ and $Ar^+(^2P_{3/2})$ PFI-PE bands. Previous measurements indicate that the accuracy of this calibration method is within ± 0.5 meV.[20-22]

The synchrotron based PFI-PE measurements were achieved by employing an electron TOF scheme and have been described in detail previously.[22] The ALS was operated in the multibunch mode with a dark gap of 80 ns per period. The pulsed electric field (height = 1.2 V/cm, width = 40 ns) was applied with a 20-ns delay with respect to the beginning of the dark gap at a frequency of 1.53 MHz. Counting time for data accumulation at a given photon energy was varied in the range of 10-30 sec. Spectra were flux normalized using the calibrated photoelectric signal observed by a tungsten detector.[23]

The NO sample was introduced as an effusive beam through a metal orifice with a diameter of 0.5 mm at room temperature and a distance of 0.5 cm from the photoionization/photoexcitation (PI/PEX) region. We estimate that the NO density in the PI/PEX region is $\approx 10^{-3}$ Torr.

III. RESULTS AND DISCUSSION

The ground $NO(X^2\Pi)$ state has the main electronic configuration, $(1\sigma)^2(2\sigma^*)^2(3\sigma)^2(4\sigma^*)^2(1\pi)^4(5\sigma)^2(2\pi^*)^1$, with an unpaired electron residing in the anti-bonding $2\pi^*$ orbital. Including the spin-orbit interaction, the ground state is $NO(X^2\Pi_{1/2})$. The excited $NO(^2\Pi_{3/2})$ spin-orbit state is known to lie 123.35 cm^{-1} above the ground $NO(X^2\Pi_{1/2})$ state. The removal of an electron from the 1π bonding orbital results in the formation of either the $NO^+(a^3\Sigma^-)$ or $NO^+(A'^1\Sigma^-)$ state, depending on the spin of the remaining electron on the 1π orbital.

A. Relative PFI-PE vibrational band intensities for $NO^+(A'^1\Sigma^-, v^+ = 0\text{-}17)$

Figures 6-1(a) and 6-1(b) shows the relative intensities of the PFI-PE bands for $NO^+(A'^1\Sigma^-, v^+ = 0\text{-}17)$ in the energy ranges of 17.70-18.80 and 18.58-20.10 eV, respectively. The positions of the $NO^+(A'^1\Sigma^-, v^+=0\text{-}17)$ vibrational bands are marked in the figures, along with the positions of vibrational bands for the $NO^+(b^3\Pi, w^3\Delta, b'^3\Sigma^-, W^1\Delta$ and $A^1\Pi)$ states. Extensive overlaps among two or more vibrational bands that belong to different electronic states are a common feature in this energy range for the PFI-PE spectra of NO.[4] For example, the $NO^+(A'^1\Sigma^-, v^+ = 2)$ band is significantly contaminated by transitions of the $NO^+(b^3\Pi, v^+=8)$ band and the energy region covering the $NO^+(A'^1\Sigma^-$.

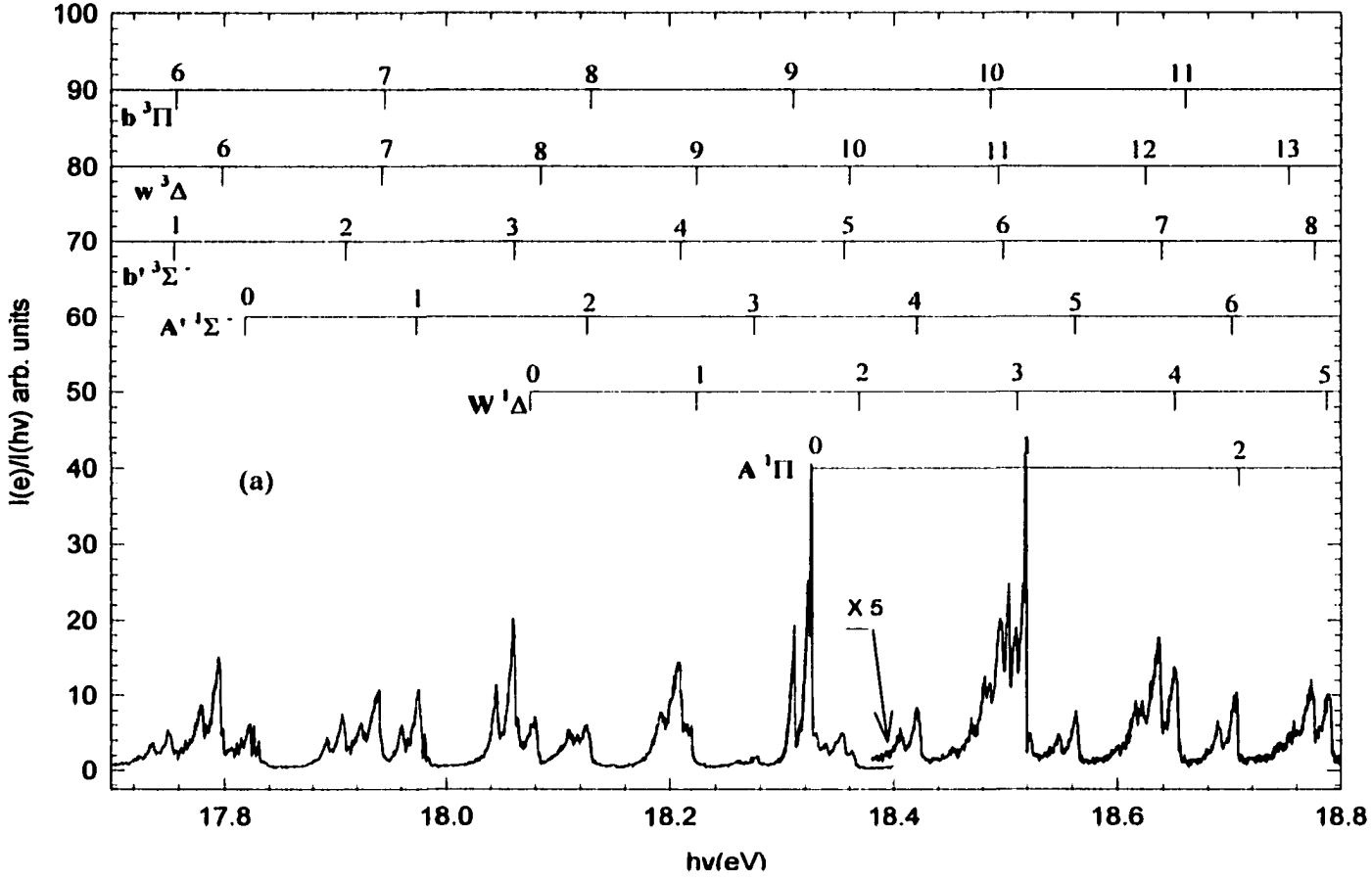

Figure 6-1 PFI-PE spectrum of NO in the range (a) 17.70–18.80 and (b) 18.58-20.10 eV showing the relative intensities for the $NO^+(A'^1\Sigma^-, v^+=0\text{-}17)$ states. Also marked in the figure are vibrational states for the $NO^+(b\,^3\Pi, w\,^3\Delta, b'\,^3\Sigma^-, W\,^1\Delta$, and $A\,^1\Pi$) states.

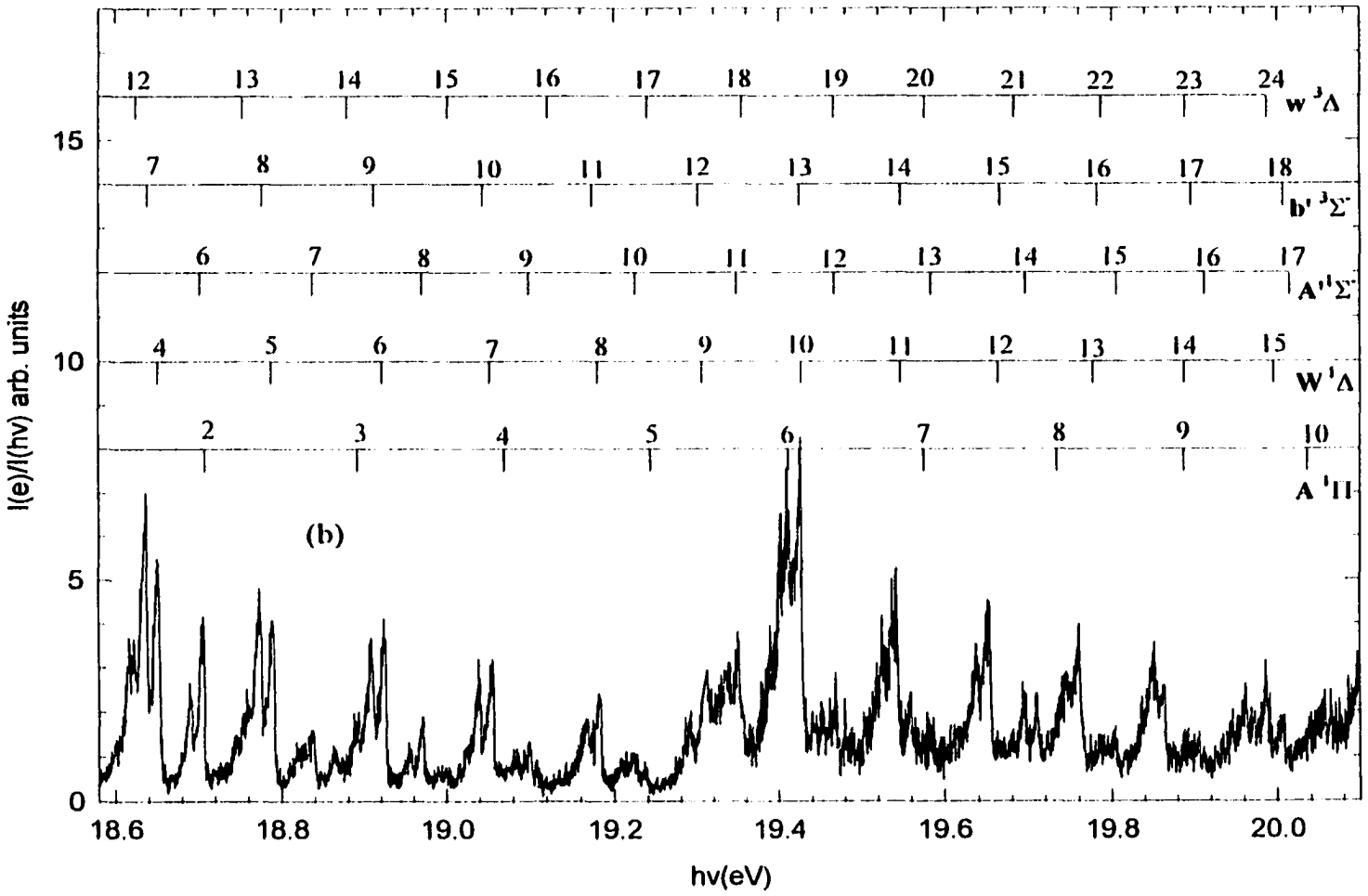

Figure 6-1 (Continued)

$v^+ = 6$) band is dominated by transitions of the $NO^+(A^1\Pi, v^+ = 2)$ band. Despite these overlaps, the spectroscopic constants for $NO^+(A'^1\Sigma^-, v^+ = 2)$ and $NO^+(A'^1\Sigma^-, v^+ = 6)$ have been derived unambiguously by simulation (not shown here) that includes the overlapping bands for $NO^+(b^3\Pi, v^+=8)$ and $NO^+(A^1\Pi, v^+ = 2)$, respectively. Due to the more serious overlapping problem and weaker band intensities for higher vibrational levels of $NO^+(A'^1\Sigma^-)$, we have not been able to identify vibrational PFI-PE bands for $NO^+(A'^1\Sigma^-, v^+>17)$.

We compare in Table 6-1 the relative peak intensities for $NO^+(A'^1\Sigma^-, v^+ = 0\text{-}17)$ PFI-PE vibrational bands with FCFs for direct photoionization[24] and relative intensities for $NO^+(A'^1\Sigma^-, v^+ = 0\text{-}7)$ observed in the HeI measurement.[4] For the convenience of comparison, the intensity for the $NO^+(A'^1\Sigma^-, v^+= 4)$ band is arbitrarily normalized to 100. The FCFs for $NO^+(A'^1\Sigma^-, v^+ = 0\text{-}7)$ have the maximum at $v^+=3$ instead of that at the $v^+=4$ band observed in the previous HeI study. Other than this, the general trend for the FCFs and HeI band intensities are in agreement, indicating that perturbative autoionizating mechanisms have not played a significant role in the HeI spectra. The relative intensities of PFI-PE bands for $NO^+(A'^1\Sigma^-, v^+=2$ and 6) given in Table 6-I have been corrected for contributions from overlapping bands based on spectral simulation. Since the intensities for $NO^+(A'^1\Sigma^-, v^+=12\text{-}17)$ bands are significantly weaker than those for $NO^+(A'^1\Sigma^-, v^+=0\text{-}11)$, the relative intensities for $NO^+(A'^1\Sigma^-, v^+ = 12\text{-}17)$ PFI-PE bands should be considered as rough estimates.

In general, the PFI-PE band intensity for $NO^+(A'^1\Sigma^-, v^+)$ decreases as a function of v^+, with local maxima at $v^+= 1$ and 8. The observation of local maxima is indicative of the involvement of perturbative autoionizing mechanisms. The relative intensities for the $NO^+(A'^1\Sigma^-, v^+=2\text{-}7)$ PFI-PE bands are roughly consistent with those obtained in Ref. 4. However, the global maximum for the PFI-PE bands resides on $NO^+(A'^1\Sigma^-, v^+=1)$ instead of $NO^+(A'^1\Sigma^-, v^+=4)$ as observed by Edquivst *et al.*[4] In addition, the relative intensities of $NO^+(A'^1\Sigma^-, v^+=0$ and 1) observed in this study are significantly greater than those in the HeI study[4] and the FCFs.[24] indicating that resonant intensity enhancement mechanisms are

Table 6-I. Spectroscopic constants for NO^+ ($A'^1\Sigma^-$, v^+=0-17)

	IE (eV)			Bv $(cm)^{-1}$		Relative Intensity		
v^+	PFI-PE [a,b]	Ref. 4	Ref. 11[c]	PFI-PE[a,b]	Ref. 11[c]	PFI-PE[a,d]	Ref. 4[d]	FCF[f]
0	17.8211 (17.8214)	17.820	17.819	1.340 (10) (1.347)	1.354	186	13	24 (0.038)
1	17.9765 (17.9762)	17.966	17.974	1.325(10) (1.329)	1.335	286	60	65 (0.104)
2	18.1277 (18.1280)	18.119	18.126	1.315(20) (1.311)	1.317	100	87	99 (0.157)
3	18.2765 (18.2767)	18.267	18.275	1.295(10) (1.292)	1.299	96	93	110 (0.174)
4	18.4226 (18.4223)	18.417	18.421	1.275(10) (1.273)	1.280	100	100	100 (0.158)
5	18.5648 (18.5647)	18.558	18.563	1.255(10) (1.253)	1.262	86	73	79 (0.125)
6	18.7040 (18.7039)	18.695	18.702	1.225(20) (1.234)	1.243	67[e]	53	57 (0.090)
7	18.8395 (18.8399)	18.837	18.838	1.215(5) (1.214)	1.225	64	40	38 (0.060)
8	18.9721 (18.9725)	----------	18.970	1.190(20) (1.193)	1.207	86	--------	--------
9	19.1025 (19.1018)	----------	19.099	1.170(5) (1.173)	1.188	31	--------	--------
10	19.2279 (19.2276)	----------	19.225	1.150(20) (1.152)	1.170	29	--------	--------
11	19.3497 (19.3500)	----------	19.348	1.130(10) (1.131)	1.151	19	--------	--------
12	19.4686 (19.4688)	----------	19.467	1.110(30) (1.109)	1.133	6	--------	--------
13	19.5839 (19.5840)	----------	19.584	1.090(30) (1.087)	1.115	4	--------	--------
14	19.6955 (19.6956)	----------	19.696	1.060(30) (1.065)	1.096	7	--------	--------
15	19.8040 (19.8034)	----------	19.806	1.040(30) (1.042)	1.078	4	--------	--------
16	19.9069 (19.9075)	----------	19.912	1.020(30) (1.019)	1.059	4	--------	--------
17	20.0080 (20.0078)	----------	20.015	1.000(30) (0.996)	1.041	5	--------	--------

Table 6-I (Continued)

a) This work. Estimated uncertainties are $\pm$0.0005 eV for IE and Δv values. The uncertainties for B_{v+} values are given beside each value in the parenthesis. There are uncertainties of $\pm$10% for the relative PFI-PE intensities of v^+=0-11 and $\pm$20% for those of v^+=12-17.

b) The best-fitted values calculated using the Dunham coefficients (see Table III) are given in parentheses.

c) Values calculated using Dunham coefficients of Ref. 11.

d) The PFI-PE (HeI) intensity at v^+=4 is arbitrarily normalized to 100.

e) Due to the domination of the intensity of $NO^+(A^1\Pi, v^+ = 2)$, the intensity of $NO^+(A'^1\Sigma^-)$, v^+ =6 is estimated based on simulation.

f) Reference 24. The values are normalized to 100 with respect to v^+=4 and original values are listed in the parenthesis underneath.

strongly operative for the $NO^+(A'^1\Sigma^-, v^+ = 0$ and 1) PFI-PE bands. Since the mechanisms for the formation of $NO^+(A'^1\Sigma^-, v^+)$ in HeI and PFI-PE measurements are different, we expect that the relative vibrational band intensities observed in HeI ionization are different from those in PFI-PE detection. The intensities for the PFI-PE bands of $NO^+(A'^1\Sigma^-, v^+=0$-17) are most likely mediated by near-resonance autoionizing Rydberg states and/or repulsive neutral states.[25,26]

B. Simulation of rotational transition intensities

. We have selected to show the rotationally resolved PFI-PE bands for $NO^+(A'^1\Sigma^-$, $v^+ = 0, 1, 4, 9$-11) in Figs. 6-2(a)~6-2(f) (upper spectra, open circles), respectively. These spectra are normalized to reflect their relative observed intensities in the ordinate. The prominent peaks resolved in the PFI-PE bands are mostly due to the rotational branch heads (or the turn around rotational transitions of rotational branches). All rotational branches are found to shade to the red with the branch heads appearing on the high-energy side. Since the appearance of other vibrational PFI-PE bands are similar to those shown in Figs. 6-2(a)~6-2(f), they are not shown here.

The rotational levels for $NO(X^2\Pi_{1/2,3/2})$ and $NO^+(A'^1\Sigma^-)$ are labeled by the total angular momentum quantum numbers J" and J^+, respectively. The J" value for the NO $(X^2\Pi_{1/2})$ [NO $(^2\Pi_{3/2})$] state is equal to N" + ½ [N" + 3/2], where N" is the rotational quantum number for NO. For $NO^+(A'^1\Sigma^-)$, J^+ is identical to the rotational quantum number N^+. Thus, for transitions originating from NO $(X^2\Pi_{1/2})$ [NO $(^2\Pi_{3/2})$], $\Delta N = N^+ - N'' = \Delta J$ +1/2 [ΔJ + 3/2]. Each rotational level in NO $(X^2\Pi)$ is split into the +/- parity levels. Since this small Λ-doubling is not resolved in the present experiment, individual J" levels can be viewed as being doubly degenerate. As a result, transitions form a J" level to all J^+ levels are allowed.

The relative intensities for rotational structures observed in individual vibrational bands for $NO^+(A'^1\Sigma^-, v^+ = 0$-17) were simulated using the BOS model[12] as described in detail previously.[9,10] Briefly, the model separates the rotational line strengths $\sigma(N^+ \leftarrow J'')$ into two factors C_k and Q according to the equation,[12]

Figure 6-2 Comparison of experimental (○) and simulated (●) PFI-PE spectra for $NO^+(A'^1\Sigma^-)$: (a) $v^+ = 0$, (b) $v^+=1$, (c) $v^+=4$, (d) $v^+=9$ (e) $v^+=10$, and (f) $v^+=11$,. All spectra were measured at a nominal wavelength resolution of 0.035 Å (FWHM). The positions of the rotational transitions for $NO(X^2\Pi_{1/2}) \rightarrow NO^+(A'^1\Sigma^-)$ and $NO(X^2\Pi_{3/2}) \rightarrow NO^+(A'^1\Sigma^-)$ are also shown as down-pointing and up-pointing lines, respectively. In each ΔJ case shown, the positions of the first and second transitions (e.g. $J^+ = 0 - J'' = 1/2$ and $J^+ = 1 - J'' = 3/2$ for $\Delta J = -1/2$) are indicated by progressively shorter lines.

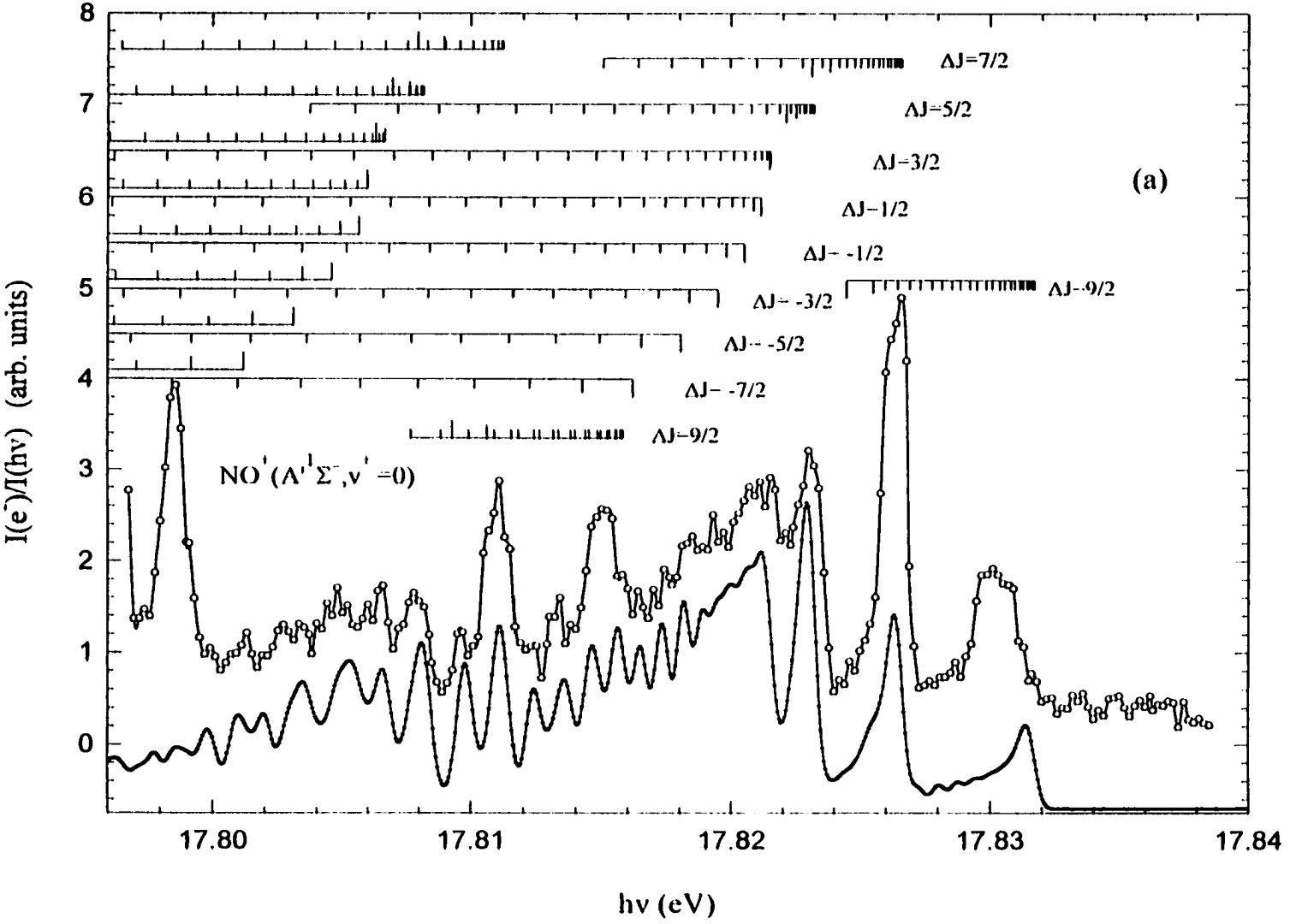
ΔJ=7/2
ΔJ=5/2
ΔJ=3/2
(a)
ΔJ=1/2
ΔJ= -1/2
ΔJ= -3/2
ΔJ=9/2
ΔJ= -5/2
ΔJ= -7/2
ΔJ=9/2
NO⁺(A'¹Σ⁻,v⁺=0)
I(e⁻)/I(hν) (arb. units)
hν (eV)
0
1
2
3
4
5
6
7
8
17.80
17.81
17.82
17.83
17.84

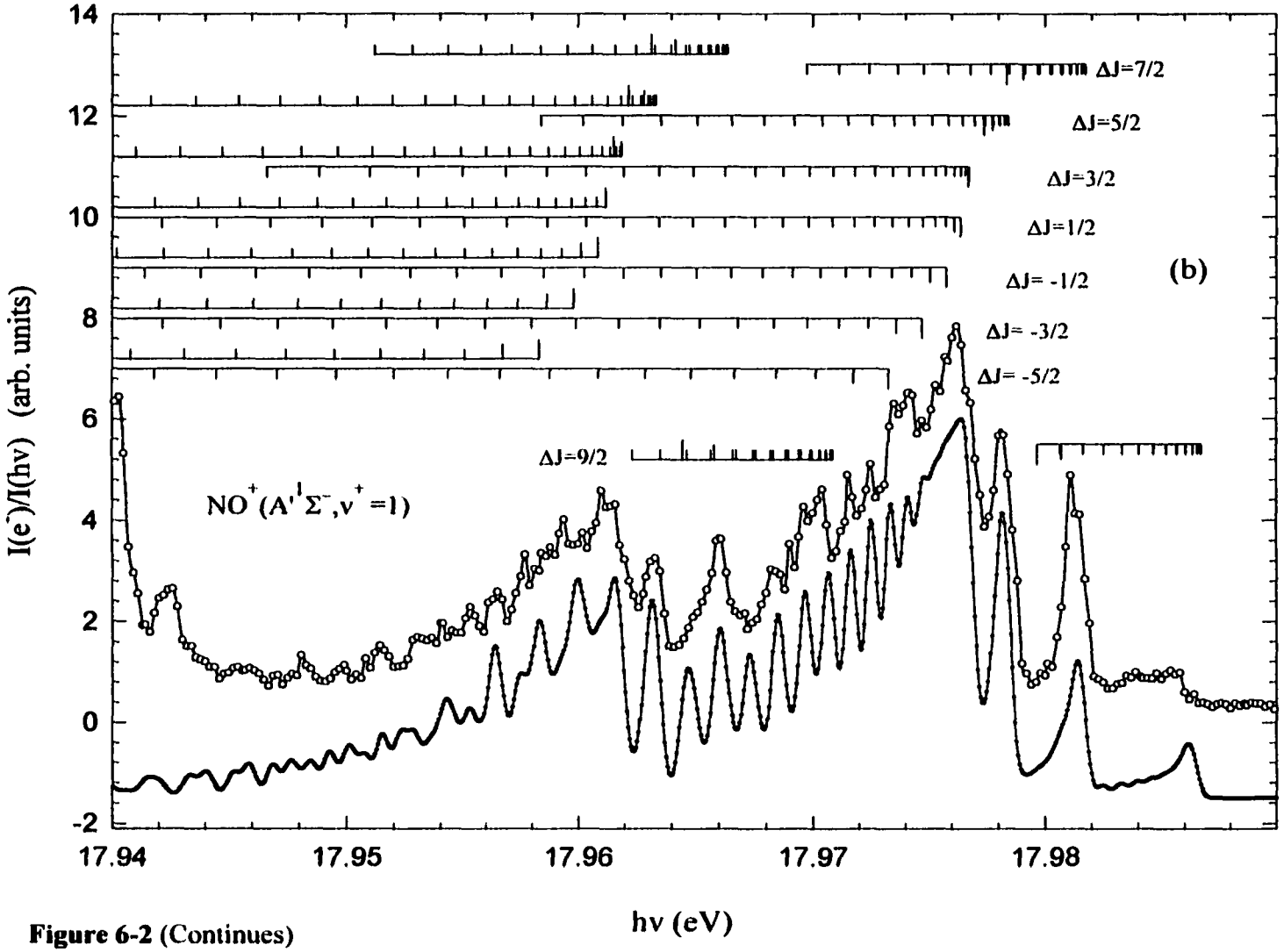

Figure 6-2 (Continues)

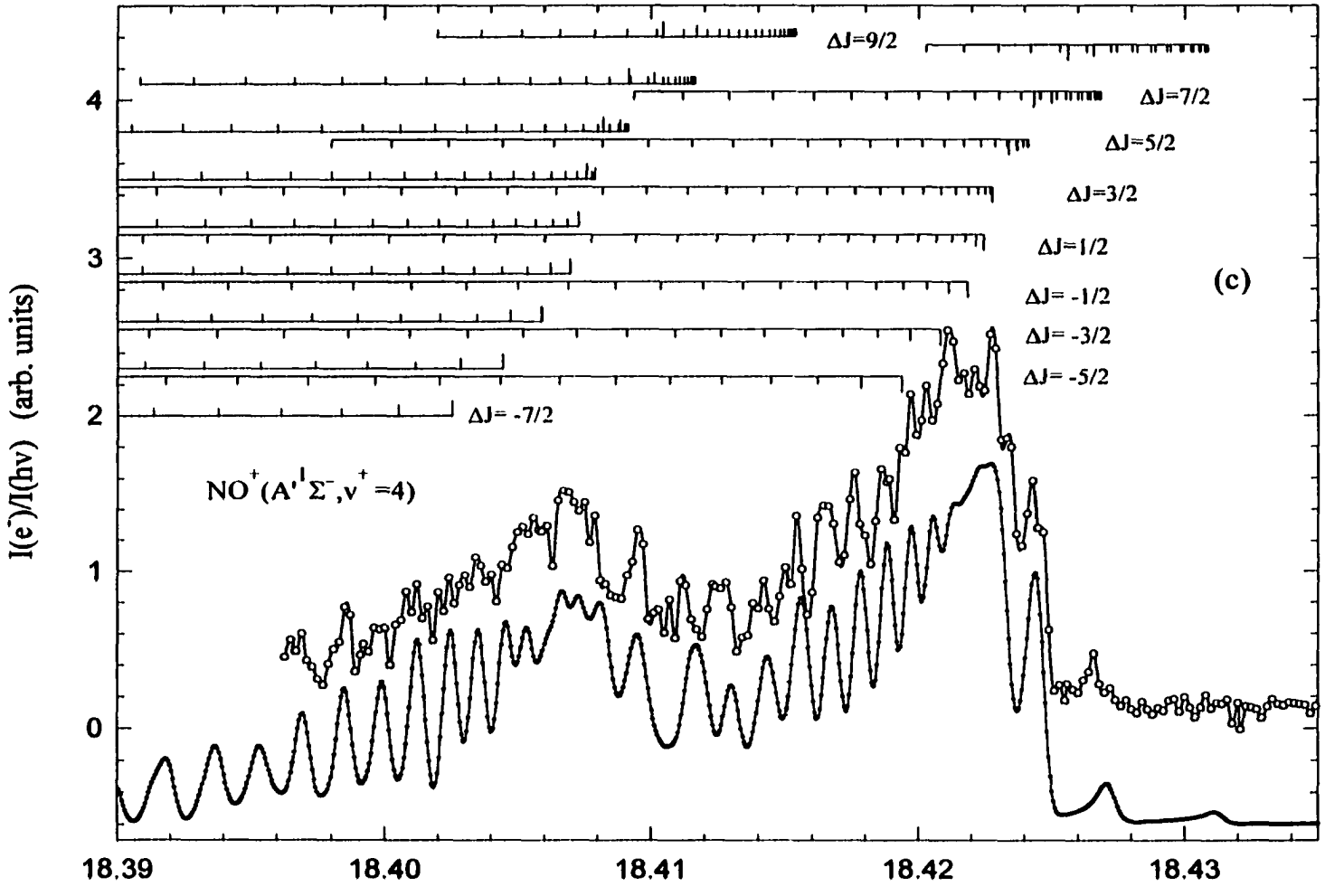

Figure 6-2 (Continues)

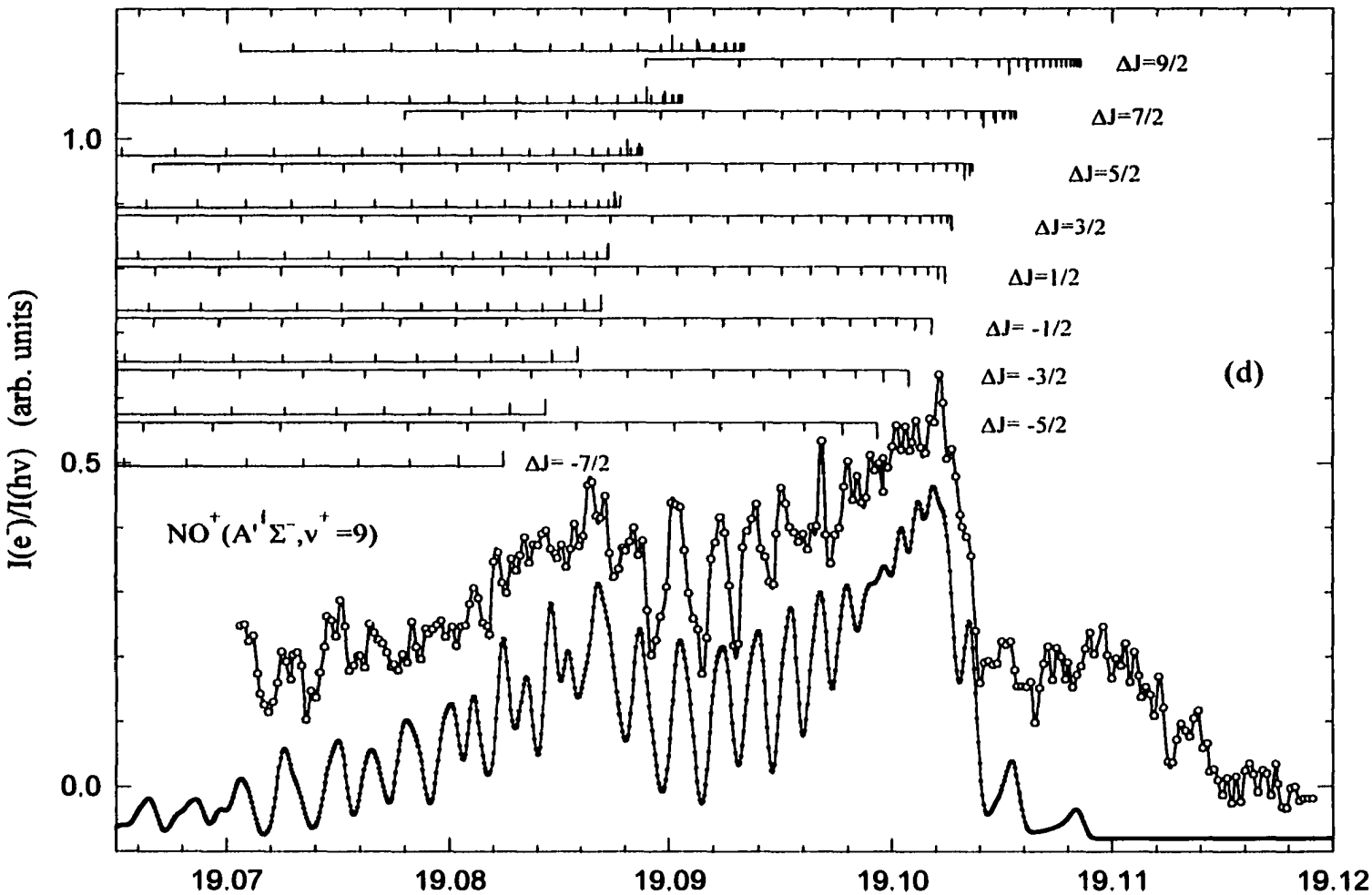

Figure 6-2 (Continues)

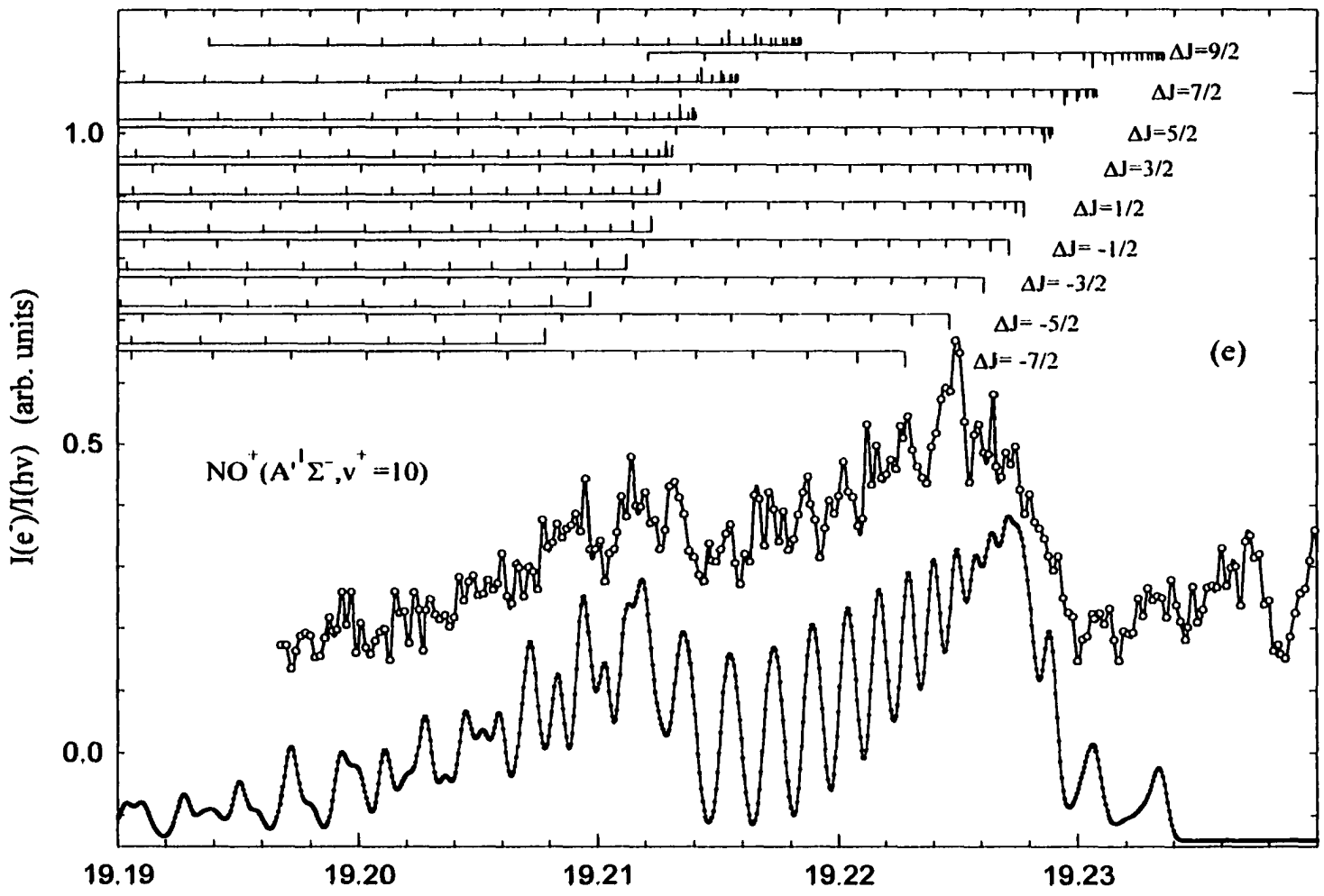

Figure 6-2 (Continues)

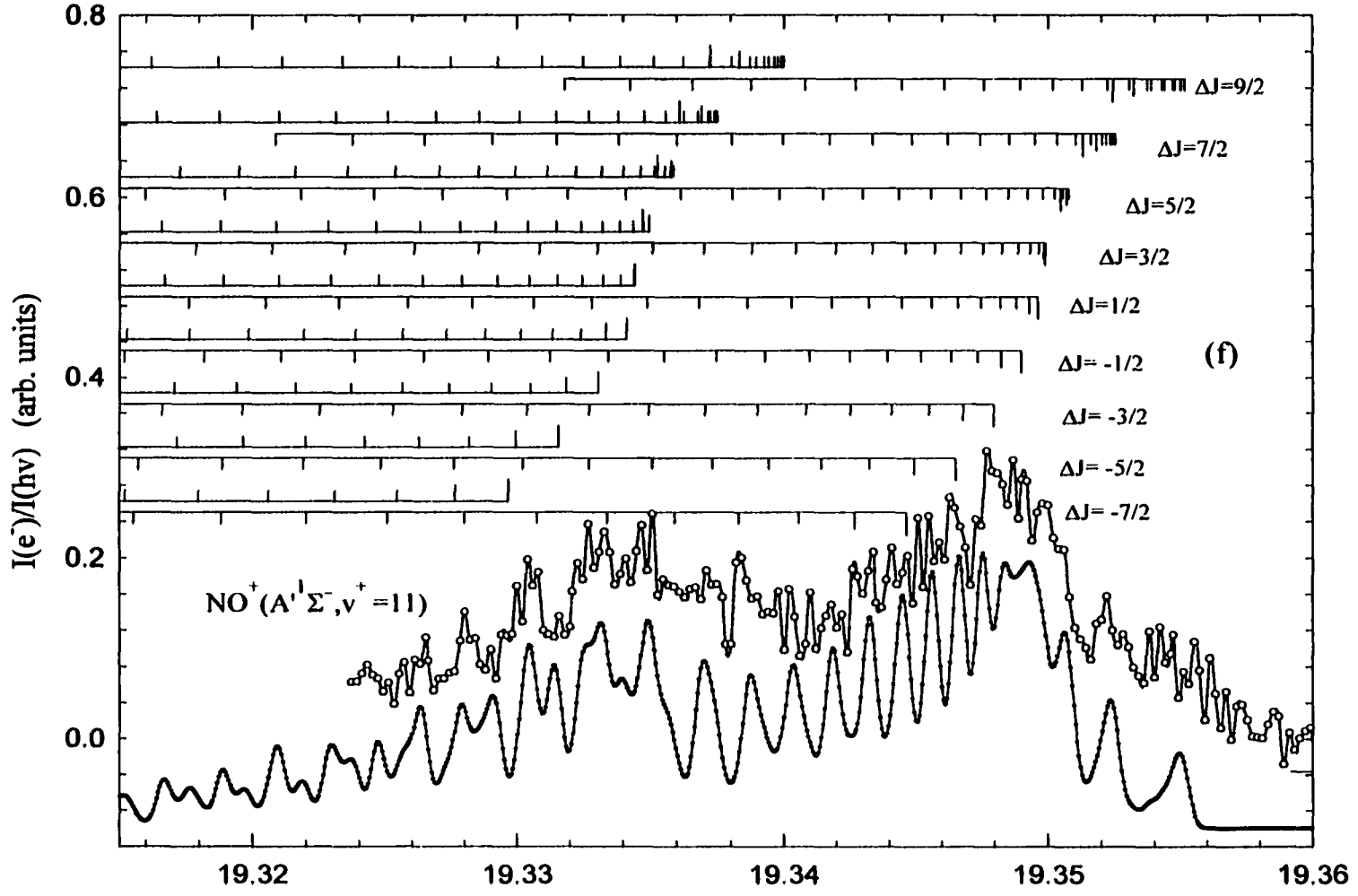

Figure 6-2 (Continues)

$$\sigma(N^{-} \leftarrow J^{-}) \propto \sum_{\lambda} Q(\lambda; J'', N^{-}) C_{\lambda} . \qquad (1)$$

The BOS coefficient C_λ is associated with the electronic transition moments, which is the linear combination of electron transition amplitudes for the possible orbital angular momenta l of the ejected photoelectron. The factor Q is determined by the standard angular momentum coupling constants (Clebsch Gordon coefficients). The angular momentum coupling constants Q were calculated here by Eq. (2) for a Hund's case (a) to (b) transition.

$$Q(\lambda, J'', N^{-}) = (2N^{-}+1) \sum_{\chi=\lambda-1/2}^{\lambda-1/2} (2\chi+1) \begin{pmatrix} \lambda & S'' & \chi \\ -\Delta\Lambda & \Sigma'' & \Lambda^{-}-\Omega'' \end{pmatrix}^{2} \begin{pmatrix} N^{-} & \chi & J'' \\ -\Lambda^{-} & \Lambda^{-}-\Omega'' & \Omega'' \end{pmatrix}^{2} \qquad (2)$$

Here, $\Delta\Lambda = \Lambda^{-} - \Lambda''$ and $\Omega'' = |\Lambda'' \pm \Sigma''|$, where Λ^{-} is the electronic orbital angular momentum projected on the axis of NO^{-} and Λ'' and Σ'' are the electronic orbital angular momentum and electron spin angular momentum projected on the axis of NO, respectively. The dummy variable χ can take on the value from λ-1/2 to λ+1/2. The value λ can be considered as the orbital angular momentum quantum number of the electron prior to photoexcitation and is related to the orbital angular momentum quantum number of the photoelectron by the relation,

$$|\lambda - 1| \leq l \leq \lambda + 1 \qquad (3)$$

The simulation uses known spectroscopy constants,[27] ω_e'' = 1904.204 cm^{-1} (1904.040 cm^{-1}), $\omega_e''\chi_e''$ = 14.075 cm^{-1} (14.100 cm^{-1}), B_e'' = 1.67195 cm^{-1} (1.72016 cm^{-1}), and α_e'' =0.0171 cm^{-1} (0.0182 cm^{-1}) for NO ($X^2\Pi_{1/2}$) [NO ($X^2\Pi_{3/2}$)]. Using these constants,

the BOS simulation allows the determination of accurate rotational constants, B_{v^+}, and IEs for the formation of $NO^+(A'^1\Sigma^+, v^+=0\text{-}17, J^+)$ from $NO(X^2\Pi_{1/2,3/2}, v''=0, J'')$.

The simulated spectra (lower spectra, solid dots) are compared to the experimental PFI-PE bands for $NO^+(A'^1\Sigma^+, v^+ = 0, 1, 4, 9\text{-}11)$ in Figs. 6-2(a)~6-2(f), respectively. The rotational temperature used for NO in the simulated spectra was 298 K. The positions of the rotational transitions for ionization transitions $NO^+(A'^1\Sigma^+, v^+, J^+) \leftarrow NO\ (X^2\Pi_{1/2}, v''=0, J'')$ and $NO^+(A'^1\Sigma^+, v^+, J^+) \leftarrow NO\ (X^2\Pi_{3/2}, v''=0, J'')$ are marked as down-pointing and up-pointing lines, respectively, in these figures. Because of the large amount of details in the figures, identifications of the markings with $J^+ \leftarrow J''$ values are not made. For individual ΔJ branches, the positions of the first and second transitions [e.g., $J^+=0 \leftarrow J''=1/2$ and $J^+=1 \leftarrow J''=3/2$ for $\Delta J = -1/2$ associated with transitions from $NO\ (X^2\Pi_{1/2})$] are indicated by progressively shorter lines, thus revealing the origin and direction of the rotational branches.

For the transition between a Π state and a Σ state, $\Delta\Lambda = -1$, the first 3-j symbol of Eq. (2) requires $\lambda \geq 1$, i.e., the C_0 term is zero. On the basis of the triangular condition of Eq. (2) implied by the second 3-j symbol, we have the relation,

$$\left|N^+ - J''\right| \leq \chi \leq N^+ + J''. \tag{4}$$

The combination of Eqs. (3) and (4) and the requirement $\lambda\text{-}1/2 \leq \chi \leq \lambda+1/2$ gives

$$\Delta J = J^+ - J'' = l + 3/2,\ l + 1/2,\ \ldots.,\ -l - 3/2. \tag{5}$$

The $\pm 3/2$ term of Eq. (5) can be thought of the addition of the spin angular momentum ($\pm 1/2$) for the photoelectron and the angular momentum of the photon (± 1).

The rotational structures observed in the ($NO^+(A'^1\Sigma^+, v^+=0\text{-}17$) PFI-PE bands can be accounted for by the BOS coefficients C_λ, $\lambda=1\text{-}4$ (see Table 6-II). Thus, the angular momentum states for the photoelectron [see Eq. (3)] can be $l=0\text{-}5$ and the rotational

Table 6-II. Best-fitted BOS coefficients obtained in the simulation of the PFI-PE bands for $NO^+(A'^1\Sigma^-, v^+ = 0\text{-}17)$. The sum of the C_λ values is normalized to 1.00.

	BOS Coefficients[a]			
v^-	C_1	C_2	C_3	C_4
0	0.40/0.40	0.20/0.20	0.20/0.20	0.20/0.20
1	0.75/0.80	0.00/0.00	0.25/0.20	0.00/0.00
2	0.70/0.60	0.10/0.20	0.10/0.10	0.10/0.10
3	0.70/0.60	0.20/0.15	0.10/0.15	0.00/0.10
4	0.90/0.55	0.05/0.20	0.05/0.15	0.00/0.10
5	0.80/0.60	0.10/0.20	0.10/0.10	0.00/0.10
6	0.80/0.80	0.10/0.10	0.10/0.10	0.00/0.00
7	0.85/0.60	0.10/0.20	0.05/0.10	0.00/0.10
8	0.80/0.60	0.10/0.20	0.10/0.10	0.00/0.10
9	0.80/0.60	0.10/0.20	0.10/0.10	0.00/0.10
10	0.70/0.70	0.10/0.30	0.10/0.00	0.10/0.00
11	0.55/0.60	0.20/0.20	0.15/0.10	0.10/0.10
12	0.60/0.80	0.20/0.10	0.10/0.10	0.10/0.00
13	0.10/0.60	0.30/0.20	0.30/0.10	0.30/0.10
14	0.60/0.80	0.20/0.10	0.10/0.10	0.10/0.00
15	0.70/0.30	0.10/0.30	0.10/0.20	0.10/0.20
16	0.60/0.80	0.20/0.10	0.10/0.10	0.10/0.00
17	0.60/0.60	0.20/0.20	0.10/0.10	0.10/0.10

a) All C_λ values have an uncertainty of ± 0.2. The first and second values for each C_λ, λ=1–4, are the components originated from $NO(X^2\Pi_{1/2})$ and $NO(^2\Pi_{3/2})$, respectively.

branches [see Eq. (5)] contributed to the spectra can be $\Delta J = \pm 1/2, \pm 3/2, \pm 5/2, \pm 7/2, \pm 9/2, \pm 11/2$, and $\pm 13/2$. However, we note that most of the values for C_3 and C_4 are <0.2 and are within the experimental uncertainty. Due to the negligible contribution of $\Delta J = \pm 11/2$ and $\pm 13/2$ in all simulations, these branches are not marked in the rotational assignment. Also in the simulated spectra for v^+=0-17, we found that the intensity for ΔJ = -9/2 branch is negligible and is significantly weaker than that of its counterpart ΔJ = +9/2. Similarly, the intensities for both spin-orbit components of the ΔJ = -7/2 branch for v^+=1, and the Ω=3/2 spin-orbit component of the ΔJ = -7/2 branch for v^+=0, 3-5,7-10 are negligible.

In our previous PFI-PE studies of $NO^+(X^1\Sigma^+)$ and $NO^+(a^3\Sigma^+)$,[9,10] an increase in the angular momentum exchanged between the photoelectron and the ion core was observed as v^+ increases. According to that mechanism, the angular momentum exchange between the outgoing photoelectron and the NO^+ ion core may be considered to result from collisions between the outgoing electron and the NO^+ ion core. The theoretical study shows that the angular momentum coupling between l partial waves is induced by the torques associated with the non-spherical nature of the NO^+ molecular ion core potential, making a photoelectron orbital an admixture of angular momentum components.[28] Since the equilibrium bond distance for NO^+ increases as v^+ is increased, the NO^+ ion core potential is thus more anisotropic at higher v^+ states. The observed intensity enhancement for higher ΔJ values as a function of v^+ may reflect the increase in inelastic cross sections for higher angular momentum transfer in electron-molecular ion core collisions, resulting from the greater bond distances of NO^+ in higher v^+ states. We note that the observation of high ΔJ values ($\Delta J = \pm 11/2$) may also be attributed to a shape-resonance enhancement.[29] Unlike the $NO^+(X^1\Sigma^+)$ and $NO^+(a^3\Sigma^+)$ states, for the $NO^+(A'^1\Sigma^-, v^+)$ state, ΔJ = +9/2 branches are consistently observed for all vibrational branches and $\Delta J = \pm 11/2$ branches have negligible contribution to the overall intensities, indicating that there is a less sensitive correlation between the maximum ΔJ values and the v^+ values or the internuclear distances. We note that while the $NO^+(X^1\Sigma^+)$ and $NO^+(a^3\Sigma^+)$ states converge to the first dissociation limit of $N(^4S^0) + O^+(^4S^0)$, the $NO^+(A'^1\Sigma^-)$ correlates to the second dissociation limit of $N^+(^4P) + O(^3P)$. This difference might play a role in the different v^+-dependencies on the total

angular momentum transfer observed in the photoionization of NO to form $NO^+(A'^1\Sigma^-)$ and $NO^+(X^1\Sigma^-)$ and $NO^+(a^3\Sigma^-)$. The full understanding of the origin of the observed difference requires a rigorous theoretical investigation.

The BOS model is a one-electron model and does not take into account any channel interactions, which necessarily occur in perturbative mechanisms involving near-resonance Rydberg states and/or dissociative neutral states. For this reason, the use of the BOS model here must be considered as empirical in nature. The BOS model requires that the positive and negative ΔJ branches have the same intensity. This requirement was not fulfilled in the present simulation. The deviation from this empirical BOS simulation usually suggests some types of perturbation by near resonance autoionizing states. As shown in Figs. 6-2(d) and 6-2(f), excellent agreement is observed between the simulated and experimental bands for $NO^+(A'^1\Sigma^-, v^+= 9,11)$, indicating that local intensity perturbation for these bands are not important. This is also the case found for the $NO^+(A'^1\Sigma^-, v^+= 3,7,12\text{-}17)$ PFI-PE bands. However, for the $NO^+(A'^1\Sigma^-, v^+=0)$ PFI-PE band [Fig. 6-2(a)], large perturbations are observed near the band heads of $\Delta J = \pm 7/2$ and $\pm 9/2$. Local intensity enhancements are also observed at the branch heads of $\Delta J = \pm 7/2$ for $v^+=1$ [Fig. 6-2(b)], $\Delta J = -3/2$ for $v^+=4$ [Fig. 6-2(c)] and 5, and $\Delta J= -5/2$ for $v^+=8$ and 10 [Fig. 6-2(e)]. These perturbations are most likely caused by the presence of nearby resonance autoionizing states.

The observation of a long vibrational progression for $NO^+(A'^1\Sigma^-)$ with a relatively smooth PFI-PE band intensity profile is also consistent with the direct excitation model.[26] This model invokes an intermediate neutral repulsive state, which has finite couplings to long-lived high-n Rydberg states converging to ionization thresholds of $NO^+(A'^1\Sigma^-, v^+, J^+)$. Due to the repulsive nature of the intermediate neutral state, no pronounced local intensity enhancements are expected in the PFI-PE spectrum. The intensity enhancement due to the nearby resonance autoionizing mechanism[25] is usually significantly greater and more local than the direct[26] excitation mechanism. Both the nearby resonance autoionizing mechanisms and the direct excitation mechanism can be operative in PFI-PE measurements.[9,10]

C. Ionization energies and rotational constants

On the basis of the BOS simulation, accurate IE and B_{v^+} values for the $NO^+(A'^1\Sigma^-, v^+=0\text{-}17)$ vibrational bands have been determined and are listed in Table 6-I. The IE values for $v^+=0\text{-}17$ correspond to energies for ionization transitions $NO^+(A'^1\Sigma^-, v^+=0\text{-}17, J^+=0) \leftarrow NO\ (X^2\Pi_{1/2}, v''=0, J''=1/2)$. The IE values reported by Ref. 4 are listed in the second column of Table 6-1. We note that there is a good agreement between the values from this study and those from Ref. 4 for $v^+=0$ (<2 meV). However, bigger deviations (up to 10.5 meV for $v^+=1$) are found for other vibrational bands. This is likely due to the lower photoelectron energy resolution used in the HeI study.[4] We estimate that the uncertainties of IE values determined here are ±0.5 meV for $v^+=0\text{-}17$. The uncertainties for B_{v^+} values vary from ±0.005 to ±0.02 cm^{-1} for $v^+=0\text{-}11$ and are estimated to be ±0.03 cm^{-1} for $v^+=12\text{-}17$ as given in the parenthesis beside each B_{v^+}. In Fig 6-3, the vibrational spacing ΔG as a function of $v^+ + 1/2$ and the rotational constants B_{v^+} as a function of v^+ for $NO^+(A'^1\Sigma^-, v^+=0\text{-}17)$ are depicted.

Vibrational and rotational constants obtained here were fitted to Eqs. (6) and (7), respectively, to obtain the vibrational and rotational Dunham coefficients (ω_e, $\omega_e\chi_e$, $\omega_e\gamma_e$, and $\omega_e z_e$) and (B_e, α_e, and γ_e).[30]

$$IE(v^+) = T_e + \omega_e (v^+ + \tfrac{1}{2}) - \omega_e\chi_e (v^+ + \tfrac{1}{2})^2 + \omega_e\gamma_e (v^+ + \tfrac{1}{2})^3 - \omega_e z_e (v^+ + \tfrac{1}{2})^4 \quad (6)$$

$$B_{v^+} = B_e - \alpha_e (v^+ + \tfrac{1}{2}) + \gamma_e (v^+ + \tfrac{1}{2})^2 \quad (7)$$

These coefficients determined by a least squares fit are listed in Table 6-III along with those obtained by Albritton *et al.*[11] The IE values for $v^+=0\text{-}17$ calculated using the vibrational Dunham coefficients of Ref. 11 are included in Table 6-I to compare with experimental values determined in this study. The comparison indicates that the IE values for $v^+<15$ calculated based on the Dunham coefficients of Albritton *et al.*[11] are accurate with deviations of ≤ 3.0 meV compared to the experimental IE values determined in the present study. However, for $v^+ = 15\text{-}17$, the disagreements were found to be larger, with

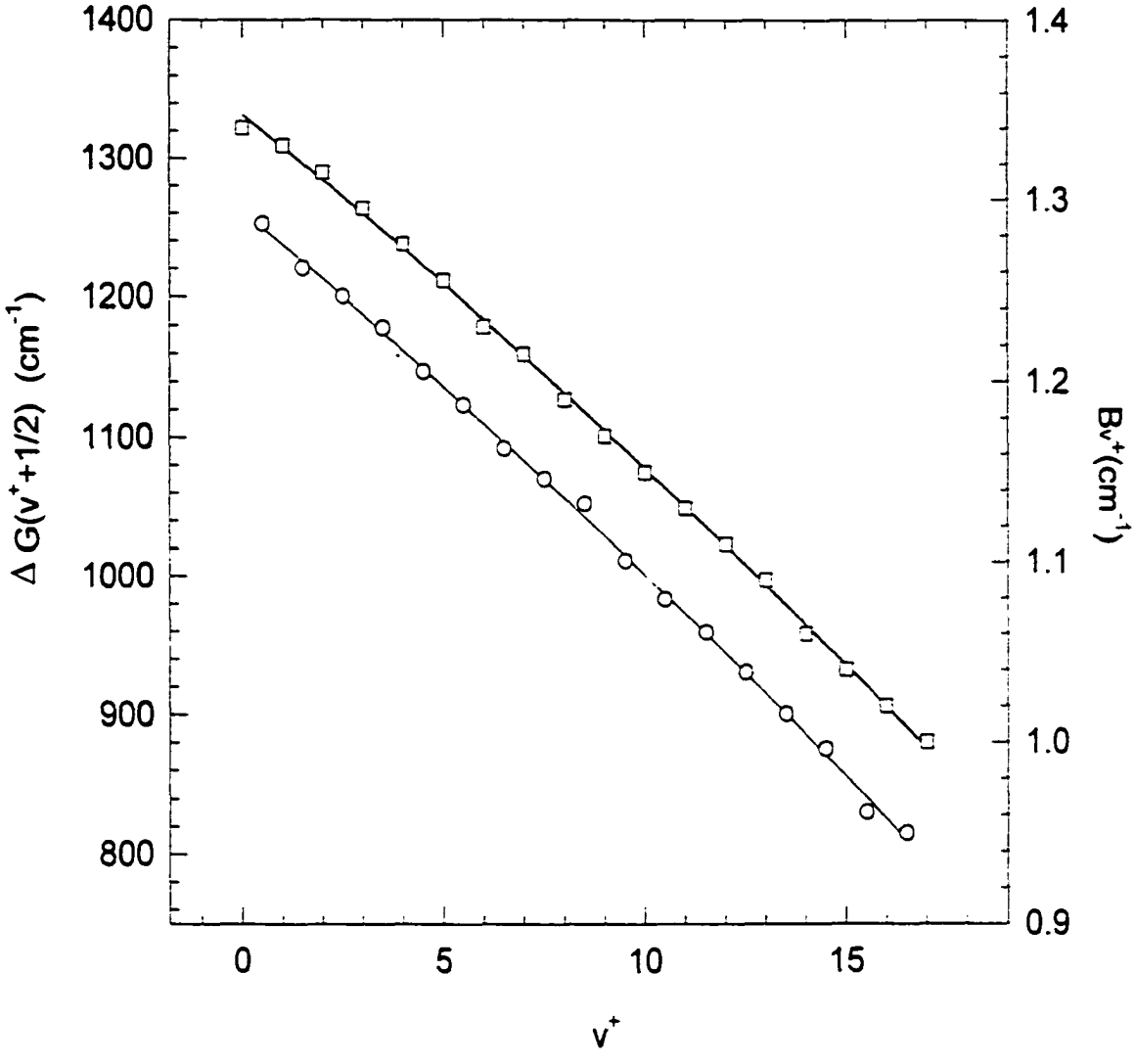

Figure 6-3 Plot of vibrational spacing ΔG (v^-) (open circles, left y-axis) vs. (v^- +1/2) and rotational constants B_{v+}(open squares, right y-axis) vs. v^- for $NO^+(A'^1\Sigma^-, v^+=0\text{-}17)$.

Table III. Comparison of vibrational and rotational constants determined here and in Ref. 11 for $NO^+(A'^1\Sigma^-, v^+=0\text{-}17)$.[a]

Dunham constants	This work (cm^{-1})	Ref. 11 (cm^{-1})
T_e^+	143106.2(3.0)	143080(40)[b]
ω_e^+	1272.03(1.45)	1279.88(2.40)
$\omega_e^+x_e^+$	11.924(0.188)	13.206(0.210)
$\omega_e^+y_e^+$	-0.059(0.007)	----------
B_e^+	1.3562(0.0024)	1.363
α_e^+	0.0178(0.00061)	0.0184
γ_e^+	-1.574×10^{-4} (3.282×10^{-5})	----------

a) The error bars are given in the parentheses.

b) The IE or the T_{00} value of the transition $NO^+(A'^1\Sigma^-, v^+, J^+) \leftarrow NO\ (X^2\Pi_{1/2}, v''=0, J''=1/2)$ is 143717(40) cm^{-1} (see Ref. 11). The T_e^+ value is calculated using T_{00}, ω_e^+, $\omega_e^+x_e^+$, and $\omega_e^+y_e^+$ values by rearranging Eq. (6).

discrepancies in the range of 4-7 meV. The larger deviations observed for IE values of higher v^+ values are to be expected because the vibrational Dunham coefficients of Ref. 11 are based on previous photoelectron data obtained for lower v^+ levels.

The B_{v+} values for $NO^+(A'^1\Sigma^-, v^+=0\text{-}17)$ calculated using the Dunham coefficients obtained by Albritton et al.[11] are also compared to B_{v+} values determined in the present study in Table 6-I. The rotational Dunham coefficients of Ref. 11 are based only on an interpolation technique devised by Field for N_2 and CO to calculate rotational constants from corresponding vibrational data.[24] Taking into account the experimental uncertainties, very good agreement is observed between corresponding B_{v+} values determined here and the calculated values for $v^+=0\text{-}7$ with deviation of about 0.01 cm^{-1}. For $v^+\geq8$, the

calculated B_{v+} values exhibit bigger deviations (0.02-0.04 cm^{-1}) with respect to corresponding experimental values.

We have included in Table 6-I the best fitted IE and B_{v+} values based on the Dunham coefficients (see Table 6-III) determined in the present study. The absolute discrepancies between the corresponding PFI-PE and best-fitted IE values for all v^+ states are <1 meV. The absolute discrepancies between experimental and best-fitted B_{v+} values are <0.01 cm^{-1}.

IV. CONCLUSIONS

We have obtained rotationally resolved photoelectron spectra for NO in the region of 17.70-20.10 eV using monochromatized synchrotron radiation at the Chemical Dynamics Beamline of the ALS. This measurement gives unambiguous identifications of the $NO^+(A'^1\Sigma^-, v^+=0\text{-}17)$ vibrational PFI-PE bands. The rotationally resolved PFI-PE data for these bands have allowed the direct determination of accurate IEs, vibrational constants, and rotational constants for $NO^+(A'^1\Sigma^-, v^+=0\text{-}17)$ for the first time. The BOS model in general provides satisfactory simulation for the experimental PFI-PE bands. Deviations observed between the experimental and BOS simulated intensities for rotational transitions are indicative of local perturbation, possibly by near resonance autoionizing states. Unlike the observation in the previous PFI-PE studies on $NO^+(X^1\Sigma^+)$ and $NO^+(a^3\Sigma^+)$, in which a generally increasing trend for the maximum ΔJ value and intensities of higher rotational ΔJ branches as a function of v^+ was observed, we found that in the case of $NO^+(A'^1\Sigma^-)$, the ΔJ =+9/2 branches are consistently observed with significant intensities for all the vibrational bands. This different behavior might arise from the fact that $NO^+(A'^1\Sigma^-)$ converges to a different dissociation limit than that for $NO^+(X^1\Sigma^+)$ and $NO^+(a^3\Sigma^+)$.

Acknowledgments

This work was supported by the Director, Office of Energy Research, Office of Basic Energy Sciences, Chemical Science Division of the U.S. Department of Energy Under Contract No. W-7405-Eng-82 for the Ames Laboratory and Contract No. DE-

AC03-76SF00098 for the Lawrence Berkeley National Laboratory. C.Y.N. and R.A.D. acknowledge partial support from the AFOSR under task 2303EP02 and Grant No. F49620-99-1-0234 (technical monitor: Dr. Michael R. Berman). Y.S. is the recipient of 1999 Wall Fellowship and 2000 Henry Gilman Fellowship at Iowa State University.

References

1. M. Oppenheimer, A. Dalgarno, E. P. Trebino, L. H. Brace, H. C. Brinton, and J. H. Hoffman, *J. Geophys. Res.* **82**, 191 (1977).
2. D. G. Torr and M. R. Torr, *J. Atmos. Terr. Phys.* **41**, 797 (1979).
3. E. E. Ferguson, in *Kinetics of Ion-Molecule Reactions*, edited by P. Ausloo (Plenum, New York, 1979), p. 377.
4. O. Edquivst, E. Lindholm, L E. Selin, H. Sjogren, L. Asbrink, *Arkiv Fysik* **40**, 439 (1970).
5. K. Müller-Dethlefs, M. Sander, and E. W. Schlag, *Chem. Phys. Lett.* **112**, 291 (1984).
6. M. Sander, L. A. Chewter, K. Müller-Dethlefs, and E. W. Schlag, *Phys. Rev.* A**36**, 4543 (1987); G. Reiser, W. Habenicht, K. Müller-Dethlefs, and E. W. Schlag, *Chem. Phys. Lett.* **119**, 152 (1988).
7. A. Strobel, I. Fischer, J. Staecker, G. Niedner-Schatteburg, K. Müller-Dethlefs, and V. E. Bondybey, *J. Chem. Phys.* **97**, 2332 (1992).
8. R. T. Weidmann, M. T. White, K. Wang and V, McKoy, *J. Chem. Phys.* **98**, 7673 (1993)
9. G. K. Jarvis, M. Evans, C. Y. Ng, and K. Mitsuke, *J. Chem. Phys.* **111**, 3058, (1999).
10. G. K. Jarvis, Y. Song, and C. Y. Ng, *J. Chem. Phys.*, **111**, 1937, (1999).
11. D. L. Albritton, A. L. Schmeltekopf and R. N. Zare, *J. Chem. Phys.* **71**, 3271 (1979).
12. A. D Buckingham, B. J. Orr, J. M. Sichel, *Phil. Trans. Roy. Soc. Lond. A*, **268**, 147 (1970).

13. Y. Song, M. Evans, C. Y. Ng, C.-W. Hsu, and G. K. Jarvis, *J. Chem. Phys.*, **111**, 1905(1999)

14. D. Fedorov, M. Evans, Y. Song, M. Gordon, and C. Y. Ng, *J. Chem. Phys.* 111, 6413 (1999).

15. M. Evans and C. Y. Ng, *J. Chem. Phys.* **111**, 8879-8892 (1999).

16. Y. Song, M. Evans, C. Y. Ng, C.-W. Hsu, and G. K. Jarvis, *J. Chem. Phys.* **112**, 1306 (2000).

17. Y. Song, M. Evans, C. Y. Ng, C.-W. Hsu, and G. K. Jarvis, *J. Chem. Phys.* **112**, 1271 (2000).

18. K. Okada and S. Iwata, J. Chem. Phys. **112**, 1804 (2000).

19. S. Iwata, private communication.

20. C. Y. Ng, in "Photoionization, and Photodetachment", edited by C. Y. Ng (World Scientific, Singapore, 2000), *Adv. Ser Phys. Chem.* **10A**, Chapter 9, p.394-538.

21. C.-W. Hsu, M. Evans, P. A. Heinmann, and C. Y. Ng, *Rev. Sci. Instrum.*, **68**, 1694 (1997).

22. G. K. Jarvis, Y. Song, and C. Y. Ng, *Rev. Sci. Instrum.* **70**, 2615 (1999).

23. R. B. Cairns and J. A. R. Samson, *J. Opt. Soc. Am.* **56**, 1568 (1966).

24. R. W. Field, *J. Mol. Spectrosc.* **47**, 194 (1973).

25. T. Baer and P.-M. Guyon, in "High Resolution Laser Photoionization and Photoelectron Studies", edited by I. Powis, T. Baer, and C. Y. Ng, *Wiley Series in Ion Chem. And Phys.* (Wiley, Chichester, 1995), Chap. 1, p. 1.

26. W. Kong and J. W. Hepburn, *Can. J. Phys.* **72**, 1284 (1994).

27. K. P. Huber and G. Herzberg, "Molecular Spectra and Molecular Structure, Vol. IV, Constants of Diatomic Molecules" (Van Nostrand, New York, 1979).

28. R. T. Weidmann, M. T. White, K. Wang and V, McKoy, *J. Chem. Phys.* **98**, 7673 (1993).

29. R. G. Tonkyn, J. W. Winniczek, and M. G. White, *Chem. Phys. Lett.* **164**, 137 (1989); M. Braunstein, V. McKoy, S. N. Dixit, R. G. Tonkyn, and M. G. White, *J. Chem. Phys.* **93**, 5345 (1990).

30. G. Herzberg, in Ref. 27.

PART II

ENERGY-SELECTED PHOTOELECTRON-PHOTOION COINCIDENCE STUDY OF NH_3, CH_3Br, CH_3I and CD_4

CHAPTER 7. HIGH RESOLUTION PULSED FIELD IONIZATION PHOTOELECTRON-PHOTOION COINCIDENCE SPECTROSCOPY USING SYNCHROTRON RADIATION

A paper published in *Review of Scientific Instruments*, **70**, 3892 (1999)

G.K Jarvis, Karl-Michael Weitzel, Marcus Malow, Tomas Baer,

Y. Song and C.Y. Ng

Abstract:

We have developed a sensitive and generally applicable scheme for performing pulsed field ionization (PFI) photoelectron (PFI-PE)-photoion coincidence (PFI-PEPICO) spectroscopy using two-bunch and multibunch synchrotron radiation at the Advanced Light Source. We show that this technique provides an ion internal state (or energy) selection limited only by the PFI-PE measurement. Employing a shaped pulse for PFI and ion extraction, a resolution of 0.6 meV (FWHM) is observed in the PFI-PEPICO bands for $Ar^+(^2P_{3/2,1/2})$. As demonstrated in the PFI-PEPICO study of the process. $O_2 + h\nu \rightarrow O_2^+(b^4\Sigma_g^-, v^+=4, N^+) + e^- \rightarrow O^+(^4S) + O(^3P) + e^-$, the dissociation of $O_2^+(b^4\Sigma_g^-, v^+=4)$ in specific rotational N^+ levels can be examined. The simulation of the experimental breakdown diagram for this reaction supports the conclusion that the threshold for the formation of $O^+(^4S) + O(^3P)$ from $O_2^+(b^4\Sigma_g^-, v^+=4)$ lies at $N^+=9$. We have also recorded the PFI-PEPICO time-of-flight (TOF) spectra of O^+ formed in the dissociation of $O_2^+(b^4\Sigma_g^-, v^+=4\text{-}7)$. The simulation of these O^+ TOF spectra indicates that the PFI-PEPICO method is applicable for the determination of kinetic energy releases. Previous PFI-PE studies on O_2 suggest that a high-n O_2 Rydberg state [$O_2^*(n)$] with a dissociative ion core undergoes prompt dissociation to yield a high-n' O-atom Rydberg state [O*(n')] [Hsu et al., *J. Chem. Phys.* **110**, 315 (1999)]. The subsequent PFI of O*(n') accounts for the formation of a PFI-PE and O^+. Since the PFI-PE intensities for O^+ and O_2^+ depend on the lifetimes of O*(n') and $O_2^*(n)$, respectively, the PFI-PE intensity enhancement observed for rotational transitions to $O_2^+(b^4\Sigma_g^-, v^+=4, N^+\geq 9)$ can be attributed to the longer lifetimes for O*(n')

than those for $O_2^*(n)$. The PFI-PEPICO study of the dissociation of CH_3^+ from CH_4 also reveals the lifetime effects and dc field effects on the observed intensities for CH_3^+ and CH_4^+. The high-resolution for PFI-PEPICO measurements, along with the ability to distinguish the CH_3^+ fragments due to the supersonically cooled CH_4 beam from those formed by the thermal CH_4 sample, has allowed the determination of a highly accurate dissociation threshold for CH_3^+ from CH_4.

I. INTRODUCTION

The study of single-photon ionization processes using mass spectrometric and photoelectron spectroscopic techniques has played an important role in providing accurate thermochemical and spectroscopic data for atomic and molecular cations.[1-5] Through appropriate energetic cycles, accurate thermochemical data for neutral species can also be obtained.[1,2] Photoelectron-photoion coincidence (PEPICO) experiments concern the detection of correlated photoelectron-photoion pairs.[6] Because of the high collection efficiency of near zero kinetic energy or threshold photoelectrons (TPEs),[7-10] the TPE detection scheme has been the preferred photoelectron spectroscopic method in the past when a tunable vacuum ultraviolet (VUV) source, such as synchrotron radiation, is used as the ionization source.[11] Hence, the coincidence scheme involving the measurement of correlated TPE-photoion pairs [referred to as the TPE-photoion coincidence (TPEPICO) method] has also been a popular technique for the study of energy- or state-selected cations.[12-14] The application of the latter method for unimolecular dissociation studies has been highly successful, providing valuable information about the dissociation threshold, dissociation rate, and kinetic energy release (KER) of fragments from parent molecular cations prepared at a well defined internal energy or state.[12-24] Plots of the percentage abundances of reactant and product ions as a function of the parent ion internal energy (i.e., breakdown diagram) is a common method used to determine thresholds for ionic dissociation processes, from which heats of formation of fragment species can be derived.[25] The TPEPICO technique has also been successfully employed for the TPE spectroscopic measurement of a neutral cluster or a specific radical prepared in cluster or radical sources containing other impurities.[26-34] The extension of the TPEPICO technique

for the detection of correlated TPEs and secondary ions formed in a collisional process, now known by the acronym of TPESICO, has been demonstrated as a powerful method for the study of state- or energy-selected ion-molecule reactions.[35-39]

The resolution and performance for all these coincidence schemes involving the TPE detection were partly limited by the hot-tail problem associated with the TPE transmission function. Recent synchrotron based studies have shown that the hot-electron problem associated with conventional TPE measurements can be greatly lessened by employing time-of-flight (TOF) discrimination in a single-bunch or a two-bunch synchrotron operation.[22,23,40] Energy resolutions for TPE measurements have typically been as good as 3-5 meV (full-width-at-half-maximum, FWHM) when electron TOF is coupled with angular discrimination against energetic or hot electrons. In these cases, the TPE resolution has been limited primarily by the monochromator optical resolution and by the incomplete TOF separation of TPEs from hot electrons.

The use of the penetrating field scheme[34,41-43] for TPE measurements has also been demonstrated to greatly reduce the hot-tail problem. We note that using the penetrating field method, along with the TOF discrimination of hot electrons, Morioka and co-workers have achieved a resolution of ≈1 meV (FWHM) for the TPE band of $Xe^+(^2P_{3/2})$, limited only by the obtainable optical resolution of the monochromator.[43] The successful application of the penetration field method for TPEPICO measurements have made possible the measurement of high-resolution TPE spectra for heterogeneous rare gas dimers, achieving resolutions of 2-3 meV.[34] As indicated above, this TOF discrimination method requires a single-bunch or a two-bunch synchrotron operation. At the ALS, the two-bunch mode has a light intensity more than twenty-fold lower than that provided in a multibunch synchrotron operation. We note that by nature of its design, the penetration field technique is not appropriate for accurate KER measurements.

The pulsed field ionization (PFI)-photoelectron (PFI-PE) technique[44-46] has been shown to overcome the hot-tail problem associated with TPE detection and achieve a significantly higher resolution than that of previous TPE measurements. This scheme, originally developed for using low repetition rate laser sources, has been recently demonstrated by Weitzel and Güthe in a PFI-PE study[47] of $Ar^+(^2P_{3/2,1/2})$ using single-bunch

synchrotron radiation, which has a repetition rate 5 to 6 orders of magnitude greater than common laser sources.[44] In the same single-bunch experiment, they have also observed the first PFI-PE-photoion coincidence (PFI-PEPICO) band for $Ar^+(^2P_{1/2})$ despite the use of a relatively poor optical resolution of 3-5 meV (FWHM).[47]

Taking advantage of the high optical resolution made possible by the 6.65 m monochromator at the Chemical Dynamics Beam line of the Advanced Light Source (ALS), we have recently developed a novel scheme for PFI-PE measurements using monchromatized multibunch synchrotron radiation, achieving routinely resolutions of 2-5 cm^{-1} (FWHM).[48-55] Most recently, we have improved the mutlibunch synchrotron based PFI-PE detection scheme using an electron TOF spectrometer, demonstrating a resolution down to 1.0 cm^{-1} (FWHM) at 12.0 eV.[56] The synchrotron radiation source at the ALS has a frequency of 3.04 MHz for the 2-bunch mode and in the range of 386-488 MHz for the multibunch operation and is a pseudo-continuum light source.[57] Hence, it is natural for us to further develop the PFI-PEPICO method, where parent and fragment ions are detected in coincidence with PFI-PEs. Since the ALS and most other synchrotron facilities dedicate only a small fraction of their total beam time to a single or two-bunch operation, the development of a multibunch PFI-PEPICO technique is highly desirable. The multibunch PFI-PEPICO scheme is expected to be far more sensitive because of the higher PFI-PE intensity. As discussed below, the difficulty encountered in perfecting such PFI-PEPICO experiments is similar to that in conventional TPEPICO studies. That is, the condition for good electron resolution (requires a low electric repeller field for electron extraction) is contrary to that for good ion collection efficiency (requires a high electric repeller field for ion extraction).

In this article, we discuss selected results of our recent PFI-PEPICO experiments performed at the ALS. All these PFI-PEPICO experiments take advantage of the 'dark-gap' in the two-bunch and multi-bunch synchrotron radiation operation. The dark gap is the part of the synchrotron ring period where no electron bunches orbit and consequently no light is emitted. The utilization of the dark gap for PFI-PE and PFI-photoion (PFI-PI) productions and extractions is an essential feature for successful PFI-PEPICO measurements.[47,49,56] For the current ALS operation, this dark gap is typically 100-150 ns

at the total period of 656 ns. The methods described here represent the culmination of much experimentation in finding the best possible way to perform PFI-PEPICO measurements. The most successful scheme was first performed whilst the synchrotron was operating in the two-bunch mode whereby two 50 ps bunches of electrons separated by 328 ns make up the synchrotron ring period. The later success in multibunch PFI-PEPICO measurements using a narrower dark gap has made this technique both highly sensitive and readily applicable to the study of any molecular systems.

Results obtained on He, Ne, Ar, H_2, HCl, O_2, and CH_4 are discussed here to illustrate the performance of different PFI-PEPICO schemes. The O_2 experiment shows that breakdown diagrams can be recorded with resolutions as good as 1.0 meV. The PFI-PEPICO TOF spectra for O^+ from O_2 taken at energies corresponding to the formation of $O_2^+(b^4\Sigma_g^-, v^+= 4\text{-}7)$ illustrate that information on KER is preserved in the TOF spectra. By employing a shaped PFI/ion-extraction pulse, we have demonstrated in the measurement of the PFI-PEPICO bands for $Ar^+(^2P_{3/2,1/2})$ that resolutions as good as 0.6 meV (FWHM) can be achieved with excellent collection efficiencies for PFI-PE and PFI-photoion (PFI-PI).

II. EXPERIMENTAL CONSIDERATIONS

The experiments were carried out at the Chemical Dynamics Beamline of the ALS associated with the Lawrence Berkeley National Laboratory.[57] Briefly, this high-resolution VUV photoionization facility consists of a 10-cm period undulator, a gas harmonic filter, a 6.65m off-plane Eagle mounted monochromator, and a multi-purpose photoelectron-photoion spectrometer.[58] All details concerning most of these elements of the Chemical Dynamics Beamline have been described in detail previously and will therefore not be elaborated upon here.

In the experiments performed here, one of two gratings, a 2400 lines/mm grating (dispersion = 0.64 Å/mm) or a 4800 lines /mm (dispersion = 0.32 Å/mm), was used to disperse the first harmonic of the undulator VUV beam with entrance/exit slits sizes in the range of 30-400 μm. The resulting monochromatic VUV beam was then focused into the photoionization/photoexcitation (PI/PEX) center of the photoelectron-photoion apparatus. The photon energy calibration was achieved using the $Ne^+(^2P_{3/2})$, $Ar^+(^2P_{3/2})$, $Kr^+(^2P_{3/2})$, and

$Xe^+(^2P_{3/2})$ PFI-PE recorded under the same experimental conditions before and after each scan. This calibration procedure assumes that the Stark shift for ionization thresholds of the molecule of interest and the rare gases are identical. On the basis of previous experiments, the accuracy of the energy calibration is believed to within ±0.5 meV.[48-55]

Figure 7-1 depicts the schematic diagram of the photoelectron-photoion coincidence spectrometer,[24] showing the lens arrangement for the electron and ion TOF detection. Here, the electrostatic lens E1-E5 and I1-I11 are associated with the electron and ion TOF spectrometers, respectively. The distance between I1 and E1 is 1.15 cm. The mid-point between I1 and E1 defines the PI/PEX center. The apertures of E1 and E4 are 6.35 and 2 mm in diameter, respectively. The electron-flight distance is 6.8 cm, which is determined by the distance between the PI/PEX center and E5. The PFI-PE detection using the electron TOF spectrometer has been described in detail in a recent publication.[56] The aperture for I1 was 10.16 cm in diameter. The ion TOF spectrometer consists of two uniform field acceleration regions and one drift region. The first uniform field region (distance = 4.83 cm) is the region from the PI/PEX center to I8, while the second uniform field region (0.54 cm) is defined by the region from I8 to I9. The field free drift region comprises of the region between I9 and I11 and has a distance of 46.63 cm. Typical voltages in V (associated with the coincidence schemes described in section II.C below) applied to the electron and ion lenses and the drift region are also shown in parentheses Fig. 7-1. Two sets of dual microchannel plates (MCP) were used for electron and ion detection.

The differential pumping arrangements for the photoelectron-photoion apparatus have been described in details previously.[48,49,51,58] In the present experiment, the gas sample was introduced into the PI/PEX center either as an effusive beam or a skimmed supersonic beam. An effusive beam was formed by a metal orifice with a diameter of 0.5 mm at 298 K and a distance of 0.5 cm from the PI/PEX center. A continuous molecular beam was produced by supersonic expansion from a stainless steel nozzle (diameter = 0.127 mm) at a stagnation pressure of 400-600 Torr and a nozzle temperature of 298 K. For most of the beam measurements, a supersonic beam was formed by a two-stage differential pumping arrangement and was skimmed by one circular skimmer before

Figure 7-1 Schematic diagram for the PFI-PEPICO spectrometer. The electron lenses and ion lenses are labeled as E1-E5 and I1-I1I, respectively. The PI/PEX center is defined by the centered between I1 and E1. Electrons and ions are detected using MCP detectors. The ion TOF spectrometer consists of acceleration region I, acceleration region II, and a drift region with the distances of 4.83, 0.54, 46.63 cm, respectively. Typical voltages in V applied to individual lenses using the PFI-PEPICO detection scheme described in section II.C are given in parentheses.

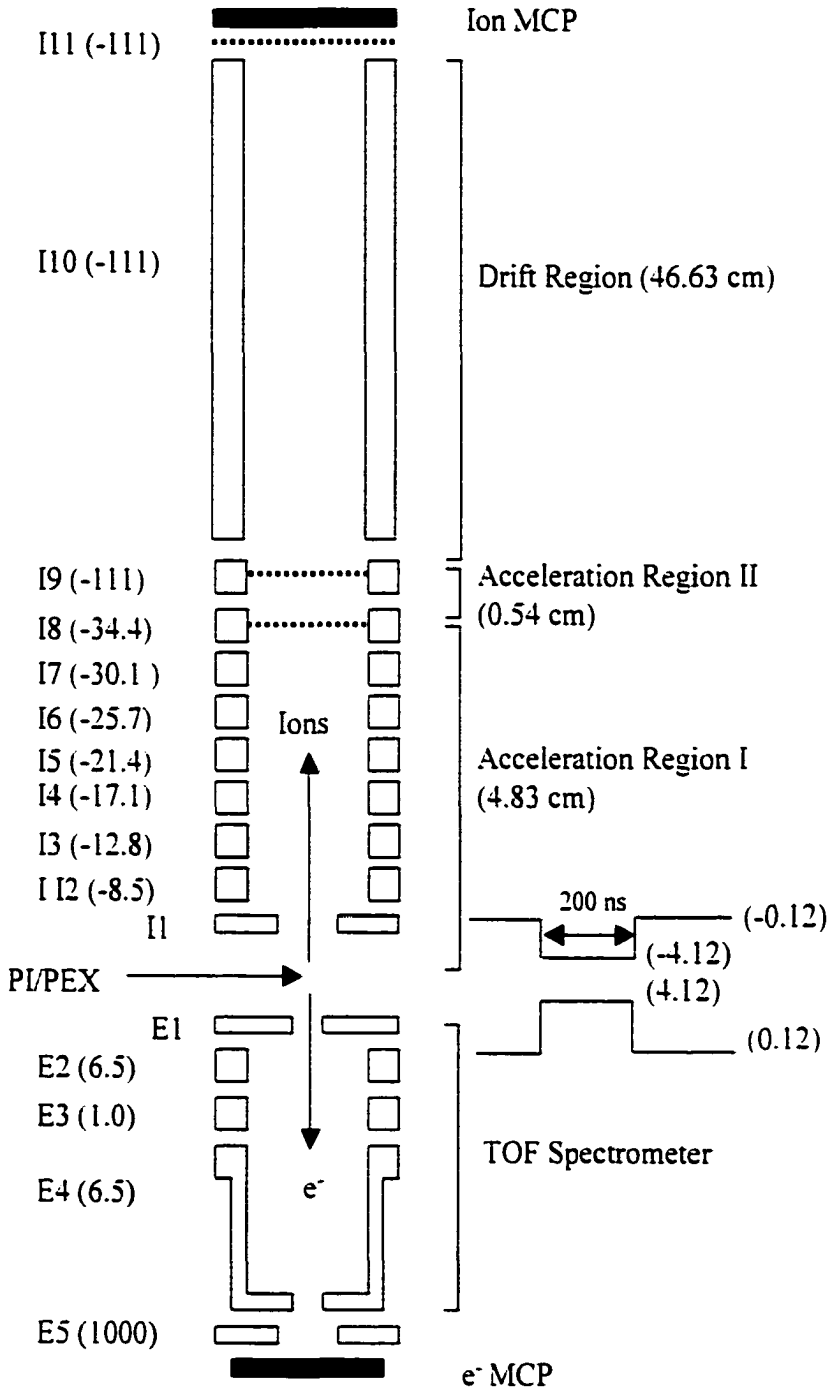
Ion MCP
I11 (-111)
I10 (-111)
Drift Region (46.63 cm)
I9 (-111)
I8 (-34.4)
Acceleration Region II
(0.54 cm)
I7 (-30.1)
I6 (-25.7)
Ions
I5 (-21.4)
I4 (-17.1)
Acceleration Region I
(4.83 cm)
I3 (-12.8)
I I2 (-8.5)
I1
200 ns
(-0.12)
(-4.12)
PI/PEX
(4.12)
E1
(0.12)
E2 (6.5)
E3 (1.0)
TOF Spectrometer
E4 (6.5)
e-
E5 (1000)
e- MCP

intersecting the monochromatized VUV beam 7 cm downstream in the PI/PEX center. A supersonic beam can also be produced in a three-stage differential pumping arrangement, in which it was shaped by two skimmers. In the latter arrangement, the distance between the nozzle and PI/PEX center was ≈11 cm. Unless specified, the beam production system used here involves mostly the doubly differentially pumped arrangement, which provides a higher beam density at the PI/PEX center.

We describe below in chronicle order our experimentation to find a generally applicable PFI-PEPICO scheme. The different modes of PFI-PEPICO schemes differ mostly in the method of ion extraction, i.e., the dc and pulsed electric field applied to I1 and E1. The earlier experiments reveal factors, which are important to the success of later methods. As shown by the performance of these PFI-PEPICO schemes, the ion extraction method described in Section II.C is the most successful.

A. Differential-pulsed ion extraction scheme

In this mode of operation, the repeller plates E1 and I1 were nominally held at ground potential. An electric field pulse (≈1.5 V/cm) for PFI was applied to E1 for 40 ns duration every synchrotron ring period (frequency ≈ 1.52 MHz). The application of this pulsed field was delayed by 40 ns with respect to the beginning of the 112-ns dark gap. This is the same arrangement used for PFI-PE measurements as described by Jarvis et al.[56] Stray electric fields from neighboring lenses push the prompt electrons created by direct photoionization and autoionization towards the electron detector leaving a window for collection of PFI-PEs generated by the PFI. Using this scheme, the PFI-PE detection was made with essentially no interference by prompt background electrons. The TOF for PFI-PEs from the PI/PEX center to the electron detector is ≈50 ns.

The PFI-PE signal pulse was used to trigger the application of an ion extraction field pulse (height = -15 V, width = 4 μs) to I1. We estimate that the delay between the PFI-ion formation and ion extraction is ≈300 ns. The use of a long ion extraction pulse is designed for efficient ion collection. The PFI-PE signal pulse was also used to trigger a multichannel scalar (MCS, Stanford Research System, Model SR430) for recording the PFI-PEPICO TOF spectrum at a preset temporal interval. We note that in all MCS

measurements described here, the MCS ignores other incoming PFI-PEs during this preset MCS interval.

The main draw-back of this technique is that since the ion extraction pulse has a significant overlap with the VUV light bunches, uncorrelated ions formed by photoionization and PFI are also extracted toward the ion detector. These ions which are timed with the ion extraction are expected to give considerable false coincidences. A remedy is to use a double pulse scheme, whereby a second ion extraction pulse with the same height and duration as the first pulse was applied at 10 μs after the first ion extraction. This second ion extraction pulse allows the generation of a background PFI-PEPICO TOF spectrum for false coincidence correction, which can also be recorded in the same MCS scan by setting an appropriate MCS interval. By taking the difference of the spectra due to the first and second ion extraction pulses, a true PFI-PEPICO TOF can thus be obtained. This differential pulsing coincidence detection scheme has been employed in previous TPEPICO studies with good results.[26-29]

We show in Figs 7-2(a) and 7-2(b) the PFI-PEPICO TOF spectra obtained for $Ar^+(^2P_{3/2})$ at 15.7596 eV and $O_2^+(b^4\Sigma_g^-, v^+ = 4, N^+=1)$ at 18.7220 eV,[51] respectively. These spectra were recorded using an effusive beam for introducing the gas sample into the PI/PEX region. The upper and middle spectra of these figures are the PFI-PEPICO TOF spectra resulted from the first and second ion extraction pulses, respectively. The bottom plots (the true coincidence spectra) are obtained by the subtraction of the middle spectra from the corresponding top spectra.

As expected, the false coincidences for $Ar^+(^2P_{3/2})$ were found to be relatively small because prompt ions cannot be formed at the PFI threshold for $Ar^+(^2P_{3/2})$. However, false coincidences for O_2^+ at 18.722 eV, which is well above the IE of O_2, prove problematic. The false coincidences due to the overlap of the ion-extraction pulse and VUV bunch are clearly discernible in Fig. 7-2(b). The O_2^+ peak at 21.8 μs of the middle spectrum of Fig. 7-2(b) results mostly from uncorrelated PFI-PIs due to the application of the second pulse. As shown in the top and middle spectra of Fig. 7-2(b), the uncorrelated prompt ions

Figure 7-2. PFI-PEPICO TOF spectra for (a) $Ar^+(^2P_{3/2})$ at 15.7596 eV and $O_2^+(b^4\Sigma_g^-,\ v^+ = 4,\ N^+=1)$ at 18.7220 eV obtained using an effusive sample beam and the differential-pulsed ion extraction scheme described in section II.A. The second ion extraction pulse was delayed by 10 μs with respect to the first ion extraction pulse. The upper and middle TOF spectra are due to the first and second ion extraction pulses, respectively. The true PFI-PEPICO TOF spectra (bottom spectra) are the difference of the respective upper and middle spectra.

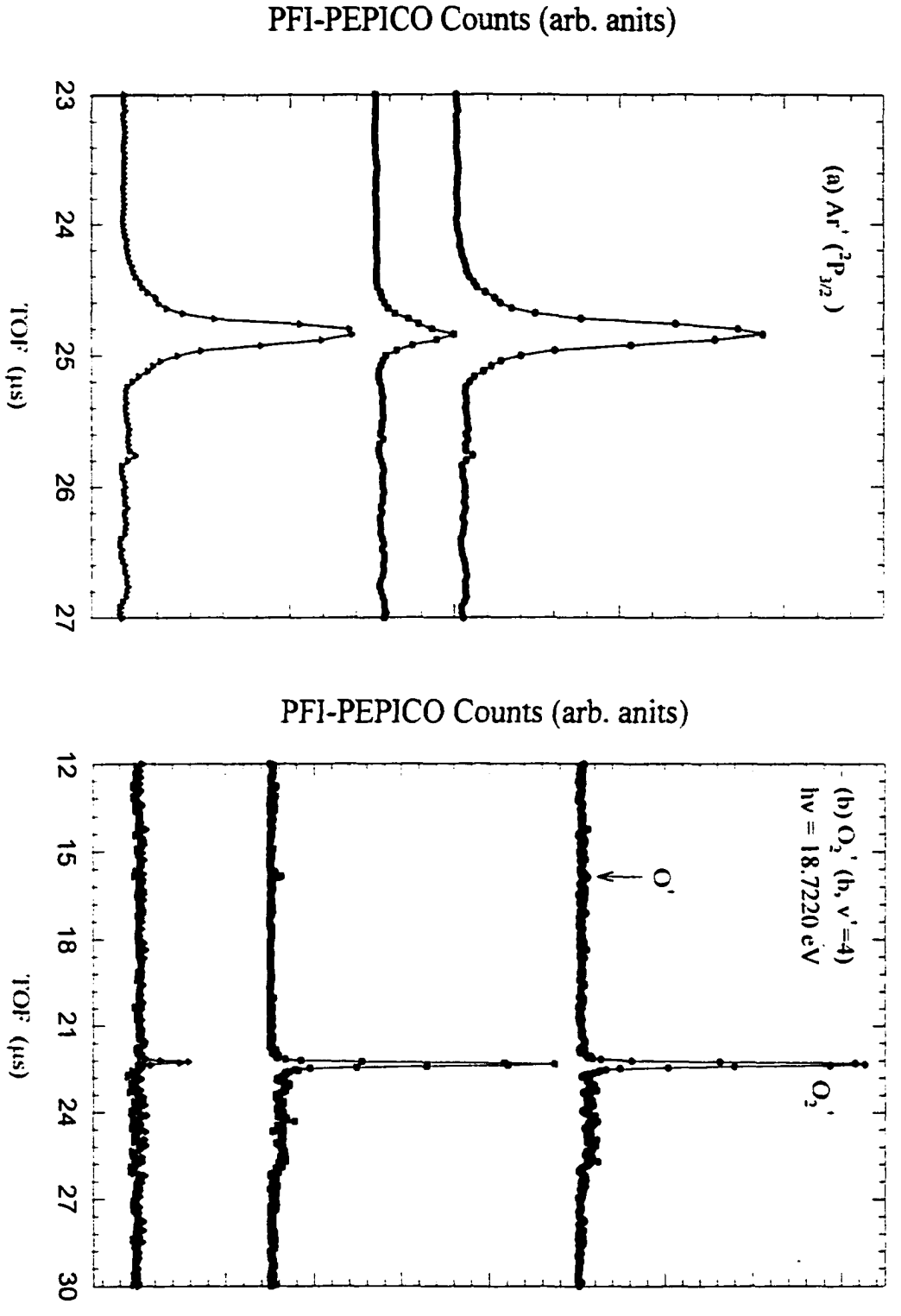
PFI-PEPICO Counts (arb. anits)
(a) Ar' ($^2P_{3/2}$)
TOF (μs)
23
24
25
26
27
PFI-PEPICO Counts (arb. anits)
(b) O_2', (h, v'=4)
hv = 18.7220 eV
O'
O_2'
TOF (μs)
12
15
18
21
24
27
30

extracted by the ion-extraction pulses give rise to a 4 μs (the duration of the ion-extraction pulse) constant background lying in the range of ≈22.2-26.2 μs.

Although a true PFI-PEPICO signal for $O_2^+(b^4\Sigma_g^-, v^+ = 4)$ is observed in the bottom spectrum of Fig. 7-2(b), the signal-to-noise (S/N) ratio is poor. The S/N ratios in the region of ≈22.2-26.2 μs of this bottom spectrum are also poor as a result of the subtraction. The first dissociation limit $O^+(^4S) + O(^3P)$ from O_2 is known to lie at $O_2^+(b^4\Sigma_g^-, v^+ = 4, N^+=9)$.[59-63] The energy of 18.7220 eV corresponds to the predominant production of $O_2^+(b^4\Sigma_g^-, v^+ = 4, N^+<5)$ and is expected to produce mostly O_2^+ ions. A small population of $O_2^+(b^4\Sigma_g^-, v^+ = 4, N\geq9)$ associated with the S-branch is expected to yield a finite O^+ coincidence signal. Indeed, it is possible to see the presence of O^+ in the raw spectra. However, background subtraction negates the O^+ signal. This observation is consistent with the conclusion that the O^+ coincidence signal is too weak to be observed due the poorer S/N ratios associated with this subtraction scheme.

B. Use of a high dc field for ion extraction and a low pulse field for pfi

In this mode, a relatively high dc field is maintained at the PI/PEX region for efficient ion extraction to the ion detector. The PFI-PE TOF selection scheme was the same as described above (Section II.A) except now that with the dc field maintained at the PI/PEX region, prompt background photoelectrons are also extracted continuously toward the electron detector. The signal pulse corresponding to the detection of a PFI-PE was used to trigger the MCS for recording the ion TOF spectrum.

Figures 7-3(a) and 7-3(b) show the PFI-PEPICO TOF spectra for the $Ar^+(^2P_{3/2})$ and $Ar^+(^2P_{1/2})$, respectively, obtained using a dc field of 8.7 V/cm at the PI/PEX region, together with an electric field pulse of 1.3 V/cm (width = 40 ns) for PFI. The intensities in the ordinates of these spectra are normalized to reflect the relative PFI-PEPICO signals for $Ar^+(^2P_{3/2})$ and $Ar^+(^2P_{1/2})$. The Ar gas sample was introduced into the PI/PEX region in the form of a doubly skimmed supersonic beam produced using a triply differential pumping arrangement. The accumulation times for the PFI-PEPICO TOF spectra of Figs. 7-3(a) and 7-3(b) were 1 and 20 min, respectively. Operating the ion TOF spectrometer in space focusing conditions[68] for the dc fields, the observed coincidence $Ar^+(^2P_{3/2})$ and $Ar^+(^2P_{1/2})$

Figure 7-3. PFI-PEPICO TOF spectra for (a) $Ar^+(^2P_{3/2})$ at 15.7596 eV and (b) $Ar^+(^2P_{1/2})$ at 15.9372 eV obtained using a doubly skimmed supersonic beam and the coincidence scheme described in section II.B. The intensities in the ordinates of these spectra are normalized to reflect the relative PFI-PEPICO signals for $Ar^+(^2P_{3/2})$ and $Ar^+(^2P_{1/2})$.

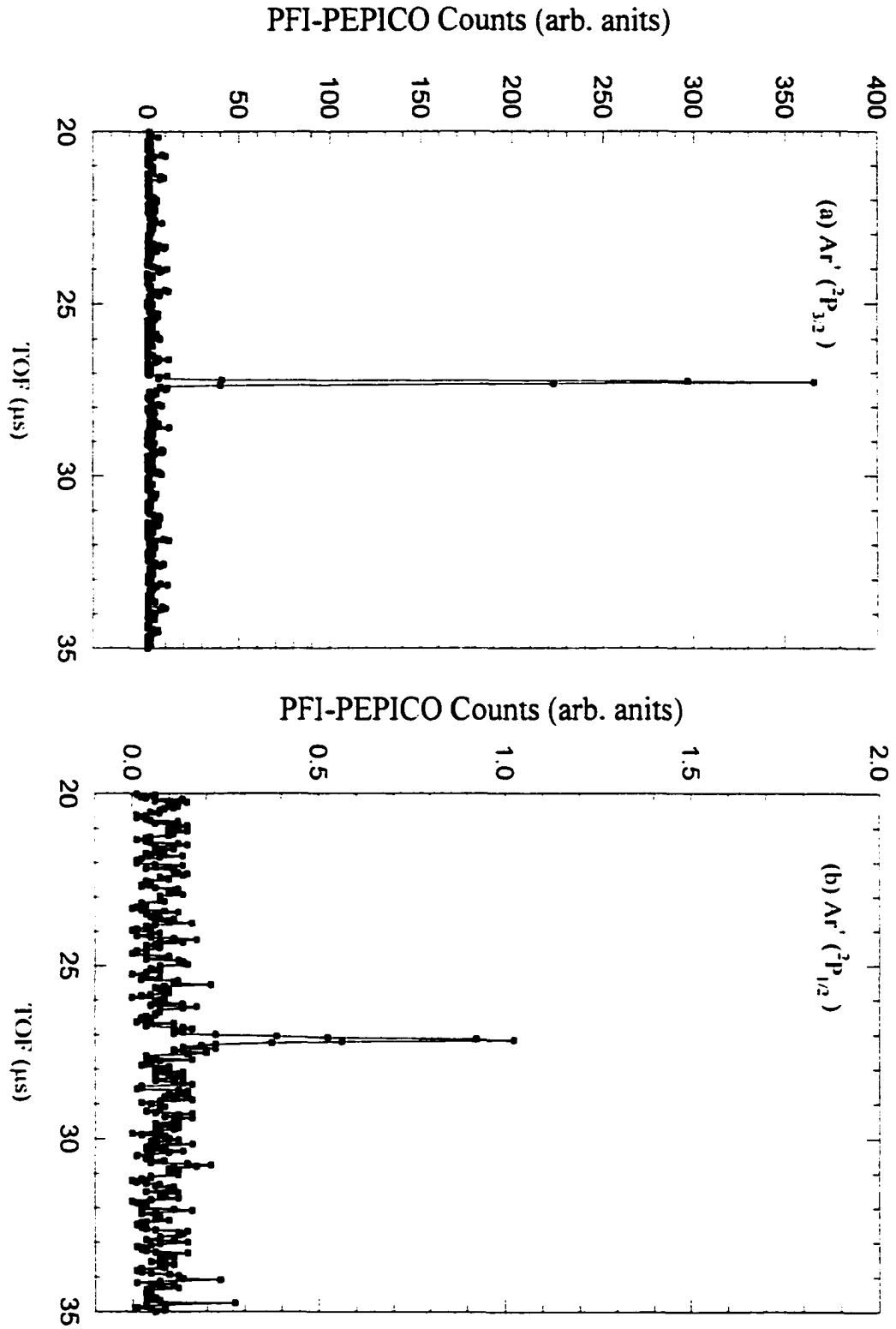
PFI-PEPICO Counts (arb. anits)
0
50
100
150
200
250
300
350
400
20
25
30
35
TOF (μs)
(a) Ar* ($^2P_{3/2}$)
PFI-PEPICO Counts (arb. anits)
0.0
0.5
1.0
1.5
2.0
20
25
30
35
TOF (μs)
(b) Ar* ($^2P_{1/2}$)

peaks are ≈ 60 ns (FWHM). The periodic spike-like structures observed in Figs. 7-3(a) and 7-3(b) are due to the false coincidences, which have a period (656 ns) identical to that of the synchrotron radiation. These false coincidence spikes result from the extraction of uncorrelated ions by the 1.3 V/cm electric pulse field intended for PFI.

By gating the Ar^+ peak intensity observed in the PFI-PEPICO TOF spectrum as a function of photon energy, we have generated the PFI-PEPICO bands for $Ar^+(^2P_{3/2})$ and $Ar^+(^2P_{1/2})$ (not shown here). As expected, these PFI-PEPICO bands are identical to the respective PFI-PE bands observed for $Ar^+(^2P_{3/2})$ and $Ar^+(^2P_{1/2})$. Using monochromator entrance/exit slits at 100/100 μm, we observed a PFI-PE and PFI-PEPICO resolution of ≈1 meV (FWHM).

If a sufficiently high dc electric field can be used to effectively extract ions from the PI/PEX region toward the ion detector, the use of a small pulsed electric field for PFI may not change the ion collection efficiency. This expectation is consistent with the observation that the spike-like false coincidence structures become blurred into a constant background as the dc field is increased relative to the electric pulse field for PFI. Figure 7-4 depicts the PFI-PEPICO TOF spectrum for H_2 observed at 15.522 eV corresponding to the (N^+=1, J"=1) transition associated with the $H_2^+(v^+=0)$ state. This spectrum was obtained using a dc field of 15 V/cm and a pulse electric field of 1.5 V/cm. The periodic spike-like structures observed in Figs. 7-3(a) and 7-3(b) are indiscernible in Fig. 7-4.

We note that since PFI-PEs and PFI-PIs are only formed during the application of the pulsed field, the PFI-PIs arriving at the ion detector should correlate with the pulsed electric field. When the conditions for obtaining a PFI-PEPICO TOF spectrum such as that of Fig. 7-4 is fulfilled, uncorrelated prompt ions should arrive at the ion detector at a nearly uniform rate as in a dc PEPICO experiment. Thus, the ion TOF spectrum triggered by the pulsed electric field should be equivalent to a PFI-PEPICO TOF spectrum. However, by recording the ion TOF spectrum only after the PFI-PE detection is expected to reduce false coincidences and thus, increase the S/N ratio of the TOF spectrum.

Another advantage of performing PFI-PEPICO using a high dc field is that it should be possible to extract kinetic energy release (KER) information from the TOF peak shape of fragment ions.[12,24] As long as the condition for space focusing is fulfilled,[64] the

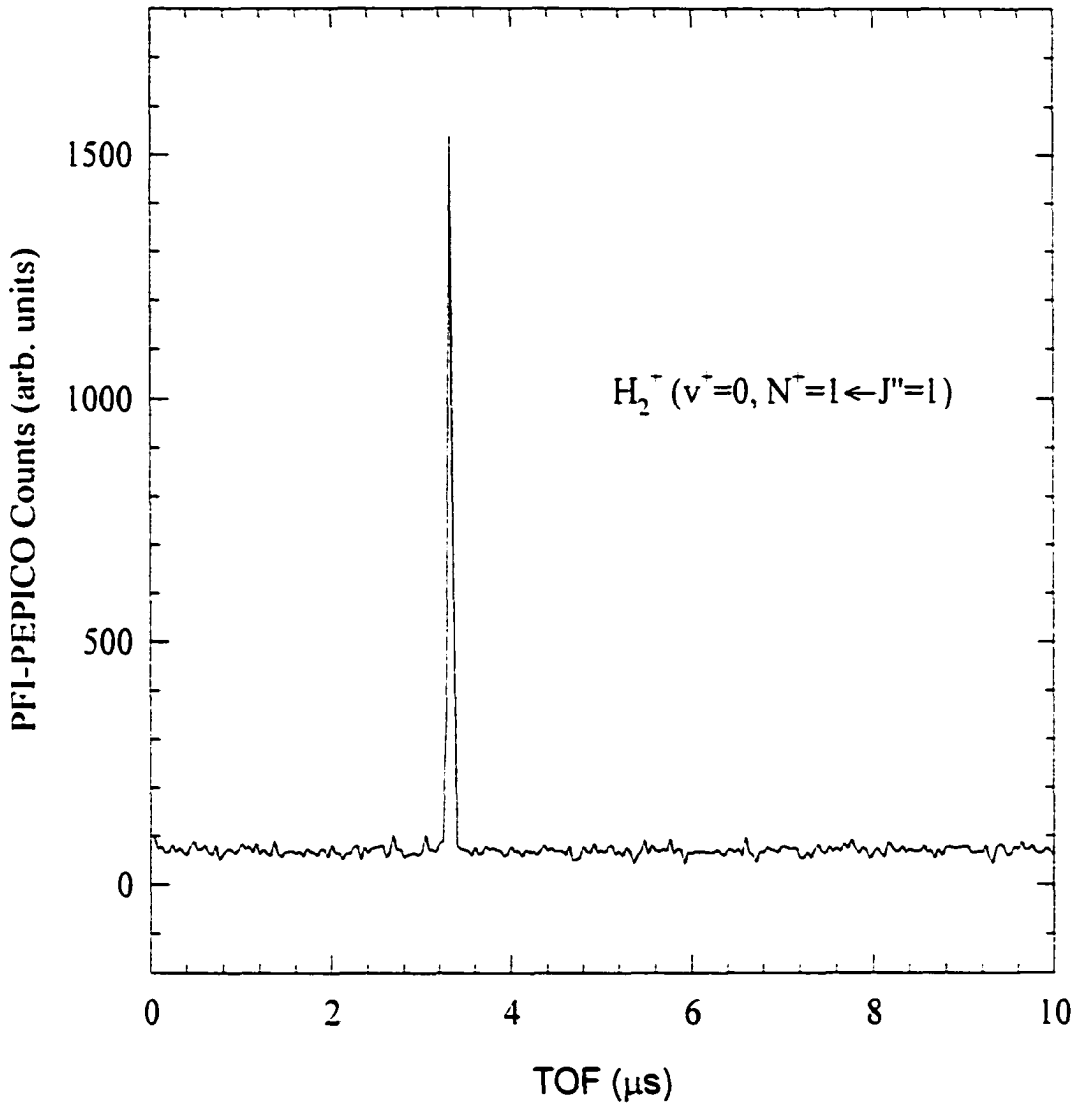

Figure 7-4. PFI-PEPICO TOF spectrum for H_2^-(v^-=0, N^-=1←J"=1) observed at 15.522 eV using the coincidence scheme described in section II.B.

analysis of the TOF peak shape should resemble that of KER measurements using a conventional TPEPICO method.

However, a high dc field generally has the effect of significantly reducing the PFI-PE (or PFI-PEPICO) signal of an excited ionic state. The low intensity for $Ar^+(^2P_{1/2})$ as compared to that for $Ar^+(^2P_{3/2})$ is clearly shown in the PFI-PEPICO spectra depicted in Figs. 7-3(a) and 7-3(b). The ratio for the PFI-PEPICO intensities for $Ar^+(^2P_{1/2})$ to that for $Ar^+(^2P_{3/2})$ is ≈0.0025, which is nearly 200 fold lower than the expected value. The most likely reason for this is that the high dc field reduces the lifetime of the high-*n* Rydberg states converging to the excited $Ar^+(^2P_{1/2})$ states. These states can autoionize, unlike those beneath the $Ar^+(^2P_{3/2})$ peak, and are therefore far more susceptible to a field induced decay mechanism.[48] This is a major drawback of this mode of operation as excited states of other ions are expected to suffer in the same way as the $Ar^+(^2P_{1/2})$ state.

One may overcome this lifetime problem by using a lower dc field. However, the ion collection efficiency would suffer accordingly, especially in the cases where fragment ions are formed with large kinetic energy releases. The ion-extraction scheme described in section II.C is aimed to solve this dilemma.

C. Use of a low dc field along with a long pulse field for PFI and ion-extraction

The use of a low dc field is necessary for the preservation of high-n Rydberg states converging to excited ionic states, i.e., the PFI-PE signal intensity. Considering that the momentum gained by an ion is proportional to the width and amplitude of the electric field pulse used, the solution to the ion-collection problem can be overcome by using a longer ion extraction pulse. This represents a compromise of the experimental scheme discussed above. We first tried this ion-extraction scheme in the two-bunch mode as the temporal interval (326 ns) between adjacent bunches is far wider than the dark gap in the multibunch mode, thus allowing the use of a wider ion-extraction pulse with no overlap of the following VUV light bunch.

In all the two-bunch experiments performed here a dc field of 0-2 V/cm was maintained at the PI/PEX region. A 6.95 V/cm field pulse (duration = 160 ns) was applied to the PI/PEX region with a delay of ≈100 ns with respect to each VUV light bunch. In addition to field ionizing high-n Rydberg states created by VUV excitation, the pulsed

field also has the function of extracting the PFI-ion toward the ion detector. As a result of this relatively high and wide PFI/ion-extraction pulse, we find the ion extraction to be very efficient. By comparing the coincidence rate with the PFI-PE and ion detection rates, we estimate collection efficiencies for PFI-PE and PFI-PI to be 7.3 and 19.3%, respectively, at the PFI-PE $Ar^+(^2P_{3/2})$ peak when a zero V dc field was maintained at the PI/PEX region.

It was discovered that a small dc field enhances the PFI-PE signal level of the spin-orbit excited $Ar^+(^2P_{1/2})$ states. Table 7-1 shows the relative PFI-PE intensities for $Ar^+(^2P_{3/2})$ and $Ar^+(^2P_{1/2})$ observed at different dc fields, while keeping the same ion extraction pulse field (height = 6.95 V/cm, width = 160 ns). The PFI-PE intensity for $Ar^+(^2P_{3/2})$ changes very little, whereas the $Ar^+(^2P_{1/2})$ PFI-PE intensity varies dramatically. The optimum voltage for these two-bunch experiments was found to be at 1.74 V/cm. This enhancement is most likely caused by lifetime lengthening of high-n Rydberg states converging to the $Ar^+(^2P_{1/2})$ ionization limit due to the Stark field and ion induced l- and m_l-mixing, where l is the angular momentum quantum number and m_l is the magnetic quantum number.[65-67] At larger l orbitals, the electron no longer penetrates the ion core and these states become very long lived. A low electric field is known to promote the decay of very high-n Rydberg states by field ionization, but at the same time has a lifetime lengthening effect for relatively low-n Rydberg states by l- mixing.[65,67]

Whilst operating with multibunch synchrotron radiation, a different situation arises whereby dc fields <0.2 V/cm are found to give the highest PFI-PE signal level for $Ar^+(^2P_{1/2})$ (see Table 7-1). The difference may be caused by the fact that in the two-bunch mode, a significantly higher ion density is formed. Each bunch is filled to a maximum current of 25 mA in the two-bunch mode, as compared to that of 1.5 mA in the multibunch operation. Thus, the ion density produced in the two-bunch mode is ≈17-fold higher than that resulted in the multibunch operation. An inhomogeneous electric field arisen from photoions thus produced adjacent to high-n Rydberg species has been ascribed to induce m_l-mixing, creating longer lived high-n Rydberg states.[65] Without this higher ion number density in the multibunch mode, m_l-mixing is expected to be more subdued. However, this scenario seems unlikely as ion count rates indicate no more than one ion per electron bunch was present in the interaction region at any one time.

Table I. The effect of dc electric field on the PFI-PE intensities for the $Ar^+(^2P_{3/2})$ and $Ar^+(^2P_{1/2})$ bands observed using two-bunch and multibunch synchrotron radiation at the ALS.

dc Field (V/cm)	Two-bunch			Multi-bunch		
	PFI-PE intensity			PFI-PE intensity		
	$Ar^+(^2P_{3/2})$	$Ar^+(^2P_{1/2})$	Ratio	$Ar^+(^2P_{3/2})$	$Ar^+(^2P_{1/2})$	Ratio
0.000	0.806	0.124	0.154	1.050	0.714	0.680
0.210	---	---	---	1.010	0.596	0.590
0.870	1.000	0.294	0.294	1.000	0.230	0.230
1.304	---	---	---	0.950	0.209	0.220
1.739	0.896	0.411	0.459	0.870	0.130	0.149
2.609	0.788	0.028	0.035	---	---	---
3.478	0.736	0.010	0.014	---	---	---
5.217	0.637	0.004	0.007	---	---	---
6.261	0.527	0.003	0.007	---	---	---

A second possibility is that the electric field may promote *l*-mixing and its prolonged use may also reduce the lifetime of Rydberg species formed from photoexcitation. In other words, *l*-mixing may occur in the pico-second time frame, which is then followed by a decay mechanism that takes place on a nano-second time frame. In the two-bunch case, PFI takes place at most 100 ns after excitation. In the multi-bunch case, those excited Rydberg states formed in the first part of the multibunch cycle are not field ionized until 400 ns later. If these states are then detrimentally affected by the dc field, even after mixing, then the overall effect in total signal in the multi-bunch case may be a decrease. We found that the dc electric fields employed in the two-bunch and multibunch modes have similar effects on PFI-PE intensities of other atoms and molecules compared to that for the $Ar^+(^2P_{1/2})$ PFI-PI peak.

A further point of note is that a small transverse dc field (≈0.5 V/cm) was also found to be advantageous to the signal levels as observed in the PFI-PE intensity for $Ar^+(^2P_{1/2})$, which increases by about 10% with the transverse field on. This again is most likely induced by m_l-mixing due to the existence of this transverse or non-cylindrical electric field.[65,67]

In the multibunch experiments described under this section, a dark gap of 144 ns was available in an ALS synchrotron period. A dc field of 0.20 V/cm was applied across the PI/PEX region. The application of a PFI-extraction electric field pulse (height = 6.96 V/cm, width = 200 ns) was delayed by ≈10 ns with respect to the beginning of the 144-ns dark gap. The employment of a lower dc field makes it necessary to use a pulse with a longer duration (200 ns) than the dark gap. The overlap of 134 ns between the pulsed field and the dark gap should not produce any prompt electron and ion backgrounds. Of course by overlapping the pulsed field with the light bunches, the pulsed field will field ionize the first set of light bunches of 66 ns measured with respect to the end of the dark gap. Any Rydberg states formed in this overlap region of 66 ns should be depleted by PFI. However, background prompt ions and PFI-PEs produced within this period may not be efficiently extracted because the momentum gained by an ion in such a pulsed field for <66 ns is inadequate for its transmission to the ion detector. An overlap of <66 ns was found to have little effect on the multibunch PFI-PE measurement. The field that all ions see is

pseudo-continuous with the consequence that false coincidences arrive at the ion detector with a time structure that depends on the ring period, or rather the electric pulse field frequency. True coincidences measured relative to the observed PFI-PEs arrive at a fixed time on top of this structured background.

Figure 7-5(a) depicts the PFI-PEPICO TOF spectrum for Cl^+ formed from HCl at 17.400 eV, corresponding to the initial formation of $HCl^+(X, v^+=7)$, which is just above the dissociation threshold for Cl^+.[2] This spectrum was recorded, whilst operating in the two-bunch mode with wide monochromator entrance/exit slits of 400/400 μm. Due to the high signal level, the false coincidences are high and have a time structure with a period identical to that of the synchrotron ring. Minimizing the signal level by narrowing the slits or by reducing the molecular beam pressure greatly reduces the periodic false coincidence background. However, even without doing this, the oscillatory background can be easily subtracted. By averaging over the first and latter part of the scans to form a background for each 656 ns block of the scan and by duplicating the averaged sections together, a full background spectrum was obtained. The subtraction of the background spectrum from the spectrum of Fig. 7-5(a) yields the true PFI-PEPICO spectrum shown in Fig. 7-5(b), which is relative free from the oscillatory false coincidence background and reveals the $^{35}Cl^+$ and $^{37}Cl^+$ fragment ion peaks. The background subtracted PFI-PEPICO spectra for HCl^+ from HCl at energies (17.1249 and 16.9712 eV) corresponding to the formation of $HCl^+(X, v^+=5$ and 6) are also plotted in Figs. 7-5(c) and 7-5(d), respectively. In these spectra, the parent $H^{35}Cl^+$ and $H^{37}Cl^+$ ion peaks are discernible. Recently the state selective predissociation spectra of HCl^+ ($X^2\Sigma^+$, v+=6,7,8) have been reported by Penno et al.[68] The current date confirm that the v+=6 state lies below the thermochemical limit for Cl^+ formation.

Figure 7-6 compares the PFI-PEPICO TOF spectra for $He^+(^2S_{1/2})$, $Ne^+(^2P_{3/2})$, and $Ar^+(^2P_{3/2})$ obtained at the multibunch operation using the molecular beam (upper spectra) and effusive beam (lower spectra) arrangements, respectively. We note that TOF peaks due to both the $^{20}Ne^+(^2P_{3/2})$ and $^{22}Ne^+(^2P_{3/2})$ isotopes are observed in Fig. 7-6. The narrower TOF peaks for $He^+(^2S_{1/2})$, $Ne^+(^2P_{3/2})$, and $Ar^+(^2P_{3/2})$ are due to the low translational temperature (≈20 K) in the direction the ion TOF axis (or perpendicular to the molecular beam) achieved in the molecular beam production arrangement. The

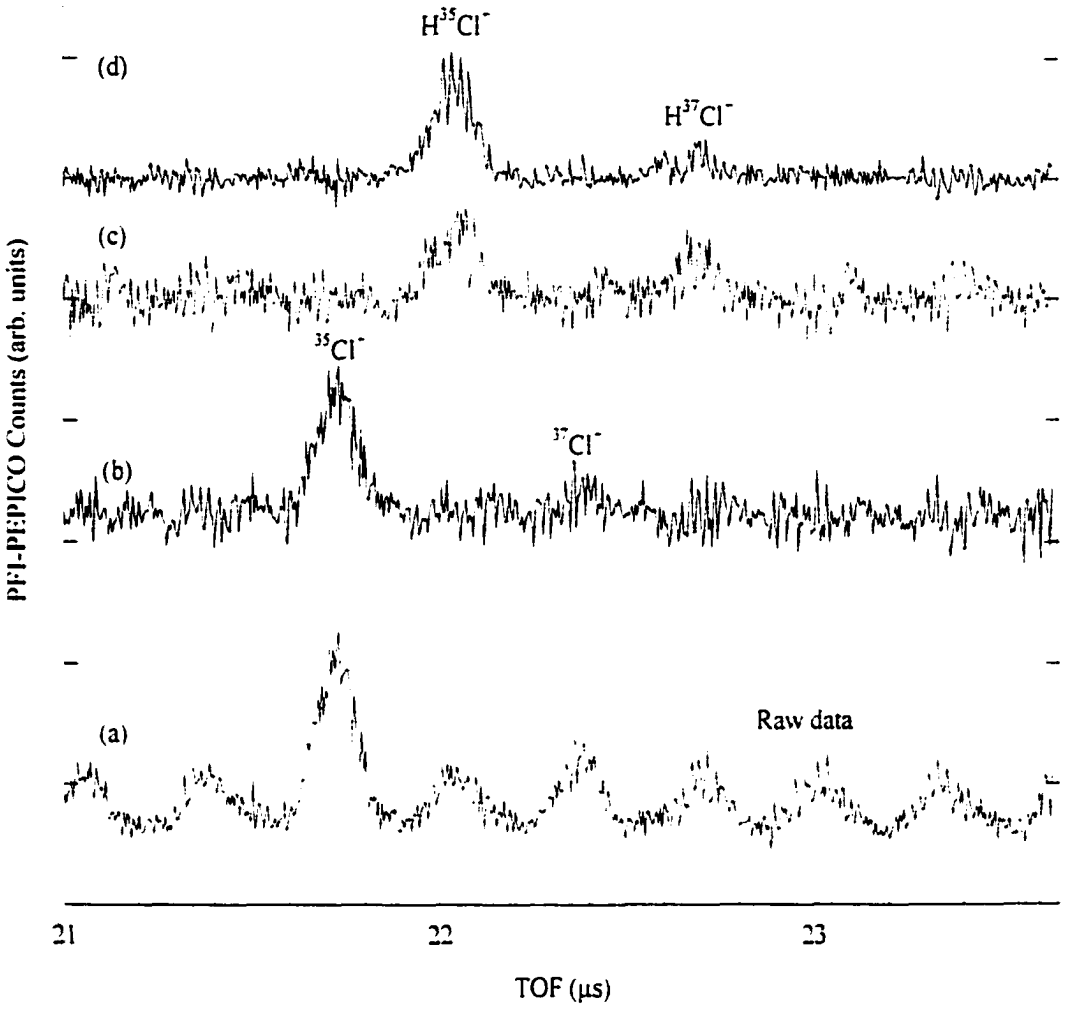

Figure 7-5. (a) The raw PFI-PEPICO TOF spectrum for Cl^+ from HCl at 17.4000 eV [$HCl^+(v^+=7)$]. (b) Background subtracted PFI-PEPICO spectrum for Cl^+ from HCl at 17.4000 eV [$HCl^+(v^+=7)$]. (c) Background subtracted PFI-PEPICO TOF spectrum for Cl^+ and HCl^+ from HCl at 17.1249 eV [$HCl^+(v^+=6)$]. (d) Background subtracted PFI-PEPICO TOF spectrum for Cl^+ and HCl^+ from HCl at 16.9712 eV [$HCl^+(v^+=5)$]. These spectra were recorded in the two-bunch mode using a HCl supersonic molecular beam and the coincidence scheme described in section II.C.

Figure 7-6. PFI-PEPICO TOF spectra for $He^+(^2S_{1/2})$, $Ne^+(^2P_{3/2})$, and $Ar^+(^2P_{3/2})$ obtained at the multibunch operation using the molecular beam (upper spectra, sharp peaks) and effusive beam (lower spectra, broad peaks) arrangements. The spectra were recorded by employing the coincidence scheme described in section II.C and were background-subtracted. The simulation of the sharp molecular beam PFI-PEPICO TOF peaks reveals a contribution of ≈15% thermal background.

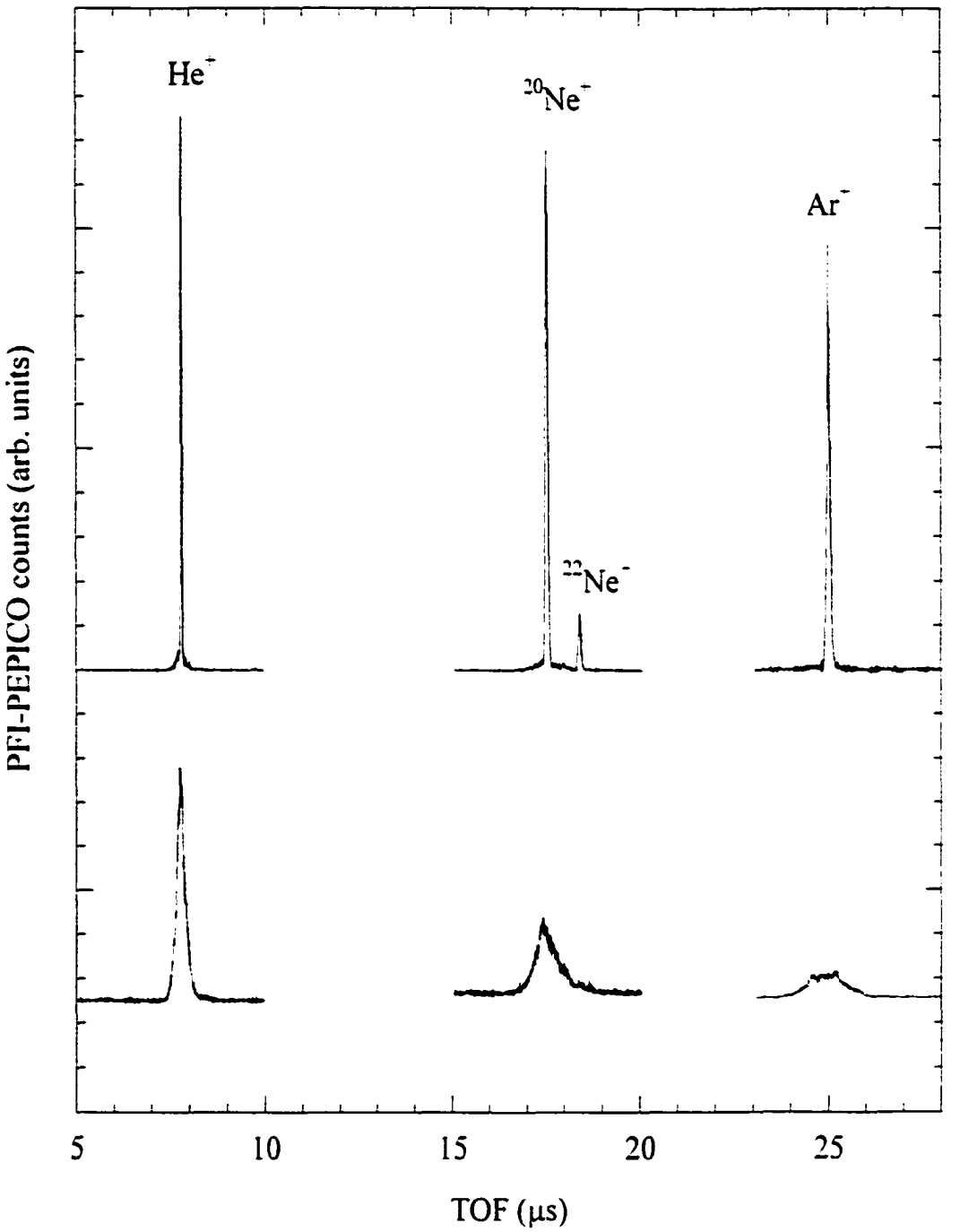
He+
20Ne+
22Ne+
Ar+
PFI-PEPICO counts (arb. units)
5
10
15
20
25
TOF (μs)

significantly greater TOF peak widths observed in the effusive beam experiment is consistent with the higher translational temperature (298 K). In addition to giving rise a periodic background structure, the pulsed ion-extraction field also affects the TOF peak shape of the coincident ions. This is particularly apparent for the broad $Ar^+(^2P_{3/2})$ ion peak observed using the thermal samples (see Fig. 7-6). The simulation of the molecular beam PFI-PEPICO TOF peaks for the rare gas ions shown in Fig. 7-6 reveals the contribution of ≈15% thermal background, resulting from photoionization of random background gases in the PI/PEX region. This background depends on the photoionization chamber pressure, which was in the low 10^{-5} Torr range during the experiment. Considering that the estimated number density of the supersonic beam at the PI/PEX center is in the 10^{-4} range, the finding of a 15% thermal background is thus reasonable.

As expected, the pulsed ion-extraction has little effect on the relative TOF of ions arriving at the detector. A plot (not shown here) of the TOF of rare gas ions versus the square root of the mass for He^+, Ne^+, Kr^+, Ar^+, and Xe^+ reveals a linear relationship as is normally observed for a static field extraction. We also found that the ion collection efficiency decreases as the ion mass is increased. This can be easily understood by the fact that for the same momentum gained by ions in a pulsed extraction arrangement, the heavier ion gains a lower velocity component toward the ion detector and thus has a lower ion transmission factor. The relative MCP detection efficiencies for ions with different masses may also play a role. The ion collection efficiencies are also found to be poorer for the effusive than for the molecular beam samples. In an effusive beam experiment, the interaction volume for the VUV beam and gas beam is significantly larger than that in the molecular beam arrangement, resulting in a higher signal for PFI-PE and ion detection. However, the ion transmission factor is expected to be very poor for ions formed at a large distance from the ion TOF axis.

III. RESULTS

Since the PFI and ion-extraction scheme described in Section II.C is the most successful, the experimental results presented below are obtained using such a scheme. As indicated above, we first learned about the important experimental conditions of PFI-

PEPICO measurements in the two-bunch experiments. The multibunch measurements provide a higher signal level, but the experimental conditions are more restrictive. Using O_2 and CH_4 as the molecular samples, the results presented below illustrate the performance of this PFI-PEPICO method in the internal state- or energy selection of ions, breakdown diagram determination, and KER measurement. Some important considerations concerning Rydberg state lifetime effects on PFI-PEPICO measurements of breakdown diagram for state- or energy-selected unimolecular dissociation processes are also discussed.

A. PFI-PEPICO study of CH_4

We have obtained detailed PFI-PEPICO TOF spectra for CH_3^+ from CH_4 near the dissociation threshold. The bulk of the data for CH_4 including important thermochemistry will be presented in a later publication. However, some of the data are presented here to illustrate factors that need to be considered when performing PFI-PEPICO experiments, especially in the measurement of accurate ion dissociation thresholds.

A most serious difficulty in the determination of ion dissociation thresholds involving a polyatomic parent species is the hot band effect.[1] Thermal populations of the parent molecules can lead to ion dissociation at energies well below the 0 K thermochemical onset. Even when a cold supersonic beam is used, the thermal contribution due to background molecules in the photoionization chamber can give rise to ambiguity in the determination of the true ion dissociation threshold. We show in Figs. 7-7(a-c) the PFI-PEPICO TOF spectra for CH_3^+ and CH_4^+ from CH_4 at 14.118eV, 14.304 eV and 14.318 eV, respectively, obtained using a MCS channel width of 5 ns. The dissociation threshold is known to occur at 14.323 eV at 0 K.[2] Figure 7-7(b) reveals a narrow TOF peak for CH_4^+ and a broad TOF peak for CH_3^+. The narrow CH_4^+ peak indicates that the CH_4^+ ions are formed predominantly from photoionization of the supersonically cooled CH_4 sample, whereas the broad CH_3^+ peak is produced exclusively by the dissociative PFI of thermal (298 K) CH_4 in the photoionization chamber. Interestingly, the broad peaks seen in the TOF spectra seem to account for far more of the total signal than they should do at energies approaching threshold. Well below threshold, only a small portion of the CH_4^+ peak ($\approx$15%) is seen to originate from the thermal CH_4

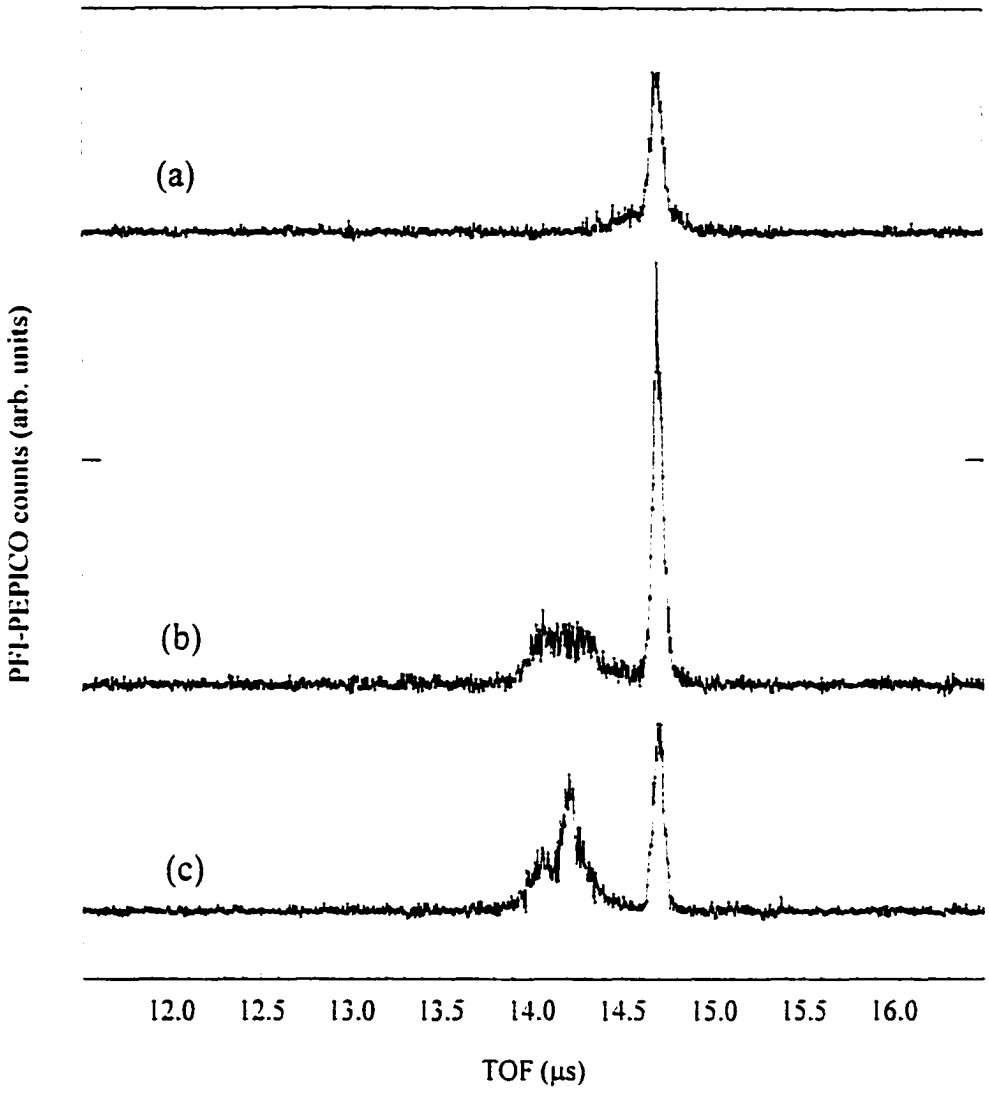

Figure 7-7. Background subtracted PFI-PEPICO TOF spectra for CH_3^+ and CH_4^+ from CH_4 at (a) 14.118eV, (b) 14.304 eV, and (c) 14.318 eV, respectively, obtained using a supersonically cooled CH_4 beam and the coincidence scheme described in section II.C. [see Fig 7-7(a)], but at 14.318 eV, the broad CH_3^+ part accounts for close to 50% of the total signal.

In the present PFI-PEPICO study of CH_3^+ from CH_4, the formation of CH_3^+ and CH_4^+ near the dissociation threshold can proceed by two mechanisms.

$$CH_4 + h\nu \rightarrow CH_4^*(n) \rightarrow CH_4^{*+} + e^- \rightarrow CH_3^+ + H \quad + e^- \qquad (1)$$

and

$$CH_4 + h\nu \rightarrow CH_4^*(n) \rightarrow CH_3^*(n') + H \rightarrow CH_3^+ + e^- + H, \qquad (2)$$

where the $CH_4^*(n)$ [$CH_3^*(n')$] is the neutral excited CH_4 [CH_3] in a high-*n* [high-n'] Rydberg state. According to mechanism (1), $CH_4^*(n)$ prepared in VUV photoexcitation is first field ionized to produce internally excited CH_4^{*+} prior to dissociation forming CH_3^+ + H. Here, CH_4^{*+} represents the ionization limit or the ion core of $CH_4^*(n)$. In mechanism (2), $CH_4^*(n)$ first undergoes prompt dissociation to form $CH_3^*(n')$ + H. The subsequent PFI of $CH_3^*(n')$ results in the formation of $CH_3^+ + e^-$.

The recent lifetime measurements for $O_2^*(n)$ converging to dissociative O_2^+ states[51,54,55,58] provide strong support for mechanism (2) as the major process for CH_3^+ formed in the PFI of $CH_4^*(n)$. The higher than expected PFI-PEPICO intensity for CH_3^+ from thermal CH_4 observed below the dissociation threshold can be accounted for by a longer lifetime for $CH_3^*(n')$ than that for $CH_4^*(n)$. As the $CH_3^*(n')$ channel becomes available, a greater PFI-PE efficiency is thus expected. The latter expectation was confirmed in the PFI-PE measurement of CH_4.[68] Since the (15%) thermal sample has a large distribution of energies, as the dissociation threshold is approached, the formation of CH_3^+ from $CH_3^*(n')$ will be favored for the thermal CH_4 sample over CH_4^+ from the supersonically cooled CH_4 sample.

Due to the magnification of the CH_3^+ intensity from thermal CH_4, the breakdown diagram will reveal a lower cross over point if CH_3^+ ions from both thermal and cold CH_4 are included in the data analysis. One important conclusion from this analysis is that we can significantly reduce this effect by constructing the breakdown diagram using only the intensity of CH_3^+ from the cooled molecular beam CH_4 sample. Although any molecular beam will have a thermal contribution from background molecules in the photoionization

chamber, the CH_3^- TOF peaks resulting from the thermal and molecular beam parts of the sample have different widths [see Figure 7-7(c)] and can be easily distinguished. By analyzing the narrow part of the spectrum to obtain the 'cold' breakdown curve, we have obtained a highly accurate value for the CH_3^- dissociation threshold.[68] Although the lifetime effect may still play a role in the cold molecular beam sample, the effect should only occur over a narrower energy range.

It was also found that the magnitude of the dc field applied in the PFI-PEPICO experiment has an effect on the breakdown diagram determination. Figures 7-8(a) and 7-8(b) show the PFI-PEPICO TOF recorded at dc fields of 1.32 and 0 V/cm, respectively, for CH_4 at 14.309 eV. All experimental conditions except the dc field were kept constant. These spectra were recorded with an optical resolution of roughly 4 meV (FWHM). The small change in energy due to the stark shift should have little consequence on the spectrum recorded. However, as can be seen, the relative intensities of the CH_3^- and CH_4^- peaks change dramatically. It seems that *l*-mixing caused by the dc electric field plays a role in lengthening the lifetime of CH_4*(n) compared to CH_3*(n'). This dramatic dc Stark field effect observed on the PFI-PE intensities of CH_3^- and CH_4^- indicates that the patterns of low-n Rydberg states for CH_3 and CH_4 near the dissociation threshold are different, resulting in different dc field dependencies for the PFI-PE intensities for CH_3^- and CH_4^-. This effect should be general for most molecules and may give rise to irregular structure of the experimental breakdown diagram based on PFI-PEPICO TOF measurements.

These findings indicate that for a PFI-PEPICO study of a polyatomic molecule, where individual vibrational and rotational states are not easily identifiable, the use of a thermally warm sample may lead to the breakdown diagram with finite irregularities in the branching ratio profiles. The analysis and interpretation of such branching ratio data for the determination of 0K ion dissociation thresholds involving polyatomic molecules will be discussed in fore coming publications.[69,70]

B. PFI-PEPICO study of O_2

We have performed PFI-PEPICO TOF measurements using both two-bunch and multibunch synchrotron radiation, obtaining the breakdown breakdown diagram for $O^-(^4S) + O(^3P)$ from $O_2^+(b^4\Sigma_g^-, v^+=4, N^+)$. The dissociation threshold is known to occur just

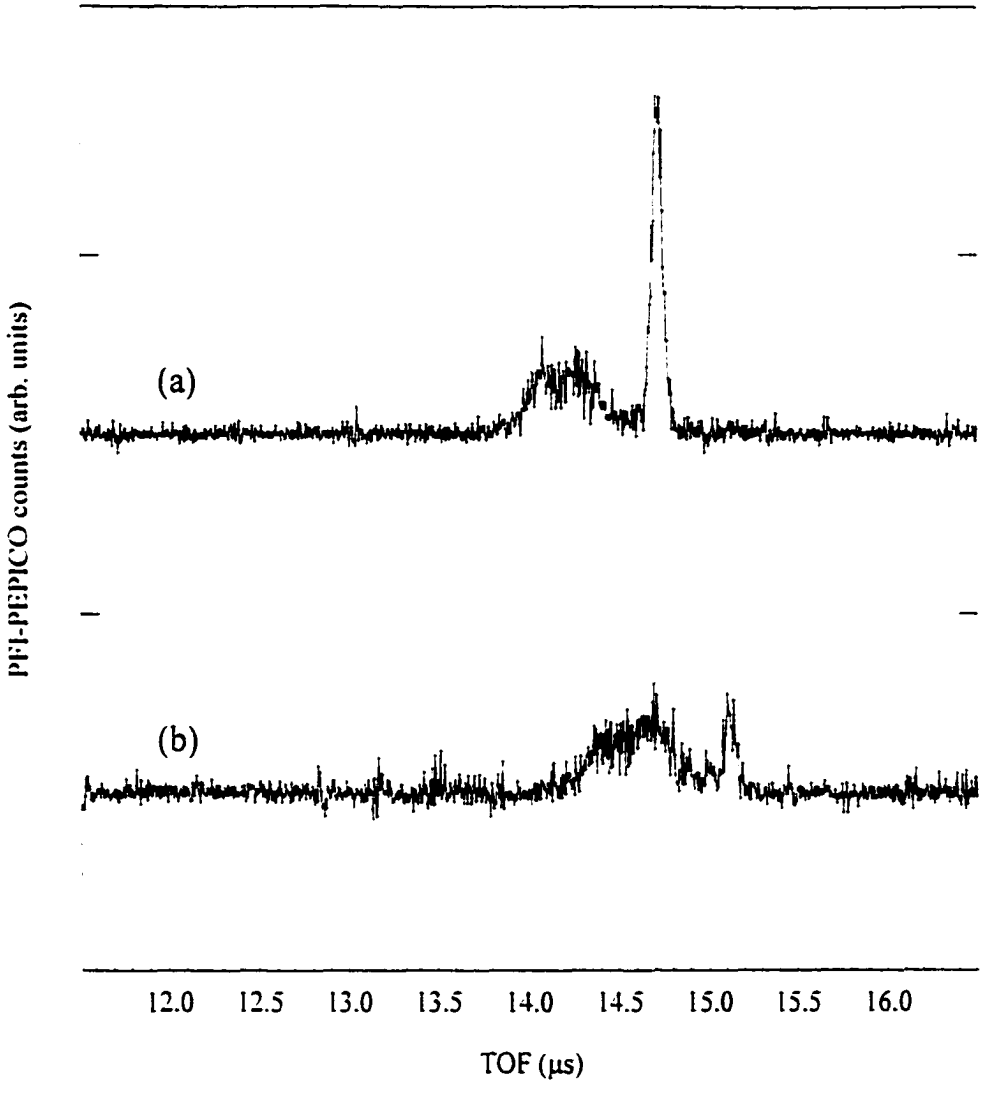

Figure 7-8. Background corrected PFI-PEPICO TOF spectra recorded at (a) 1.32 and (b) 0 V/cm for CH_4 at 14.309 eV obtained using a supersonically cooled CH_4 beam and the coincidence scheme described in section II.C.

below $O_2^+(b^4\Sigma_g^-, v^+=4, N^+=9)$.[64-67] The two-bunch mode measurements were made using the O_2 molecular beam sample, achieving a rotational temperature of ≈10 K, which is too low to promote a significant population for N″=9. Since the thermal O_2 sample promotes the populations of $N^+ \geq 9$, which are responsible for the observed O^+ fragment ions in the PFI-PEPICO measurements, we have examined in detail the branching ratios for O^+ and O_2^+ from O_2 in a multibunch PFI-PEPICO TOF experiment using an effusive O_2 sample. We have obtained PFI-PEPICO TOF spectra in the energy region of 18.7129-18.7253 eV at an energy increment of 0.5 meV. Selected TOF spectra measured at photon energies of 18.7193-18.7227 eV are depicted in Fig. 7-9. The resulting breakdown diagram can be seen in Fig. 7-10(a), where the solid circles represent the branching ratios of O^+ and the solid squares are those for O_2^+. At a given photon energy in the breakdown diagram, the sum of the branching ratios for O^+ and O_2^+ is normalized to 100.

In order to simulate of the breakdown diagram, it is necessary to find the rotational population of $O_2^+(b^4\Sigma_g^-, v^+=4)$. For this reason, we have recorded the PFI-PE band for $O_2^+(b^4\Sigma_g^-, v^+=4)$ [open circles shown in Fig. 7-10(b)] employing monochromator entrance/exit slits of 30/30 μm, together with the simulation based on the Buckingham-Orr-Sichel (BOS) model. The marking of the $\Delta N = N^+ - N'' = -2, 0,$ and $+2$ (or O, Q, and S, repsectively) rotational branches are also shown in Fig. 7-10(b). Here N^+ and N″ are the rotational quantum numbers for O_2^+ and O_2, respectively. We note that the numbers given in Fig. 7-10(b) are N″ values. The BOS simulation of this spectrum was made using the known rotational constants for $O_2(X^3\Sigma_g^-, v''=0)$ and $O_2^+(b^4\Sigma_g^-, v^+=4)$, the IE value for the formation of $O_2^+(b^4\Sigma_g^-, v^+=4)$, and BOS coefficients ($C_0$, C_2) were set at (0.3 , 0.7) as determined previously by Hsu et al.[53] Similar to the previous study, the initial BOS fit was relatively poor in the region of 18.717-18.722 eV. An excellent fit [solid line shown in Fig. 7-10(a)] to the experimental PFI-PE spectrum was only observed after scaling the BOS line strengths resulting in N^+ = 7, 9,11, 13 and 15 by 0.34, 1.50, 1.36, 1.21 and 1.41 respectively. The necessity to scale up the transitions for $N^+ \geq 9$ by a factor of 1.2-1.5 is consistent with the conclusion that the rotational line strengths for the formation of $N^+ \geq 9$ in the $O_2^+(b^4\Sigma_g^-, v^+=4)$ PFI-PE band are enhanced. No such enhancements are found in the

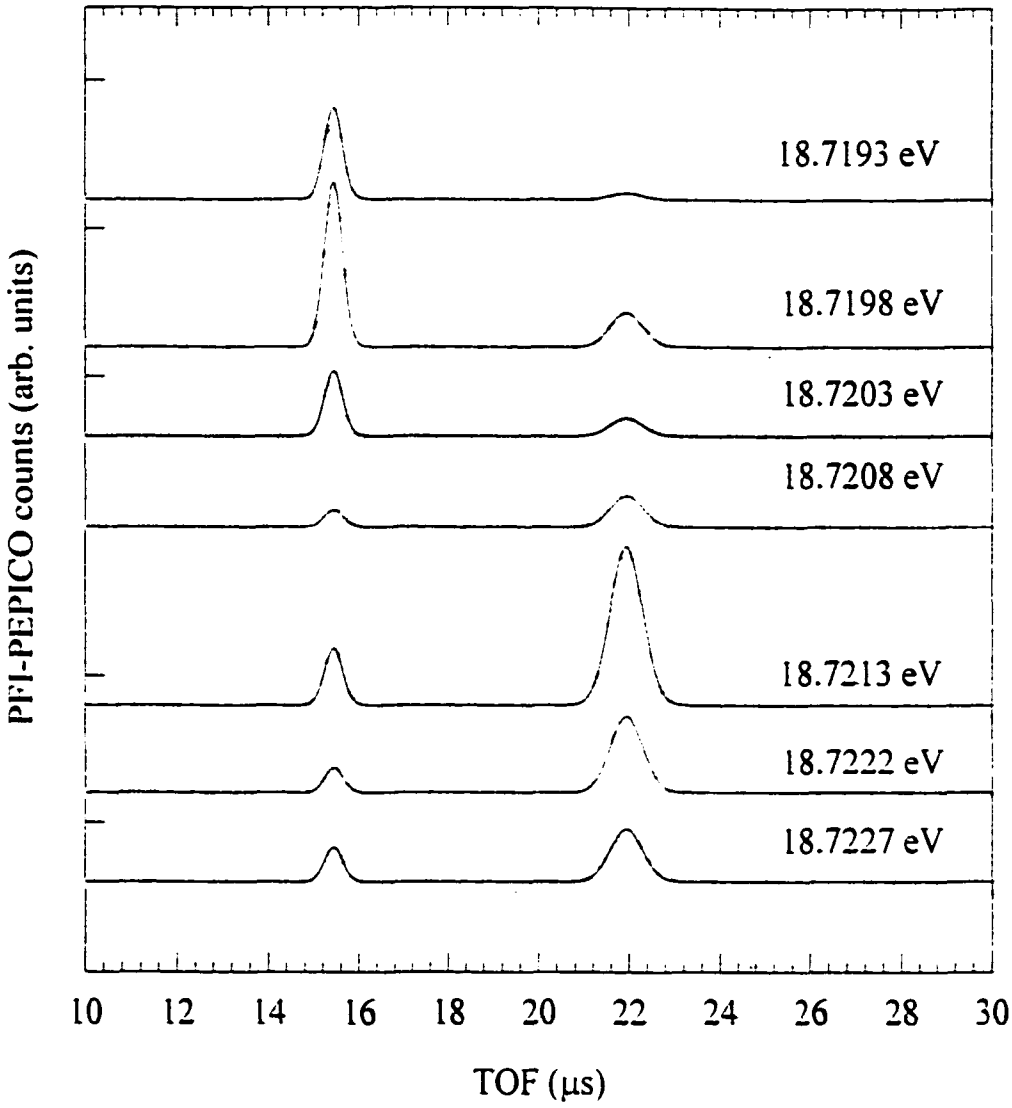

Figure 7-9. Background subtracted PFI-PEPICO TOF spectra for O^- and O_2^- from O_2 at 18.7193-18.7227 eV obtained using an effusive O_2 beam and the coincidence scheme described in section II.C.

Figure 7-10. (a) Breakdown diagram for the formation of $O^+(^4S) + O(^3P)$ from O_2 in the energy range of 18.705-18.730 eV. The solid circles represent the branching ratios of O^+ and the solid squares are those for O_2^+. At a given photon energy, the sum of the branching ratios for O^+ and O_2^+ is normalized to 100. (b) PFI-PE spectrum (open circles) for $O_2^+(b^4\Sigma_g^-, v^+ = 4)$ in the energy range of 18.705-18.730 eV. The simulation based on the BOS model is shown in solid line (see the text). The marking of the ΔN = -2, 0, and +2 (or O, Q, and S, respectively) rotational branches are also shown in (b). The numbers given in (b) are N″ values. The dashed line of (b) shows the population of $O_2^+(b^4\Sigma_g^-, v^+ = 4, N^+<9)$ estimated based on the BOS simulation.

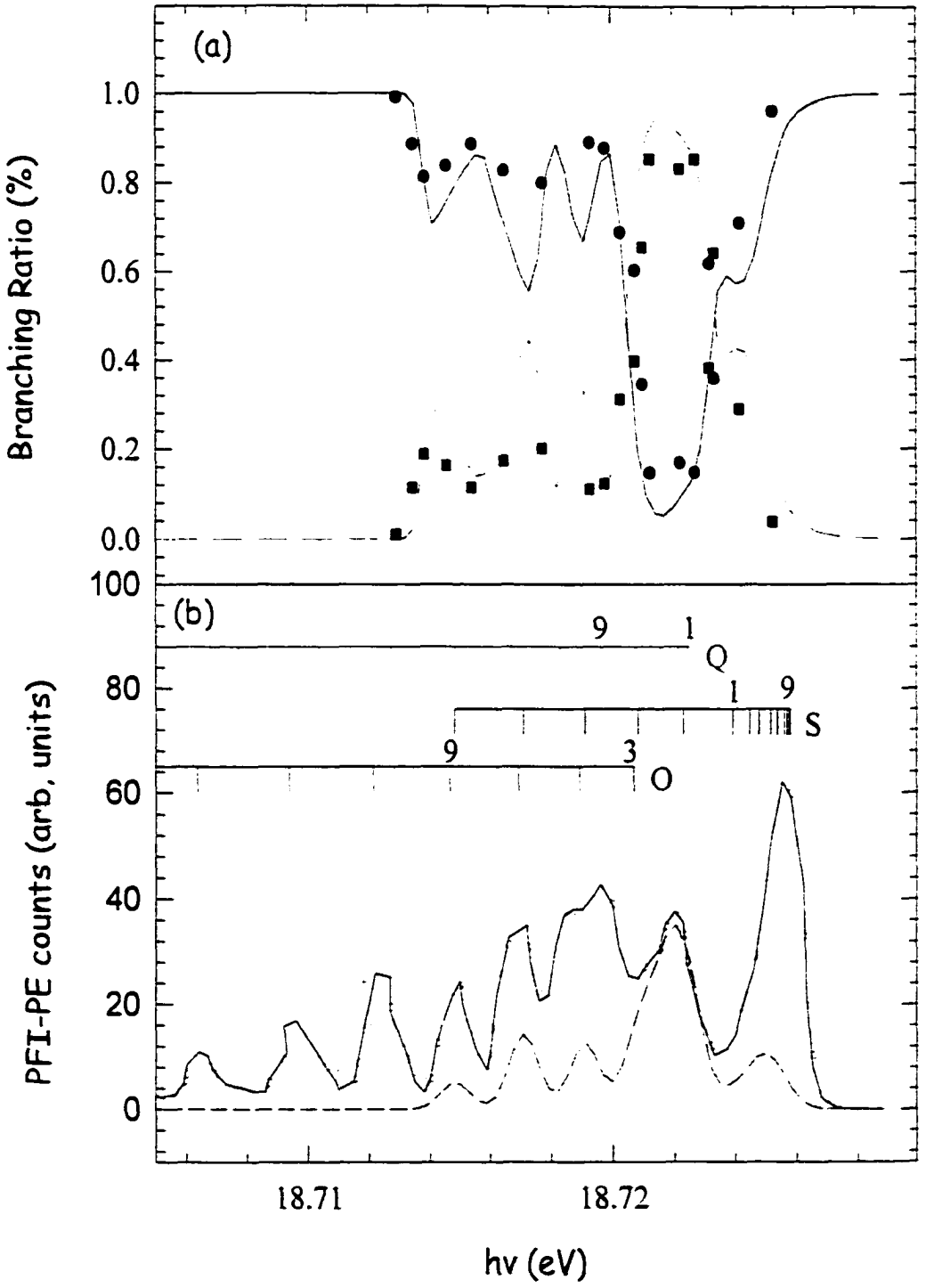
(a)
Branching Ratio (%)
1.0
0.8
0.6
0.4
0.2
0.0
(b)
PFI-PE counts (arb. units)
100
80
60
40
20
0
9
1
Q
1
9
S
9
3
O
18.71
18.72
hv (eV)

$O_2^+(b^4\Sigma_g^-, v^+<4$ and $>5)$ PFI-PE bands. In the previous PFI-PE study of Hsu et al.,[53] the rotational intensity distribution observed in the $O_2^+(b^4\Sigma_g^-, v^+=5)$ PFI-PE band is also different from other PFI-PE bands. For this reason, Hsu et al. have interpreted the line strength enhancements for $O_2^+(b^4\Sigma_g^-, v^+=4, N^+\geq 9)$ as due to the crossing by the $d^4\Sigma_g^-$ potential curve in between the $O_2^+(b^4\Sigma_g^-, v^+=4$ and 5) levels.[64-67] The latter repulsive state is believed to be responsible for the predissociation of $O_2^+(b^4\Sigma_g^-, v^+\geq 4)$.

Two crossover points were observed in this breakdown diagram because the population of $Q(N^+>7)$ occurs on the low energy side and that of $S(N^+>7)$ lies on the high energy side of the $O_2^+(b^4\Sigma_g^-, v^+=4)$ band. The crossover point at 18.7207 eV locates between $Q(N^+=7$ and 9). The other crossover point at 18.7234 eV results from the population of N^+ (>7) levels via the S-branch.

If $O^+(^4S)$ is formed by excited $O_2^+(b^4\Sigma_g^-, v^+\geq 4, N^+)$ prepared by the PFI of high-n O_2 Rydberg states $[O_2^*(n)]$ as indicated in process (3), we may not expect intensity enhancements for rotational levels ($N^+\geq 9$) disregarding any local perturbations due to low-n Rydberg states.

$$O_2 + h\nu \rightarrow O_2^*(n) \rightarrow O_2^+(b^4\Sigma_g^-, v^+=4, N^+\geq 9) + e^- \rightarrow O^+(^4S) + O(^3P) + e^- \qquad (3)$$

Our previous lifetime measurements for $O_2^*(n)$ converging to dissociative[53,57,58,62] $O_2^+($ $b^4\Sigma_g^-$, $B^2\Sigma_g^-$, and $c^4\Sigma_u^-$) states provide strong evidence indicating that prompt dissociation of $O_2^*(n)$ occurs to form $O^*(n')$ + O prior to PFI, where $O^*(n')$ represents an excited O atom in a high-n′ Rydberg level. That is, the formation PFI-PEs are most likely resulted from PFI of $O^*(n')$. In this case, the $O^*(n')$ state converges to the $O^+(^4S)$ limit and the sequential steps for the PFI-PE formation is shown in process (4).

$$O_2 + h\nu \rightarrow O_2^*(n) \rightarrow O^*(n') + O(^3P) \rightarrow O^+(^4S) + e^- + O(^3P) \qquad (4)$$

If the lifetimes for $O^*(n')$ species formed above the dissociation threshold ($N^+\geq 9$) are longer than those for $O_2^*(n)$ below the dissociation threshold ($N\leq 7$), an increase in the

PFI-PE intensity at $N^+ \geq 9$ should be observed. A relative increase in rotational line strength for $N^+ \geq 9$ levels lying about the dissociation limit can therefore be explained by this lifetime switching mechanism. We note that for the best fit, the levels resulting in $N^+ = 7$ had to be decreased. This may indicate that the lifetimes of $O_2^*(n)$ species converging to $N^+ = 7$ are shortened due to perturbation of low-n Rydberg states. We believe that the dissociation mechansim shown in processes (2) and (4) are valid for high-n Rydberg states converging to a dissociative ion core with a lifetime much shorter than the experimental time scale of ≈0.02-0.6 μs. The dissociative lifetimes for $O_2^+(b^4\Sigma_g^-, v^+ \geq 4)$ have been measured to be < 4 ns.

Once a good fit to the experimental PFI-PE is obtained, we were able to estimate the population for $N^+ < 9$. This population is shown in Fig. 7-10(a) by the dashed curve, revealing that the PFI-PE peak at 18.7220 eV corresponds predominantly to the formation of $O_2^+(b^4\Sigma_g^-, v^+=4, N^+<9)$. If we assume that the population of $O_2^+(b^4\Sigma_g^-, v^+=4, N^+\geq 9)$ led to prompt dissociation, the population for $O_2^+(b^4\Sigma_g^-, v^+=4, N^+<9)$ represents the intensity of O_2^+ observed in the PFI-PEPICO TOF spectrum. The calculated branching ratios for O^+ and O_2^+ are shown as the solid and dashed curves, respectively, in Fig. 7-10(b). We have also calculated the breakdown diagrams assuming that the dissociation thresholds for O^+ are at $N^+=7$ and 11. The comparison between the calculated and experimental breakdown curves for the assumed thresholds at $N^+=7$ and 11 are shown in Figs 7-11 (a) and 7-11(b), respectively. The respective populations for $O_2^+(b^4\Sigma_g^-, v^+=4, N^+<7)$ and $O_2^+(b^4\Sigma_g^-, v^+=4, N^+<11)$ along with the PFI-PE band for $O_2^+(b^4\Sigma_g^-, v^+=4)$ are depicted in Fig. 7-11(aa) and 7-11(bb). As pointed out above, the population of $O_2^+(b^4\Sigma_g^-, v^+=4, N^+<7)$ [$O_2^+(b^4\Sigma_g^-, v^+=4, N^+<11)$] represents the intensity of O_2^+ for the assumed threshold of $N^+=7$ ($N^+=11$). The simulation based on the assumed $N^+ = 11$ threshold produces a poor fit in the region 18.718 to 18.721 eV, while that for the N+ = 7 threshold yields a poor fit in the region 18.712 to 18.716 eV. The assumed threshold of $N^+ = 9$ results in the best overall fit [Fig. 7-10(b)]. Since the optical resolution used in the branching ratio determination of Fig. 7-10(a) is different from that used in the PFI-PE measurement of Fig. 7-10(b), finite discrepancies between the simulated and measured branching ratios as shown in Fig. 7-

Figure 7-11. The comparison between experimental breakdown diagram for the formation of $O^+(^4S)$ + $O(^3P)$ from O_2 and that based on the assumed thresholds at $N^+=7$ and 11 are shown in (a) and (b), respectively. The solid circles represent the branching ratios of O^+ and the solid squares are those for O_2^+. At a given photon energy, the sum of the branching ratios for O^+ and O_2^+ is normalized to 100. The estimated populations (dashed curves) for $O_2^+(b^4\Sigma_g^-, v^+=4, N^+<7)$ and $O_2^+(b^4\Sigma_g^-, v^+=4, N^+<11)$ obtained based on the BOS simulation, along with the PFI-PE band (open circles) for $O_2^+(b^4\Sigma_g^-, v^+=4)$ are depicted in (aa) and (bb), respectively. The marking of the ΔN = -2, 0, and +2 (or O, Q, and S, respectively) rotational branches are also shown in (aa) and (bb). T numbers given in (aa) and (bb) are N″ values.

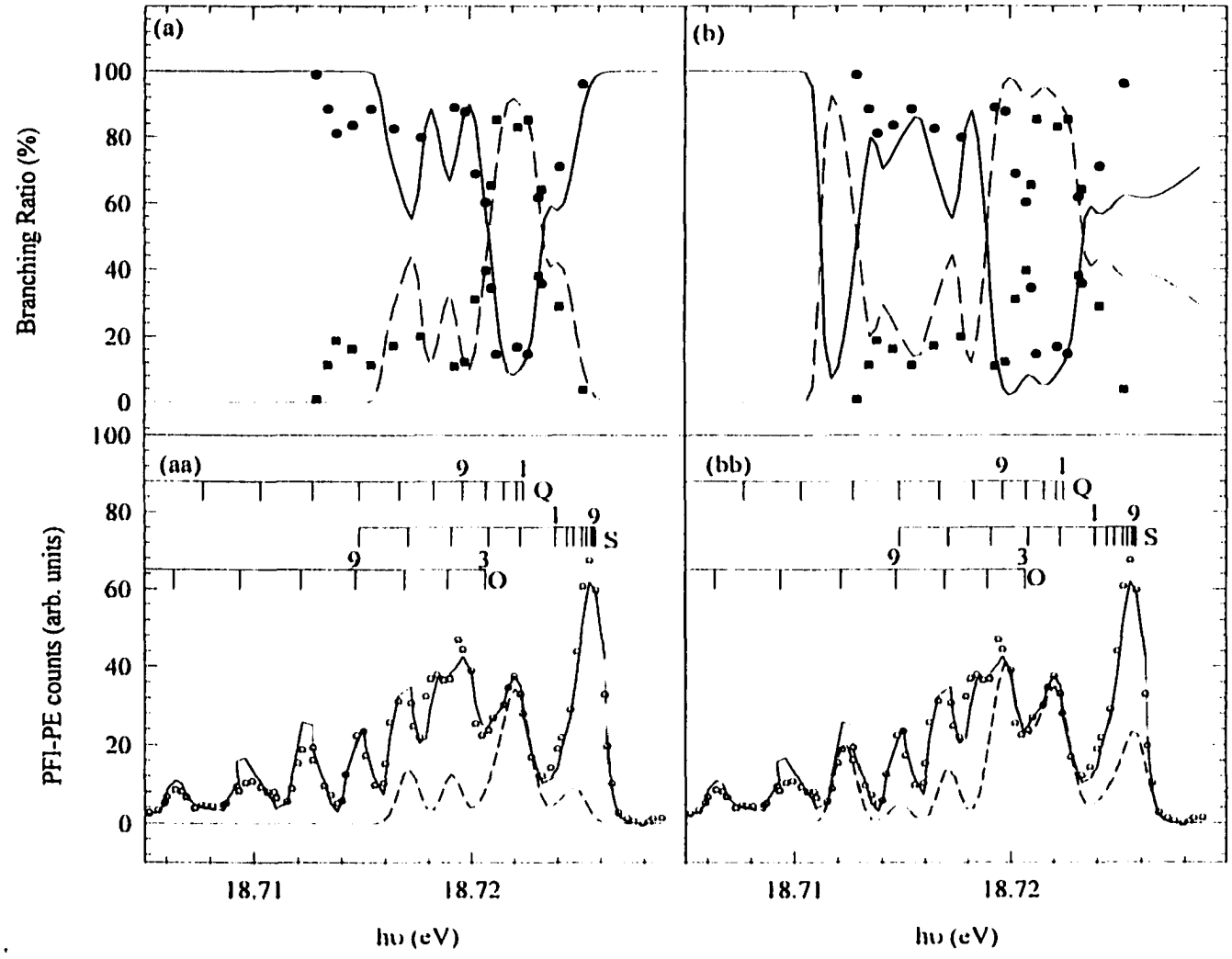
(a)
(b)
(aa)
(bb)
Branching Ratio (%)
PFI-PE counts (arb. units)
100
80
60
40
20
0
9
1
Q
1
9
S
9
3
O
18.71
18.72
hυ (eV)

10(b) are to be expected. The discrepancies can be attributed to the uncertainty of the determination of rotational population of O_2 using the BOS model. In addition to correctly predict the crossover points, the N^+=9 simulation also predicts the experimental observation that complete dissociation of O_2^+ occurs at energies >18.7253 eV and <18.7129 eV. Thus, the results of the present PFI-PEPICO study of O_2 support the previous conclusion[64-67] that the dissociation threshold for $O^+(^4S) + O(^3P)$ lies at $O_2^+(b^4\Sigma_g^-, v^+=4, N^+=9)$. This finding, together with the observation of the rotational intensity enhancement at $N^+ \geq 9$ can be taken as strong support for the $O_2^*(n)/O^*(n')$ lifetime switching effect at the dissociation threshold.

An important aspect of a PEPICO experiment is the ability to determine the fragment KER of a prompt dissociation reaction.[12,24] Assuming that the mechanism for the O^+ formation proceeds by process (4), some information about the KER for the actual ion dissociation process may be lost because the formation of O^+ is mediated by the initial production of $O^*(n')$. If the delay of PFI with respect to the formation of $O^*(n')$ from $O_2^*(n)$ is short, the KER information may still be obtained with accuracy. In order to demonstrate this capability, we have measured the PFI-PEPICO TOF spectra for O^+ at energies 18.7171, 18.8501, 18.9717 eV, and 19.0900 eV as shown in Figs. 7-12(a)- 7-12(d), corresponding to the PFI-PE bands for $O_2^+(b^4\Sigma_g^-, v^+=4, 5, 6, \text{and } 7)$, respectively. The latter three energies are set at the respective highest intensity peak positions of the v^+ =5-7 PFI-PE bands. These spectra were measured using a supersonically cooled O_2 sample and the two-bunch synchrotron radiation at the ALS.

Although the S/N ratios of these spectra are relatively poor, they reveal a nearly symmetric doublet structure. Assuming a single kinetic energy release (KER) and an isotropic distribution, . we expect to observe a rectangular TOF distribution in a static field experiment, whose full width Δt is predicted by the equation,[24,69]

$$\Delta t = \sqrt{\frac{8mE_{c.m.}}{(qF)^2}}. \qquad (5)$$

Here, $E_{c.m.}$ is the center-of-mass kinetic energy of the ion with a mass (m), F is the electric field at the PI/PEX region, and q is the elementary charge. The Δt value of these TOF peaks simply corresponds to the turn around time of the most energetic O^- ion moving away from the TOF ion detector. In the dissociation reaction of O_2^- into O^- + O, the entire excess energy must be released into the kinetic energy of the fragments, suggesting a single KER value disregarding the spin-orbit splitting of $O(^3P)$. The concave peak profile observed is indicative of the discrimination in the collection efficiency of energetic ions produced with velocity components perpendicular to the ion TOF axis. The Δt value is found to increase as v^- is varied from 5 to 7, consistent with the expected increase in KER. The KER of the dissociation process can be obtained from the measured Δt value provided that the effective electric field at the PI/PEX region is known. Since the ion-extraction field pulse is only on for <160 ns and the O^- ions remain in the PI/PEX region at the end of the field pulse, it is difficult to estimate the effective field at the PI/PEX region. This is especially the case when considering finite imperfections, such as ringing, of the applied electric field pulse for ion extraction.

We have satisfactorily simulated the TOF distributions observed in Figs. 7-12(a)-7-12(d) using an effective electric field of 4.5 V/cm. The simulated spectra (solid lines) of Figs. 7-12(b)- 7-12(d) are obtained by assuming an O_2 temperature of ≈10 K. The simulated curve (solid line) of Fig. 7-12(a) is obtained assuming an O_2 temperature of ≈100 K, indicating a higher contribution of O^- from thermal O_2 in the photoionization chamber. As pointed out above, the thermal O_2 background is estimated to be ≈15%. The higher thermal O_2 contribution associated with the $O_2^+(b^4\Sigma_g^-, v^+=4)$ spectrum can be accounted for by the fact that at 18.7171 eV the thermal PFI-PE spectrum dominates. The higher thermal contribution is also due partly to the lifetime switching effect, i.e., the enhancement of line strengths for rotational levels $N^+ \geq 9$ as manifested in the PFI-PE band for $O_2^+(b^4\Sigma_g^-, v^+=4)$. The dissociation arising from thermal O_2 molecules will lead to a distribution of kinetic energies for O^+. In this case, the TOF distribution can be obtained as the sum of many rectangular basis functions with appropriate weighting determined by the transformation from the energy to the TOF domain. The simulated TOF spectra for O^+

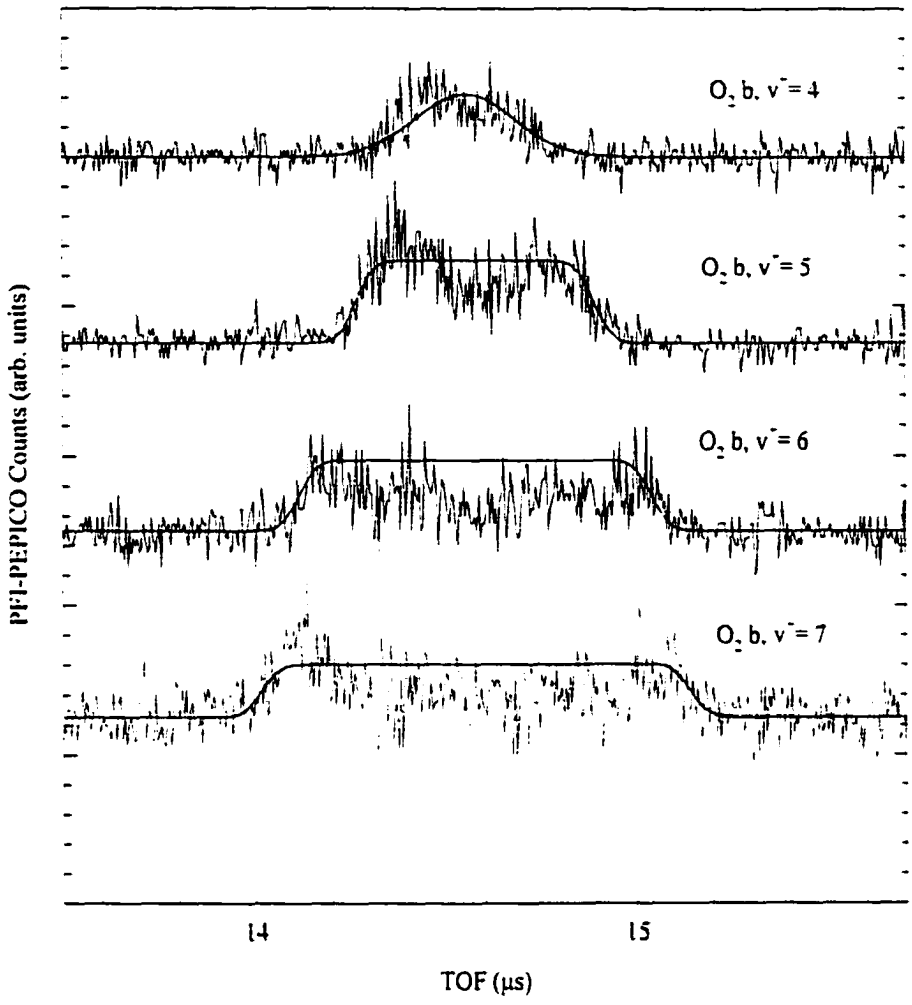

Figure 7-12. Background subtracted PFI-PEPICO TOF spectra for O^- obtained at energies 18.7171, 18.8501, 18.9717 eV, and 19.0900 eV, corresponding to the PFI-PE bands for $O_2^-(b^4\Sigma_g^-, v^-=4, 5, 6, \text{and } 7)$, respectively. These spectra were measured using a supersonically cooled O_2 molecular beam and the two-bunch synchrotron radiation. The simulated the TOF spectra (solid line) were obtained using an effective electric field of 4.5 V/cm. An O_2 temperature of ≈10 K was assumed in the simulation of the spectra measured at 18.8501, 18.9717 eV, and 19.0900 eV. The simulated curve (solid line) at 18.7171 eV is obtained assuming an O_2 temperature of ≈100 K, indicating a higher contribution O^+ from thermal O_2 in the photoionization chamber.

from $O_2^+(b^4\Sigma_g^-, v^+=4\text{-}7)$ shown in Figs. 7-12(a)- 7-12(d) are in reasonably good agreement with the PFI-PEPICO TOF spectra.

The known KERs for the dissociation of $O_2^+(b^4\Sigma_g^-, v^+=4\text{-}7)$ are plotted versus the simulated KERs in Fig. 7-13. The simulated and experimental KERs are in good accord. Due to the difficulty in assessing the thermal background contribution, we assign an uncertainty of 39 meV (the average translational energy for thermal O_2 molecules) for the simulated KER values.

IV. Further Advances

A major disadvantage of the PFI-PEPICO scheme described in section II.C is that the use of a relatively high pulsed electric field limits the achievable PFI-PE or PFI-PEPICO resolution to ≈1.0 meV. One way of improving this is to use a shaped pulse, which consists of a low field (<1 V/cm, duration ≈ 20-40 ns) for PFI immediately followed by a higher field pulse (>7 V/cm, duration≈150 ns) for ion extraction. We note that since the ion-extraction pulse has a finite overlap with VUV light bunches, PFI-PEs will also be generated. However, PFI-PEs produced by the low and high pulses should arrive in two time windows. By collecting only PFI-PEs from the low field pulse, the resolution is expected to be higher than that obtained in the scheme of section II.C, where a 7 V/cm height pulsed field is used for PFI. In this shaped pulse scheme, an important experimental consideration is that the PFI-PEs formed by PFI due to the low field pulse must exit the PI/PEX region prior to the employment of the high field pulse. As the PFI-PEs exit the PI/PEX region and enter the electron TOF spectrometer, they are shielded from the high field pulse by the grid located at the aperture of lens E1 (see Fig. 7-1). As a result, the TOF of the PFI-PEs formed by the low field pulse is not disturbed by the high field pulse for ion extraction.

We have just fabricated the necessary pulser and electronics for this shaped pulse scheme. The advantage of this scheme in yielding higher PFI-PEPICO resolution is shown Fig. 7-14, where the PFI-PE (open circles) and PFI-PEPICO (solid circles) bands for $Ar^+(^2P_{3/2,1/2})$ are compared. These spectra were obtained using a 0.5 V/cm low field pulse

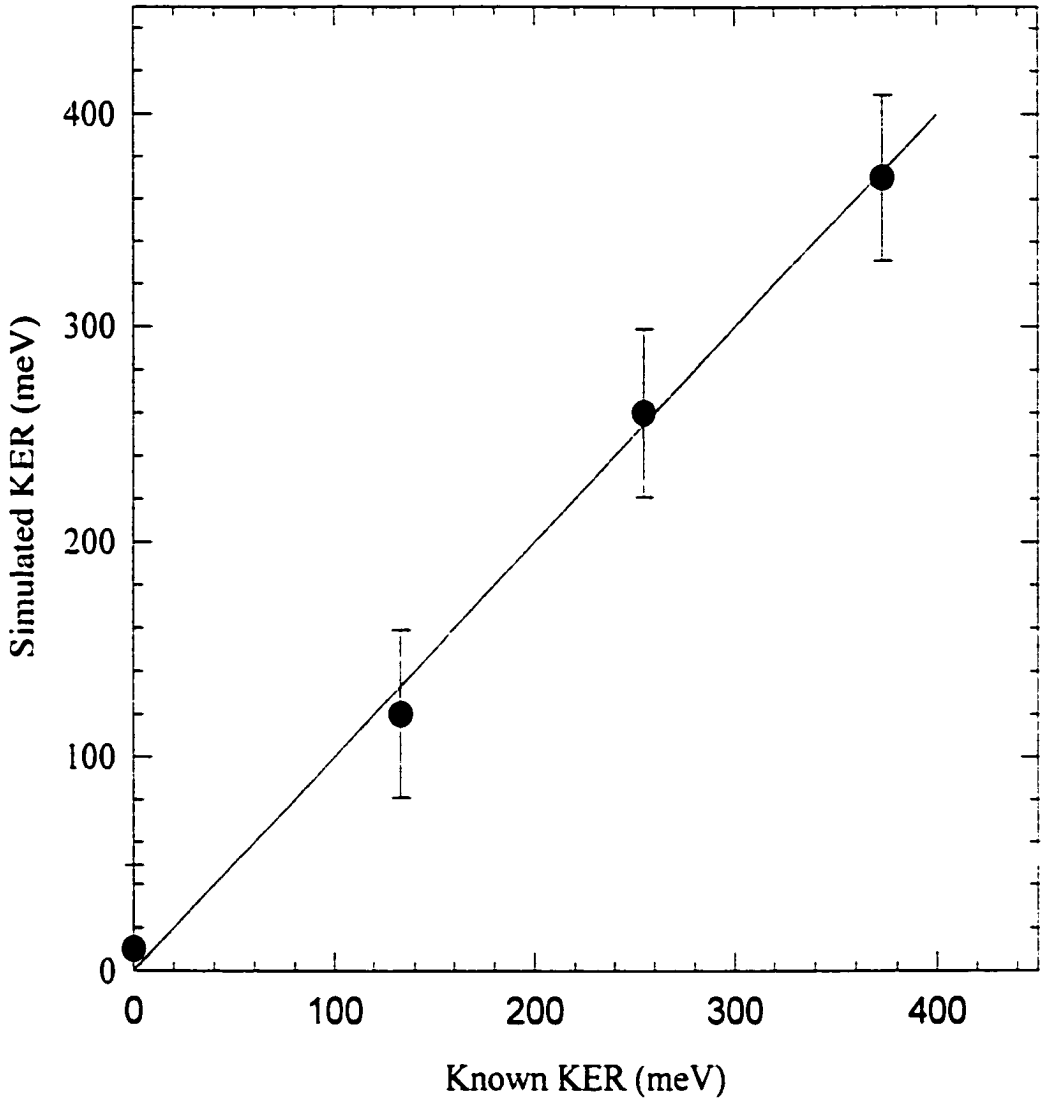

Figure 7-13. The known KER for the dissociation of $O_2^+(b^4\Sigma_g^-, v^+=4\text{-}7)$ plotted versus the simulated KER. Due to the difficulty in assessing the thermal background contribution, an uncertainty of 39 meV (the average translational energy for thermal O_2 molecules) is assigned for the simulated KER values.

Figure 7-14. Comparison of the PFI-PE (open circles) and PFI-PEPICO (solid circles) bands for $Ar^+(^2P_{3/2,1/2})$ obtained using the shaped pulse coincidence scheme. The shaped pulse is shown in the inset. It consists of a 0.5 V/cm low field pulse (duration = 40 ns) followed by a 7 V/cm high field pulse (duration =150 ns). The Gaussian fit to these bands yields a resolution of 0.6 meV (FWHM) for both the PFI-PE and PFI-PEPICO bands.

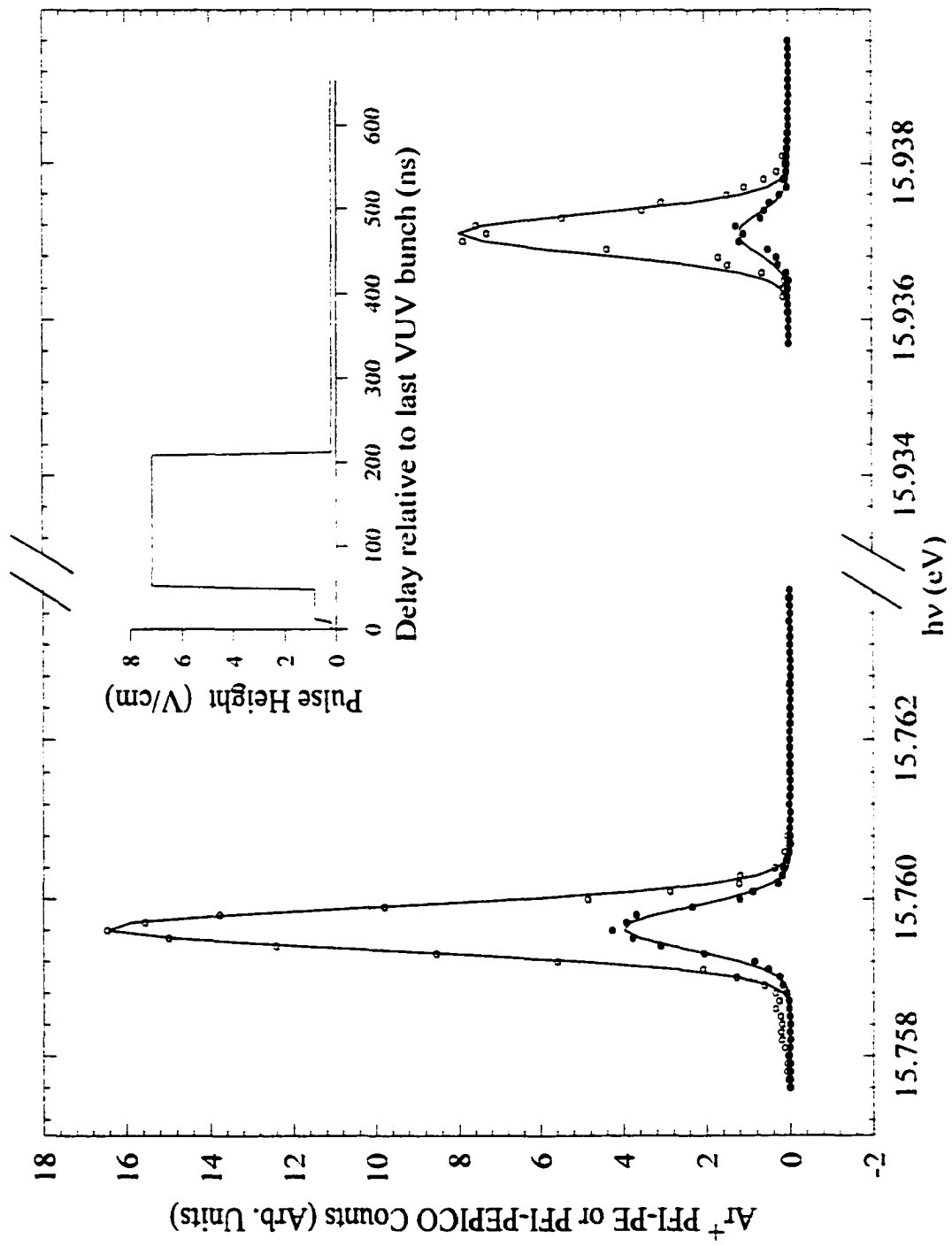
Ar+ PFI-PE or PFI-PEPICO Counts (Arb. Units)
18
16
14
12
10
8
6
4
2
0
-2
15.758
15.760
15.762
15.934
15.936
15.938
hν (eV)
Pulse Height (V/cm)
8
6
4
2
0
0
100
200
300
400
500
600
Delay relative to last VUV bunch (ns)

(duration = 40 ns) followed by a 7 V/cm high field pulse (duration =150 ns). The pulse shape used is shown in the inset of Fig. 7-14. The Gaussian fit to the $Ar^+(^2P_{3/2})$ and $Ar^+(^2P_{1/2})$ bands gives experimental resolutions of 0.6 meV (FWHM) and 0.5 meV (FWHM), respectively. The slightly higher resolution for the $Ar^+(^2P_{1/2})$ band is most likely caused by a shorter lifetime of the Rydberg states converging to this ionization limit. We note that PFI-PEPICO intensity is about 25% of the PFI-PE intensity, indicating good collection efficiencies for both PFI-PEs and PFI-ions. The shaped pulse basically solves the dilemma of achieving a high photoelectron resolution (requires a low electric field pulse) and a high ion transmission (requires a high electric field pulse). We believe that this new synchrotron-based PFI-PEPICO method will have a significant impact to thermochemistry and unimolecular and bimolecular reaction dynamics studies of cations.

ACKNOWLEDGMENTS

This work was supported by the Director, Office of Energy Research, Office of Basic Energy Sciences, Chemical Science Division of the U.S. Department of Energy under Contract No. W-7405-Eng-82 for the Ames Laboratory and Contract No. DE-AC03-76SF00098 for the Lawrence Berkeley National Laboratory. K.M.W. and M.M. acknowledge financial supported by the Deutsche Forschungsgemeinschaft. CYN acknowledges the support of the Alexander von Humboldt Senior Scientist Award. Y.S. is the recipient of the 1999 Wall Fellowship at Iowa State University.

References

1. H. M. Rosenstock, M. K. Draxl, B. W. Steiner, and J. T. Herron, J. Phys. Ref. Data, **6**, Suppl. 1 (1977).
2. S. G. Lias, J. E. Bartmess, J. L. Holmes, R. D. Levin, and W. G. Mallard, *J. Phys. Ref. Data*, **17**, Suppl. 1 (1988).
3. D. W. Turner, C. Baker, A. D. Baker, C. R. Brundle, *Molecular Photoelectron Spectroscopy* (Wiley, London 1970).

4. J. W. Rabalais, *Principle of Ultraviolet Photoelectron Spectroscopy* (Wiley, New York, 1977).

5. K. Kimura, S. Katsumata, Y. Achibi, T. Yamazaki, and S. Iwata, *Handbook of HeI Photoelectron Spectra of Fundamental Organic Molecules*, Halsted Press (1981).

6. E. v. Puttkammer, Z. Naturforsch. A **25**, 1062 (1970).

7. D. Villarejo, R. R. Herm, and M. G. Inghram, *J. Chem. Phys.* **46**, 4495 (1967).

8. W. B. Peatman, T. B. Borne, and E. W. Schlag, *Chem. Phys. Lett.* **3**, 492 (1969).

9. T. Baer, W. B. Peatman, and E. W. Schlag, *Chem. Phys. Lett.* **4**, 243 (1969).

10. R. Spohr, P. M. Guyon, W. A. Chupka, and J. Berkowitz, *Rev. Sci. Instrum.* **42**, 1872 (1971).

11. P.-M. Guyon and T. Baer, in *High Resolution Laser Photoionization and Photoelectron Studies*, edited by I. Powis, T. Baer, and C. Y. Ng, Wiley Series in Ion Chemistry and Physics (Wiley, Chichester, 1995), Chap. 1.

12. T. Baer, in *Gas Phase Ion Chemistry*, edited by M. T. Bowers (Academic Press, New York, 1979) Vol. 1, p. 153.

13. T. Baer, *Adv. Chem. Phys.* **64**, 111 (1986).

14. T. Baer, J. Booze, and K.-M. Weitzel, in *Vacuum Ultraviolet Photoionization and Photodissociation of Molecules and Clusters*, edited by C. Y. Ng (World Scientific, Singapore, 1991), p. 259.

15. H. M. Rosenstock, R. Buff, M. A. A. Ferreira, S. G. Lias, A. C. Parr, R. Stockbauer, and J. L. Holmes, *J. Am. Chem. Soc.* **104**, 2337 (1982).

16. J. P. Gilman, T. Hsieh, and G. G. Meisels, *J. Chem. Phys.* **78**, 3767 (1983).

17. T. Nishimura, P. R. Das, and G. G. Meisels, *J. Chem. Phys.* **84**, 6190 (1986).

18. T. Baer, J. C. Morrow, J. D. Shao, and S. Olesik, *J. Am. Chem. Soc.* **110**, 5633-5638 (1988).

19. K. Norwood, A. Ali, G. D. Flesch, and C. Y. Ng, *J. Am. Chem. Soc.* **112**, 7502 (1990).

20. K. Norwood and C. Y. Ng, *J. Chem. Phy.* **93**, 6440 (1990).

21. O. Dutuit, T. Baer, C. Metayer, and J. Lemaire, *Int. J. Mass Spectrom. Ion. Proc.* **110**, 67 (1991).

22. K. M. Weitzel, J. Mahnert, and M. Penno, *Chem. Phys. Lett.* **224**, 371 (1994).

23. F. Güthe and K.-M. Weitzel, *Ber. Bunsenges. Phys. Chem.* **104**, 484 (1997).

24. M. Evans, C. Y. Ng, C.-W. Hsu, and P. Heimann, *J. Chem. Phys.* **106**, 978 (1997).

25. J. Mähnert, F. Güthe, and K.-M. Weitzel, *Ber. Bunsenges. Phys. Chem.* **100**, 1899 (1996).

26. K. Norwood, J. H. Guo, G. Luo, C. Y. and Ng, *J. Chem. Phys.* **90**, 6026 (1989).

27. K. Norwood, A. Ali, and C. Y. Ng, *J. Chem. Phys.* **95**, 8029 (1991).

28. K. Norwood and C. Y. Ng, *Chem. Phys. Lett.* **156**, 145 (1989).

29. C. Y. Ng, in *Vacuum Ultraviolet Photoionization and Photodissociation of Molecules and Clusters*, edited by C. Y. Ng (World Scientific, Singapore, 1991), p. 169-257.

30. W. Kamke, in *Cluster Ions*, edited by C. Y. Ng, T. Baer, and I. Powis, (John Wiley & Sons, Chichester, 1993), p. 1.

31. K. Mitsuke and K. Ohno, *J. Phys. Chem.* **93**, 501 (1989).

32. J. A. Booze and T. Baer, *J. Chem. Phys.* **96**, 5541 (1992).

33. J. Mahnert, H. Baumgärtel, and K.-M. Weitzel, *J. Chem. Phys.* **103**, 7016-7024 (1995).

34. Y. Morioka, T. Tanaka, H. Yoshii and T. Hayaishi, J. Chem. Phys. **109**, xxxx (1998).

35. P. M. Guyon, T. R. Govers, and T. Baer, *Z. Phys. D* **4**, 89 (1986).

36. P. M. Guyon, T. Baer, S. K. Cole, and T. R. Govers, *Chem. Phys.* **119**, 145 (1988).

37. C. Y. Ng, in *Techniques for the Study of Ion-Molecule Reactions*, edited by J. M. Farrar, J.M. W. H. and Saunders Jr., (John Wiley & Sons, New York, 1988), p. 417.

38. T. Baer, L. Squires, and A. S. Werner, *Chem. Phys.* **6**, 325 (1974).

39. I. Koyano and K. Tanaka, in *State-Selected and State-to-State Ion-Molecule Reaction Dynamics I: Experiment*, edited by C. Y. Ng and M. Baer (Wiley, New York, 1992), Adv. Chem. Phys. **82**, p. 263.

40. E. Waterstradt. R. Jung. H.-J Deitrich and K. Muller-Dethlefs. *Rev. Sci Instrum.* **64**. 3104 (1993).

41. R. I. Hall. A. McConkey. K. Ellis. G. Dawber. L. Avaldi. M. A. MacDonald. and G. C. King, *Meas. Sci. Technol.* **3**. 316 (1992).

42. Y. Lu. Y. Morioka. T. Matsui. T. Tanaka. H. Hoshii. R. I. Hall. T. Hayaishi. and K. Ito, *J. Chem. Phys.* **102**. 1553 (1995).

43. Y. Morioka. Y. Lu. T. Matsui. T. Tanaka. H. Yoshii. T. Hayaishi. and R. I. Hall. J. Chem. Phys. **104**. 9357 (1996).

44. *High Resolution Laser Photoionization and Photoelectron Studies*. edited by I. Powis. T. Baer and C. Y. Ng. Wiley Series in Ion Chemistry and Phsics. (Wiley. Chichester 1995).

45. G. Reiser. W. Habenicht. K. Muller-Dethlefs and E. W Schlag. *Chem. Phys. Lett.* **152**. 119 (1988)

46. K. Muller-Dethlefs. M. Sander. and E. W Schlag. *Z Naturforsch. Teil A*. **39**. 1089 (1984).

47. K.-M. Weitzel. K.M. and F. Güthe. *Chem. Phys. Lett.* **251**. 295 (1996).

48. C.-W. Hsu. M. Evans. P. Heimann. K. T. Lu. and C. Y. Ng. *J. Chem. Phys.* **105**. 3950 (1996).

49. C.-W. Hsu. M. Evans. C. Y. Ng. P. Heimann. *Rev. Sci. Instrum.* **68**. 1694 (1997).

50. R. C. Shiell. M. Evans. S. Stimson. C.-W. Hsu. C. Y. Ng. and J. W. Hepburn. *Phys. Rev. Lett.* **80**. 472 (1998).

51. C.-H. Hsu. P. Heimann. M. Evans. S. Stimson. and C. Y. Ng. *Chem. Phys.* **231**. 121-143 (1998).

52. S. Stimson. Y.-J. Chen. M. Evans. C.-L. Liao. C. Y. Ng. C.-W. Hsu. and P. Heimann. *Chem. Phys. Lett.* **289**. 507 (1998).

53. S. Stimson. M. Evans. C. Y. Ng. C. Destandau. G. Chambaud. P. Rosmus. C.-W. Hsu. and P. Heimann. *J. Chem. Phys.* **108**. 6205 (1998).

54. C.-W. Hsu. M. Evans. S. Stimson. and C. Y. Ng. *J. Chem. Phys.* **109**. 1285 (1998).

55. C.-W. Hsu. M. Evans. S. Stimson. C. Y. Ng. and G. K. Jarvis. *J. Chem. Phys.* **110**. 315 (1999).

56. G. K. Jarvis, Y. Song, and C. Y. Ng, *Rev. Sci. Instrum.*, **70**, 2615 (1999).

57. P. Heimann, M. Koike, C.-W. Hsu, M. Evans, K. T. Lu, C. Y. Ng, A. Suits, and Y. T. Lee, *Rev. Sci. Instrum.***68**, 1945 (1997).

58. C. Y. Ng, in *Photoionization and photodetachment*, edited by C. Y. Ng, *Adv. Ser. Phys. Chem.*(World Scientific, Singapore, 1999), Vol. 10A, in press.

59. A. Tabché-Fouhailé, I. Nenner, P. M. Guyon, and J. Delwiche, *J. Chem. Phys.* **75**, 1129 (1981).

60. P. C. Cosby, J. -B. Ozenne, J. T. Moseley, and D. L. Albritton, *J. Mol. Spect.* **79**, 203 (1980).

61. J. T. Moseley, P. C. Cosby, J.-B. Ozenne, and J. Durup, *J.Chem. Phys.***70**, 1474 (1979).

62. J. C. Hansen, J. T. Moseley, A. L. Roche, and P. C. Cosby, *J. Chem. Phys.* **77**, 1206 (1982).

63. H. Helm, P. C. Cosby, and D. L. Huestis, *J. Chem. Phys.* **73**, 2629 (1980).

64. Wiley McC. and I.H. McLaren, *Rev. Sci. Instrum.* **26**, 1150 (1955).

65. W. A. Chupka, J. Chem. Phys. **98**, 4520 (1993).

66. J. Jortner and M. Bixon, J. Chem. Phys. **99**, 3133 (1995).

67. T. F. Gallagher, *Rydberg Atoms* (Cambridge University Press, Cambridge, 1994).

68. M. Penno, A. Holzwarth, and K.-M. Weitzel, *Mol. Phys.*, in press.

69. K.-M. Weitzel, M. Malow, G. K. Jarvis, T. Baer, Y. Song, and C. Y. Ng, *J. Chem. Phys.*, submitted.

70. G. K. Jarvis, K.-M. Weitzel, M. Malow, T. Baer, Y. Song, and C. Y. Ng, *Phys. Chem. Chem. Phys.*, submitted.

71. J. L. Franklin, P. M. Hierl, and D. A. Whan, *J. Chem. Phys.* **47**, 3148 (1967).

CHAPTER 8. HIGH-RESOLUTION ENERGY-SELECTED STUDY OF THE REACTION $NH_3^+ \rightarrow NH_2^+ + H$: ACCURATE THERMOCHEMISTRY FOR THE NH_2/NH_2^+ AND NH_3/NH_3^+ SYSTEMS

A paper to be published in *Journal of Chemical Physics*, **115**, (2001)

Y. Song, X.-M. Qian, K.-C. Lau and C.Y. Ng

Jianbo Liu and Wenwu Chen

Abstract:

Employing the newly developed high-resolution pulsed field ionization-photoelectron (PFI-PE)-photoion coincidence (PFI-PEPICO) technique, we have examined the dissociation of energy-selected NH_3^+ to form $NH_2^+ + H$ near its threshold. The breakdown curves for NH_2^+ and NH_3^+ thus obtained yield a value of 15.765±0.001 eV for the 0 K dissociation threshold or appearance energy (AE) for NH_2^+ from NH_3. This value, together with the known ionization energy (IE=10.1864±0.0001 eV) and 0 K bond dissociation energy (D_0=4.6017±0.0025 eV) for NH_3, allows the determination of the $D_0(NH_2^+\text{-}H)$ and $IE(NH_2)$, which are 5.5786±0.0010 and 11.1633±0.0025 eV, respectively. Using the known 0 K heats of formation ($\Delta H°_{f0}$) for NH_3 and H and the $AE(NH_2^+)$, we obtain the $\Delta H°_{f0}(NH_2^+)$ = 302.60±0.08 kcal/mol. The PFI-PE spectrum for NH_3 exhibits a step-like feature at the 0 K $AE(NH_2^+)$, indicating that the dissociation of excited NH_3 in high-n ($n \geq 100$) Rydberg states at energies slightly above the dissociation threshold occurs on a time scale $\leq 10^{-7}$ s. This step confirms the $AE(NH_2^+)$ value derived from the PFI-PEPICO measurements. Highly accurate energetic data with well-founded error limits, such as those obtained in the present and other studies using the PFI techniques, are expected to play an important role for the development of the next generation of *ab initio* quantum computation procedures. This experiment has stimulated a state-of-the-art *ab initio* quantum chemical calculation (Dixon *et al.*, J. Chem. Phys., accepted). The comparison between theoretical predictions and the best experimental results for the

NH_2/NH_2^+ and NH_3/NH_3^- systems indicates that the accuracy of the computational scheme used is ≤0.4 kcal/mol.

I. Introduction

As the simplest amine, ammonia (NH_3) is of fundamental interest to both chemistry and biology, especially considering its ability of forming hydrogen bond. For this reason, it is important to establish accurate energetic information for NH_2, NH_3, NH_2^-, and NH_3^-. Bond dissociation energies at 0 K (D_0) for NH_2-H [$D_0(NH_2\text{-H})$] and NH_2^+-H [$D_0(NH_2^+\text{-H})$] can be determined by measurements of the ionization energies (IEs) for NH_2 [$IE(NH_2)$] and NH_3 [$IE(NH_3)$] and the 0 K dissociation threshold or appearance energy (AE) for NH_2^- [$AE(NH_2^-)$] from NH_3 according to Eqs. (1) and (2).[1]

$$D_0(NH_2^+\text{-H}) = AE(NH_2^-) - IE(NH_3) \quad (1)$$

$$D_0(NH_2\text{-H}) = AE(NH_2^-) - IE(NH_2) \quad (2)$$

The uncertainties for $D_0(NH_2^-\text{-H})$ and $D_0(NH_2\text{-H})$ thus obtained depend on the error limits of $IE(NH_2)$, $IE(NH_3)$, and $AE(NH_2^-)$.

In traditional photoionization and photoelectron studies using laboratory discharge lamps and second generation synchrotron radiation sources, the uncertainties for IE and AE values obtained for polyatomic molecules generally fall in the range of 5-100 meV.[2,3] The AE values for most molecules have been determined by dissociative photoionization onsets of fragment ions obtained in photoionization efficiency (PIE) measurements. Although the PIE measurement is straightforward, the determination of the "true" ion dissociation threshold based on the PIE onset for a fragment ion can be ambiguous. Partly due to the hot band and kinetic shift effects and/or the lack of Franck-Condon factors for photoionization transitions,[2] the PIE onset for a fragment ion formed in the dissociative photoionization of a polyatomic molecule can be very gradual, resulting in a large uncertainty.

A more reliable method for AE determinations is the conventional vacuum ultraviolet (VUV) threshold photoelectron (TPE)-photoion coincidence (TPEPICO)

technique.[4,5] which involves the detection of correlated TPE-photoion pairs. The TPEPICO scheme has been widely used for the study of state- or energy-selected ion dissociation dynamics.[4,5] The analysis of the breakdown curves for parent and fragment ions based on TPEPICO time-of-flight (TOF) data is made to recover information concerning the AE for the fragment ion.[5] The simulation of the breakdown curves applies statistical theories and takes into account the internal energy population of the parent ion. However, the precision of AE values derived from this method has been limited by the relatively low TPE resolution. In TPEPICO measurements, a particular difficulty is that the intensity for the cold parent ion is always finite at energies above the 0 K AE because of the hot-electron tail associated with the TPE transmission function. Since the actual shape of the TPE transmission function can also be complicated by near resonance autoionization features, the detailed simulation of breakdown curves can be difficult. As a result of these difficulties, uncertainties for 0 K AE values derived in previous TPEPICO studies are often comparable to those obtained in PIE measurements.[2,3] Since the actual contributions of these various experimental difficulties to the error limits are hard to account for, experimental uncertainties for IE and AE values obtained in many previous PIE and TPEPICO measurements, especially those for polyatomic molecules, are often assigned improperly. Thus, it is not surprising to find that most IE and AE values thus obtained and reported in the literature do not agree after taking into account their assigned experimental uncertainties.

The development of laser based pulsed field ionization (PFI) techniques has made possible the measurement of PFI-photoelectron (PFI-PE) spectra for diatomic molecules and simple triatomic and polyatomic hydrides to the rotational resolved level.[6-8] The proper analyses of rotationally resolved PFI-PE spectra have provided definitive IE values for these molecules with uncertainties limited only by energy calibrations. In the case of NH_3, the rotationally resolved PFI-PE spectrum has been measured using the non-resonant two-photon (N2P) PFI-PE scheme.[9] This measurement, together with the rotational-resolved infrared study of NH_3^+,[10] provides an IE(NH_3) value of 10.1864±0.0001 eV.[9]

The recent successful implementation of synchrotron-based high-resolution PFI techniques using the monochromatized VUV facility at the Chemical Dynamics Beamline

of the Advanced Light Source (ALS) has greatly enhanced the potential of the PFI-PE method for routine, accurate IE measurements of gaseous molecules.[1,11,12] Most recently, we have developed a synchrotron based PFI-PE-photoion coincidence (PFI-PEPICO) scheme achieving resolutions for ion internal energy selections similar to that made in PFI-PE measurements.[13] Since the transmission function for PFI-PEs is free from the hot-electron tail problem, we have demonstrated previously that highly reliable 0 K AEs for CH_3^+ from CH_4 and C_2H^+ from C_2H_2 can be determined unambiguously with unprecedented precision using this PFI-PEPICO scheme.[14,15] Furthermore, step-like features in the PFI-PE spectrum for CH_4 and C_2H_2 were observed,[16] which confirm the AE values. In this report, we present the results of a similar PFI-PE and PFI-PEPICO study of the dissociative photoionization process (3).

$$NH_3 + h\nu \rightarrow NH_2^+ + H + e^- \qquad (3)$$

On the basis of the $AE(NH_2^+)$ value determined in the present study, together with the known $IE(NH_3)$,[9,10] we have obtained an accurate value for the $D_0(H_2N^+\text{-}H)$. By using the known $D_0(H_2N\text{-}H)$[17] and appropriate thermochemical cycle, we have derived values for the $IE(NH_2)$, and the 0 K heat of formation of NH_2^+ [$\Delta H_{f0}^0(NH_2^+)$].

We note that in early PIE measurements, Dibeler *et al.*[18] and McCulloh[19] reported $AE(NH_2^+)$ values of 15.73±0.02 and 15.768±0.004 eV, respectively. However, in later TPEPICO studies, significantly lower $AE(NH_2^+)$ values of 15.60±0.02 and 15.50 eV were obtained by Ruede *et al.*[20] and Powis,[21] respectively. The 0 K $AE(NH_2^+)$ value of 15.768±0.004 eV, which was deduced by McCulloh based on a simulation of PIE curves for NH_2^+ from NH_3 recorded at 160 K and 298 K, was likely the most reliable among previous measurements. Similar to the conclusion of previous PFI-PEPICO studies,[14-16] the 0 K $AE(NH_2^+)$ value determined in the present PFI-PEPICO study is marked unambiguously by the disappearance energy[14,15] of the parent NH_3^+ ion and the step-like feature resolved in the PFI-PE spectrum of NH_3 and is thus not dependent on any

simulation. This, together with a higher energy resolution used, has resulted in a smaller error limit for the 0 K AE(NH_2^+) obtained in the present experiment.

II. Experiment

The PFI-PE and PFI-PEPICO experiments were conducted using the high-resolution VUV photoelectron-photoion facility of the Chemical Dynamics Beamline at the ALS, which was operated in the multibunch mode (period=656 ns, dark gap=112 ns).[1,10,12,22-25] In the present experiment, Ar was used in the gas filter to suppress higher undulator harmonics with photon energies (hν) greater than 15.76 eV. A 2400 lines/mm grating (dispersion = 0.64 Å/mm) was used to disperse the first order harmonic of the undulator VUV beam with entrance/exit slits set in the range of 30-100 μm. The resulting monochromatic VUV beam was then focused into the photoionization/photoexcitation (PI/PEX) center of the photoelectron-photoion apparatus. The hν calibration was achieved using the $Ne^+(^2P_{3/2})$, $Ar^+(^2P_{3/2})$, and $Xe^+(^2P_{3/2})$ PFI-PE bands. On the basis of previous experiments, the accuracy of the energy calibration is believed to be within ±0.5 meV.[1,11,26]

The PFI-PE and PFI-PEPCO measurements were achieved by employing the TOF scheme.[13,24] The PFI pulse (height =7.3 V/cm, width=180 ns) was applied ≈10 ns after the start of the dark gap. The PFI pulse also served to extract PFI-photoions toward the ion detector.[13] The average accumulation time for a PFI-PEPICO TOF spectrum is ≈20 min. The PFI-PEPICO resolution achieved is ≈1.0 meV (FWHM).[13-15]

The NH_3 sample (obtained from Aldrich, purity = 99.99%) is introduced into the PI/PEX region as a skimmed neat NH_3 supersonic beam (stagnation pressure = 600 Torr and stagnation temperature = 298 K). We estimate that NH_3 at the PI/PEX region consists of ≈85% cold beam sample and ≈15% thermal background in the photoionization chamber.[13-15]

III. Results and discussion

A. PFI-PEPICO TOF spectra for NH_2^+ and NH_3^+

We have obtained PFI-PEPICO TOF spectra for NH_2^+ and NH_3^+ in the hν region of 15.65-15.85 eV, which is near the NH_3^+ dissociation threshold. Selected PFI-PEPICO TOF spectra measured at hν=15.7129, 15.7513, 15.7561, 15.7629, 15.7800 and 15.8279 eV are depicted in Fig. 8-1. These spectra have been background corrected using procedures as described in previous studies.[13-15] At hν=15.7129 eV, which is below the AE(NH_2^+), only the parent ion TOF peak at 20.34 μs was observed. As the hν is increased, the relative abundance for the daughter ion at 19.78 μs increases correspondingly. The spectra shown at hν=15.7800 and 15.8279 eV are dominated by the TOF peak for the daughter ion with only a small residual parent ion peak. As shown in the analysis below, the relative abundance for the parent NH_3^+ was found to remain essentially constant at 0.10 at hν values above the AE(NH_2^+). The residual coincidence intensity for the parent NH_3^+ ion peak observed at hν=15.7800 and 15.8279 eV can be attributed to background coincidences associated with hot electrons dispersed into the dark gap and the dissociative photoionization of ammonia dimers and clusters formed in the supersonic expansion.

B. Simulation of breakdown curves for NH_2^+ and NH_3^+

Similar to previous PFI-PEPICO studies,[13-15] the TOF peak shapes for the parent NH_3^+ and daughter NH_2^+ ions are analyzed to consist of the contribution of a narrow component due to the cold NH_3 beam sample and a broad component arising from the thermal NH_3 background. As shown in Fig. 8-1, the daughter ion TOF peak is broad at hν=15.7513 eV, indicating that daughter ions are mostly formed at this energy by photoionization of thermal (298 K) background NH_3. The daughter peak at hν=15.7561 eV clearly exhibits a narrow cold component and a broad thermal component. The broad shape of the TOF peak for NH_2^+ observed at hν=15.8279 eV can be attributed to the finite kinetic energy release of process (3). We note that the NH_3^+ PFI-PEPICO peaks at hν=15.7561, 15.7513, and 15.7129 eV appear to be asymmetric. This is likely caused by a finite misalignment of the molecular beam and the VUV beam, such that the average flight

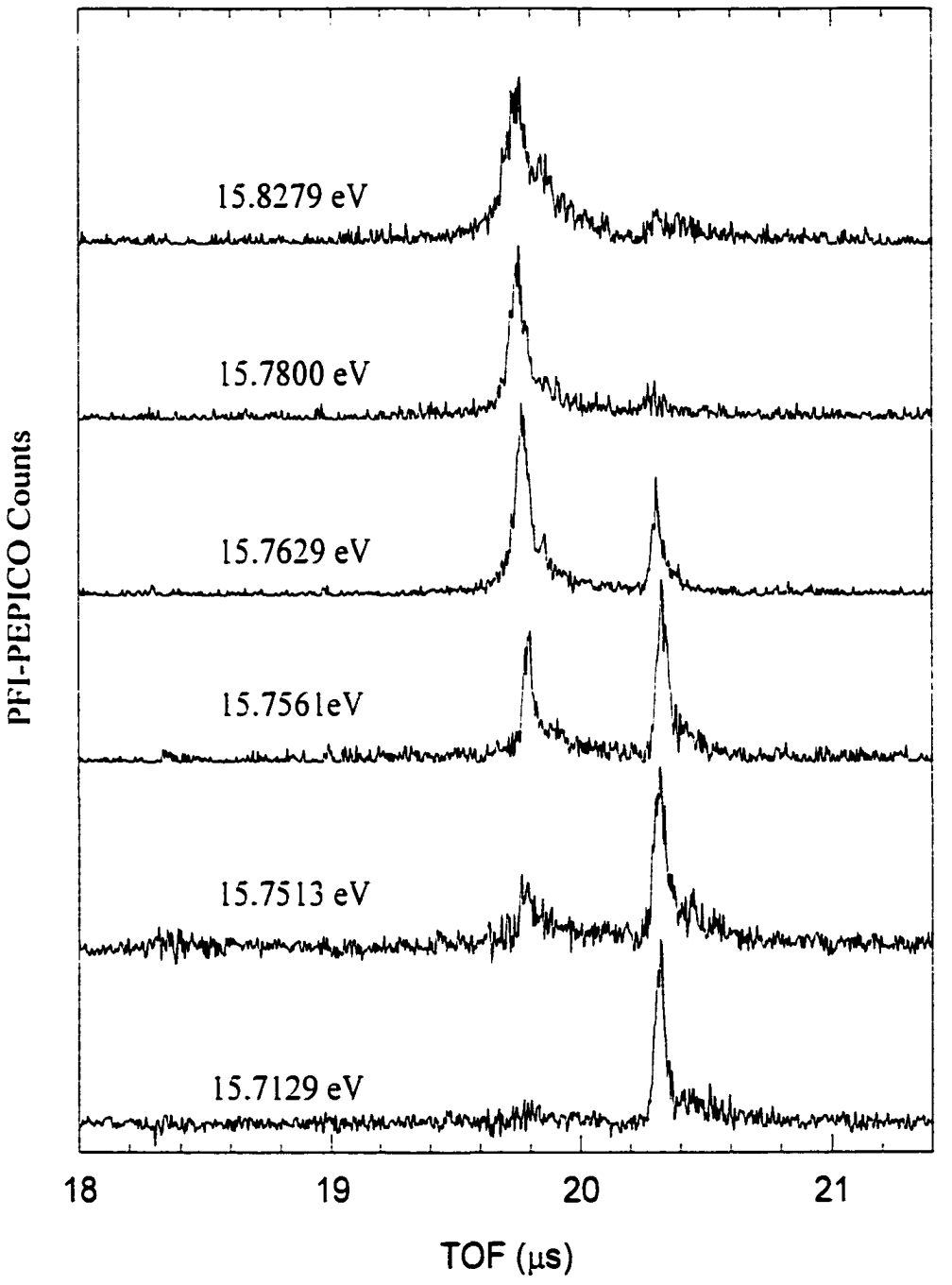

Figure 8-1 Selected PFI-PEPICO TOF spectra for NH_2^+ and NH_3^- at photon energies hν=15.7129, 15.7513, 15.7561, 15.7629, 15.7800, and 15.8279 eV. The TOF peaks centered at 19.78 and 20.34 μs are due to NH_2^- and NH_3^-, respectively.

times for ions formed by photoionization of the thermal and cold samples are slightly different. The previous studies indicated that the TOF peak could be distorted due to the pulsed extraction scheme used in the PFI-PEPICO measurements.[13]

In order to construct the breakdown curves for the parent NH_3^+ and daughter NH_2^+ ions, we first obtained the relative intensities for NH_3^+ and NH_2^+ ions based on their respective TOF peak areas observed in the PFI-PEPICO TOF spectra. The fractional abundance for NH_3^+ (NH_2^+) at a given hν was obtained by dividing the NH_3^+ (NH_2^+) ion intensity by the sum of the NH_3^+ and NH_2^+ ion intensities. These breakdown curves for NH_3^+ (open circles) and NH_2^+ (open squares) representing the plots of the fractional abundances for NH_3^+ and NH_2^+ as a function of hν are shown in Fig. 8-2(a). These breakdown curves include both the cold and thermal ion signals for NH_2^+ and NH_3^+. In order to derive the relative abundances for NH_3^+ and NH_2^+ due to the cold beam NH_3 sample, we have simulated the NH_2^+ and NH_3^+ ion peaks resolved in PFI-PEPICO TOF spectra obtained in the hν range of hν=15.65-15.85 eV using two Gaussian functions with widths of ≈100 ns and ≈300 ns for the cold and thermal components, respectively, as described in the previous PFI-PEPICO studies.[14,15] Figure 8-2(b) depicts the breakdown curves for NH_3^+ (solid circles) and NH_2^+ (solid squares) taking into account only the cold NH_2^+ and NH_3^+ ion signals. As expected, due to the rotational cooling of NH_3 achieved by the supersonic expansion, the cold breakdown curves shown in Fig. 8-2(b) are sharper, showing that the dissociation of NH_3^+ to $NH_2^+ + H$ is complete in an energy interval of ≈15 meV.

We have simulated the breakdown diagrams of Figs. 8-2(a) and 8-2(b) using procedure described previously.[27] The simulation assumes that the ion energy resolution is infinitely narrow and that the broadening of the breakdown diagram is due solely to the thermal excitation of parent NH_3. The thermal energy distribution in NH_3 was determined by calculating the density of rovibrational states using the Beyer-Swinehart direct count algorithm[28] based on the known vibrational frequencies and rotational constants for NH_3. Due to the relatively high vibration frequencies for NH_3, the thermal energy for this system

Figure 8-2 (a) Breakdown curves for NH_3^+ (O) and NH_2^+ (□) in the hν range of 15.69-15.83 eV obtained using the entire (thermal and cold) NH_3^+ and NH_2^+ ion signals. The dashed (– –) curves are simulation calculated assuming 10% thermal (298 K) and 90% cold (60 K) NH_3 sample. (b) Breakdown curves for NH_3^+ (•) and NH_2^+ (■) in the hν range of 15.69-15.83 eV obtained using only the cold NH_2^+ and NH_3^+ ion signals. The solid lines (—) are simulated curves obtained assuming a cold NH_3 sample at 60 K. See the text. (c) The PFI-PE spectrum of NH_3 in the hν range of 15.69-15.83 eV.

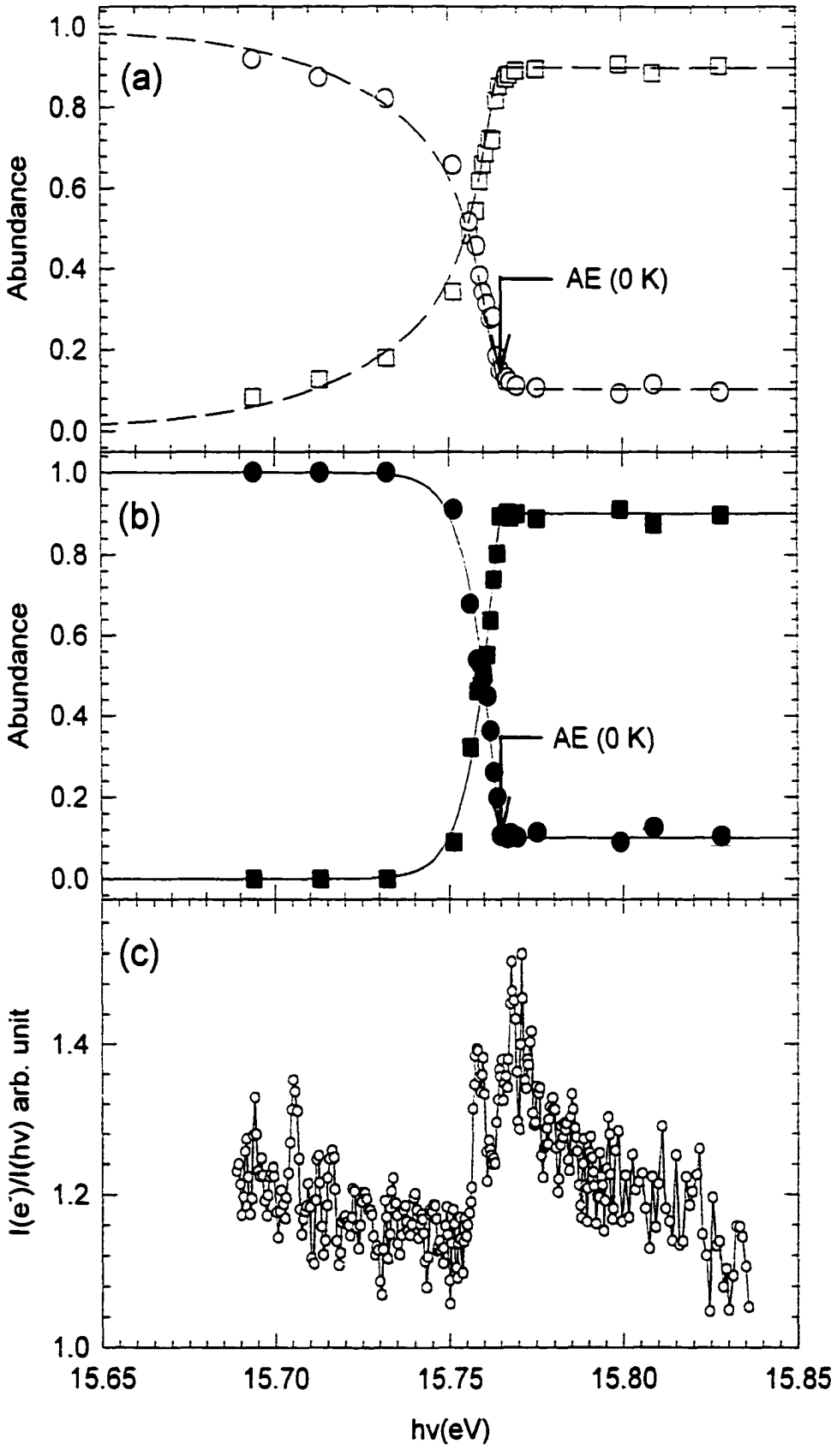
(a)
Abundance
AE (0 K)
(b)
Abundance
AE (0 K)
(c)
I(e⁻)/I(hv) arb. unit
hv(eV)
1.0
0.8
0.6
0.4
0.2
0.0
1.4
1.2
15.65
15.70
15.75
15.80
15.85

is mainly contributed by rotational excitations. By assuming a temperature of 60 K for NH_3 in the molecular beam, we have obtained an excellent fit (solid lines) of the cold breakdown curves shown in Fig. 8-2(b), yielding a value of 15.765±0.001 eV for the 0 K AE(NH_2^+) from NH_3. The dashed lines in Fig. 8-2(a) are calculated breakdown curves assuming the NH_3 sample to consist of ≈10 % thermal background and ≈90 % cold (60 K) beam sample. The simulation of the breakdown curves also assumes a constant false coincidence background of 10% at hν values above the AE, resulting in the fractional abundances for parent NH_3^+ and daughter NH_2^+ to attain constant values of 0.1 and 0.90, respectively, at the hν ≥ AE.

There are two types of coincidence background associated with the present PFI-PEPICO experiment. One does not correlate with PFI-PEs formed at the dark gap. In this experiment, the ALS gap (112 ns) is narrower than that (144 ns) used in the PFI-PEPICO studies.[13-15] Thus, the contamination due to a finite dispersion of hot electrons into the dark gap in the present study is higher than that in the latter studies. The hot electrons occur at the dark gap are probably responsible for the majority of background coincidences, manifesting as stable, cold parent ions in the PFI-PEPICO TOF spectra detected at hν≥AE(NH_2^+), e.g., at hν = 15.7800 and 15.8279 eV (see Fig. 8-1).

The other type of coincidence background arises from PFI-PEs produced by the electric field pulses applied during the dark gaps. Under the conditions for supersonic expansion of NH_3 in the present experiment, we expect the formation of NH_3 dimers [$(NH_3)_2$] and clusters in the beam sample.[29] At photon energies well above the IE(NH_3), the dissociative photoionization of $(NH_3)_2$ according to reaction (4) is expected to be the dominant channel.

$$(NH_3)_2 + h\nu \rightarrow NH_3^+ + NH_3 + e^- \qquad (4)$$

In this reaction, NH_3^+ is stabilized by the ejection of NH_3. We believe that this type of background is also responsible for the observation of a finite intensity for the NH_3^+ TOF peak at photon energies above the AE for reaction (3). Since these photon energies

involved here are well above the dissociative photoionization threshold for $(NH_3)_2$, the cross section of reaction (4) should be essentially independent of energy in the narrow energy range of concern in the present study. Thus, the constant, finite fractional abundance for NH_3^+ beyond the AE(NH_2^+) from NH_3 as observed in Figs. 8-2(a) and 8-2(b) may also be partly attributed to dissociative photoionization processes such as reaction (4).

In the previous experiment on CH_4 (C_2H_2), the 0 K AE(CH_3^+) [AE(C_2H^+)] is found to be marked by the disappearance energy for the parent CH_4^+ ($C_2H_2^+$), i.e., the energy at which the fractional abundance for the parent CH_4^+ ($C_2H_2^+$) equal to *zero*.[14,15] Although the fractional abundance for the parent NH_3^+ ion does not go to zero at the AE in this case, the 0 K AE(NH_2^+) value is distinctly identified by the sharp break [marked as 0 K AE in Figs. 8-2(a) and 8-2(b)] of the breakdown curves, at which the fractional abundance for the parent NH_3^+ reaches its lowest value. The use of the sharp breaks of the breakdown curves observed both in Figs. 8-2(a) and 8-2(b) for the 0 K AE determination is supported by the simulation. Nevertheless, we emphasize that the 0 K AE(NH_2^+) value determined here by the sharp break is distinct and does not depend on a detailed simulation of the breakdown curves.

To illustrate the high precision of the 0 K AE(NH_2^+) value determined in this study, we have shown in Fig. 8-3 a magnified view of the breakdown data, together with their error bars, for parent NH_3^+ in the hν range of 15.755-15.830 eV. Here, the breakdown data for NH_3^+ obtained using the entire (thermal and cold) NH_3^+ and NH_2^+ ion signals are shown as open squares and those using only the cold NH_3^+ and NH_2^+ ion signals are given as solid circles. The dashed and solid curves are simulation curves for the open squares and solid circles data, respectively. As clearly shown in Fig. 8-3, both breakdown curves resolved a sharp break at 15.765±0.001 eV, which is taken here as the 0 K AE(NH_2^+).

C. PFI-PE spectrum for NH_3

Figure 8-2(c) depicts the PFI-PE spectrum for NH_3 in the energy range of 15.68-15.84 eV. In addition to some sharp spectral features (notably at hν = 15.705, 15.757, and 15.768 eV; not discussed here) an obvious step is observed in the region of 15.755-15.765 eV. The top of this step at 15.7652 eV coincides with the 0 K AE(NH_2^+) identified in the

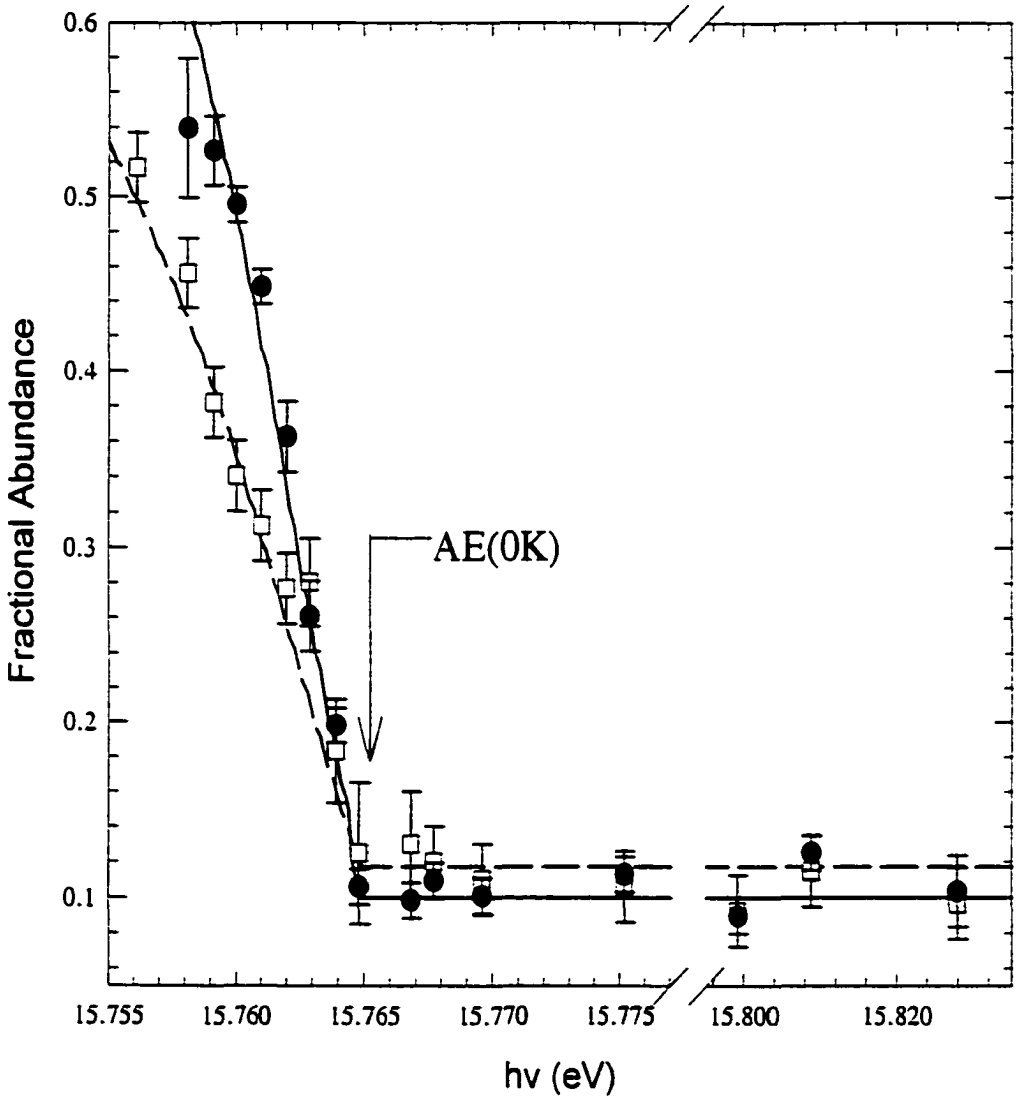

Figure 8-3 A magnified view of the breakdown curves for NH_3^+ in the hv range of 15.755-15.830 eV. The breakdown data for NH_3^+ obtained using the entire NH_3^+ and NH_2^+ ion signals are shown as open squares (□) and those obtained using only the cold ion signals are shown as solid circles (•). The dashed (– –) and solid (—) curves are simulated curves for the open squares and solid circles breakdown data, respectively.

breakdown diagrams of Figs. 8-2(a) and 8-2(b). A detailed discussion concerning the conditions for the observation of a step at the 0 K ion dissociation threshold has been given previously.[16] This step, which marks the 0 K AE in the PFI-PE spectrum, is attributed to the lifetime switching effect[16] at the AE, where NH_3* species with shorter lifetimes are converted into NH_2* fragments with longer lifetimes. Here, NH_3* and NH_2* represent excited NH_3 and NH_2, respectively, in long-lived high-n ($n \geq 100$) Rydberg states. The longer lifetime for NH_2* results from the fact that NH_2* formed at the AE has an energy below the IE(CD_3) and thus cannot decay via autoionization. The observation of the sharp step in the PFI-PE spectrum indicates[16] that the conversion from NH_3* to NH_2* at energy above the AE of reaction (3) is complete prior to PFI and that process (3) has a dissociation rate constant $\geq 10^7$ s^{-1}. This step resolved in the PFI-PE spectrum for NH_3 can be taken as a confirmation for the 0 K AE(NH_3^+)=15.765±0.001 eV determined in the PFI-PEPICO study.

The dissociation leading to the production of NH_2* from NH_3* formed by VUV excitation of thermally excited NH_3 molecules occurs below the 0 K AE. Considering the fact that the lifetimes for NH_2* are longer than those for NH_3*, we expect that the PFI-PE signal from NH_2* produced by thermally excited NH_3 molecules at photon energies below the 0 K AE is also magnified. As a result of this magnification effect of PFI events for NH_2*, the nominal temperature of 60 K estimated in the simulation for the breakdown curves of NH_2^+ and NH_3^+ is likely higher than the actual temperature for the cold NH_3 sample achieved in the supersonic expansion.

D. Thermochemistry of the NH_2/NH_2^+ and NH_3/NH_3^+ systems

Table 8-I compares the AE(NH_2^+) value obtained in the present experiment with literature values determined by photoionization[18,19,30-33] and TPEPEPCO[20,21] studies. Taking into account the experimental uncertainties, the value of 15.765±0.001 eV for the AE(NH_2^+) determined here is consistent with the PIE value (15.768±0.004 eV) of McCulloh.[19]

We have included in Table 8-I IE values for NH_3 measured in previous PIE,[18,30,32-36] TPEPICO,[20] and N2P-PFI-PE[9,10] studies. These IE values fall in the range of 10.07-

Table 8-I. Comparison of values for 0 K heats of formation ($\Delta H°_{f0}$) for NH_2, NH_2^+, NH_3, and NH_3^+ and 0 K AE for NH_2^+ [$AE(NH_2^+)$] from NH_3.[a]

$AE(NH_2^+)$ (eV)	IE (eV)		$\Delta H°_{f0}$ (kcal/mol)			
	NH_3	NH_2	NH_3	NH_3^+	NH_2	NH_2^+
15.765±0.001[b]	**10.1864±0.0001[c]**	**11.1633 ±0.0025[b]**	**-9.31±0.08[d] (-10.98±0.08)**	**225.59±0.08[e] (223.92±0.08)**	**45.17±0.09[f] (44.50±0.09)**	**302.60±0.08[b] (301.93±0.08)**
15.768±0.004[g]	10.069±0.02[h]	11.14±0.01[g]	-9.30±0.10[i]	222.9±0.09[j]	45.8±0.2[k]	302.7±0.3[k]
15.60±0.02[l]	10.07±0.01[l,m]	11.46±0.01[n]				
15.76±0.05[o]	10.17[p]					
15.50[q]	10.160 ±0.008[r]					
15.75[s]	10.154 ±0.010[t]					
15.73±0.02[r]	10.02 ±0.02[u]					
Semi-empirical G3/G2 values[v]						
15.68/15.79	10.14/10.19	11.12/11.18	-8.5/-9.1 (-10.2/-10.8)	225.4/225.9 (223.6/224.3)	45.2/45.7 (44.5/45.0)	301.6/303.4 (300.9/302.8)
Ab initio predictions[w]						
15.77	10.171	11.176	-9.1 (-10.8)	225.4 (223.7)	45.3 (44.6)	303.0 (302.3)

Table 8-I (Continued)

a. The values in bold are recommended values. The values in parentheses are $\Delta H°_{f298}$ values. The thermal corrections from $\Delta H°_{f0}$'s to $\Delta H°_{f298}$'s are computed at the MP2 level of theory.

b. This work.

c. Reference 9.

d. Reference 42.

e. References 9 and 42.

f. References 17 and 42.

g. Reference 19.

h. Reference 32.

i. Reference 41.

j. Calculated using IE(NH_3)=10.07±0.02 eV as recommended by Ref. 37 and $\Delta H°_{f0}(NH_3)$ = -9.31±0.08 kcal/mol of Ref. 42.

k. References 19 and 38.

l. Reference 20.

m. Reference 33.

n. Reference 40.

o. Reference 31.

p. Reference 35.

q. Reference 21.

r. Reference 18.

s. References 30 and 32.

t. Reference 36.

u. Reference 30.

v. References 43 and 44.

w. Reference 45.

10.186 eV. The latest NIST compilation[37] recommended an IE(NH_3) value of 10.070±0.020 eV. However, since the recent N2P-PFI-PE measurement[9] and infrared study[10] of NH_3^+ are rotationally resolved studies, the IE(NH_3) value of 10.1864±0.0001 eV derived from these experiments should be the most reliable. This value, together with the AE(NH_2^+) = 15.765±0.001 eV determined here, gives the D_0(H-NH_2^+) = 5.579±0.001 eV.

The adiabatic IE(NH_2) has been measured to be 11.14±0.01 eV (see Table 8-I) in a PIE study of NH_2 formed in the reaction of N_2H_4 + H.[38] In a recent photodissociation study using the high-resolution TOF technique involving the PFI detection of H atoms formed in high-n Rydberg states, Mordaunt *et al.* obtained a value of 4.6017±0.0025 eV for D_0(H-NH_2).[17] Combining this D_0(H-NH_2) value and the AE(NH_2^+) value of the present study, we obtain a value of 11.1633±0.0025 eV for IE(NH_2). The latter value is higher than the PIE value by ≈23 meV. The ionization of NH_2 involves the transition from the bent NH_2 radical (103°) to the less bent NH_2^+ (140°-150°). The unfavorable Franck-Condon factors for photoionization transitions, together with finite internal excitations of NH_2 acquired in the reaction, results in a very gradual PIE onset for NH_2^+. Although a substantial effort was made, calculating P, Q and R branches, to fit the rotational tailing near the onset, the IE(NH_2) value thus determined is subject to a certain uncertainty of such a fitting scheme. Gibson et al.[38] assigned the IE(NH_2) to be 1113±1 Å (11.14±0.01 eV). Referring to Fig. 5 of Ref. 38, the IE(NH_2) assignment may also be influenced by an autoionization feature at 1110 Å. Hence, a more conservative estimate for the IE(NH_2) would be 1112±2 Å = 11.15±0.02 eV.[39] Taking into account the experimental error limits, the latter value would have agreed with the IE(NH_2) of 11.1633±0.0025 eV derived using the AE(NH_2^+) value obtained here and the D_0(H-NH_2) value of Ref. 17. To confirm the consistency of these AE(NH_2^+) and D_0(H-NH_2) values, it is necessary to re-examine the IE(NH_2) value at a higher resolution using a cold NH_2 sample. We note that an IE(NH_2)=11.46±0.01 eV has also been reported by Dunlavey et al. in a photoelectron study.[40]

The $\Delta H°_{f0}(NH_3)$ value is well known. A 1977 *JANAF* revision[41] recommends -9.30±0.1 kcal/mol, which is in excellent accord with the -9.31±0.08 kcal/mol[42] given by

the compilation of Glushko *et al.* Using the latter value, IE(NH_3)=234.9034±0.0023 kcal/mol (10.1864±0.0001 eV), $\Delta H°_{f0}(H)$=51.643±0.001 kcal/mol, $D_0(H\text{-}NH_2)$ = 106.118±0.046 kcal/mol (4.6017±0.0025 eV), and AE(NH_2^-) = 363.549±0.023 kcal/mol (15.765±0.001 eV), we have calculated the $\Delta H°_{f0}(NH_3^-)$ = 225.59±0.08 kcal/mol, $\Delta H°_{f0}(NH_2)$= 45.17±0.09 kcal/mol, and $\Delta H°_{f0}(NH_2^+)$= 302.60±0.08 kcal/mol. The values in bold fonts given in Table 8-I represent the most precise energetic data for the NH_2/NH_2^- and NH_3/NH_3^+ systems. It is interesting to note that the error limits of the best $\Delta H°_{f0}(NH_2)$ and $\Delta H°_{f0}(NH_2^+)$ values are now predominantly limited by the uncertainty of $\Delta H°_{f0}(NH_3)$.[41,42]

These highly precise energetic data (values in bold fonts in Table 8-I) would provide a challenge for state-of-the-art *ab initio* computational quantum theories. Currently, the Gaussian-2/Gaussian-3 (G2/G3) procedures are among the most popular quantum chemical computation schemes.[43,44] The G2/G3 theories are "slightly" semi-empirical in nature because they contain a high level correction (HLC) obtained empirically from a fit to a set of experimental energetic data, such as IEs, electron affinities, and heats of formation, by minimizing the deviations between corresponding experimental results and calculated values for atomic and molecular energies. The G2 theory has a more primitive HLC fitting scheme, which only involves a test set of 55 molecules,[43] whereas that for the G3 theory[44] is obtained by fitting a test set of 299 molecules. The reliability of such a fitting scheme demands a precise set of experimental energetic data. As shown Table 8-I, even for a small molecule such as NH_3, the literature IE and AE values have maximum discrepancies of ≈0.17 and ≈0.27 eV, respectively. We note that the error limits assigned for many of these previous experiments do not correspond, indicating that the error assignments for many previous experiments are ill founded. This situation is general for most molecules listed in the NIST[37] and other[2,3] compilations.

We have compiled the AE(NH_2^-), IE(NH_3), IE(NH_2), and $\Delta H°_{f0}/\Delta H°_{f298}$ values for NH_2, NH_2^+, NH_3, and NH_3^+ at the G2/G3 levels of theory for comparison with experimental values in Table 8-I.[42,43] The theoretical G2 and G3 values for $D_0(H\text{-}NH_2)$

[$D_0(H\text{-}NH_2^+)$] are 4.62 eV [5.60 eV] and 4.57 eV [5.54 eV], respectively. These latter values are found to deviate by ≈0.02-0.03 eV from the best experimental $D_0(H\text{-}NH_2)$ [$D_0(H\text{-}NH_2^+)$] value of 4.6017±0.0025 eV (5.5786 ±0.0010 eV). It is interesting to note that the comparisons show that the G2 predictions are in better agreement with the most precise experimental results. The G3 IE(NH_3) and G3 IE(NH_2) are ≈40 meV lower than the corresponding best experimental values. While the G3 $\Delta H°_{f0}(NH_2)$ is in excellent agreement with the most precise experimental value, the G3 $\Delta H°_{f0}(NH_3)$ is higher than the most precise experimental value by 0.8 kcal/mol. This observation indicates that the excellent agreement found between the most precise experimental $\Delta H°_{f0}(NH_3^+)$ and G3 value for $\Delta H°_{f0}(NH_3^+)$ [obtained by summing up G3 IE(NH_3) and G3 $\Delta H°_{f0}(NH_3^+)$ values] is fortuitous and is due mostly to the cancellation of errors. The maximum deviation of ≈0.09 eV (2 kcal/mol) is observed between the best experimental value and G3 prediction for AE(NH_2^+). The range of errors (≤2 kcal/mol) observed here between the best experimental results and G2/G3 predictions is consistent with the error limits targeted in the formulation of G2/G3 procedures.

The better theoretical predictions of G2 over G3 in comparison with the best experimental values of Table 8-I indicates that the HLC fitting scheme in G3 is not better than that in G2 for the NH_2/NH_2^+ and NH_3/NH_3^+ systems. This is expected because the error limits for experimental data set used in the HLC fitting for G3 theory is not improved compared to those for G2 theory. In order to yield more accurate theoretical predictions, the HLC fitting for Gaussion type theories would require a better set of experimental energetic data with smaller error limits. Without doubt, accurate AE, IE, and $\Delta H°_{f0}$ values, such as those presented here with well-founded error limits in the meV range, would serve as an impetus for the development of the next generation of *ab initio* quantum computational procedures.[43,44]

Highly precise energetic data obtained in the present and previous[9,17] PFI-PE studies have stimulated a state-of-the-art *ab initio* quantum chemical calculation by Dixon *et al.*,[45] that is published as an accompanying theoretical article in this journal issue. The computational scheme used is purely *ab initio* except for the use of experimental $\Delta H°_{f0}$'s

for the atoms and available experimental vibrational frequencies for the molecular species. The *ab initio* predictions of Dixon *et al.* are listed in the last row of Table 8-I. The $IE(NH_3)$ = 10.171 eV and $IE(NH_2)$ = 11.176 eV predictions obtained in this calculation are in better agreement with the best experimental values than are the G2/G3 results. The comparison between theoretical results and the best experimental energetic data listed in Table 8-I for the NH_2/NH_2^+ and NH_3/NH_3^+ systems shows that the accuracy of the *ab initio* theory of Dixon *et al* is ≤0.4 kcal/mol).

III. Conclusions

We have examined the unimolecular dissociation of energy-selected NH_3^+ near its threshold for the formation of NH_2^+ + H using a high-resolution PFI-PEPICO technique. The 0 K $AE(NH_2^+)$ thus measured has made possible the determination of highly accurate values for $D_0(H\text{-}NH_2^+)$, $IE(NH_2)$, and $\Delta H°_{f0}(NH_2^+)$ through appropriate thermochemical cycles. Similar to previous studies, a sharp step-like feature is observed in the PFI-PE spectrum of NH_3. The position of this step is in excellent agreement with the 0 K $AE(NH_2^+)$ determined based on the PFI-PEPICO data. Thus, the observation can be taken as a confirmation for the 0 K $AE(NH_2^+)$ determined in the PFI-PEPICO measurement. Furthermore, the observation of the step, together with the breakdown curves for NH_3^+ and NH_2^+, shows that the production of NH_2^* + H (NH_2^+ + H) from excited NH_3^* (NH_3^{*+}) at the dissociation threshold is prompt, occurring in a time scale $\leq 10^{-7}$ s. We believe that accurate thermochemical data with well-founded error limits obtained in the present and similar experiments[13-15] using the PFI-PFIPECO technique would play an essential role for development of the next generation of *ab initio* quantum chemical calculation schemes.

Acknowledgments

This work was supported by the Director, Office of Energy Research, Office of Basic Energy Sciences, Chemical Science Division of the U.S. Department of Energy under Contract No. W-7405-Eng-82 for the Ames Laboratory and Contract No. DE-AC03-76SF00098 for the Lawrence Berkeley National Laboratory. Y.S. is the recipient of the

2000 Henry Gilman Fellowship at Iowa State University. C.Y.N. is grateful for discussions with Prof. T. Baer, Dr. J. Berkowitz, Dr. D. A. Dixon, and Prof. K. M. Ervin.

References

1 C. Y. Ng, *J. Electron Spectroscopy & Related Phenomena*, **112**, 31-46 (2000); C. Y. Ng, *Int. J. Mass Spectrometry*, **204**, 357-386 (2000).

2 H. M. Rosenstock, M. K. Draxl, B. W. Steiner, and J. T. Herron, *J. Phys. Ref. Data*, **6**, Suppl. 1 (1977).

3 S. G. Lias, J. E. Bartmess, J. L. Holmes, R. D. Levin, and W. G. Mallard, *J. Phys. Ref. Data*, **17**, Suppl. 1 (1988).

4. K. Norwood and C. Y. Ng, *J. Chem. Phys.* **91**, 2898 (1989); ibid. **92**, 1513 (1990).

5. K.-M. Weitzel, J. Mähnert, and H. Baumgärtel, *Ber. Bunsenges. Phys. Chem.* **97**, 134, (1993).

6. K. Müller-Dethlefs, M. Sander, and E.W. Schlag, *Z. Naturforsch.*, A **39**, 1089 (1984).

7. E. W. Schlag, "ZEKE Spectroscopy" (Cambridge Univ. Press, Cambridge, 1998).

8. "High Resolution Laser Photoionization and Photoelectron Studies", edited by I. Powis, T. Baer, and C. Y. Ng, *Wiley Series in Ion Chem. & Phys.* (Wiley, Chichester, 1995).

9. G. Reiser, W. Habenicht, and K. Müller-Dethlefs, *J. Chem. Phys.* **98**, 8462 (1993).

10. S. S. Lee and T. Oka, *J. Chem. Phys.* **94**, 1698 (1991).

11. C. Y. Ng, in "Photoionization, and Photodetachment", edited by C. Y. Ng (World Scientific, Singapore, 2000). *Adv. Ser Phys. Chem.* **10A**, Chapter 9, p.394-538.

12. M. Evans and C. Y. Ng, *J. Chem. Phys.* **111**, 8879-8892 (1999); Y. Song, M. Evans, C. Y. Ng, C.-W. Hsu, and G. K. Jarvis, *J. Chem. Phys.* **111**, 1905 (1999); G. K. Jarvis, M. Evans, C. Y. Ng, and K Mitsuke, *J. Chem. Phys.***111**, 3058 (1999).

13. G. K. Jarvis, K.-M. Weitzel, M. Malow, T. Baer, Y. Song, and C. Y. Ng, *Rev. Sci. Instrum.* **70**, 3892-3906 (1999).

14. K.-M. Weitzel, M. Malow, G. K. Jarvis, T. Baer, Y. Song, and C. Y. Ng, *J. Chem. Phys. (Communication)* **111**, 8267-8270 (1999).

15. G. K. Jarvis, K.-M. Weitzel, M. Malow, T. Baer, Y. Song, and C. Y. Ng, *Phys. Chem. Chem. Phys. (Communication)*, **1**, 5259 (1999).

16. K.-M. Weitzel, G. Jarvis, M. Malow, T. Baer, Y. Song, and C. Y. Ng, *Phys. Rev. Lett.* **86**, 3526 (2001).

17. D. H. Mordaunt, R. N. Dixon, and M. N. R. Ashfold, *J. Chem. Phys.* **104**, 6460, 6472 (1996).

18. H. Dibeler, J. A. Walker, and H. M. Rosenstock, *J. Res. NBS*, **70A**, 459 (1966).

19. K. E. McCulloh, *Int. J. Mass Spectrom. Ion Phys.* **21**, 333 (1976).

20. R. Ruede, H. Troxler, C. Beglinger, and M. Jungen, *Chem. Phys. Lett.* **203**, 477 (1993).

21. I. Powis, *J. Chem. Soc. Faraday Trans.* **2**, **77**, 1433 (1981).

22. C.-W. Hsu, M. Evans, P. Heimann, K. T. Lu, and C. Y. Ng, *J. Chem. Phys.* **105**, 3950 (1996).

23. P. Heimann, M. Koike, C.-W. Hsu, D. Blank, X. M. Yang, A. Suits, Y. T. Lee, M. Evans, C. Y. Ng, C. Flaim, and H. A. Padmore, *Rev. Sci. Instrum.* **68**, 1945 (1997).

24. G. K. Jarvis, Y. Song, and C. Y. Ng, *Rev. Sci. Instrum.* **70**, 2615 (1999).

25. C.-W. Hsu, P. Heimann, M. Evans, and C. Y. Ng, *Rev. Sci. Instrum.* **68**, 1694 (1997).

26. S. Stimson, Y.-J. Chen, M. Evans, C.-L. Liao, C. Y. Ng, C.-W. Hsu, and P. Heimann, *Chem. Phys. Lett.* **289**, 507 (1998).

27. T. Baer, Y. Song, C. Y. Ng, J. Liu, and W. Chen, *Faraday Discussion* **115**, 137-145, 2000.

28. T. Beyer and D. F. Swinehart, *Assoc. Comput. Mach., Commun.*,**16**, 379(1973); and J. A. Pople, A. P. Scott, M.W. Wong, and L. Radom, *Isr. J. Chem.* **33**, 345 (1993).

29. C. Y. Ng, *Adv. Chem. Phys.* **52**, 265-362 (1983).

30. F. Qi, L. Sheng, Y. Zhang, S. Yu, and W.-K. Li, *Chem. Phys. Lett.* **234**, 450 (1995).

31. R. Locht, C. Servais, M. Ligot, F. Derwa, and J. Momigny, *Chem. Phys.* **123**, 443 (1988).

32. R. Locht, K. Hottmann, G. Hagenow, W. Denzer, and H. Baumgartel, *Chem. Phys. Lett.* **190**, 124 (1992).

33. R. Locht, B. Leyh, W. Denzer, and G. Hagenow, *Chem. Phys.* **155**, 407 (1991).

34. V. K. Potapov, *Dokl. Akad. Nauk SSSR*,**183**, 386 (1968).

35. W. A. Chupka and M. E. Russell, *J. Chem. Phys.* **48**, 1527 (1968).

36. K. Watanabe and J. R. Mottl, *J. Chem. Phys.* **26**, 1773 (1957).

37. NIST website: http://webbook.nist.gov/chemistry/

38. S. T. Gibson, J. P. Greene, and J. Berkowitz, *J. Chem. Phys.* **83**, 4319 (1985).

39. J. Berkowitz, private communication.

40. S. J. Dunlavey, J. M. Dyke, N. Jonathan, and A. Morris, *Mol. Phys.* **39**, 1121 (1980).

41. *JANAF Thermochemical Tables* (Dow Chemical, Midland, MI, 1977); *J. Phys. Chem. Ref. Data* **11**, 695 (1982).

42. V. P. Glushko, L. V. Gurvich, G. A. Bergman, I. V. Veits, V. A. Medvedev, G. A. Khachkunuzov and V. S. Yungman, Termodinamicheski *Svoistva Individual'nikh Veshchestv* (Nauka, Moscow, 1978), Vol. I, Books 1 and 2.

43. L. A. Curtiss, K. Raghavachari, P. C. Redfern, V. Rassolov, and J. A. Pople, *J. Chem. Phys.* **109**, 7794 (1998).

44. L. A. Curtiss, K. Raghavachari, G. W. Trucks, and J. A. Pople, *J. Chem. Phys.* **94**, 7221 (1991).

45. The accompanying theoretical article of the present experimental report. See D. A. Dixon, D. Feller, and K. A. Peterson, *J. Chem. Phys.*, accepted.

CHAPTER 9. HIGH-RESOLUTION ENERGY-SELECTED STUDY OF THE REACTION $CH_3X^+ \rightarrow CH_3^+ + X$: ACCURATE THERMOCHEMISTRY FOR THE CH_3X/CH_3X^+ (X=Br, I) SYSTEM

A paper to be published in *Journal of Chemical Physics*, (2001)

Y. Song, X.-M. Qian, K.-C. Lau and C.Y. Ng

Jianbo Liu and Wenwu Chen

Abstract:

Using the high-resolution pulsed field ionization-photoelectron (PFI-PE) and PFI-PE-photoion coincidence (PFI-PEPICO) techniques, we have examined the formation of methyl cation (CH_3^+) from the dissociation of energy-selected CH_3X^+ (X=Br and I) near their dissociation thresholds. The breakdown diagrams for CH_3X thus obtained yield values of 12.834±0.002 eV and 12.269±0.003 eV for the 0 K dissociative threshold or appearance energy (AE) for CH_3^+ from CH_3Br and CH_3I, respectively. Similar to the observation in PFI-PE studies of CH_4, C_2H_2, and NH_3, the PFI-PE spectrum for CH_3Br exhibits a step at the 0 K AE for CH_3^+, indicating that the dissociation of excited CH_3Br in high-n (≥100) Rydberg states at energies slightly above the dissociation threshold occurs in a time scale of $\leq 10^{-7}$ s. The observed step is a confirmation of the 0 K AE(CH_3^+) from CH_3Br determined in the PFI-PEPICO study. The adiabatic ionization energies (IEs) for the $CH_3Br^+(\tilde{X}\,^2E_{3/2,1/2})$ spin-orbit states were determined by PFI-PE measurements to be 10.5427±0.0010 and 10.8615±0.0010 eV, respectively, yielding the spin-orbit coupling constant to be 2571±4 cm^{-1}. The AE(CH_3^+) values from CH_3Br and CH_3I and the IE[$CH_3Br^+(\tilde{X}\,^2E_{3/2})$] value obtained here, when combined with the known IE of CH_3 (9.8380±0.0004 eV) and IE[$CH_3I^+(\tilde{X}\,^2E_{3/2})$] (9.5381±0.0001 eV), have allowed accurate determination of the 0 K bond dissociation energies for CH_3-Br (2.996±0.002 eV), CH_3^+-Br (2.291±0.002 eV), CH_3-I (2.431±0.003 eV), and CH_3^+-I (2.731±0.003 eV). Using the AE(CH_3^+) from CH_3Br and CH_3I, together with the known 0 K heats of formation ($\Delta_fH°_0$)

for Br (117.93±0.13 kJ/mol), I (107.16±0.04 kJ/mol), and CH_3^+ (1099.05±0.33 kJ/mol), we have obtained more precise $\Delta_fH°_0$ values for CH_3Br (–21.30±0.42 kJ/mol) and CH_3I (22.43±0.50 kJ/mol). This experiment demonstrated that highly reliable $\Delta_fH°_0$ values for a range of molecules with error limits comparable to those for some of the most precisely measured values, such as $\Delta_fH°_0(CH_4)$, can be obtained by PFI-PE and PFI-PEPICO measurements.

I. Introduction

Reliable predictions of chemical reactivity require accurate energetic information for a broad range of molecular species. For this reason, to establish an accurate thermochemical database for molecules has been a major pursuit of both experimental and theoretical research in physical science.[1-3] The photoionization techniques based on the detection of photoelectrons and photoions have a distinguished history in providing reliable energetic information for molecules and their ions.[4] Important energetic data obtainable from photoionization experiments include ionization energies (IEs) and 0 K dissociative photoionization thresholds or appearance energies (AEs) of molecules, from which 0 K bond dissociation energies (D_0's) and 0 K heats of formation ($\Delta_fH°_0$) for the neutral and ionic species can be derived by using appropriate thermochemical cycles. In conventional photoelectron spectroscopy and photoionization efficiency (PIE) studies, the error limits for measured energetic data are generally in the range of 1.3-8.4 kJ/mol.[1-3] Considering that photoelectron spectroscopy and photoionization efficiency (PIE) measurements are gas phase techniques and work well for relatively small molecules, we believe that a realistic goal of these photoionization experiments should be to build the best possible energetic data set for guiding the development of quantum chemical computation procedures.[5,6] The establishment of reliable computation codes would then allow the prediction of energetic properties for molecular species that are not accessible to experimental investigations.

Experimental energetic data for small molecules, including those obtained in photoionization experiments, have indeed played an essential role in the development of

quantum chemical computation procedures.[5,6] Due to the advance in computer technologies, significant progress has been made in computation chemistry in the past decade. Currently, the Gaussian-2/Gaussian-3 (G2/G3) procedures[5,6] are among the most popular quantum chemical computation schemes for energetic calculations. These theories are "slightly" semi-empirical in nature because they contain a high level correction obtained empirically from a fit to a set of experimental energetic data, such as IEs, electron affinities, and heats of formation, by minimizing the deviations between corresponding experimental and theoretical results. The G2 theory[5] uses a data set of 55 molecules as compared to the use of a larger set of 299 molecules in the fitting for the G3 procedures.[6] As a result, the accuracy of G2/G3 predictions is dictated by error limits of experimental data used in the fitting. At present, the G2/G3 predictions for IEs, electron affinities, and heats of formation for small main group molecular species are known to achieve an accuracy of ≈3.8-5.4 kJ/mol as measured by the average deviations between theoretical and experimental results.[5,6] Without doubt, the development of the next generation of computation procedures would demand a more accurate experimental database.

The fact that standard computation codes can now achieve experimental accuracy has set a challenge for modern photoionization studies. The recent introduction of an array of pulsed field ionization (PFI) techniques, involving PFI-photoelectron (PFI-PE),[7-9] PFI-photoion,[10] and PFI-ion-pair[11] detection using lasers[9] and high-resolution monochromatized vacuum ultraviolet (VUV) synchrotron radiation,[12-14] have greatly improved the achievable energy resolution for photoionization measurements. These PFI studies have shown to provide IE values with error limits about 10-100 fold smaller than those observed in conventional photoelectron and PIE studies.[9] The recent implementation of a high-resolution synchrotron based PFI-PE-photoion coincidence (PFI-PEPICO) method has made possible the examination of unimolecular dissociation reactions of ions with an internal energy selection of 0.6-1.0 meV (full width at half maximum, FWHM), limited only by PFI-PE measurements. Furthermore, we have discovered that 0 K AEs for dissociative photoionization processes involving a range of molecules can be identified by a sharp step resolved in the PFI-PE spectrum.[15,16] The origin of this step is attributed to the lifetime switching effect at the 0 K AE, where excited parent molecules in high-n ($n \geq 100$)

Rydberg states with shorter lifetimes are converted into excited fragments in high-n ($n \geq 100$) Rydberg states with longer lifetimes.[15] The measurement of breakdown curves for the parent and daughter ions in PFI-PEPICO measurements, together with the observation of the PFI-PE step, has yielded highly reliable 0 K AE values for a range of molecules achieving error limits of about ±0.001 eV (0.10 kJ/mol).[16-18] The 0 K AE values obtained in PFI-PE and PFI-PEPICO measurements have made possible the determination of 0 K dissociation energies (D_0's), and 0 K heats of formation ($\Delta_f H°_0$'s) for many neutrals and ions with unprecedented precision.[16-18] These 0 K energetic values, which measure differences between well defined molecular energy levels, are most appropriate for direct comparison with theoretical calculations. We note that many energetic data for molecular species in the literature were obtained by equilibrium and kinetic measurements with temperatures well above 0 K.

We have employed the PFI-PE and PFI-PEPICO methods for investigating the photoionization and dissociative photoionization of a series of small molecules, such as CH_4, C_2H_2, C_2H_4, NH_3, C_2H_5Cl, C_2H_5Br, C_3H_7Cl, C_3H_7Br, and C_3H_7I, with excellent results.[15-20] We found that the uncertainties of some $\Delta_f H°_0$ values for the radicals and ion fragments derived from these studies, such as CH_3 and CH_3^+, are now limited by the error limit for $\Delta_f H°_0(CH_4)$.[21,22] In the case of CH_3X (X = Br and I), the maximum differences or discrepancies among their previously reported $\Delta_f H°_{298}$ values are 1.7-3.3 kJ/mol .[3] These discrepancies are significantly larger than the error limit of 0.33 kJ/mol for $\Delta_f H°_0(CH_3^+)$ derived in the previous PFI-PEPICO study of CH_4.[17] We show here that by measuring accurate 0 K $AE(CH_3^+)$ values for reaction (1) using the PFI-PE and PFI-PEPICO method, we have obtained values for $\Delta_f H°_0(CH_3X)$ with significantly improved precision.

$$CH_3X + h\nu \rightarrow CH_3^+ + X + e^- \qquad (1)$$

We have also re-examined the IE of CH_3Br using the PFI-PE method. By measuring the 0 K $AE(CH_3^+)$ values for reaction (1) and IE of CH_3Br, together with the known IE of CH_3,[23] we have deduced highly precise D_0 values for CH_3-X and CH_3^+-X.

II. Experiment

The PFI-PE and PFI-PEPICO experiments were conducted using the high-resolution VUV photoelectron-photoion facility of the Chemical Dynamics Beamline at the Advanced Light Source (ALS).[12,24] The experimental procedures have been described in detail previously.[12-14,25,26] Thus, only a brief description is given here.

In the present experiment, Ar was used in the harmonic gas to filter higher undulator harmonics with photon energies greater than 15.76 eV. The ALS was operated in the multi-bunch mode with a period of 656 ns. The multi-bunch light structure consisted of 272 micro-VUV light pulses (pulse width = 50 ps, separation of adjacent pulses = 2 ns) followed by a dark gap (light off period) of 112 ns. A 2400 lines/mm grating (dispersion = 0.64 Å/mm) was used to disperse the first order harmonic of the undulator VUV beam with entrance/exit slits set in the range of 30-100 μm. The resulting monochromatic VUV beam was then focused into the photoionization/photoexcitation (PI/PEX) center of the photoelectron-photoion apparatus. The photon energy (hν) calibration was achieved using the $Ar^+(^2P_{3/2})$, $Xe^+(^2P_{3/2})$, and $NO^+(X^1\Sigma^+, v^+ = 0)$ PFI-PE bands[27] recorded under the same experimental conditions before and after each scan. This calibration procedure assumes that the Stark shift for ionization thresholds of CH_3X and the rare gases and NO are identical. On the basis of previous experiments, the accuracy of the energy calibration is believed to be within ±0.5 meV.[28]

The PFI-PE detection was achieved by employing the electron TOF scheme.[13] A dc field of 0.2 V/cm was maintained at the PI/PEX region to sweep background electrons formed by direct and prompt autoionization toward the electron detector prior to the application of the electric field pulse for Stark ionization. The PFI pulse (height =7.3 V/cm, width=200 ns) was applied ≈10 ns after the start of the dark gap. The PFI pulse also served to extract PFI-photoions toward the ion detector. Since the dark gap was only 112 ns in duration, a finite overlap occurred between the PFI pulse and micro-light pulses of the subsequent period, resulting in the destruction of finite high-n Rydberg CH_3X molecules.

The ion PFI-PEPICO TOF spectra were recorded using a multichannel scaler triggered by the detection of PFI electrons.[14] The average accumulation time for a PFI-PEPICO TOF spectrum for CH_3X is ≈ 20 min. The current setup is sensitive to the ion kinetic energy.[14] The analysis of the Ar TOF peak obtained using a supersonic Ar beam reveals that the thermal background of Ar in the photoionization chamber contributes ≈15% to the experimental Ar sample. This 85:15 ratio is roughly consistent with the estimated CH_3X densities for the molecular beam sample and thermal background gas at the PI/PEX region. On the basis of the measured PFI-PE band for $Xe^+(^2P_{3/2})$, we estimate that the ion-energy selection achieved here is ≈1.0 meV (FWHM).[14]

The CH_3Br (CH_3I) sample with a specified purity of 99 % was obtained from Aldrich and used without further purification. All PFI-PEPICO TOF spectra for CH_3Br were recorded by introducing the CH_3Br sample into the PI/PEX region in the form of a skimmed neat CH_3Br supersonic beam (nozzle diameter = 127 μm, stagnation pressure = 760 Torr, and stagnation temperature = 298 K). The vapor pressure for CH_3I at room temperature (298 K) is about 400 Torr. The vapor of a liquid CH_3I sample at 298 K was mixed with Ar to a total stagnation pressure of about 760 Torr prior to expansion through the nozzle. The PFI-PE spectra for CH_3X near their dissociation region were recorded using both the supersonic and effusive beam samples.

III. Results and discussion

A. PFI-PEPICO TOF spectra and breakdown diagrams for CH_3X

We have collected PFI-PEPICO TOF spectra for CH_3Br in the photon energy region of 12.68-12.89 eV, which is near the 0 K AE(CH_3^+) from CH_3Br. Figure 9-1(a) depicts typical PFI-PEPICO spectra of CH_3Br at selected photon energies, hν=10.5427, 12.7749, 12.8048, 12.8347, and 12.8556 eV. These spectra have been background corrected using procedures described in previous studies.[14] At photon energies well below the dissociation threshold, we measured the PFI-PEPICO TOF spectra at a step size of 10 meV, while a step size of 1.0 meV was used at photon energies close to the 0 K AE of reaction (1). The bottom TOF spectrum of Fig. 9-1(a) was recorded at the IE of CH_3Br

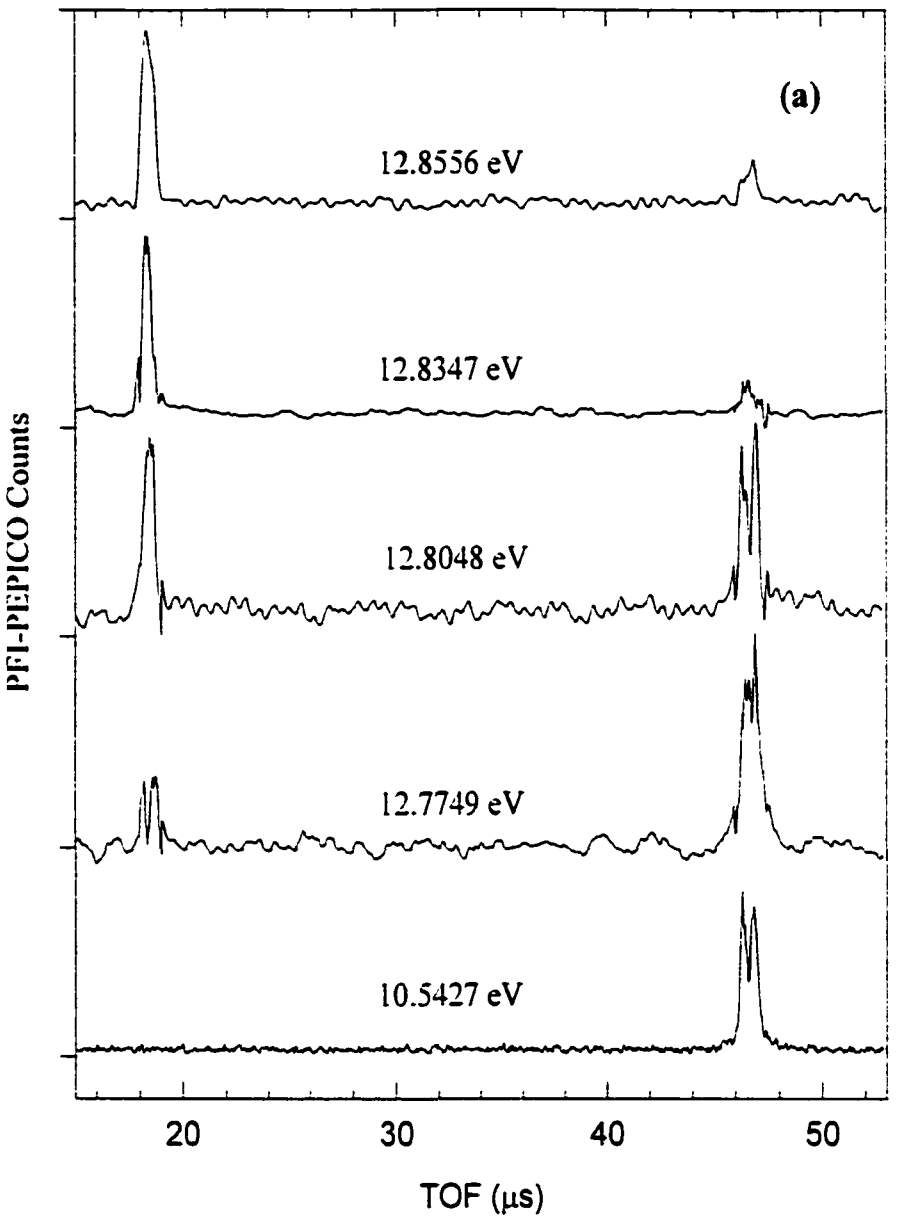

Figure 9-1 (a) Selected PFI-PEPICO TOF spectra for CH_3^+ and CH_3Br^+ from CH_3Br at hν = 10.5427, 12.7749, 12.8048, 12.8347, and 12.8556 eV. The TOF peak centered at 19.78 μs is due to CH_3^+, and the doublet peaks resolved at 46.32 and 46.84 μs are associated with $CH_3{}^{79}Br$ and $CH_3{}^{81}Br$, respectively. (b) PFI-PEPICO TOF spectra for CH_3^+ and CH_3I^+ from CH_3I at hν = 9.5378, 12.2072, 12.2320, 12.2697, and 12.2967 eV. The TOF peaks centered at 19.78 and 57.12 μs are due to CH_3^+ and CH_3I^+, respectively.

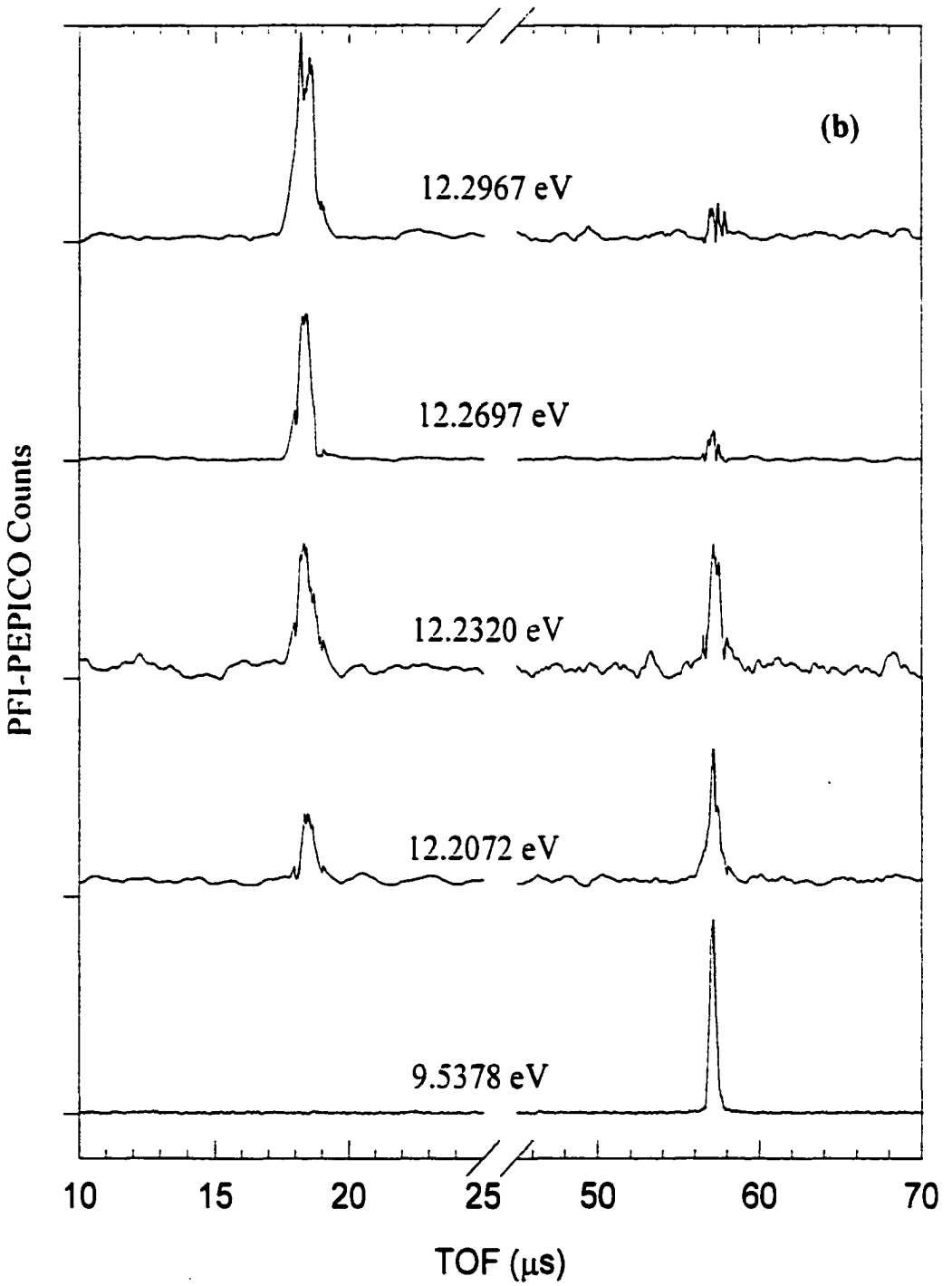

Figure 9-1 (Continued)

with an accumulation time of 5 min. The fact that the photoion background at the IE is low results in excellent signal-to-noise (S/N) ratios for the PFI-PEPICO TOF data. As expected, this spectrum at hν=10.5427 eV only manifests the formation of parent CH_3Br ions. The TOF peak for the parent ion is resolved into a doublet at 46.32 and 46.84 μs, which can be assigned to ion masses of 94 and 96 amu. The relative intensities of the doublet reflect the nearly 1:1 natural isotopic distribution for ^{79}Br and ^{81}Br in CH_3Br^+. The deconvoluted TOF peaks for $CH_3{}^{79}Br^+$ and $CH_3{}^{81}Br^+$ have a peak width of 0.3 μs (FWHM). Other PFI-PEPICO TOF spectra taken at photon energies near the dissociation onset show poorer S/N ratios. The poorer S/N ratios for the PFI-PEPICO TOF spectra observed at hν=12.7749 and 12.8048 eV are also caused by the fact that these energies lie close to the Franck-Condon gap region of the photoelectron spectrum for CH_3Br.[29] Consequently, a significantly lower PFI-PE counts are observed in this region than those found at the IE of CH_3Br.

We have recorded PFI-PEPICO TOF spectra for CH_3I in the photon energy region of 12.15-12.32 eV. Selected spectra at hν = 9.5378, 12.2072, 12.2320, 12.2697, and 12.2967 eV are depicted in Fig. 9-1(b). The bottom spectrum of Fig. 9-1(b), which was taken at the IE of CH_3I, shows the best S/N ratio compared to those for other spectra.

Table 9-I lists the known vibrational frequencies for CH_3X.[3,30] Since these vibrational frequencies are relatively high, we expect that the thermal energy for CH_3X at 298 K due to vibrational excitation is small. The thermal vibrational energies for CH_3X molecules in the supersonic beam should be lower because their vibrational temperatures are expected to be <298 K. The average rotational energy for thermal CH_3X at 298 K amounts to ≈30-40 meV. Assuming that all thermal rotational and vibrational energies are available to dissociation, we expect to observe daughter CH_3^+ ions below the 0 K AE for reaction (1). The daughter CH_3^+ ions observed in the PFI-PEPICO TOF spectra at hν= 12.7749 and 12.8048 eV for CH_3Br and at hν= 12.2072 and 12.2320 eV for CH_3I are due to dissociation of thermally excited parent molecules. This observation is consistent with the AEs measured below. As the photon energy is increased, the abundance for the parent ion decreases relative to that for the daughter ion.

At photon energies higher than the 0 K AE, complete dissociation should be observed. This is the case in the PFI-PEPICO studies of CH_4 and C_2H_2.[17,18] We showed that the 0 K AE for CH_3^+ from CH_4 (C_2H^+ from C_2H_2) can be determined unambiguously by the energy at which the intensity for the parent CH_4^+ ($C_2H_2^+$) ion goes to zero. However, in the PFI-PEPICO study of NH_3, we observed residual background coincidence intensities for the parent NH_3^+ ion peak at energies beyond the 0 K AE(NH_2^+).[16] An observation similar to the case of NH_3 is found here. As shown in Fig. 9-1(a) [9-1(b)], finite residual intensities for the parent CH_3Br^+ (CH_3I^+) ion peaks were found in the TOF spectra at hν=12.8347 and 12.8556 eV (hν=12.2697 and 12.2967 eV), which are shown (see discussion below) to be higher than the 0 K AE(CH_3^+) from CH_3Br (CH_3I). This observation can be attributed to coincidence background from hot electrons and dissociative photoionization of dimers and clusters formed in the supersonic beam. In the NH_3 and present experiment, the ALS dark gap (112 ns) is narrower than that (144 ns) used in the PFI-PEPICO studies of CH_4 and C_2H_2.[14,15] Thus, the contamination due to a finite dispersion of hot electrons into the dark gap in the present study is higher than that in the latter studies. The hot photoelectrons occurring at the dark gap are probably responsible for the majority of coincidence background associated with the detection of stable, cold parent ions. Under the conditions for supersonic expansion in the present experiment, we expect the formation of CH_3X dimers [$(CH_3X)_2$] and clusters in the beam sample. Stemming from the fact that the photon energy range of interest near the 0 K AE for reaction (1) is well above the IE of CH_3X, we expect the formation of CH_3X^+ from the dissociative photoionization process, such as Reaction (2), to be a dominant channel.

$$(CH_3X)_2 + h\nu \rightarrow CH_3X^+ + CH_3X + e^- \qquad (2)$$

In this reaction, CH_3X^+ is stabilized by the ejection of CH_3X. Thus, the PFI-PEPICO detection of reaction (2) may contribute to a finite coincidence background for CH_3X^+. Considering that the narrow photon energy range involved here, we also expect the cross section for reaction (2) to be independent of photon energy. The argument favoring a finite contribution to the coincidence background for CH_3X^+ by dissociative photoionization of

dimers and clusters is consistent with the finding that the abundances for parent CH_4^+ and $C_2H_2^+$ are negligible at photon energies higher than their respective 0 K AEs because dimers and clusters for these species are not easily formed under the supersonic expansion conditions used in these experiments.

In order to construct the breakdown curves for the parent CH_3X^+ and daughter CH_3^+ ions, we first obtained the relative intensities for CH_3X^+ and CH_3^+ ions based on their respective TOF peak areas observed in the PFI-PEPICO TOF spectra. The fractional abundance for CH_3X^+ (CH_3^+) at a given photon energy was obtained by dividing the CH_3X^+ (CH_3^+) ion intensity by the sum of the CH_3X^+ and CH_3^+ ion intensities. These breakdown curves for CH_3X^+ (open squares) and CH_3^+ (open circles) representing the plots of the fractional abundances for CH_3X^+ and CH_3^+ as a function of photon energy are shown in Fig. 9-2(a) for CH_3Br and in Fig. 9-3(a) for CH_3I. Error bars for individual data points shown in Figs. 9-2(a) and 9-3(a) represent their standard deviations.

As shown in Figs. 9-2(a) and 9-3(a), the fractional abundance for parent ion (daughter ion) decreases (increases) as the photon energy is increased. The distinct feature of the breakdown diagram for CH_3Br is the break observed at 12.834 eV, where the fractional abundance for CH_3Br^+ (CH_3^+) becomes a constant of 0.22 (0.78). The S/N ratios of the breakdown data for CH_3I are poorer than those for CH_3Br. A similar break is observed in breakdown diagram for CH_3I at 12.269 eV, where the fractional abundance for CH_3I^+ (CH_3^+) reaches a constant of 0.18 (0.82). Similar to the analysis of PFI-PEPICO data for NH_3, we have assigned the break of the breakdown curve of CH_3Br^+ at 12.834±0.002 eV to be the 0 K AE(CH_3^+) from CH_3Br and that of CH_3I^+ at 12.269±0.003 eV to be the 0 K AE(CH_3^+) from CH_3I. The respective error ranges of 4 meV and 6 meV for the 0 K AE(CH_3^+) from CH_3Br and CH_3I are consistent with the simulation of the breakdown diagrams for CH_3X to be described in section III.B.

B. Simulation of the breakdown diagrams for CH_3X

The breakdown curves for CH_3X^+ and CH_3^+ were simulated by assuming that the ion energy resolution is infinitely narrow and that the broadening of the breakdown diagram is due solely to the thermal energy in the CH_3X molecule. The distribution of

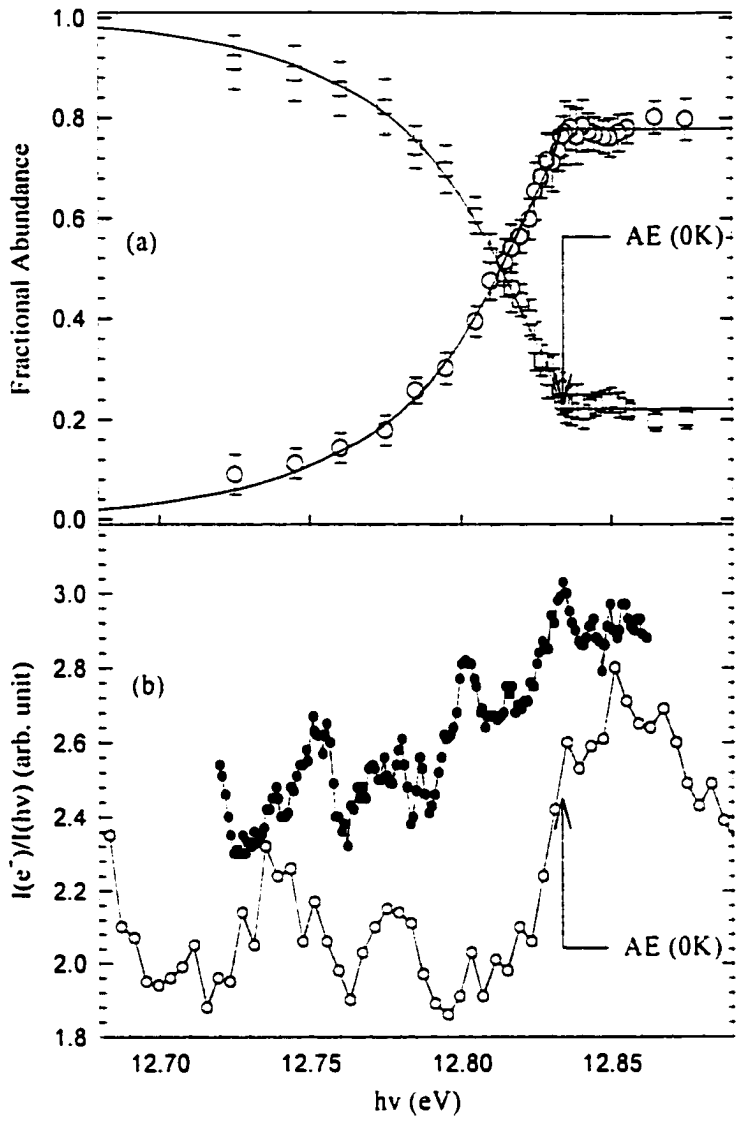

Figure 9-2 (a) Breakdown curves for CH_3^+ (open circles) and CH_3Br^+ (open squares) from CH_3Br in the hv range of 12.68-12.89 eV. The solid lines are simulations curves obtained by assuming 80% cold beam (20 K) and 20% thermal (298 K) CH_3Br sample. The error bars represent one standard deviation. The 0 K AE is marked by the break of the breakdown curve for the parent CH_3Br^+ ion. (b) PFI-PE spectra for CH_3Br in the range of 12.68-12.89 eV obtained using an effusive beam (solid circles, upper spectrum) and a supersonic beam (open circles, lower spectrum) sample of CH_3Br. The step at the 0 K AE is discernible in the cold (lower) PFI-PE spectrum.

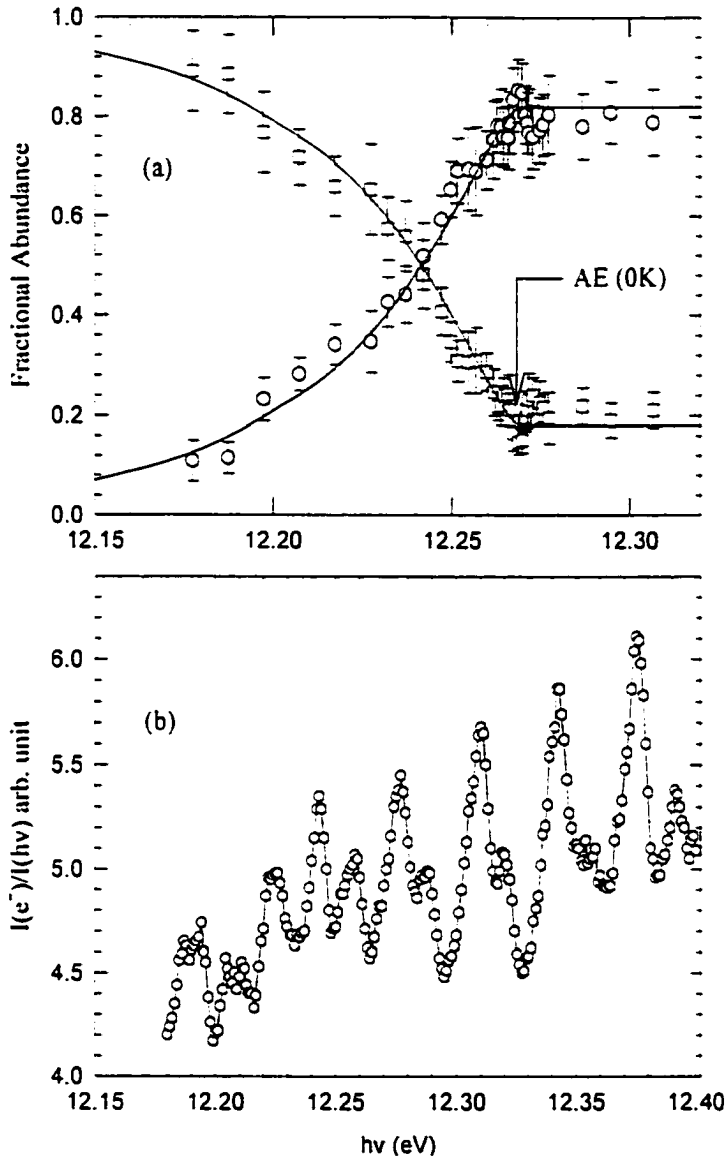

Figure 9-3 (a) Breakdown curves for CH_3^+ (open circles) and CH_3I^+ (open squares) from CH_3I in the hv range of 12.15-12.32 eV. The solid lines are simulations curves obtained by assuming a CH_3I sample at 298 K with no contribution from the cold sample. The error bars represent one standard deviations. The 0 K AE is marked by the break of the breakdown curve for CH_3I^+. (b) PFI-PE spectra for CH_3I in the range of 12.15-12.40 eV obtained using a supersonic beam of CH_3I. A step at the 0 K AE is not clearly discernible due to interference by the strong vibrational structure appearing in this region.

internal thermal energy $P(E, T)$,[16,19,20] was determined by Eq. (3), which depends on the density of the rovibrational states $\rho(E)$.

$$P(E,T) = \frac{\rho(E)\, e^{-E/RT}}{\int_0^\infty \rho(E)\, e^{-E/RT}} \tag{3}$$

The density of rovibrational states for CH_3X was calculated using the Beyer-Swinehart direct count algorithm[31] based on the vibrational frequencies and rotational constants listed in Table 9-I.

Table I. Vibrational and rotational constants for CH_3Br and CH_3I.

	Vibrational frequencies (cm^{-1})[a]						Rotational constants (cm^{-1})[b]	
	ν_1(a)	ν_2 (a)	ν_3(a)	ν_4 (e)	ν_5 (e)	ν_6 (e)		
CH_3Br	2935	1306	611	3056	1443	955	5.08	0.3192
CH_3I	2933	1252	533	3060	1436	822	5.11	0.2502

a) Reference 3.

b) Reference 30

The simulation were obtained by convoluting this thermal energy distribution with a step function at the 0 K AE as given by Eqs. (4) and (5).

$$Parent(h\nu) = \int_0^{AE - h\nu \text{ or } 0} P(E)dE \tag{4}$$

$$Daughter(h\nu) = \int_{AE - h\nu \text{ or } 0}^{\infty} P(E)dE \tag{5}$$

We note that the parent ion integral is valid only up to the hν equal to the AE. Ideally, beyond that hν value the parent ion signal is zero. The simulation of the breakdown curves also assumes a constant false coincidence background, resulting in a constant fractional abundance (0.22 for X=Br and 0.18 for X=I) for CH_3X^+ at hν ≥ AE. The breakdown data were fitted by two independent parameters, namely, the CH_3X temperature and the 0 K AE. The sample temperature governs the slope at which the 0 K AE is approached. If the sample temperature was 0 K and in the absence of thermal background gas in the chamber, the breakdown curves for CH_3X^+ and CH_3^+ would be a step function. Assuming the CH_3Br sample to consist of ≈20% thermal (298 K) background and ≈80% cold (20 K) beam sample, we have obtained an excellent simulation [solid lines, Fig. 9-2(a)] of the breakdown curves for CH_3Br^+ and CH_3^+, yielding a value of 12.834±0.002 eV for the 0 K AE(CH_3^+) from CH_3Br. In Fig. 9-3(a), the solid lines represent the simulated breakdown curves for CH_3I^+ and CH_3^+ calculated by assuming that the temperature for CH_3I is 298 K with little contribution from the cold beam sample. This simulation provides a value of 12.269±0.003 eV for the 0 K AE(CH_3^+) from CH_3I. As shown in previous study,[17] the detailed structure of breakdown curves derived from PFI-PEPICO measurements depends on the Stark field. Thus, the temperatures used in the simulation of the breakdown curves are not expected to reflect the actual temperatures of the gas sample involved.

We emphasize that the 0 K AE(CH_3^+) value determined here is based on the intrinsic feature, i.e., the break observed in the breakdown curve for CH_3X^+, and is not dependent on the detailed simulation of the breakdown curves. However, the successful simulation of the breakdown curves can be taken as support of the rationale for the AE assignment. In order to illustrate the precision of the present AE determination, we have plotted in Fig. 9-4 a magnified view of the breakdown data for CH_3Br^+ (open squares), together with their error bars (two standard deviations), in the photon energy region of 12.811-12.881 eV. The solid curve represents the best simulation curve. It is clear from this figure that the break (marked as 0 K AE by the arrow) of the CH_3Br^+ breakdown curve can be identified at 12.834 eV with an error limit better than ±3 meV. The assigned error limit of ±0.002 eV (± one standard deviation) is consistent with that obtained by

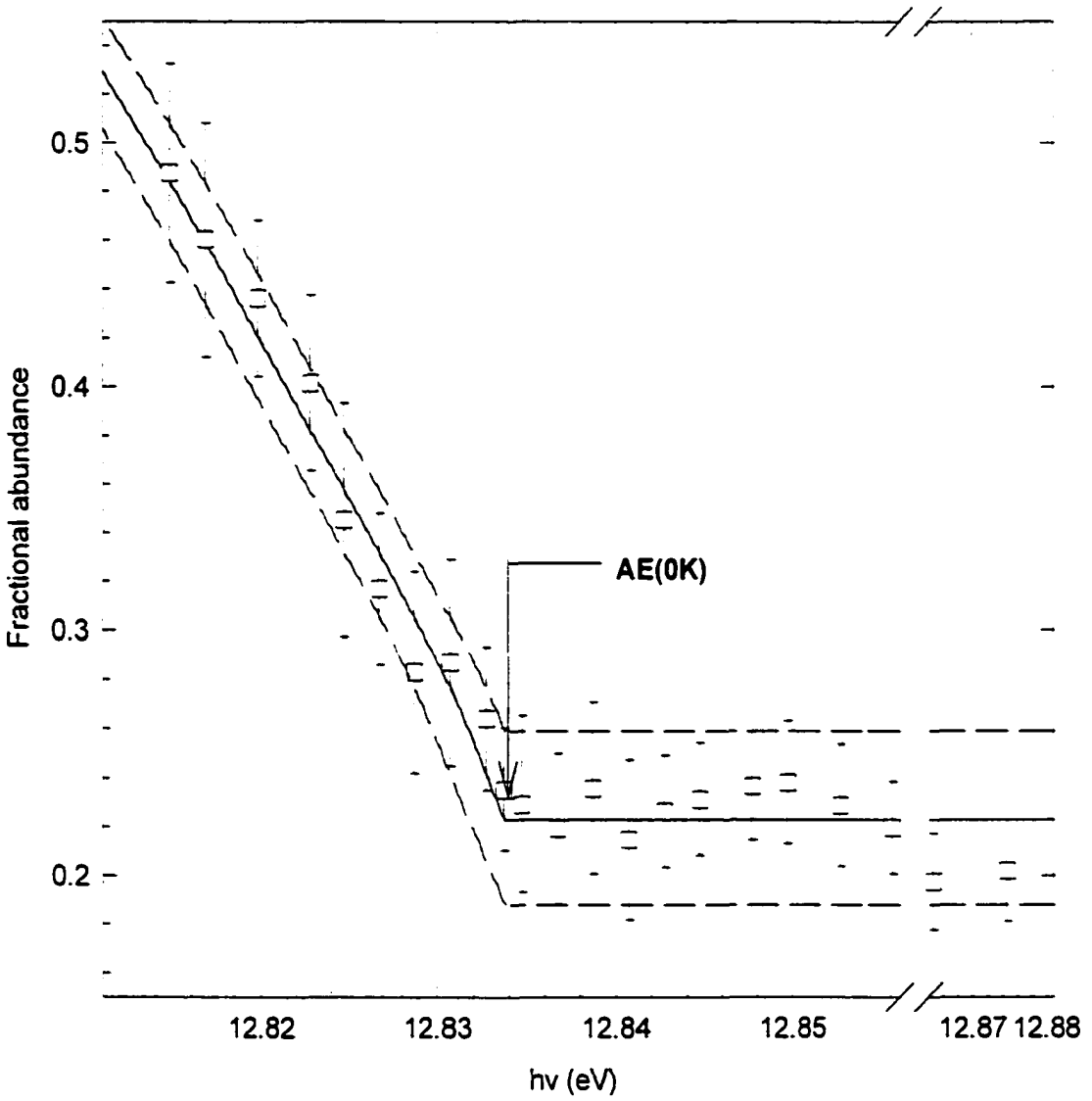

Figure 9-4 A magnified view of the breakdown data for CH_3Br^- (□) in the hν range of 12.811-12.881 eV. The break resolved at 12.834 eV marks the 0 K AE(CH_3^-) from CH_3Br. The middle solid curve represents the best simulation curve. The assigned error limit of ±0.002 eV for the latter 0 K AE is consistent with that obtained by simulation, which has taken into account the data fluctuation in the range bounded by the upper and lower dashed curves.

simulation. which has taken into account the data fluctuation in the range bounded by the upper and lower dashed curves of Fig. 9-4.

C. PFI-PE Spectra for CH_3X

The neutral $CH_3X(\tilde{X}\,^1A_1)$ ground state possesses C_{3v} symmetry and has the main electronic configuration $...(1a_1)^2(2a_1)^2(1e)^4(3a_1)^2(2e)^4$.[29] The ejection of an electron from the highest occupied 2e-orbital results in the formation of the ionic $CH_3X^+(\tilde{X}\,^2E)$ ground state. This state with the configuration $...(2e)^3$ is subject to the Jahn-Teller vibronic distortion. However, to a first approximation. we can label the ground ionic state to consist of the spin-orbit components $CH_3X^+(\tilde{X}\,^2E_{3/2,1/2})$.[29]

The $IE[CH_3Br^+(\tilde{X}\,^2E_{3/2})]$ measurements reported in previous photoionization,[32] photoelectron,[29] and spectroscopic[33] measurements are in excellent agreement with values mostly in the range of 10.53-10.54 eV. In order to obtain a more precise value for the IE of CH_3Br. we have measured the PFI-PE spectrum near the ionization onset of CH_3Br (not shown here). The spectrum was measured using an effusive CH_3Br beam with a step size of 0.5 meV. The PFI-PE resolution achieved was better than 1 meV (FWHM) as indicated by the PFI-PE peak for $Ar^+(^2P_{3/2})$. The PFI-PE bands for $CH_3Br^+(\tilde{X}\,^2E_{3/2,1/2})$ thus obtained exhibit a FWHM of ≈3-5 meV. Since the electron removed from the 2e-orbital is a lone-pair electron associated with the Br atom and is not involved in bonding of CH_3Br,[29] the peak positions of the PFI-PE bands are expected to provide accurate measures for the $IE[CH_3Br^+(\tilde{X}\,^2E_{3/2,1/2})]$ values. Based on the peak positions of the PFI-PE bands for $CH_3Br^+(\tilde{X}\,^2E_{3/2,1/2})$. we obtained $IE[CH_3Br^+(\tilde{X}\,^2E_{3/2})]$= 10.5427±0.0010 eV and $IE[CH_3Br^+(^2E_{1/2})]$=10.8615±0.0010 eV.

The respective $IE[CH_3I^+(\tilde{X}\,^2E_{3/2})]$ and $IE[CH_3I^+(^2E_{1/2})]$ have been determined previously to be 76932±5 cm^{-1} (9.5386±0.0006 eV) and 81983±5 cm^{-1} (10.1646±0.0006 eV) in a non-resonant two photon (N2P) laser PFI-PE by Strobel et al.[34] These values are in excellent agreement with the values $IE[CH_3I^+(\tilde{X}\,^2E_{3/2})]$ = 76930 ± 1 cm^{-1} (9.5381 ± 0.0001 eV) and $IE[CH_3I^+(^2E_{1/2})]$ = 81979 ± 1 cm^{-1} (10.1641 ± 0.0001 eV) determined by the extrapolation of Rydberg series.[35] We have measured the PFI-PE bands for

$CH_3I^+(\tilde{X}\,^2E_{3/2,1/2})$ and obtained values of $IE[CH_3I^+(\tilde{X}\,^2E_{3/2})]$ = 9.5377±0.0010 eV and $IE[CH_3I^+(^2E_{1/2})]$ = 10.1639 ± 0.0010 eV. The fact that these latter measurements are in excellent agreement with results of the previous N2P-PFI-PE and Rydberg series extrapolation studies indicates that the $IE[CH_3Br^+(\tilde{X}\,^2E_{3/2,1/2})]$ values determined here are highly reliable.

Figure 9-2(b) shows the PFI-PE spectra for CH_3Br in the energy region of 12.68-12.89 eV obtained using an effusive sample (upper spectrum, solid circles) and a supersonic beam sample (lower spectrum, solid circles) of CH_3Br. This energy region covers the 0 K $AE(CH_3^+)$ from CH_3Br. In the previous PFI studies, sharp steps were found in the PFI-PE spectra for CH_4, C_2H_2, and NH_3, marking precisely the corresponding 0 K AEs for CH_3^+, C_2H^+, and NH_2^+ determined in PFI-PEPICO measurements.[15-18] A detailed discussion concerning the conditions for the observation of a step at the 0 K ion dissociation threshold has been given previously.[15,16] As shown in Fig. 9-2(b), the PFI-PE spectra for CH_3Br are highly structured, consisting of complex vibrational bands for the $CH_3Br^+(\tilde{A}\,^2A_1)$ state.[29] Although the PFI-PE spectrum obtained using an effusive CH_3Br sample at 298 K shows a general increase in PFI-PE intensity as the photon energy is increased, a step at the 0 K $AE(CH_3^+)$ is not discernible. Comparing the PFI-PE spectra using effusive and supersonic beam , we can clearly identify a sharp step at the 0 K $AE(CH_3^+)$ as marked in Fig. 9-2(b). This observation is a confirmation for the 0 K $AE(CH_3^+)$ = 12.834 ± 0.002 eV determined in the PFI-PEPICO TOF study of CH_3Br.

In accordance with the conclusion of previous studies,[15-18] the formation of CH_3^+ from CH_3Br in the present PFI experiment is believed to proceed via processes 6(a), 6(b), and 6(d) at energies slightly above the $AE(CH_3^+)$, while CH_3Br^+ ions are produced by processes 6(a) and 6(c) below the $AE(CH_3^+)$.

$$\begin{array}{ccccc} & \overset{(a)}{} & & \overset{(b)}{} & \\ CH_3Br + h\nu & \longrightarrow & CH_3Br^* & \longrightarrow & CH_3^* + Br \\ & & \downarrow (c) & & \downarrow (d) \\ & & CH_3Br^{+*} + e^- & & CH_3^+ + e^- \end{array} \qquad (6)$$

Here, CH_3Br^* and CH_3^* represent excited CH_3Br and CH_3, respectively, in long-lived high-n ($n \geq 100$) Rydberg states and CH_3Br^{+*} stands for internally excited CH_3Br^+. Processes 6(c) and 6(d) are PFI processes. This mechanism suggests that CH_3Br^* fragments into CH_3^* + Br at energies above the $AE(CH_3^+)$ prior to the PFI process 6(d) and is responsible for the sharp step at 12.834 eV observed in the cold beam PFI-PE spectrum of CH_3Br shown in Fig. 9-2(b).

The dominant decay channels for CH_3Br^* are autoionization and fragmentation. At energies below the $AE(CH_3^+)$, the PFI-PE signal is due to process 6(c) and is proportional to the concentration of CH_3Br^* species that have survived the decay for a time longer than the delay ($\Delta\tau \approx 10^{-7}$ s) of the PFI pulse relative to the excitation VUV light pulse. For CH_3Br^* species that have spontaneously autoionized at a time shorter than $\Delta\tau$ are lost to PFI detection. The CH_3^* species formed at the AE are expected to converge to the ground state of CH_3^+, i.e., below the IE of CH_3. Consequently, autoionization is not accessible to CH_3^* fragments. The CH_3^* fragments produced at energies slightly above the AE can only autoionize by rotational autoionization. The latter process is expected to be slower than vibrational and electronic autoionization for the case of CH_3Br^*, which lies well above the IE of CH_3Br. Assuming that the decay rates via fragmentation for CH_3Br^* and CH_3^* are similar, we expect that a larger fraction of CH_3^* survives the decay than that of CH_3Br^*. This explains why the PFI-PE signals derived from process 6(d) at photon energies slightly above the AE are higher than that observed below the AE. The observation of the sharp step feature in the PFI-PE spectrum is consistent with the conclusion that the conversion from CH_3Br^* to CH_3^* is complete prior to process 6(d) and that the dissociation process has a rate constant $>> 1/\Delta\tau$ ($\approx 10^7$ s^{-1}).[15,16]

As pointed out above, the dissociation leading to the production of CH_3^* from CH_3Br^* formed by VUV excitation of thermally excited CH_3Br molecules occurs below the 0 K AE. As a result of the magnification of PFI events for CH_3^* fragments, the PFI-PE spectrum observed using an effusive beam of CH_3Br [upper spectrum in Fig. 9-2(b)] is expected to manifest a higher nominal temperature than the actual temperature of the thermal CH_3Br sample. This would result in the efficient filling of the step in the PFI-PE

spectrum. This analysis indicates that the step occurring at the 0 K AE of a dissociative photoionization process is more readily identified using a cold sample.

The PFI-PE spectrum for CH_3I in the region of 12.15-12.40 eV measured using a supersonic CH_3I beam sample is shown in Fig. 9-3(b). This spectrum reveals strong vibrational PFI-PE bands for the $CH_3I^+(\tilde{A}\,^2A_1)$ state, which is formed by the removal an electron from the $3a_1$-orbital in the $CH_3X(\tilde{X}\,^1A_1)$ state.[29] These vibrational bands have been observed and assigned previously to excitations of the umbrella mode (ν_2) and C-I stretching mode (ν_3) of $CH_3I^+(\tilde{A}\,^2A_1)$.[36] The excitation of these modes is to be expected considering that the $3a_1$-orbital has predominantly C-I bonding character. The step expected at the 0 K AE(CH_3^+) [marked in Fig. 9-3(a)] coincides with the rising edge of a strong vibrational PFI-PE peak, and thus cannot be identified. The previous threshold photoelectron-photoion coincidence (TPEPICO) study[37] indicated that the dissociation rate of CH_3I^+ is slow near threshold with a value of $\approx 10^7$ s^{-1}. Thus, a step might not be observable in the PFI-PE spectrum of CH_3I.

D. Thermochemistry of the CH_3X/CH_3X^+ system

We have listed in Table 9-II selected experimental[3,17,23,29,32,33,38-41] and theoretical[6] values for the IEs of CH_3Br and CH_3, $\Delta_fH°_0$'s of CH_3Br, CH_3Br^+, CH_3, and CH_3^+, 0 K AE for CH_3^+ from CH_3Br, and D_0's for CH_3-Br and CH_3^+-Br. The 0 K AE(CH_3^+) = 12.835±0.001 eV obtained here is higher than the literature values determined by PIE measurements,[32,40] which are in the range of 12.77-12.80 eV. The latest NIST compilation recommended a value of 10.541±0.003 eV for the IE of CH_3Br,[3] which is in excellent accord with the IE[$CH_3Br^+(\tilde{X}\,^2E_{3/2})$] value of 10.5427±0.0010 eV determined in the present study. The IE[$CH_3Br^+(\tilde{X}\,^2E_{3/2})$] and 0 K AE($CH_3^+$) from CH_3Br determined here give the $D_0(CH_3^+\text{-Br})$ = 2.291±0.002 eV. Combining the 0 K AE(CH_3^+) from CH_3Br and the known IE for CH_3 obtained in a previous PFI-PE study,[23] we calculate a value of 2.996±0.002 eV for $D_0(CH_3\text{-Br})$.

The 0 K AE(CH_3^+) from CH_4 was determined to be 14.323 ± 0.001 eV (1381.975 ± 0.084 kJ/mol) in a previous PFI-PEPICO study.[17] Using the latter value, together with the

Table 9-II. Comparison of values for ionization energies (IEs) of CH_3Br and CH_3, 0 K heats of formation ($\Delta_fH°_0$) for CH_3Br, CH_3Br^+, CH_3, and CH_3^+, 0 K AE for CH_3^+ [$AE(CH_3^+)$] from CH_3Br, and 0 K bond dissociation energies (D_0's) for CH_3-Br and CH_3^+-Br.

AE(CH_3^+) (eV)	IE(eV)		$\Delta_fH°_0$ (kJ/mol)[a]				D_0 (eV)[b]	
	CH_3Br	CH_3	CH_3Br	CH_3Br^+	CH_3	CH_3^+	CH_3-Br	CH_3^+-Br
12.834±0.002[b]	**10.5427±0.0010[c]** **[10.8615±0.0010][c]**	**9.8380 ±0.0004[d]**	**-21.30±0.42[b]** **(-36.36±0.42)[b]**	**995.88±0.42[b]** **(981.52±0.42)[b]**	**149.83±0.33[e]** **(147.23±0.33)[e]**	**1099.05±0.33[f]** **(1095.62±0.33)[f]**	**2.996 ±0.002**	**2.291 ±0.003**
12.77[g]	10.541±0.003[i]	9.84 ±0.01[i]	-23.0±1.3[n] (-38.1±1.3)[n]					
12.80±0.03[h]	10.54±0.01[j]	9.843 ±0.002[m]	-19.24±0.84[o] (-34.31±0.84)[o]					
	10.53[k]		-22.5±1.5[q,p] (-37.5±1.5)[q]					
			-22.6±1.3[q,p] (-37.7±1.3)[q]					
G2/G3 predictions[r]								
12.75/12.83	10.62/10.63	9.77/9.85	-14.6/-19.2 (-29.7/-34.3)	1009.6/1006.7 (995.4/992.0)	154.8/149.8 (152.3/146.9)	1097.0/1100.4 (1093.7/1097.0)	2.98/2.97	2.13/2.20

Table 9-II (Continued)

a) The values in parentheses are $\Delta_f H°_{f298}$ values converted from $\Delta_f H°_0$ values. See the text.

b) This work.

c) The upper value is IE[$CH_3Br'(\tilde{X}\ ^2E_{3/2})$]. The value in square bracket is IE[$CH_3Br'(^2E_{1/2})$].

d) Reference 23.

e) References 17 and 23.

f) Reference 17.

g) Reference 38.

h) Reference 32.

i) Reference 33.

j) Reference 32.

k) Reference 29.

l) Reference 3.

m) Reference 39.

n) Reference 2.

o) Reference 40.

p) The $\Delta_f H°_{f0}$ value is converted from $\Delta_f H°_{f298}$ value.

q) Reference 41.

r) References 5 and 6.

known $\Delta_fH°_0(CH_4)$ = -66.90±0.33 kJ/mol[21] and $\Delta_fH°_0(H)$ = 216.020±0.004 kJ/mol,[21] we have obtained $\Delta_fH°_0(CH_3^+)$ = 1099.05±0.33 kJ/mol.[17] We note that the precision of this $\Delta_fH°_0(CH_3^+)$ value is limited mainly by the error limit for $\Delta_fH°_0(CH_4)$. The $\Delta_fH°_0(Br)$ = 117.93± 0.13 kJ/mol[3,21] is also well known. Combining these values for $\Delta_fH°_0(Br)$ and $\Delta_fH°_0(CH_3^+)$ and the 0 K $AE(CH_3^+)$ from CH_3Br determined here, we obtained a value of –21.30±0.42 kJ/mol for $\Delta_fH°_0(CH_3Br)$. The NIST WebBook[3] lists three experimental $\Delta_fH°_{298}(CH_3Br)$ values: -37.7±1.3, -37.5±1.5, and –34.31±0.84 kJ/mol.[40,41] Using the known vibrational frequencies for CH_3Br, we have converted these values to $\Delta_fH°_0(CH_3Br)$ values of –22.6±1.3, -22.18±1.5, and –19.25±0.84 kJ/mol, respectively. The present value $\Delta_fH°_0(CH_3Br)$ = –21.30±0.42 kJ/mol lies in the range of previous experimental measurements,[38,39] and has a lower error limit than those for the latter values.

We have listed in Table 9-III selected experimental[34,35,37,42-45] and theoretical[5,6] values for the IEs of CH_3I, $\Delta_fH°_0$'s for CH_3I and CH_3I^+, 0 K $AE(CH_3^+)$ from CH_3I, D_0's for CH_3-I and CH_3^+-I. The previous PIE[38,42] and TPEPICO[37] studies yield values in the range of 12.18-12.60 eV for the 0 K $AE(CH_3^+)$ from CH_3I. The present value $AE(CH_3^+)$ = 12.269±0.003 eV lies on the high energy side of these values. In view of the excellent agreement between results obtained in the spectroscopic and N2P-PFI-PE studies,[34,35] we consider that the IE values for the formation of $CH_3I^+(\tilde{X}\,^2E_{3/2,1/2})$ from $CH_3I(\tilde{X}\,^1A_1)$ are well known. The more precise spectroscopic determinations,[35] $IE[CH_3I^+(\tilde{X}\,^2E_{3/2})]$= 9.5381±0.0001 eV and $IE[CH_3I^+(^2E_{1/2})]$ = 10.1641±0.0001 eV, are recommended here. Using the known $\Delta_fH°_0(I)$ = 107.165 ± 0.042 kJ/mol,[22] $\Delta_fH°_0(CH_3^+)$ = 1099.05±0.33 kJ/mol,[17] and the 0 K $AE(CH_3^+)$ of 1183.78±0.29 kJ/mol (12.269±0.003 eV) from CH_3I, we calculated a value $\Delta_fH°_0(CH_3I)$ = 22.43 ± 0.50 kJ/mol. We have converted this value into $\Delta_fH°_{298}(CH_3I)$ = 12.80±0.05 kJ/mol. Three experimental values,[43-45] 14.3±1.4, 14.6±1.0, and 15.9±1.3 kJ/mol, are listed in the NIST WebBook[3] for $\Delta_fH°_{298}(CH_3I)$. Taking into account of experimental uncertainties, the present result is in agreement with the value $\Delta_fH°_{298}(CH_3I)$ = 14.3±1.4 kJ/mol obtained by Golden *et al.*[43]

Table 9-III. Comparison of values for ionization energies of CH_3I, 0 K heats of formation ($\Delta_fH°_0$) for CH_3I and CH_3I^+, CH_3, and 0 K AE for CH_3^+ [$AE(CH_3^+)$] from CH_3I, and and 0 K bond dissociation energies (D_0's) for CH_3-I and CH_3^+-I.

$AE(CH_3^+)$ (eV)	IE (eV)[a]	$\Delta_fH°_0$ (kJ/mol)[b]		D_0 (eV)[c]	
	CH_3I	CH_3I	CH_3I^+	CH_3–I	CH_3^+-I
12.269±0.003	**9.5381±0.0001[d]** **[10.1641±0.0001][d]**	**22.43±0.50[e]** **(13.22±0.50)[e]**	**941.11±0.50[e]** **(932.66±0.50)[e]**	**2.431±0.003**	**2.731±0.003**
12.24±0.01[f]	9.5377±0.0010[e] [10.1639±0.0010][e]	23.5±1.4[i,j] (14.3±1.4)[j]			
12.18[g]	9.5386±0.0006[h] [10.1646±0.0006][h]	23.8±1.0[j,k] (14.6±1.0)[j]			
12.260±0.013[l]		25.1±1.3[j,m] (15.9±1.3)[m]			
G2 predictions[n]					
12.17	9.74	30.5 (21.3)	970.3 (961.9)	2.40	2.43

Table 9-III (Continued)

a) The upper value is IE[$CH_3I'(\widetilde{X}\ ^2E_{3/2})$], and the value in square bracket is IE[$CH_3I'(^2E_{1/2})$].

b) The values in parentheses are $\Delta_fH°_{f298}$ values converted from $\Delta_fH°_0$ values. See the text.

c) This work.

d) Reference 35.

e) Obtained by combining the IE of Ref. 35 and $\Delta_fH°_0$ determined in the present study.

f) Reference 37.

g) Reference 38.

h) Reference 34.

i) Reference 43.

j) The $\Delta_fH°_{f0}$ value is converted from $\Delta_fH°_{f298}$ value.

k) Reference 44.

l) Reference 42.

m) Reference 45.

n) Reference 5.

The best or most precise energetic data for the CH_3/CH_3^+, CH_3Br/CH_3Br^+, and CH_3I/CH_3I^+ systems are highlighted in bold font in Tables 9-II and 9-III. These energetic data, including IEs, 0 K AEs, $\Delta_fH°_0$'s, and D_0's with error limits ≤0.50 kJ/mol, for CH_3/CH_3^+ and CH_3Br/CH_3Br^+ and CH_3I/CH_3I^+ obtained in the present and previous PFI-PE and PFI-PEPICO measurements should provide a challenge for state-of-the-art *ab initio* computational quantum theories. We have compared the most precise experimental values with G2/G3 predictions[5,6] in Tables 9-II and 9-III. The G3 predictions for the CH_3Br/CH_3Br^+ system are calculated using the new basis set for Br provided by Curtiss et al.[46] and are generally in better agreement with the experimental results than the G2 predictions. However, the G3 prediction for the IE of CH_3Br shows no significant improvement over the G2 prediction. The maximum deviations of 13.8 and 10.9 kJ/mol are observed for the respective G2 and G3 predictions for $\Delta H°_{f0}(CH_3Br^+)/\Delta H°_{f298}(CH_3Br^+)$. These errors are greater than the targeted errors of the G2/G3 computational procedures.[5,6] The larger errors observed here are caused by involvement of the heavy elements X=Br and I in CH_3X/CH_3X^+. At present, G3 calculations cannot be made for iodine-containing compounds. We have only computed the G2 predictions for the IE, 0 K AE, $\Delta_fH°_0$, and D_0 for the CH_3I/CH_3I^+ system. As expected, the G2 predictions for CH_3I/CH_3I^+ are considerably poorer than those for CH_3Br/CH_3Br^+. The discrepancies between G2 predictions and the most precise experimental data for CH_3I/CH_3I^+ as shown in Table 9-III are in the range of 2.9-29.3 kJ/mol.

IV. Conclusions

We have performed a high-resolution energy-selected study on the unimolecular dissociation reaction, $CH_3X^+ \rightarrow CH_3^+ + X$, using the PFI-PE and PFI-PEPICO methods. The 0 K AE(CH_3^+) from CH_3X and IE value for CH_3Br obtained in the present study, together with well known energetic data for Br, I, CH_3, CH_3^+, and CH_3I, have made possible the determination of more precise $\Delta_fH°_0$ and D_0 values for CH_3X and CH_3X^+. This study shows that using the PFI-PE and PFI-PEPICO methods, highly reliable $\Delta_fH°_0$ values for a range of neutral species can be determined to a precision comparable to those

achieved for some of the most well known $\Delta_f H°_0$ values reported in the literature, such as $\Delta_f H°_0(CH_4)$. The comparison of the best experimental energetic data for the CH_3X/CH_3X^- system with G2/G3 predictions indicates that the G2/G3 values have errors up to 29.3 kJ/mol. We believe that energetic data such as those presented here with significantly smaller error limits compared to current literature values would play an important role in the development of the next generation of quantum chemical computation schemes.

Acknowledgements

This work was supported by the Director, Office of Energy Research, Office of Basic Energy Sciences, Chemical Science Division of the U.S. Department of Energy under Contract No. W-7405-Eng-82 for the Ames Laboratory and Contract No. DE-AC03-76SF00098 for the Lawrence Berkeley National Laboratory. Y.S. is the receipient of the Wall Fellowship in 1999 and the Henry Gilman Fellowship in 2000 at Iowa State University. C.Y.N. acknowledges helpful discussions with Prof. Tomas Baer.

References

1. H. M. Rosenstock, M. K. Draxl, B. W. Steiner, and J. T. Herron, *J. Phys. Ref. Data*, **6**, Suppl. 1 (1977).
2. S. G. Lias, J. E. Bartmess, J. L. Holmes, R. D. Levin, and W. G. Mallard, *J. Phys. Ref. Data*, **17**, Suppl. 1 (1988).
3. The NIST Chemistry WebBook, http://webbook.nist.gov/chemistry/.
4. J. Berkowitz, "Photoabsorption, Photoionization, and Photoelectron Spectroscopy" (Academic, New York, 1979).
5. L. A. Curtiss, K. Raghavachari, G. W. Trucks, and J. A. Pople, *J. Chem. Phys.* **94**, 7221 (1991); M. N. Glukhovtsev, A. Pross, M. P. McGrath, and L. Radom, J. Chem. Phys. 103, 1878 (1995).
6. L. A. Curtiss, K. Raghavachari, P. C. Redfern, V. Rassolov, and J. A. Pople, *J. Chem. Phys.* **109**, 7794 (1998).
7. K. Müller-Dethlefs, M. Sander, and E.W. Schlag, *Z. Naturforsch.*, A **39**, 1089 (1984).

8. E. W. Schlag, "ZEKE Spectroscopy" (Cambridge Univ. Press, Cambridge, 1998).

9. "High Resolution Laser Photoionization and Photoelectron Studies", edited by I. Powis, T. Baer, and C. Y. Ng, *Wiley Series in Ion Chem. & Phys.* (Wiley, Chichester, 1995).

10. P. M. Johnson, in "Photoionization and Photodetachment", edited by C. Y. Ng (World Scientific, Singapore, 2000), *Adv. Ser Phys. Chem.*, Vol. 10A, p. 296-346.

11. D. D. Martin and J. W. Hepburn, *Phys. Rev. Lett.* **79**, 3154 (1997); ibid., *J. Chem. Phys.* **109**, 8139 (1998).

12. C. Y. Ng, in "Photoionization, and Photodetachment", edited by C. Y. Ng (World Scientific, Singapore, 2000), *Adv. Ser Phys. Chem.* **10A**, Chapter 9, p.394-538.

13 G. K. Jarvis, Y. Song, and C. Y. Ng, *Rev. Sci. Instrum.* **70**, 2615 (1999).

14. G. K. Jarvis, K.-M. Weitzel, M. Malow, T. Baer, Y. Song, and C. Y. Ng, *Rev. Sci. Instrum.* **70**, 3892 (1999).

15. K.-M. Weitzel, G. Jarvis, M. Malow, T. Baer, Y. Song, and C. Y. Ng, *Phys. Rev. Lett.* **86**, 3526 (2001).

16. Y. Song, X.-M. Qian, K.-C. Lau, and C. Y. Ng, J. Liu and W. Chen, *J. Chem. Phys.*, submitted.

17. Karl-Michael Weitzel, Marcus Malow, G. K. Jarvis, Tomas Baer, Y. Song, and C. Y. Ng, *J. Chem. Phys.*, **111**, 8267 (1999).

18. G. K. Jarvis, Karl-Michael Weitzel, Marcus Malow, Tomas Baer, Y. Song, and C. Y. Ng, *Phys. Chem. Chem. Phys.* **1**, 5259 (1999).

19. T. Baer, Y. Song, C. Y. Ng, J. Liu, and W. Chen, *Faraday Discussion* **115**, 137, 2000.

20. T. Baer, Y. Song, C. Y. Ng, W. Chen, and J. Liu, *J. Phys. Chem.* 104, 1959 (2000).

21. *JANAF Thermochemical Tables* (Dow Chemical, Midland, MI, 1977); *J. Phys. Chem. Ref. Data* **11**, 695 (1982).

22. V. P. Glushko, L. V. Gurvich, G. A. Bergman, I. V. Veits, V. A. Medvedev, G. A. Khachkunuzov and V. S. Yungman, Termodinamicheski *Svoistva Individual'nikh Veshchestv* (Nauka, Moscow, 1978), Vol. I, Books 1 and 2.

23. J.A. Blush, P. Chen, R.T. Wiedmann and M.G. White, *J. Chem. Phys.* **98**, 3557 (1993).

24. P. Heimann, M. Koike, C.-W. Hsu, D. Blank, X. M. Yang, A. Suits, Y. T. Lee, M. Evans, C. Y. Ng, C. Flaim, and H. A. Padmore, *Rev. Sci. Instrum.* **68**, 1945 (1997).

25. C.-W. Hsu, M. Evans, P. A. Heimann, and C. Y. Ng, *Rev. Sci. Instrum.* **68**, 1694 (1997).

26. C.-W. Hsu, M. Evans, S. Stimson, C. Y. Ng, and P. Heimann, *Chem. Phys.* **231**, 121 (1998).

27. G. K. Jarvis, M. Evans, C. Y. Ng, and K. Mitsuke, *J. Chem. Phys.* **111**, 3058 (1999).

28. S. Stimson, Y.-J. Chen, M. Evans, C.-L. Liao, C. Y. Ng, C.-W. Hsu, and P. Heimann, *Chem. Phys. Lett.* **289**, 507 (1998).

29. K. Kimura, S.Katsumata, Y. Achiba, T.Yamazaki and S. Iwata, *Handbook of HeI Photoelectron Spectra of Fundamental Organic Compounds*, Japan Scientific Soc. Press, Tokyo, 1981.

30. G. Herzberg, *Molecular Spectra and Molecular Structure, Vol. III. Electronic spectra and Electronic structure of Polyatmoic Molecules*, Florida, 1991.

31. T. Beyer and D. F. Swinehart, *Assoc. Comput. Mach., Commun.*, **16**, 379(1973).

32. B. P. Tsai, T. Baer, A. S. Werner, and S. F. Lin, J. Phys. Chem. **79**, 570 (1975).

33. P. Hochmann, P. H. Templet, H.-T. Wang, and S. P. McGlynn, J. Chem. Phys. **62**, 2588 (1975); W. C. Price, J. Chem. Phys. **4**, 539 (1936).

34. A. Strobel, A. Lochschmidt, I. Fischer, G. Niedner-Schatteburg and V.E. Bondybey, *J. Chem. Phys.* **99**, 733 (1993). A. Strobel, I. Fischer, A. Lochschmidt, K. M , J. Phys. Chem. **98**, 2024 (1994).

35. M. A. Baig, J. P. Connerade, J. Dagata, and S. P. McGlynn, J. Phys. **B14**, L25 (1981).

36. K. Walter, R. Weinkauf, U. Boesl, and E. W. Schlag, J. Chem. Phys. **89**, 1914 (1988).

37. D. M. Mintz and T. Baer, J. Chem. Phys. **65**, 2407 (1976).

38. M. Krauss, J. A. Walker, and V. H. Dibeler, J. Res. NBS, **72A**, 281 (1968); J. C. Traeger and R. G. McLoughlin, J. Am. Chem. Soc. **103**, 3647 (1981).

39. J. Berkowitz, G. B. Ellison, and D. Gutman, J. Phys. Chem. **98**, 2744 (1994).

40. K. C. Ferguson, E. N. Okafo, and E. Whittle, J. Chem. Soc. Faraday Trans. 1, **69**, 295 (1973).

41. G. P. Adams, A. S. Carson, and P. G. Laye, Trans. Faraday Soc. **62**, 1324 (1965); P. Fowell, J. R. Lacher, and J. D. Park, Trans. Faraday Soc. **61**, 1324 (1965).

42. A. J. C. Nickolson, in "Recent Developments in Mass spectrometroscopy", edited by K. Ogata and T. Hayakawa (Univ. Park Press, Baltimore, 1970), p.745.

43. D. M. Golden, R. Walsh, S. W. Benson, J. Am. Chem. Soc. **87**, 4053 (1965).

44. J. D. Cox and G. Pilcher, "Thermochemistry of Organic and Organometallic Compounds" (Academic Press, New York, 1965).

45. C. A. Goy and H. O. Pritchard, J. Phys. Chem. **69**, 3040 (1965).

46. L. A. Curtiss, P. C. Redfern, V. Rassolov, G. Kedziora, and J. A. Pople, J. Chem. Phys., submitted.

CHAPTER 10. A PULSED FIELD IONIZATION STUDY OF THE DISSOCIATIVE PHOTOIONIZATION REACTION $CD_4 + h\nu \rightarrow CD_3^+ + D + e^-$

A paper to be published in *Chemical Physics Letters*, (2001)

Y. Song, X.-M. Qian, K.-C. Lau and C.Y. Ng

Abstract:

We have examined the energetics and dynamics of the reaction $CD_4 + h\nu \rightarrow CD_3^+ + D + e^-$ near its 0 K threshold or appearance energy (AE) using the pulsed field ionization-photoelectron (PFI-PE) and PFI-PE-photoion coincidence methods. This study yields a value of 14.4184±0.0010 eV for the 0 K AE, which has allowed accurate determination of the 0 K bond dissociation energies for $D\text{-}CD_3^+$ (1.746±0.003 eV) and $D\text{-}CD_3$ (4.5881±0.0012 eV). The PFI-PE spectrum for CD_4 is found to exhibit a sharp step at the 0 K AE(CD_3^+), indicating that the dissociation of excited CD_4 in high-n ($n \geq 100$) Rydberg states at energies above the AE occurs in $\leq 10^{-7}$ s. We have examined the consistency of the available energetic data for CD_3/CD_3^+ and CD_4/CD_4^+ with those for CH_3/CH_3^+ and CH_4/CH_4^+ and found that the two data sets are in excellent accord after taking into account the zero point vibrational energy corrections.

I. Introduction

The recent successful implementation of synchrotron-based pulsed field ionization (PFI)-photoelectron (PFI-PE)[1,2] and PFI-PE-photoion coincidence (PFI-PEPICO)[3] methods at the Chemical Dynamics Beamline of the Advanced Light Source (ALS) has greatly enhanced the potential of PFI techniques for routine high-resolution photoionization measurements. Since the PFI-PE detection is free from the hot-electron tail problem, we have demonstrated in previous PFI-PEPICO studies[4,5] that accurate 0 K dissociative photoionization threshold or appearance energies (AEs) for a range of molecules can be determined unambiguously by the disappearance energy for the parent ion.

Due to the importance of CH_4/CH_4^+ and CH_3/CH_3^+ in combustion, atmospheric and interstellar chemistry, numerous photoionization studies have been made on CH_4, resulting in highly accurate energetic data for these species.[4] In comparison, the investigation of the deuterated species CD_4/CD_4^+ and CD_3/CD_3^+ was sparse. The only previous AE measurement for the reaction

$$CD_4 + h\nu \rightarrow CD_3^+ + D + e^- \qquad (1)$$

was made by a photoionization efficiency (PIE) study, obtaining an AE value of 14.38±0.03 eV.[6]

This Letter presents the results of a PFI-PE and PFI-PEPICO study of reaction (1) near its 0 K AE. We show that the 0 K AE(CD_3^+) from CD_4 can be determined unambiguously by the disappearance energy of parent CD_4^+ with an error limit of ±0.001 eV.[4,5] Furthermore, a sharp step at the 0 K AE(CD_3^+) is resolved in the PFI-PE spectrum for CD_4, indicating that excited CD_4^* fragments into CD_3^* + D in a time scale $\leq 10^{-7}$ s, where CD_4^* and CD_3^* represents CD_4 and CD_3 in high-n ($n \geq 100$) Rydberg states.[7] We have also found that the available energetic data for CD_4/CD_4^+ and CD_3/CD_3^+ are consistent with those for CH_4/CH_4^+ and CH_3/CH_3^+ after taking into account the zero point vibrational energies (ZPVEs) for these molecular species.

II. Experimental

The PFI-PE and PFI-PEPICO experiments were conducted using the high-resolution VUV facility of the Chemical Dynamics Beamline with the ALS operating in the two-bunch mode.[1-3,8] In the present experiment, Ar was used in the gas filter to suppress higher undulator harmonics with photon energies (hν) greater than 15.76 eV. In the two-bunch operation, the ALS period (656 ns) consists of two VUV bunches (bunch width = 50 ps) separated by a dark gap of 328 ns. A 2400 lines/mm grating (dispersion = 0.64 Å/mm) was used to disperse the first order undulator harmonic with entrance/exit slits set in the range of 30-100 μm. The hν calibration was achieved using the $Ar^+(^2P_{3/2})$ and

$Xe^+(^2P_{3/2})$ PFI-PE bands. Previous experiments indicate that the accuracy of such a calibration is within ±0.5 meV.[8]

The PFI-PE and PFI-PEPCO measurements were achieved by employing the time-of-flight (TOF) scheme.[2,3] The PFI pulse (height =7.3 V/cm, width=180 ns) was applied ≈20 ns after the start of the dark gap. The PFI pulse also served to extract PFI-photoions toward the ion detector.[3] The average accumulation time for a PFI-PEPICO TOF spectrum is ≈20 min. Although the overall light intensity is significantly lower in this two-bunch mode operation, the larger dark gap available is more favorable for PFI-PEPICO measurements.[3] The PFI-PEPICO resolution achieved is ≈1.0 meV (FWHM).

The CD_4 sample (obtained from Aldrich, purity = 99.99%) was mixed with high purity He at a 1:10 ratio prior to expansion through a stainless steel nozzle at a stagnation pressure of 760 Torr and a stagnation temperature of 298 K. Using the same beam production system described previously,[4,5,8] the photoionization chamber maintained a pressure of $<10^{-6}$ Torr during the experiment. All PFI-PEPICO measurements were made using the supersonic CD_4/He beam sample. We estimate that CD_4 at the photoionization/photoexcitation region consists of ≈85% cold beam sample and ≈15% thermal background in the photoionization chamber. We have also recorded a PEI-PE spectrum for CD_4 using an effusive CD_4 sample for comparison with that obtained using the supersonic beam sample

III. Results and Discussion

Selected PFI-PEPICO TOF spectra for CD_3^+ and CD_4^+ in the hν region of 14.35-14.43 eV are depicted in Fig. 10-1. At hν<14.40 eV, the parent CD_4^+ ion peak at 21.84 μs has the dominant intensity. As the hν is increased in the range of 14.400-14.418 eV, the intensity for the daughter CD_3^+ ion peak at 20.70 μs increases rapidly with the concomitant decrease for CD_4^+. Although the CD_3^+ peak is overwhelmingly dominant at hν≥14.4184 eV, a small CD_4^+ peak is discernible in the TOF spectrum. This small CD_4^+ signal is attributed to coincidence background caused by hot electrons dispersed into the dark gap.[9,10]

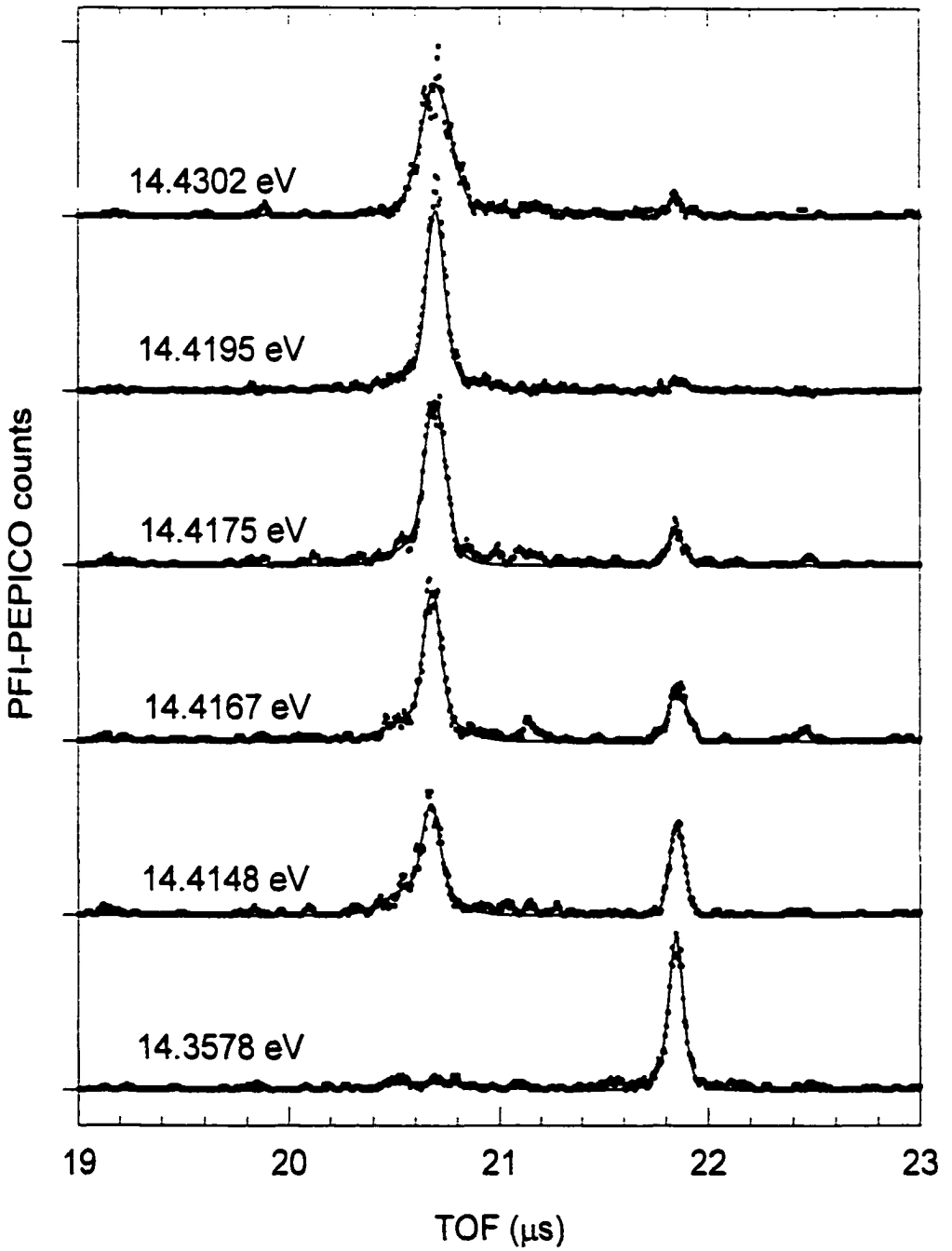

Figure 10-1 Selected PFI-PEPICO TOF spectra for CD_3^+ and CD_4^+ in the hν range of 14.3578-14.4302 eV. The respective TOF peaks for CD_3^+ and CD_4^+ are centered at 20.69 and 21.87 μs. The solid lines are simulated spectra (see the text).

Similar to previous PFI-PEPICO studies.[3,4] the TOF peak shapes for parent CD_4^+ and daughter CD_3^+ are analyzed to consist of the contribution of a narrow component due to the cold CD_4 beam sample and a broad component arising from the thermal CD_4 background using two Gaussian functions with widths of ≈100 ns and ≈300 ns, respectively. We note that the PFI-PEPICO TOF peaks appear to be slightly asymmetric. This is likely caused by a finite misalignment of the molecular beam and the VUV beam, such that the average flight times for ions formed by photoionization of the thermal and cold samples are slightly different.[10] The previous studies indicated that the TOF peak could be distorted due to the pulsed extraction scheme used in the PFI-PEPICO measurements.[3,4] The overall fits are indicated as solid lines in Fig. 10-1. The broad CD_3^+ peak observed in the TOF spectrum at hν=14.4302 eV is caused by the kinetic energy release of reaction (1). Figure 10-2(a) shows the breakdown curves (i.e., fractional abundances plotted as a function of hν)[3,4] for CD_3^+ (open squares) and CD_4^+ (open circles) constructed by including the entire (cold and thermal) ion signals for CD_3^+ and CD_4^+. The breakdown curves constructed based only on the cold CD^+ and CD_4^+ ion signals are shown in Fig. 10-2(b). The rise and fall of the respective breakdown curves for CD_3^+ and CD_4^+ manifest finite internal rovibrational excitations of parent CD_4. Due to the rotational cooling of CD_4 achieved in the supersonic expansion, the cold breakdown curves of Fig. 10-2(b) are sharper, showing the complete dissociation of excited CD_4^+ to $CD_3^+ + D$ in an energy interval of ≈15 meV.

We have shown previously that the 0 K AE can be determined by the disappearance energy of the parent ion in a PFI-PEPICO study.[3,4] Due to the small coincidence background for CD_4^+, the disappearance energy is manifested as the sharp break [marked by arrows in Figs. 10-2(a) and 10-2(b)] of the breakdown curves for CD_4^+. Although the shapes of the two sets of break down curves obtained by including and excluding the dissociation of thermal CD_4 are quite different, the disappearance energies for the parent CD_4^+ are identical. The disappearance energy of CD_4^+ is the energy at which even the coldest part of the CD_4 energy distribution reaches above the dissociation threshold. Thus, the disappearance energy of CD_4^+ is an intrinsic feature and can be used to provide an

Figure 10-2 Breakdown curves of CD_3^- and CD_4^- in the hv range of 14.30-14.47 eV. (a) The experimental fractional abundances for CD_3^- and CD_4^- obtained based on the entire ion signal are shown as (O) and (□). respectively. The dashed lines (– –) are the simulated curves. (b) The experimental fractional abundances for CD_3^- and CD_4^- obtained based only on the cold ion signals are indicated as (●) and (■), respectively. The continuous lines (—) are the simulated curves obtained by assuming a sample temperature of 40 K. (c) PFI-PE spectra obtained using an effusive sample (solid circles, upper spectrum) and a supersonic molecular beam sample (open circles, lower spectrum). The step at the 0 K AE is discernible in the lower PFI-PE spectrum.

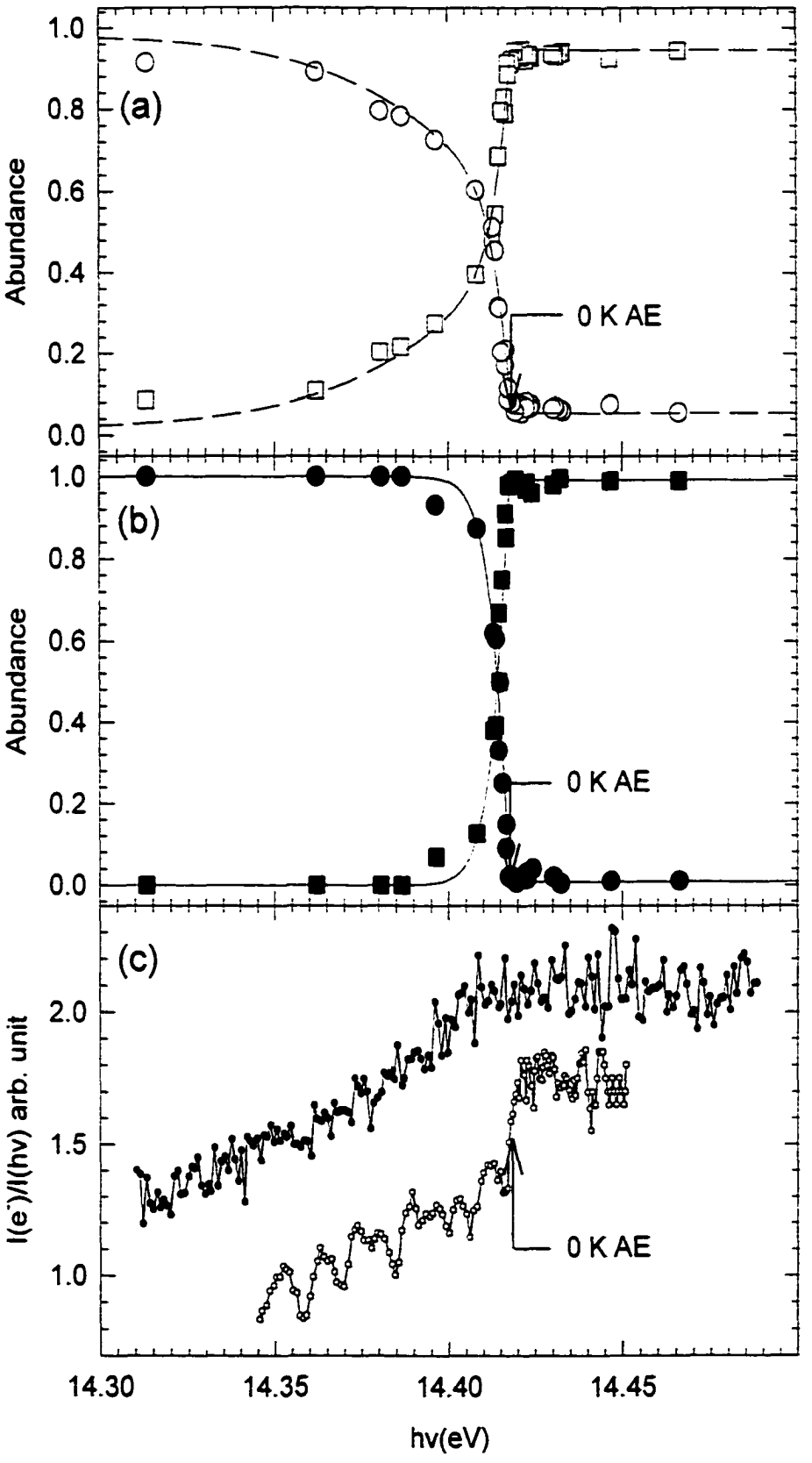
(a)
Abundance
0 K AE
(b)
Abundance
0 K AE
(c)
I(e⁻)/I(hv) arb. unit
0 K AE
hv(eV)

unambiguous determination of the 0 K AE(CD_3^+) independent of the internal energy distribution of CD_4.

We have also simulated the breakdown diagrams of Figs. 10-2(a) and 10-2(b) using procedures described previously.[9,10] The simulation assumes that the ion energy resolution is infinitely narrow and that the broadening of the breakdown diagram is due solely to the thermal excitation of parent CD_4. The thermal energy distribution in CD_4 was determined by calculating the density of rovibrational states using the Beyer-Swinehart direct count algorithm[11] based on the known vibrational frequencies and rotational constants for CD_4. Due to the relatively high vibration frequencies for CD_4, the thermal energy for this system is mainly contributed by rotational excitations. By assuming a temperature of 40 K for cold CD_4 in the supersonic beam, we have obtained an excellent fit (solid lines) of the cold breakdown curves shown in Fig. 10-2(b). The dashed lines in Fig. 10-2(a) are simulated breakdown curves, which have taken into account the contribution of a minor component of thermal CD_4 background together with the major component of cold CD_4 in the supersonic beam.[10] The simulation also assumes a constant coincidence background for CD_4^+, which results in a constant fractional abundances of ≈6% and ≈3% for CD_4^+ in Figs. 10-2(a) and 10-2(b), respectively.[10] This simulation is consistent with the conclusion that the break at 14.4184±0.0010 eV resolved in the breakdown curves of Figs. 10-2(a) and 10-2(b) is a distinct feature, which can be taken as the 0 K AE(CD_3^+). Figure 10-3 shows a magnified view of the simulated and experimental breakdown data for CD_4^+, together with their error bars, in the region of 14.410-14.447 eV. The designations of symbols used in Figs 10-2(a), 10-2(b), and 10-3 are identical. It is clear in Fig. 10-3 that the break marking the 0 K AE(CD_3^+) at 14.4184eV can be determined unambiguously to within ±0.0010 eV by the breakdown curve for CD_4^+ shown in either Fig. 10-2(a) or Fig. 10-2(b).

In previous studies, we have identified sharp step-like features in the PFI-PE spectra for CH_4 and C_2H_2, marking precisely the corresponding 0 K AEs for CH_3^+ and C_2H^+ determined in PFI-PEPICO measurements.[3,4,7] A detailed discussion concerning the conditions for the observation of a step at the 0 K AE of a dissociative photoionization process has been given.[7] Figure 10-2(c) compares the PFI-PE spectra for CD_4 in the region of 14.30-14.50 eV obtained using an effusive sample (upper spectrum, solid circles) and a

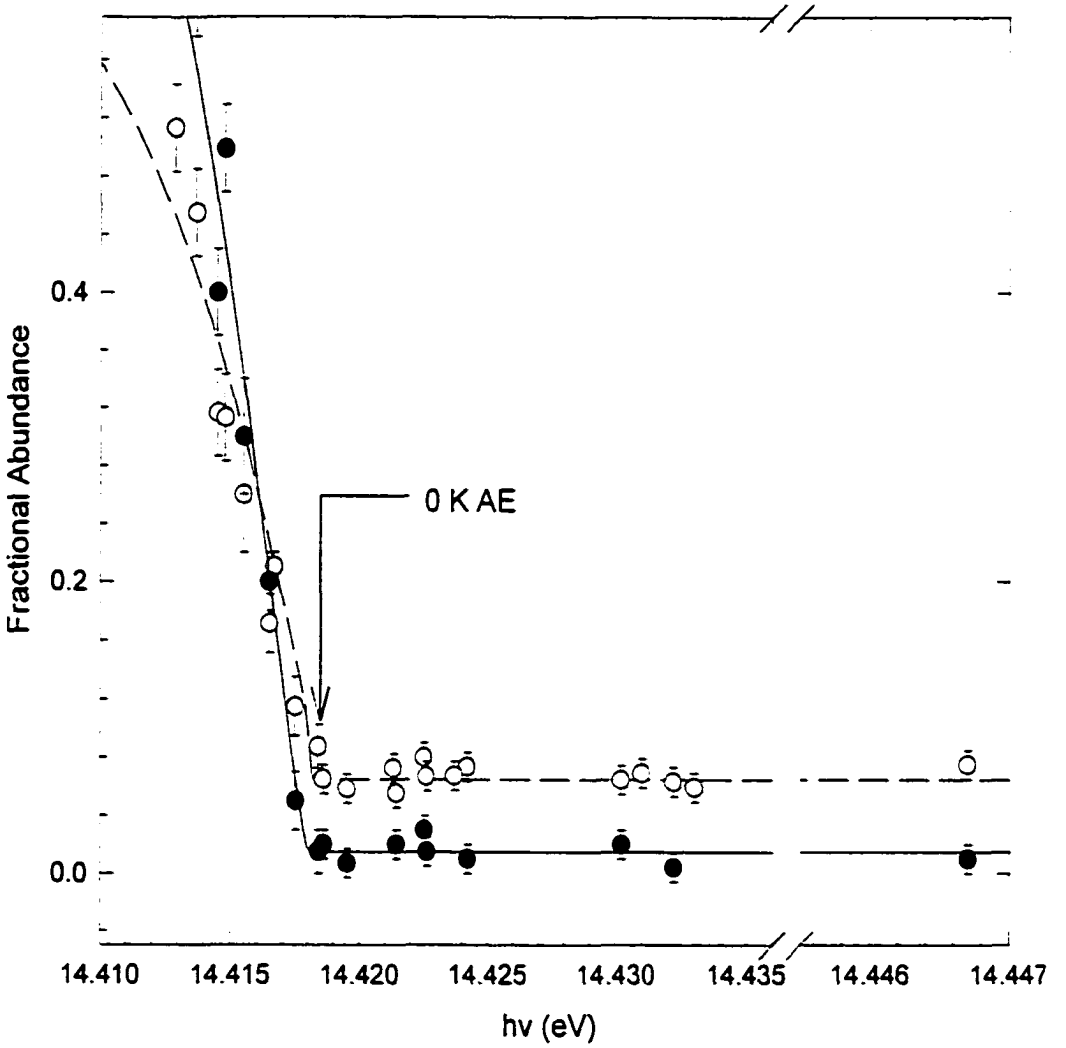

Figure 10-3 A magnified view of the breakdown curve for CD_4^- based on the entire ion signals (O) and that based only on the cold ion signals (●) in the hv range of 14.410-14.447 eV. Both curves show a sharp break at 14.4184±0.0010 eV, which is taken to be the 0 K AE(CD_3^-).

supersonic beam sample (lower spectrum, open circles). Although the PFI-PE spectrum obtained using an effusive CD_4 sample shows a general increase in PFI-PE intensity as the hν is increased, a step at the 0 K AE(CD_3^+) is not discernible. The PFI-PE spectrum for CD_4 obtained using the cold beam sample clearly reveals a sharp step [marked as 0 K AE in Fig. 10-2(c)]. The observation of this step can be attributed to the lifetime switching effect[7] at the 0 K AE(CD_3^+), where CD_4* species with shorter lifetimes are converted into CD_3* fragments with longer lifetimes. The longer lifetime observed for CD_3* results from the fact that CD_3* formed at the AE has an energy below the IE(CD_3) and thus cannot decay via autoionization. The observation of the sharp step in the PFI-PE spectrum indicates[7] that the conversion from CD_4* to CD_3* at energy above the AE of reaction (1) is complete prior to PFI and that process (1) has a dissociation rate constant $\geq 10^7$ s^{-1}. This step resolved in the PFI-PE spectrum for CD_4 can be taken as a confirmation for the 0 K AE(CD_3^+)=14.4184±0.0010 eV determined in the PFI-PEPICO study.

The dissociation leading to the production of CD_3* from CD_4* formed by VUV excitation of thermally excited CD_4 occurs below the 0 K AE. As a result of the magnification of PFI events for CD_3* fragments, the PFI-PE spectrum observed using an effusive beam of CD_4 [upper spectrum in Fig. 10-2(c)] is expected to manifest a higher nominal temperature than the actual temperature of the effusive sample. This would result in the efficient filling of the step in the PFI-PE spectrum. Thus, the step associated with the 0 K AE cannot be readily identified in the PFI-PE spectrum using a thermal sample.

The 0 K AE(CD_3^+) =14.4184±0.0010 eV determined here is significantly more precise compared to the previous PIE value of 14.38 ± 0.03 eV.[6] These values along with selected literature IE values[12-17] for CD_3 and CD_4 are listed in Table 10-I. The IE(CD_4)=12.672±0.003 eV[12] and IE(CD_3)=9.8303±0.0006 eV[15] determined in recent PFI studies are likely the most accurate among previous measurements. Based on these IE values and the 0 K AE(CD_3^+) determined here, we have calculated the 0 K bond dissociation energies as D_0(D-CD_3^+) = AE(CD_3^+)–IE(CD_4) = 1.746±0.003 eV and D_0(D-CD_3) = AE(CD_3^+)-IE(CD_3) = 4.5881±0.0012 eV. The experimental 0 K or 298 K heats of formation ($\Delta_f H°_0$ or $\Delta_f H°_{298}$) for CD_3 and CD_4 are not available. Krishna et al.[18] has

Table I. Comparison of $\Delta H°_{f0}$ values for CD_3, CD_3^+, CD_4, and CD_4^+, 0 K $AE(CD_3^+)$ from CD_4, and D_0 values for CD_3-D and CD_3^+-D.[a]

$AE(CD_3^+)$ (eV)	IE(eV)		$\Delta H°_{f0}$ (kcal/mol)[c]				D_0(eV)[b]	
	CD_4	CD_3	CD_4[f]	CD_4^+[g]	CD_3[f]	CD_3^+[h]	CD_3-D	CD_3^+-D
14.4184±0.0010[b]	**12.672±0.003[c]**	**9.8303± 0.0006[d]**	**-19.21±0.10 (-21.09±0.10)**	**273.01±0.12 (271.50±0.12)**	**33.90±0.10[f] (33.14±0.10)**	**260.75±0.10 (259.93±0.10)**	**4.5881 ±0.0012**	**1.746 ±0.003**
14.38±0.03[i]	12.658 ± 0.015[j]	9.832±0.002[k]						
	12.882 ± 0.008[l]	9.831 ± 0.007[m]						
Semi-empirical G3/G2 values[n]								
14.41/14.39	12.70/12.73	9.86/9.77	-19.8/-20.2 (-21.6/-22.1)	273.2/273.4 (271.6/271.8)	32.7/33.8 (32.2/33.3)	260.0/259.1 (259.1/258.3)	4.55/4.62	1.71/1.66

a) The values in bold fonts are the best experimental values.
b) This work
c) Reference 12
d) Reference 15
e) The values in parentheses are $\Delta H°_{f298}$ values. The $\Delta H°_{f298}$ values for CD_3 and CD_4 are from Ref. 18 and those for CD_3^+ and CD_4^+ are converted from the corresponding
f) Reference 18
g). References. 12 and 18
h)This work and Ref. 18. Calculated using reaction
i) Reference 6.
j) Reference 16
k) Reference 13
l) Reference 17
m)Reference 14
n) References 22 and 23

279

calculated the $\Delta_fH°_0$ and $\Delta_fH°_{298}$ values for CD_3 and CD_4 by statistical methods using the known $\Delta_fH°_0$ and $\Delta_fH°_{298}$ values for CH_3 and CH_4. The conversion requires the ZPVEs for CH_4, CD_4, CH_3, and CD_3 (see Table 10-II),[18] which are calculated using known experimental vibrational frequencies of these species. The D_0 values for CD_4 and CD_4^+ and the statistically derived $\Delta_fH°_0$ and $\Delta_fH°_{298}$ values for CD_3 and CD_4 are also listed in Table 10-I.

Using the $\Delta_fH°_0(D)$=52.535±0.001 kcal/mol,[19] together with the 0 K $AE(CD_3^+)$ (332.50±0.02 kcal/mol) and $\Delta_fH°_0(CD_4)$ (-19.214±0.1 kcal/mol),[18] we obtain $\Delta_fH°_0(CD_3^+)$ = 260.75±0.10 kcal/mol based on process (1). If we combine the $IE(CD_3)$=9.8303±0.0006 eV[15] and $\Delta_fH°_0(CD_3)$ (33.90±0.10 kcal/mol),[18] we derive the value $\Delta_fH°_0(CD_3^+)$ =260.59±0.10 kcal. The excellent agreement of the latter value with that of 260.75±0.10 kcal/mol derived using process (1) indicates that the experimental 0 K $AE(CD_3^+)$, $IE(CD_3)$, and derived $\Delta_fH°_0(CD_3)$ and $\Delta_fH°_0(CD_4)$ values are highly reliable. Combining the $IE(CD_4^+)$ (292.22±0.07 kcal/mol) and $\Delta_fH°_0(CD_4)$ gives $\Delta_fH°_0(CD_4^+)$ = 273.01±0.12 kcal/mol. The latter value along with the $\Delta_fH°_0(CD_3^+)$ value derived using process (1) is included in Table 10-I.

Since not all the vibrational frequencies for CH_4^+, CD_4^+, CH_3^+, and CD_3^+ are known, accurate experimental ZPVEs for these cations cannot be obtained. We have calculated the ZPVEs at the MP2(Full)/6-311++G(3d2f,2pd) level of theory.[20] Comparing the experimental and theoretical ZPVEs for the neutral species,[18] we obtain an average scaling factor of 0.957 for the theoretical ZPVEs. The scaled theoretical ZPVEs are given in Table 10-II. Using these scaled theoretical ZPVEs, we have calculated values (given in parentheses in Table 10-II) for the $IE(CD_3)$, $IE(CD_4)$, $D_0(D\text{-}CD_3)$, $D_0(D\text{-}CD_3^+)$, and $AE(CD_3^+)$ based on corresponding values for $IE(CH_3)$,[21] $IE(CH_4)$, $D_0(H\text{-}CH_3)$, $D_0(H\text{-}CH_3^+)$, and $AE(CH_3^+)$.[12,20] Since the error bars assigned to these calculated values have ignored the uncertainties associated with the theoretical ZPVEs, they represent lower limits. As shown in Table 10-II, the calculated (values in parentheses) and experimental (values in bold fonts) are in good agreement, indicating that the available experimental IE, D_0, AE, values for CH_4/CH_4^+, CH_3/CH_3^+, CD_4/CD_4^+ and CD_3/CD_3^+ are reliable. The small

Table 10-II. Zero point vibrational energies (ZPVEs), IE, D_0, and AE values for CH_4/CH_4^+, CH_3/CH_3^+, CD_4/CD_4^+, and CD_3/CD_3^+.[a]

X	ZPVE (eV)[b]				IE (eV)		D_0 (eV)		AE (eV)
	CX_4	CX_3	CX_4^+	CX_3^+	CX_4	CX_3	CX_3^+-X	CX_3-X	CX_3^+
H	1.183 **1.1755**[c]	0.790 **0.7896**[c]	1.014	0.832	**12.618±0.004**[d]	**9.8380±0.0004**[e]	**1.705±0.004**[g]	**4.485±0.001**[g]	**14.323±0.001**[g]
D	0.868 **0.8683**[c]	0.580 **0.5850**[c]	0.744	0.615	**12.672±0.003**[d] (12.664±0.004)[i]	**9.8303±0.0006**[f] (9.8291±0.0004)[i]	**1.746±0.003**[h] (1.754±0.004)[i]	**4.5881±0.0012**[h] (4.591±0.001)[i]	**14.4184±0.0010**[h] (14.421±0.001)[i]

a) The values in bold fonts represent the best experimental values. The values in parentheses are converted from corresponding IE or D_0 or AE values of CH_n or CH_n^+ (n=3, 4) using the scaled theoretical ZPVEs (see the text).

b) The upper values are scaled (scaling factor=0.957) ZPVEs calculated at the MP2(Full)/6-311++G(3d2f,2pd) level of theory.

c) Calculated using the experimental vibrational frequencies given in Ref. 18

d) Reference 12

e) Reference 20

f) Reference 15

g) Reference 4

h) This work

i) The error limits have not taken into account the errors for the scaled ZPVEs and are thus lower bounds.

discrepancies between the calculated and experimental IE, D_0, and AE values for CD_4/CD_4^+ and CD_3/CD_3^+ can be attributed to errors of the theoretical ZPVEs used.

The highly accurate energetic data (values in bold fonts in Tables 10-I and 10-II) would provide a challenge for state-of-the-art *ab initio* computational quantum theories. Currently, the Gaussian2/Gaussian-3 (G2/G3) procedures[22,23] are among the most popular quantum chemical computation schemes. The G2/G3 theories are slightly semi-empirical in nature because they contain a high level correction obtained empirically from a fit to a set of experimental energetic data by minimizing the deviations between corresponding experimental results and predicted values. The accuracy of such a fitting scheme is limited by the accuracy of experimental data used. We have compiled the G2/G3 values for $AE(CD_3^+)$, $IE(CD_4)$, $IE(CD_3)$, and $\Delta H°_{f0}/\Delta H°_{f298}$ of CD_3, CD_3^+, CD_4, and CD_4^+ for comparison with the best experimental values in Table 10-I.[22,23] As expected, the G3 predictions show a consistently better agreement with the best experimental values than the G2 results. The G2/G3 predictions are generally in agreement with the experimental values, achieving the target accuracy[22,23] of ≈1 kcal/mol for the computational procedures. We note that the precisions of the best experimental values listed in Tables 10-I and 10-II are significantly better than that can be achieved by G2/G3 calculations. Accurate AE, IE, and $\Delta H°_{f0}$ values, such as those listed in Tables 10-I and 10-II with error limits in the meV range, should play an important role in the development of the next generation of *ab initio* quantum computational procedures.

IV. Conclusions

We have examined the dissociation reaction of energy-selected CD_4^+ to form CD_3^+ + D near its threshold using PFI techniques. The 0 K $AE(CD_3^+)$ obtained has made possible the determination of accurate $D_0(D\text{-}CD_3^+)$, $D_0(D\text{-}CD_3)$, and $\Delta H°_{f0}(CD_3^+)$ values through appropriate thermochemical cycles. The sharp step-like feature appearing at the 0 K $AE(CD_3^+)$ observed in the PFI-PE spectrum of CD_4 is consistent with the lifetime switching effect,[7] indicating that the dissociation of reaction (1) at energies above its threshold occurs in a time scale of $\leq 10^{-7}$ s. We found that the energetic data for CH_4/CH_4^+

and CH_3/CH_3^+ are in excellent accord with those for CD_3/CD_3^+ and CD_3/CD_3^+ after taking into accounts the ZPVEs of these species.

Acknowledgments

This work was supported by the Director, Office of Energy Research, Office of Basic Energy Sciences, Chemical Science Division of the U.S. Department of Energy under Contract No. W-7405-Eng-82 for the Ames Laboratory and Contract No. DE-AC03-76SF00098 for the Lawrence Berkeley National Laboratory. The authors are grateful to Drs. J. Liu and W. Chen for their experimental assistance.

References

1. C.-W. Hsu, P. Heimann, M. Evans, and C. Y. Ng, Rev. Sci. Instrum. 68 (1997) 1694.
2. G. K. Jarvis, Y. Song, and C. Y. Ng, Rev. Sci. Instrum. 70 (1999) 2615.
3. G.K. Jarvis, K.-M. Weitzel, M. Malow, T. Baer, Y. Song, and C. Y. Ng, Rev. Sci. Instrum. 70 (1999) 3892.
4. Karl-Michael Weitzel, Marcus Malow, G. K. Jarvis, Tomas Baer, Y. Song, and C. Y. Ng, J. Chem. Phys. 111 (1999) 8267.
5. G. K. Jarvis, Karl-Michael Weitzel, Marcus Malow, Tomas Baer, Y. Song, and C. Y. Ng, Phys. Chem. Chem. Phys. 1 (1999) 5259.
6. V.H. Dibeler, M. Krauss, R.M. Reese and F.N. Harllee, J. Chem. Phys. 42 (1965) 3791.
7. K.-M. Weitzel, G. Jarvis, M. Malow, T. Baer, Y. Song, and C. Y. Ng, Phys. Rev. Lett. 86 (2001) 3526.
8. C. Y. Ng, in "Photoionization, and Photodetachment", edited by C. Y. Ng (World Scientific, Singapore, 2000), Adv. Ser Phys. Chem. 10A, Chapter 9, p.394-538.
9. T. Baer, Y. Song, C. Y. Ng, W. Chen, and J. Liu, J. Phys. Chem. 104 (2000) 1959.
10. Y. Song, X.-M. Qian, K.-C. Lau, and C. Y. Ng, J. Liu and W. Chen, J. Chem. Phys., accepted.
11. T. Beyer and D. F. Swinehart, Assoc. Comput. Mach., Commun. 16 (1973) 379.

12. R. Signorell and F. Merkt, J. Chem. Phys. 110 (1999) 2309.

13. G. Herzberg and J. Shoosmith, Can. J. Phys. 34 (1956) 523.

14. J. Dyke, N. Jonathan, E. Lee, A. Morris, J. Chem. Soc. Faraday Trans. 2, 72 (1976) 1385.

15. H. Dickenson, T. Chelmick, and T. P. Softly, Chem. Phys. Lett. 338 (2001) 37.

16. J. Berkowitz, J. P. Greene, H. Cho, B. Ruscic, J. Chem. Phys. 86 (1987) 674.

17. A. J. C. Nicholson, J. Chem.. Phys. 43 (1965) 1171.

18. Krishna M. Pamidimukkala, David Rogers and Gordon B. Skinner, J. Phys. Chem. Ref. Data, 11 (1982) 83.

19. The NIST Chemistry WebBook, http://webbook.nist.gov/chemistry/.

20. M. J. Frisch, et al., GAUSSIAN 98, Revision A7: Gaussian, Inc.: Pittsburgh, PA, 1998.

21. J. A. Blush, P. Chen, and R. T. Wiedman, and M. G. White, J. Chem. Phys. 98 (1993) 3557.

22. L. A. Curtiss, K. Raghavachari, G. W. Trucks, and J. A. Pople, J. Chem. Phys. 94 (1991) 7221.

23. L. A. Curtiss, K. Raghavachari, P. C. Redfern, V. Rassolov, and J. A. Pople, J. Chem. Phys. 109, (1998) 7794.

CHAPTER 11. OBSERVATION OF ACCURATE ION DISSOCIATION THRESHOLDS IN PULSED FIELD IONIZATION-PHOTOELECTRON STUDIES

A paper published in *Physical Review Letters*, **86**, 3526 (2001)

Karl-Michael Weitzel, G. K. Jarvis, Marcus Malow, Tomas Baer,
Y. Song, and C. Y. Ng

Abstract:

We report the first observation, together with a mechanism for such an observation, of a step-like feature in the pulsed field ionization photoelectron (PFI-PE) measurement of CH_4 (C_2H_2), marking the 0 K dissociation threshold for the formation of $CH_3^+ + H$ ($C_2H^+ + H$) from CH_4 (C_2H_2). The non-existence of a step in the PFI-PE spectrum for C_2H_4 at its dissociation threshold for $C_2H_2^+$ formation provides strong support for the proposed mechanism. This experiment shows that for a range of molecules, where the ion dissociation lifetimes near the dissociation thresholds are $<10^{-7}$ s, PFI-PE measurements will yield not only highly accurate ionization energies, but also 0 K dissociation thresholds.

Text:

Photoionization and photoelectron spectroscopy is a major technique for research in physical sciences. The most important data obtainable in a photoionization-photoelectron experiment are ionization energies (IEs) and ion dissociation thresholds or appearance energies (AEs), from which bond dissociation energies for neutrals and cations can be deduced [1]. The recent development in vacuum ultraviolet (VUV) lasers [2,3] and third generation synchrotron source [4,5], together with the introduction of pulsed field ionization (PFI) techniques [6-8], has revolutionized this field by significantly improving the energy resolution close to the optical bandwidth [9]. For many simple molecules, the PFI-photoelectron (PFI-PE) method allows the measurement of rotationally resolved photoelectron spectra, yielding definitive IEs with uncertainties limited only by the energy

calibration [3,5-9]. The recent successful implementation of PFI schemes [10-13] using the high-resolution VUV synchrotron radiation at the Advanced Light Source (ALS) has made possible the routine examination of molecular dissociative photoionization processes employing PFI techniques [12, 14-16]. Here, we show for the first time that highly accurate 0 K AE values [17] for a range of molecules can also be determined in PFI-PE studies.

The PFI-PE experiment presented here was conducted at the ALS utilizing the high-resolution monochromatized VUV source of the Chemical Dynamics Beamline, which has demonstrated an optical resolution close to that of VUV lasers [4,5]. The greatest advantage of this source is its ease of tunability covering the full VUV range of 8-30 eV. The procedures for PFI-PE measurements using the photoelectron-photoion facility of the Chemical Dynamics Beamline have been described previously [11]. Briefly, the gaseous samples (CH_4, C_2H_2, and C_2H_4) are introduced into the photoionization/photoexcitation (PI/PEX) region of the apparatus as a skimmed supersonic beam, achieving a temperature of ≈30 K [12]. The ALS light pattern in the present multibunch operation consists of 256 light pulses (duration of each light pulse = 50 ps) with a time separation of 2 ns between successive light pulses and a dark gap of 144 ns in one period (656 ns) [12]. Excited parent species in high-n (n>100) Rydberg states, formed by excitation of the beam sample at the PI/PEX center by the dispersed synchrotron radiation, are field ionized by an electric field pulse (height ≈ 1.5 V/cm, width ≈ 40 ns) applied in the dark gap. This PFI pulse is delayed by 20 ns with respect to the beginning of the dark gap. Electrons formed by PFI in the dark gap are selected by a time-of-flight scheme using a detection time gate [11]. The photon energy calibration was achieved using rare gas PFI-PE bands recorded under the same experimental conditions. Previous experiments indicate that the accuracy of this calibration method is within ±0.5 meV [4,5,18].

The PFI-PE spectrum for CH_4 (C_2H_2) measured in the region of 14.25-14.40 eV (17.26-17.40 eV) is depicted in Figs. 11-1(a) [11-2(a)]. The most distinct feature discovered in the spectrum of Fig. 11-1(a) [11-2(a)] is the sharp steplike feature at 14.323 eV (17.358 eV). In recent PFI-PE-photoion coincidence (PFI-PEPICO) studies at the

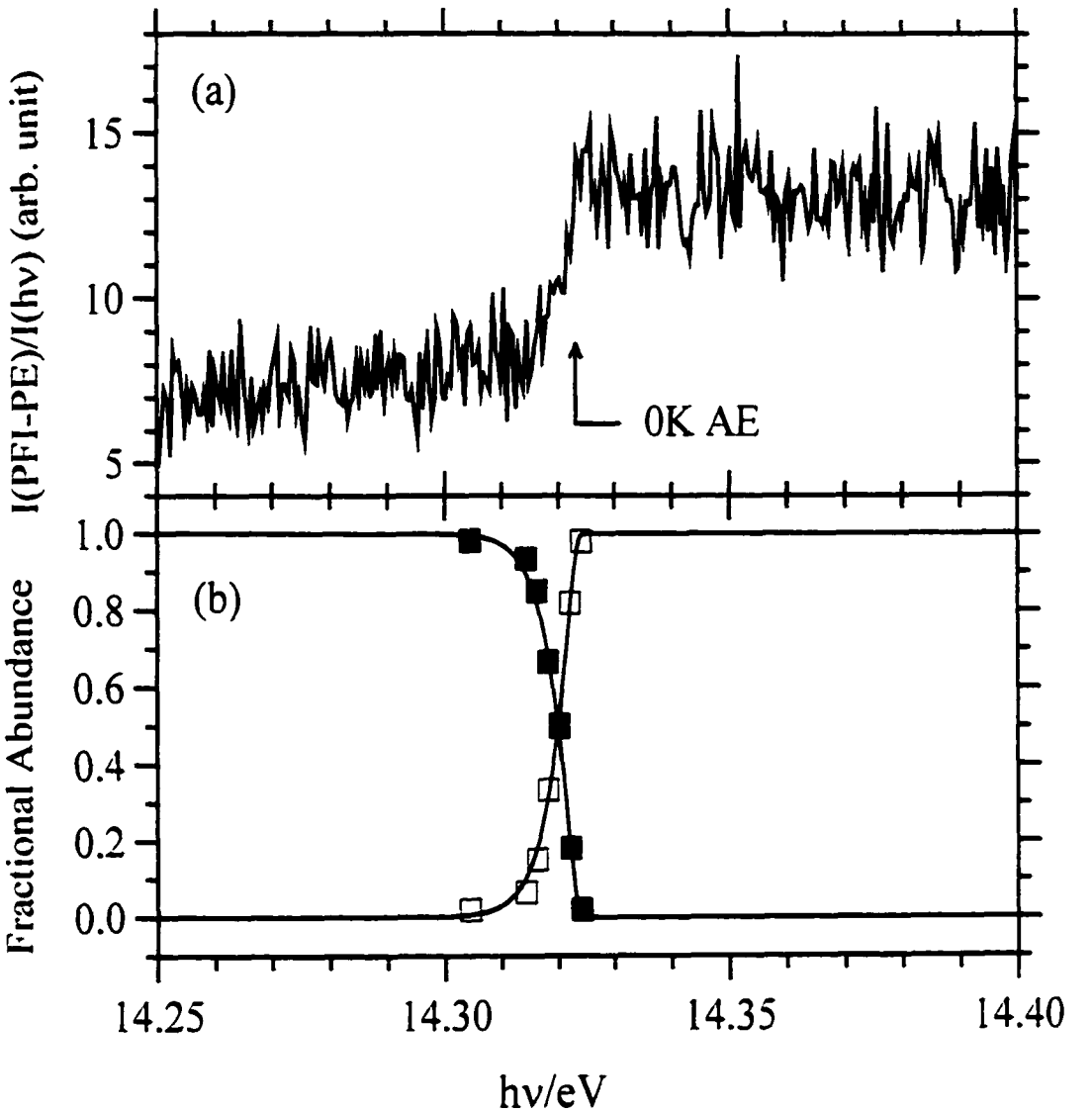

Figure 11-1 Comparison of the PFI-PE spectrum and breakdown diagram for CH_4 in the energy range of 14.25-14.44 eV. **a.** PFI-PE spectrum for CH_4. I(PFI-PE) and I(hν) represent the PFI-PE and VUV intensity, respectively. The arrow marks the 0 K AE for CH_3^+. **b.** The breakdown curves for CH_3^+ (open squares) and CH_4^+ (solid squares) [14].

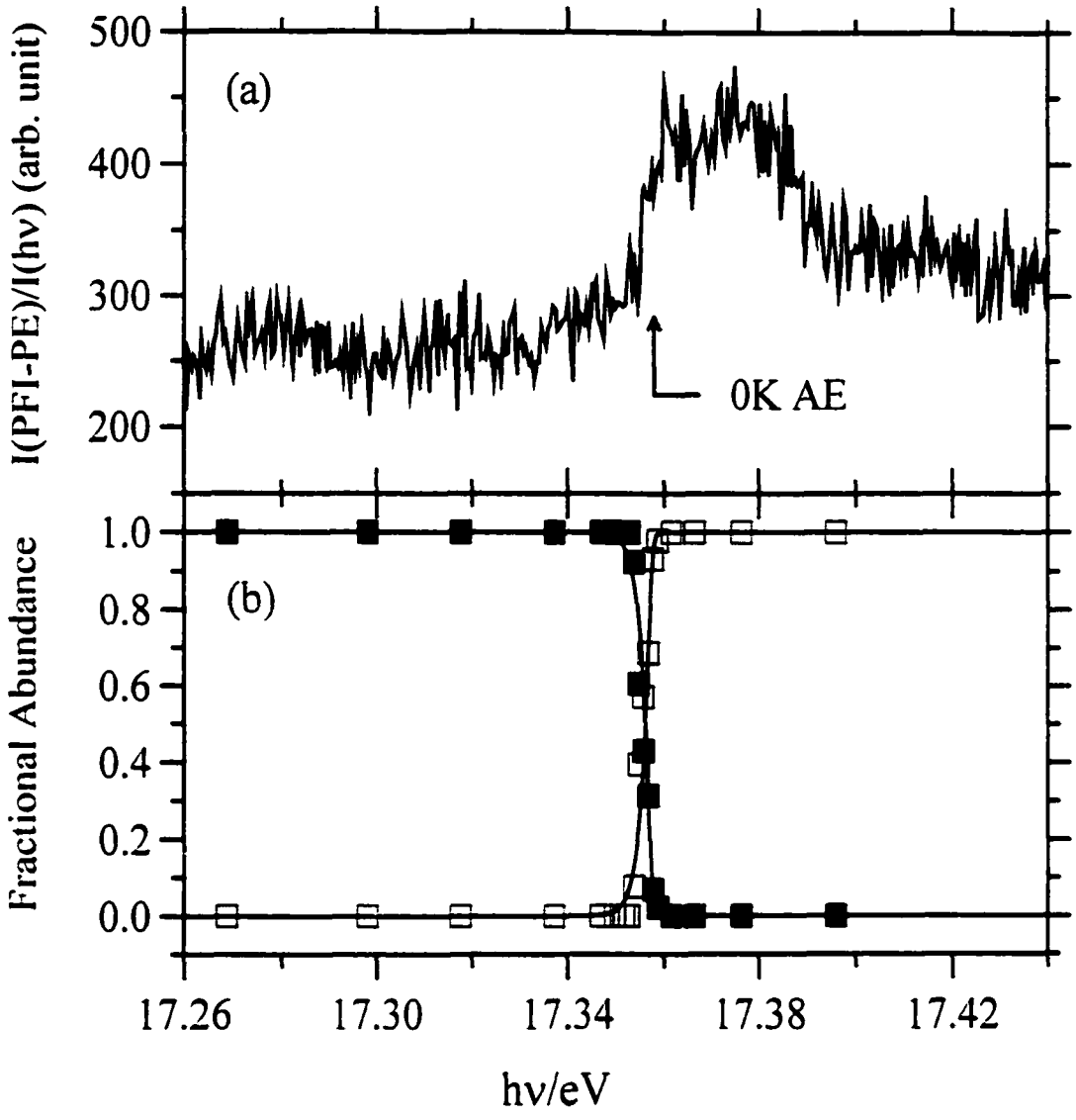

Figure 11-2 Comparison of the PFI-PE spectrum and breakdown diagram for C_2H_2 in the energy range of 17.26-17.40 eV. **a.** PFI-PE spectrum for C_2H_2. I(PFI-PE) and I(hν) represent the PFI-PE and VUV intensity, respectively. The arrow marks the 0 K AE for C_2H^+. **b.** The breakdown curves for C_2H^+ (open squares) and $C_2H_2^+$ (solid squares) [15].

Chemical Dynamics Beamline, we have examined the formation of CH_3^+ (C_2H^+) from CH_4 (C_2H_2) near its threshold [12,14,15]. The breakdown curves for CH_3^+ and CH_4^+ (C_2H^+ and $C_2H_2^+$) are depicted in Fig. 11-1(b) [11-2(b)] for comparison with the PFI-PE spectrum of CH_4 (C_2H_2). The 0 K AE for CH_3^+ (C_2H^+) has been determined as 14.323±0.001 eV (17.3576±0.0010 eV) by the disappearance energy of the parent CH_4^+ ($C_2H_2^+$) ion, i.e. the lowest energy at which the branching ratio for CH_4^+ ($C_2H_2^+$) becomes zero [14,15]. This 0 K AE value for CH_3^+ (C_2H^+) based on the analysis of the breakdown curves of Fig. 11-1(b) [11-2(b)] represents the most accurate experimental value in comparison with previous measurements [1], which fall in the range of 14.23-14.33 eV (17.22-17.36 eV).

The comparison of the PFI-PE spectrum and the breakdown diagram of CH_4 (C_2H_2) reveals excellent correlation between the step observed and the 0 K AE for CH_3^+ (C_2H^+). The analysis of the PFI-PEPICO data for CH_3^+ and CH_4^+ (C_2H^+ and $C_2H_2^+$) has suggested that the formation of CH_3^+ (C_2H^+) from CH_4 (C_2H_2) in PFI proceeds via processes 1(a), 1(b), and 1(d) at energies slightly above the AE, while CH_4^+ ($C_2H_2^+$) ions are produced by processes 1(a) and 1(c) below the AE.

$$\begin{array}{lcccl} & \overset{(a)}{} & & \overset{(b)}{} & \\ CH_4\,(C_2H_2) + h\nu & \longrightarrow & CH_4^*\,(C_2H_2^*) & \longrightarrow & CH_3^*\,(C_2H^*) + H \\ & & \downarrow (c) & & \downarrow (d) \\ & & CH_4^{+*}\,(C_2H_2^{+*}) + e^- & & CH_3^+\,(C_2H^+) + e^- \end{array} \qquad (1)$$

Here, CH_4^* ($C_2H_2^*$) and CH_3^* (C_2H^*) represent excited CH_4 (C_2H_2) and CH_3 (C_2H), respectively, in long-lived high-n Rydberg states and CH_4^{+*} ($C_2H_2^{+*}$) stands for excited CH_4^+ ($C_2H_2^+$). The formation of fragment neutrals in high-n Rydberg states from dissociation of parent species in high-n Rydberg states as shown in process 1(b) has been documented previously [19]. Processes 1(c) and 1(d) are PFI steps. This mechanism, which indicates that CH_4^* ($C_2H_2^*$) fragments into CH_3^* + H (C_2H^* + H) at energies above the AE prior to PFI, is also consistent with the step at the 0 K AE observed in the PFI-PE spectrum. The dominant decay channels for CH_4^* ($C_2H_2^*$) are autoionization and fragmentation. At energies below the AE for CH_3^+ (C_2H^+), the PFI-PE signal is due to

process 1(c) and is proportional to the concentration of CH_4^* ($C_2H_2^*$) species that have survived the decay for a time longer than the delay (Δt) of the PFI pulse relative to the excitation light pulse. For CH_4^* ($C_2H_2^*$) species that have spontaneously autoionized faster than Δt are lost to PFI detection. Assuming that all CH_4^* ($C_2H_2^*$) species are destroyed by the PFI pulse, we estimate Δt to be in the range of 20-552 ns.

The CH_3^* (C_2H^*) species formed at the AE are expected to be in high-n Rydberg levels converging to the ground state of CH_3^+ (C_2H^+), i.e., below the IE of CH_3 (C_2H). Consequently, autoionization is not accessible to these CH_3^* (C_2H^*) fragments. The CH_3^* (C_2H^*) fragments produced at energies slightly above the AE can only autoionize by rotational autoionization. The latter process is known to be much slower than vibrational and electronic autoionization for the case of CH_4^* ($C_2H_2^*$), which lies well above the IE of CH_4 (C_2H_2). Assuming that the decay rates via fragmentation for CH_4^* ($C_2H_2^*$) and CH_3^* (C_2H^*) are similar, we expect that a larger fraction of CH_3^* (C_2H^*) survives the decay than that of CH_4^* ($C_2H_2^*$). Thus, the PFI-PE signal derived from process 1(d) slightly above the AE is higher than that obtained from process 1(c) below the AE. The step marking the 0 K AE in the PFI-PE spectrum can be attributed to the lifetime switching effect at the AE, where CH_4^* ($C_2H_2^*$) species with shorter lifetimes are converted into CH_3^* (C_2H^*) fragments with longer lifetimes. The observation of the sharp steplike feature in the PFI-PE spectrum is consistent with the conclusion that the conversion from CH_4^* ($C_2H_2^*$) to CH_3^* (C_2H^*) is complete prior to process 1(d) and that the dissociation process has a rate constant >> $1/\Delta t$ ($\approx 10^7$ s^{-1}) [14,15]. The observation of a sharp step at the 0 K AE in the PFI-PE spectrum is a sufficient condition for observing sharp breakdown curves as shown in Figs. 11-1(b) and 11-2(b).

For a slow dissociation reaction that the dissociation lifetimes for excited high-n Rydberg species for parent species are longer than Δt, the PFI-PE signal should originate entirely from PFI of excited parent species at energies both below and above the AE. Hence, the PFI-PE spectrum should be smooth across the AE. However, if excited parent ions thus formed completely dissociate within the time scale of the PFI-PEPICO experiment ($\approx 10^{-5}$ s) [12], we still expect to observe complete dissociation at the AE, such

that the disappearance energy of the parent ion can still be used to identify of the 0 K AE [14,15]. This can be considered as an intermediate case, in which the 0 K AE can be determined in a PFI-PEPICO experiment, but not in a PFI-PE study.

According to a previous coincidence study [20], the reaction $C_2H_4 + h\nu \rightarrow C_2H_2^+ + H_2 + e^-$ has dissociation rates of 10^3-10^5 s^{-1} near its 0 K AE (13.135 eV). Thus, the dissociation lifetime of excited $C_2H_4^{+*}$ formed at the AE should be significantly longer than the time scale of the PFI-PEPICO experiment. Figures 11-3(a) and 11-3(b) compare the PFI-PE and PFI-PEPICO data of C_2H_4 in the energy range of 13.11-13.17 eV. The slow varying breakdown curves observed for $C_2H_4^+$ (solid squares) and $C_2H_2^+$ (open squares) are characteristic of the metastable decay of parent $C_2H_4^{+*}$ ions. The fractional abundance for parent $C_2H_4^+$ remains very high (0.7) at the 0 K AE for $C_2H_2^+$ as marked in Fig. 11-3(b). We have simulated these breakdown curves [solid lines of Fig. 11-3(b)] employing a similar procedure described in previous studies [14.15] and using the known 0 K AE and dissociation rate constants [20]. The simulation has taken into account contributions from the dissociation of excited $C_2H_4^{+*}$ and a competition between autoionization and fragmentation of excited neutral species. As expected, the PFI-PE spectrum for C_2H_4 shown in Fig. 11-3(a) is smooth across the 0 K AE for $C_2H_2^+$.

As pointed out above, the requirement for observing a step at the 0 K AE in the PFI-PE spectrum is that the dissociation lifetimes of high-n Rydberg parent species are shorter than Δt, which is in the range of 20-552 ns in the present experiment. We note that the Δt value can be extended by a multiple of 656 ns, i.e., the synchrotron ring period, to a range from 20 ns to several μs [5]. Thus, the 0 K AE values for dissociation reactions with rate constants $\approx 10^6$ s^{-1} can be determined in PFI-PE measurements.

In summary, we report here the first observation of a step at the 0 K AE for CH_3^+ ($C_2H_2^+$) in the PFI-PE spectrum of CH_4 (C_2H_2) and have established the mechanism for such an observation. Similar observations have now been found for other dissociative photoionization reactions [21], which lend further support of this mechanism. For diatomic and triatomic species that have a lower density of states, a discrete peak instead of a step should be discernible at the 0 K AE. This observation in PFI-PE measurements,

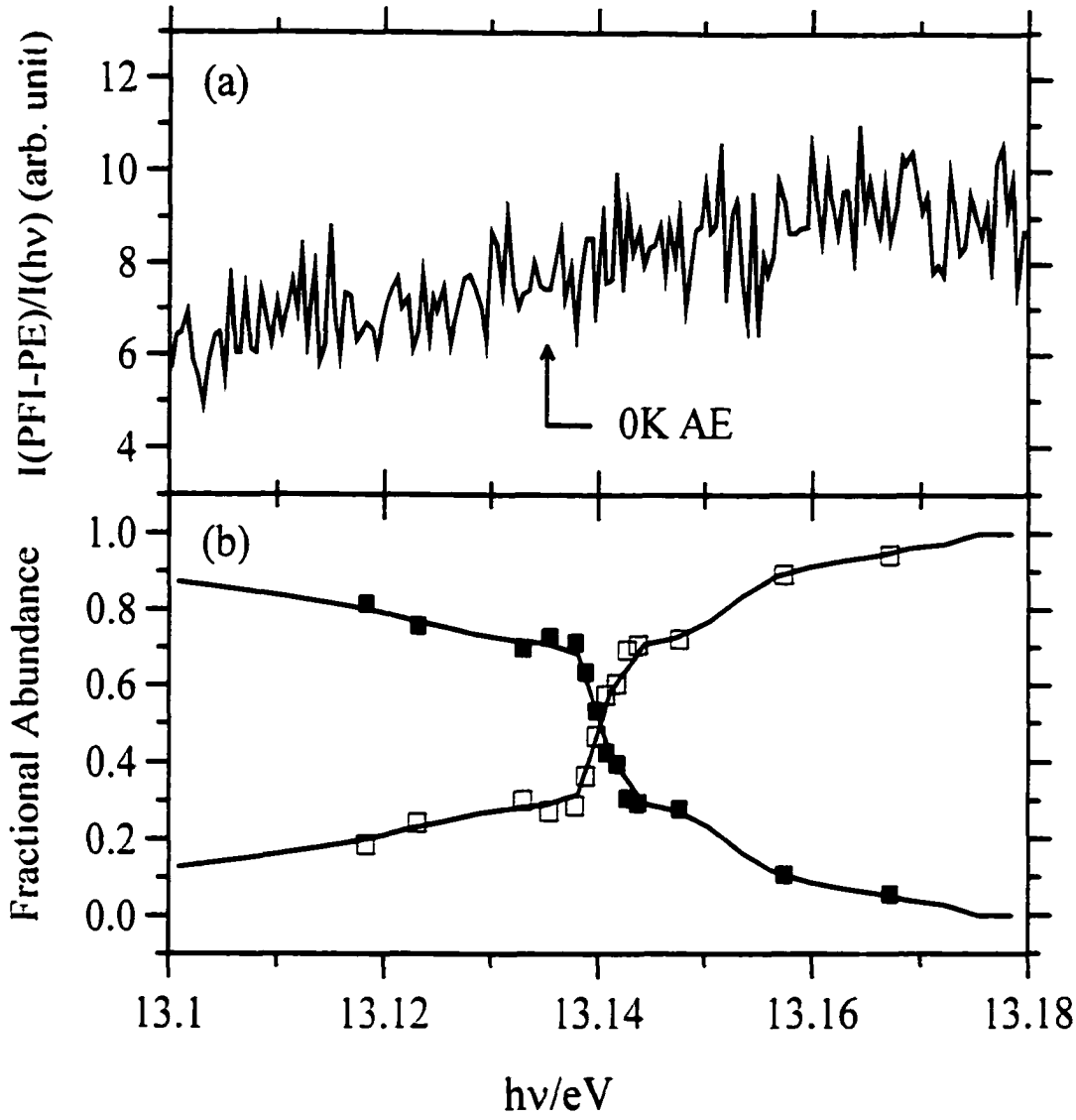

Figure 11-3 Comparison of the PFI-PE spectrum and breakdown diagram for C_2H_4 in the energy range of 13.10-13.18 eve. **a.** PFI-PE spectrum for C_2H_4. I(PFI-PE) and I(hν) represent the PFI-PE and VUV intensity, respectively. The arrow marks the 0 K AE for $C_2H_2^+$. **b.** The breakdown curves for $C_2H_2^+$ (open squares) and $C_2H_4^+$ (solid squares).

together with the breakdown curves obtained in PFI-PEPICO studies, can provide unambiguous 0 K AE values for the dissociation reactions involved, which in turn can yield highly accurate energetic information for simple neutrals and cations.

Acknowledgements

This work was supported by the Director, Office of Energy Research, Office of Basic Energy Sciences, Chemical Science Division of the U.S. Department of Energy. K.M.W. and M.M. acknowledge support by the Deutsche Forschungsgemeinschaft. Y.S. is the recipient of the 2000 Henry Gilman Fellowship at Iowa State University. C.Y.N acknowledges partial support from AFOSR.

References

1. The NIST Chemistry WebBook, http://webbook.nist.gov/chemistry/.
2. J. W. Hepburn, in "Vacuum ultraviolet photoionization and photodissociation of molecules and clusters", edited by C. Y. Ng (World Scientific, Singapore, 1991), p. 435-485.
3. R. T. Wiedmann and M. G. White, in "High resolution laser photoionization and photoelectron studies", edited by I. Powis, T. Baer, T. and C. Y. Ng, *Wiley Series in Ion Chem. and Phys.* (Wiley, Chichester, 1995), p. 79-115.
4. P. Heimann, M. Koike, C. W. Hsu, D. Blank, X.-M. Yang, A. Suits, Y. T. Lee, M. Evans, C. Y. Ng, C. Flaim, and H. A. Padmore, *Rev. Sci. Instrum.* **68**, 1945-1951 (1997).
5. C. Y. Ng, in "Photoionization and photodetachment", edited by C. Y. Ng (World Scientific, Singapore, 2000). *Adv. Ser Phys. Chem.*, Vol. 10A, p. 394-538.
6. K. Müller-Dethlefs, M. Sander, and E. W. Schlag, *Chem. Phys. Lett.* **112**, 291-294 (1984).
7. G. Reiser, W. Habenicht, K. Müller-Dethlefs, and E. W. Schlag, *Chem. Phys. Lett.* **152**, 119-123 (1988).
8. P. M. Johnson, in "Photoionization and Photodetachment", edited by C. Y. Ng (World Scientific, Singapore, 2000), *Adv. Ser Phys. Chem.*, Vol. 10A, p. 296-346.

9. H. Palm and F. Merkt, *Phys. Rev. Lett.* **81**, 1385-1388 (1998).

10. C. W. Hsu, M. Evans, C. Y. Ng, and P. Heimann, *Rev. Sci. Instrum.* **68**, 1694-1702 (1997).

11. G. K. Jarvis, Y. Song, and C. Y. Ng, *Rev. Sci. Instrum.* **70**, 2615-2621 (1999).

12. G. K. Jarvis, K.-M. Weitzel, M. Malow, T. Baer, Y. Song, and C. Y. Ng, *Rev. Sci. Instrum.* **70**, 3892-3906 (1999).

13. G. K. Jarvis, R. C. Shiell, J. Hepburn, Y. Song, and C. Y. Ng, *Rev. Sci. Instrum.* **71**, 1325 (2000).

14. K.-M. Weitzel, M. Malow, G. K. Jarvis, T. Baer, Y. Song, and C. Y. Ng, *J. Chem. Phys.* **111**, 8267-8270 (1999).

15. G. K. Jarvis, K.-M. Weitzel, M. Malow, T. Baer, Y. Song, and C. Y. Ng, *Phys. Chem. Chem. Phys.* **1**, 5259-5262 (1999).

16. T. Baer, Y. Song, C. Y. Ng, W. Chen, and J. Liu, *J. Phys. Chem.* **104**, 1959-1964 (2000).

17. The 0 K AE is defined to be the energy difference between the ground state of the parent neutral molecule and the top of the dissociation barrier for the corresponding parent cation.

18. S. Stimson, Y.-J. Chen, M. Evans, C.-L. Liao, and C. Y. Ng, C.-W. Hsu, and P Heimann, *Chem. Phys. Lett.* **289**, 507-515 (1998).

19. M. Ukai, S. Machida, K. Kamera, M. Kitajima, N. Kouchi, Y. Hatano, and K. Ito, *Phys. Rev. Lett.* **74**, 239-242 (1995).

20. M. Malow, F. Güthe, and K.-M. Weitzel, *Phys. Chem. Chem. Phys.* **1**, 1425-1429 (1999).

21. Y. Song, X.-M. Qian, K.-C. Lau, C. Y. Ng, J. Liu, and W. Chen, to be published.

CHAPTER 12. SUMMARY

In this thesis, we discussed two major applications developed at Chemical Dynamics Beamline (CDB) at the Advanced Light Source (ALS), i.e. the high-resolution pulsed field ionization photoelectron spectroscopy and photoelectron photoion coincidence spectroscopy.

In chapter 2, we demonstrated the powerfulness of photoelectron spectroscopy realized by the VUV synchrotron radiation. Due to the extreme brightness, the ease of continuous tenability in a broad VUV energy range and its stability, the third generation synchrotron radiation light source plays a key role in the high efficiency and productivity achieved in the research projects at ALS, making the high-resolution photoelectron spectrum measurement an routine operation. Using the 6.65 eagle monochromator together with the electron time-of-flight selection scheme in the multi-bunch operation mode of ALS synchrotron radiation, we successfully achieved a hot-electron free background suppression and a spectral resolution almost comparable to the traditional VUV laser light source.

We applied this efficient electron time-of-flight selection scheme to the investigation of pulsed field ionization photoelectron spectra of several excited electronic states of oxygen cation and nitrogen oxide cation. Chapter 3-5 discussed the first three excited states of O_2^+, i.e. $X^2\Pi_g$, $A^2\Pi_u$ and $a^4\Pi_u$ in the energy range of 12.05-18.20 eV chapter 6 reported the analysis of $NO^+(A'^1\Sigma^-, v^+ = 0\text{-}17)$ in the energy range of 17.70-20.10 eV. Many of these vibrational bands are rotationally resolved for the first time. The most useful information obtainable from these high-resolution studies is the spectroscopic constant, including the ionization energies, vibrational constants, rotational constants and spin-orbit coupling constant if applicable. The comprehensive simulation based on BOS model not only allows the unambiguous identification of individual vibrational bands in case of degeneracy, but also provides useful information of the intensity distribution, which indicates possible excitation, ionization or interaction/perturbation mechanisms.

Section II focuses on the application of the pulse field ionization technique on the photoelectron photoion coincidence spectroscopy. In chapter 7, we discussed in detail the

development of the so-called PFI-PEPICO under different stages. Using this scheme in tow and multi-bunch sychrotron radiation mode, we have studied the dissociation of O_2^+ in a roational level, $O_2^+(b^4\Sigma_g^-, v^+=4, N^+=9)$. We also demonstrated the PFI-PEPICO investigation on other molecules, such as HCl, CH_4 and some noble gases. Compared to the traditional threshold photoelectron photoion coincidence (TPEPICO) method, the resolution achieved in PFI-PEPICO is greatly improved, with a routine energy resolution of 0.5~1 meV, which is only limited by the PFI photoelectron detection.

One piece of important information derivable from the PFI-PEPICO study is the accurate determination of 0K appearance energy (AE) of fragment ion from the dissociation of parent molecules. In chapter 8-10, we determined the 0K AE of NH_2^+, CH_3^+ from CH_3Br and CH_3I, and CD_3^+ with unprecedented precisions. Using appropriated thermochemical cycles, other thermochemical quantities, such as the 0K heat of formation, bond dissociation energy can be derived accurately. In addition, we consistently observed step-like feature in the photoelectron spectrum exactly at the dissociation energy point. This important observation has shed light on the possible lifetime switching mechanism between the parent and daughter ions in the ionization and dissociation processes, which was discussed in detail in chapter 11.

ACKNOWLEDGEMENT

The first person I should thank is my advisor, Prof. Cheuk-Yiu Ng, who gives me a unique chance to work in the Advance Light Source, where I believe is one of the best laboratories in the world in this field. I greatly appreciate his academic support, technical guidance, even personal care on me.

I would like to thank Dr. Gary K. Jarvis, who was a postdoctoral fellow at the Chemical Science Division of LBL from 1998-1999. He was the person who introduced me into experiment at the beamline before we formed a research team of two people for about one year. His experimental as well as theoretical expertise has been a precious resource to me for a long time even after he left.

Matt Evans, a former graduate student of this group, who graduated in the summer of 1999, is one of the most helpful people I have ever met since I came to the United States. As a senior student, he not only shared with me his precious experience in many aspects without any reservation, but also helped me a lot for either academic or non-academic needs.

Working in ALS with visiting or local scientist and technician has been a very valuable experience in my career. These outstanding people give me lots help in many ways. I would like to thank Dr. Arthur Suits, who was the group leader of the Chemical Dynamic Beamline for his supervision in the capacity of my immediate advisor for my research. I would also like to thank those whom I had worked with and who had helped me, such as Tomas Baer, Philip Heimann, Wayne McKinney, Alan Robb, Frank Zucca, Donna Hamamoto, Vladimir Moroz, Ed Wong, Harry Meyer, Steve Klingler, Cheryl Hauck, Steve Irick, Charles Knopf, Dennis Hull, Gary Giangrasso, Barbara Srulovitz, Musa Ahmed, Darcy Peterka, Fei Qi, Wenwu Chen, Jianbo Liu and Ximei Qian.

At last, I also would like to thank the support from my family in China. Within four years of graduate study in the United States, I believe I learned lots of useful expertise for my lifelong career. The publication of my thesis, the honorary fellowships and the title of Ph.D. will be a great reward to me, my family and all the people who had helped me.